EFFECTS OF GEOMETRIC CONFIGURATION ON PERFORMANCE OF A SOLAR AIR HEATER

Kishor Kulkarni and Kwang-Yong Kim.*
*Author for correspondence
Department of Mechanical Engineering,
Inha University,
253 Younghyun-dong, Incheon, 402-751,
Republic of Korea,
E-mail: kykim@inha.ac.kr

ABSTRACT

The objective of this study is to investigate the thermal-hydraulic performance of a solar air heater (SAH) using three-dimensional Reynolds-averaged Navier-Stokes (RANS) analysis. The performance evaluation of SAH is examined to find out the optimum shape of obstacles mounted on the absorber plate. Four different obstacle shapes and three configurations were tested to determine the performance of SAH. The effect of the obstacle shape and configuration on heat transfer, friction factor and performance enhancement was investigated covering different range of Reynolds number. The maximum heat transfer augmentation by using an obstacle mounted SAH was 3 times higher compared with the smooth duct under similar geometrical and flow condition. Temperature and velocity contours are analysed in order to have better insight of SAH.

INTRODUCTION

Solar air heater is one of the simplest and cost effective solar energy utilization systems, utilized for various heating and drying applications. The thermal efficiency of solar air heaters is poor due low heat transfer coefficient between absorber plate and the air flowing in the collector. In order to make the SAH economically viable, their thermal efficiency needs to be improved by enhancing the heat transfer coefficient. Thermal performance of the SAH depends upon the material, shape, dimension and layout of the collector. The modification to improve the performance of SAH includes absorber with fin attached, corrugated absorber, ribs and regular geometrical roughness. However, increase in heat transfer is accompanied by an increase in the resistance to fluid flow. Comprehensive review on roughness geometries and correlations of SAH is highlighted [1] and detailed survey about different CFD investigations has been presented [2]. Numerical investigation [3-7] is performed for the improvement of performance factor of artificially roughened SAH having arc shape, circular, square, semi-circular and triangle transverse wire rib roughness on the absorber plate. Experimental investigation for energy and exergy analysis of a novel flat plate SAH with and without obstacles has been approached [8]. They showed that largest irreversibility occurs at the SAH without obstacle. Evaluation of heat transfer performance of rib roughened rectangular cooling channel having 16 rib shapes has been performed [9]. In this paper, the performances of the SAH with different shapes (U-shaped, rectangular, trapezoidal, and pentagonal) and configurations of obstacles were evaluated. The friction factor and Nusselt number were used to examine the thermal performance of the SAH configurations.

NOMENCLATURE

b	[m]	base of obstacles
D_h	[m]	equivalent hydraulic diameter of the air passage
e	[m]	obstacle height
e/H	[-]	height of relative obstacle
f	[-]	friction factor
h	[W/m^{2}K]	convective heat transfer coefficient
H	[m]	duct height
k	[W/mK]	thermal conductivity of air
L	[m]	test section duct length
Nu	[-]	Nusselt number
ΔP	[Pa]	pressure drop across the test section
PF	[-]	performance factor
P_l	[m]	longitudinal space between rows of obstacles
P_t	[m]	transverse distance between two obstacles
$P_{l/e}$	[-]	relative obstacle longitudinal pitch
$P_{t/b}$	[-]	relative obstacle transversal pitch
Re	[-]	Reynolds number
U	[m/s]	Average velocity of air
W	[m]	duct width
W/H	[-]	W/H aspect ratio

Special characters

ρ	[kg/m^3]	density of air

Subscripts

o	Obstacle duct
s	Smooth duct

NUMERICAL ANALYSIS

Figure. 1 show the SAH model and Figure 2 shows the shape of obstacles and different configurations used to analyse the SAH model having dimension 1.2m x 0.3m x 0.05m. The top wall (absorber plate) is heated, and the air gets heated as it moves

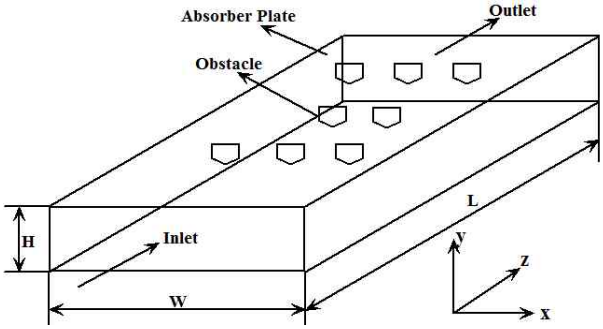

Figure 1.SAH Model

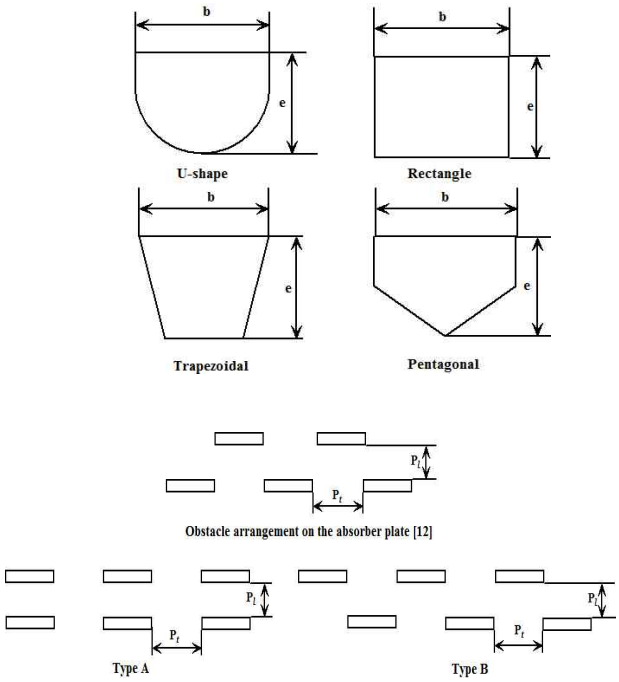

Figure 2. Obstacle shape and Configuration

from inlet to outlet. Different shaped obstacles are mounted on the underside of the absorber plate while the other sides are considered as smooth surface. The width (b = 0.03m) and height of obstacle (e = 0.025m) were kept constant for all obstacle shapes. Numerical analyses of fluid flow and heat transfer were carried out using the commercial CFD code, ANSYS CFX-14.5 [10]. Turbulence is taken into account by using the k-ε model and advanced wall treatment [6, 11]. Unstructured tetra mesh was used in most of the computational domain and prism mesh was used near walls. High resolution scheme was selected for discretizing the advection terms of the governing equations. A turbulence intensity of 5% and auto computed length scale were selected for inlet turbulence conditions. The convergence criterion for monitoring residuals is of order of 10^{-8}.

BOUNDARY CONDITION

The computational domain was selected as a half of the SAH domain enclosed by inlet, outlet, symmetric plane, and walls. A constant hear flux was supplied to the absorber plate. The thermo-physical properties of the working fluid (air) were obtained at ambient temperature. No-slip conditions were assumed on walls for momentum equations.

PERFORMANCE PARAMETER

The average heat transfer coefficient is given in terms of Nusselt number (Nu) as follows:

$$Nu = hD_h/k \quad (1)$$

The friction factor, f was evaluated from the measured value of the pressure drop across the test section (ΔP) as follows:

$$f = (\Delta P)D_h/2\rho LU^2 \quad (2)$$

To evaluate the performance of the SAH based on heat transfer characteristics and pressure drop, the performance factor [12] is defined as

$$PF = \left(Nu_o/Nu_s\right)\Big/\left(f_o/f_s\right)^{1/3} \quad (3)$$

RESULTS AND DISCUSSION

For validation of numerical scheme with experimental results for triangular shape obstacle was performed for both ducts with and without obstacles. The numerical results exhibit average relative errors of 3.5% and 3.8%, respectively, for Nusselt number (Figure 3) compared to experimental data [12].

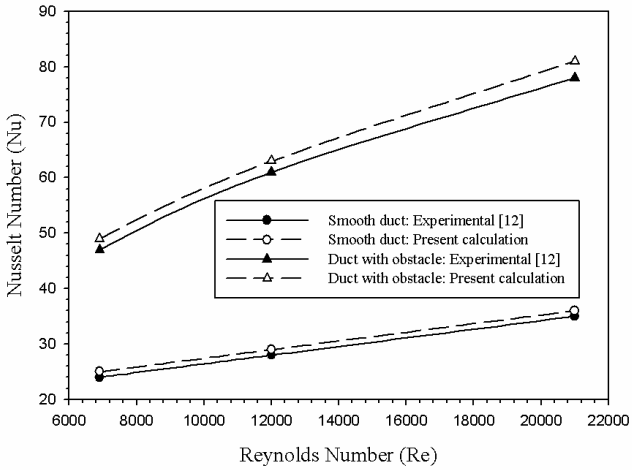

Figure 3 Validation of numerical results for Nusselt number compared to experimental data [12].

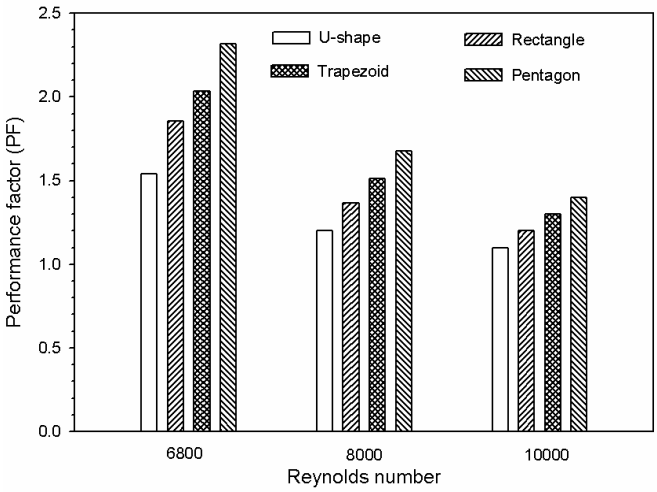

Figure 4 Variation of performance factor (PF) with Reynolds number for different obstacle shapes.

The numerical analysis has been performed for SAH, for various shape obstacle attached to the duct wall over a range of Re numbers. The average heat transfer/flow friction characteristics of the SAH are explored first, and then the effects of flow/roughness parameters are discussed. Figure 4 shows variations of the performance factor (PF) with Reynolds number for various obstacle shapes. It has been found that the PFs are greater than unity for the different obstacle shapes, with the pentagonal shape indicating the highest value of 2.31 at Re = 6,800. The performance factor decreases with an increase in the Reynolds number. To study the effect of obstacle arrangement on heat transfer characteristics and friction factor, additional two configurations of obstacles were tested (Type A and Type B, as shown in Fig. 2. Compared to the arrangement shown [12], an additional row of obstacles was inserted in both configurations. The average ratios of Nu, and friction factors (*f*) for U-shaped, rectangular, trapezoidal, and pentagonal obstacles to those of a smooth duct are shown in Figure 5 and Figure 6. The predicted values of Nu number indicates significant enhancement compared to the results of smooth duct. Comparison of the heat transfer results for the configuration A with those of configuration B indicates that there is marginal variation in heat transfer characteristics [Figure 5] and a significant reduction in friction factor [Figure 6]. The improvement in the performance factor for different configuration is shown in Figure 7. The performance factor incorporates both the thermal as well as hydraulic consideration with respect to the performance of the SAH. The PFs are above unity for different obstacle shapes and configurations. The performance factor for configuration Type-A is relatively good with those of Type-B. Also, the performance factor deteriorates with an increase in the Reynolds number for the cases studied.

A 3-D temperature contour plot for SAH with pentagonal shaped obstacle mounted on the absorber plate for Re = 6,800 is shown in Figure 8. A variation in temperature inside the SAH

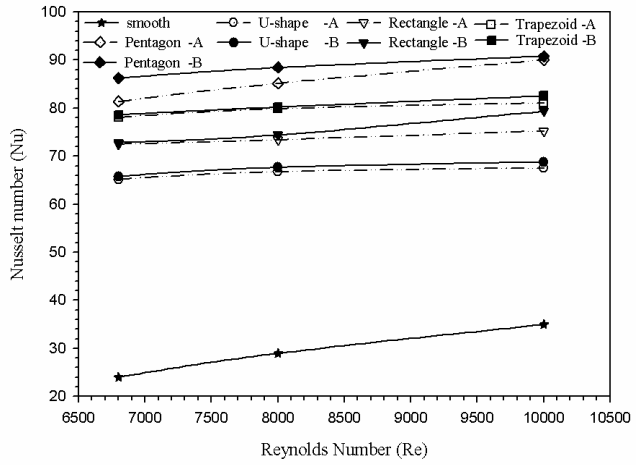

Figure 5 Variation of Nusselt number with Reynolds number for different configuration.

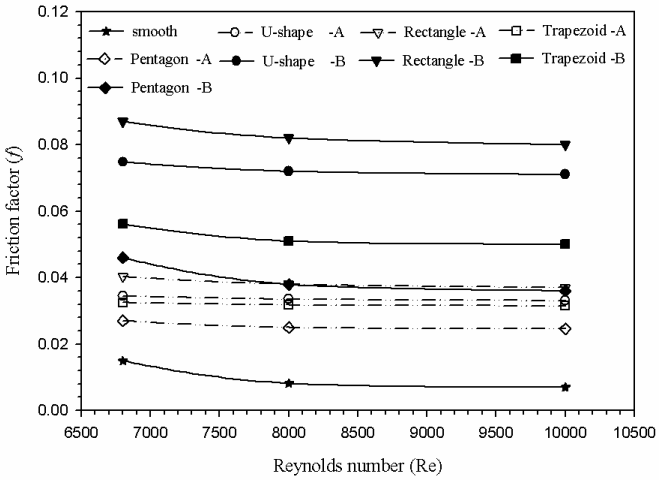

Figure 6 Variation of friction factor with Reynolds number for different configuration.

is induced by air flowing from the inlet to the outlet. The temperature is higher near the obstacle, periphery which contributes to higher heat transfer. The production of turbulent kinetic energy is promoted near the edges of the obstacles and near the walls. The adiabatic side wall of the SAH affects the temperature uniformity because higher temperature zones are found near the wall. Figure 9 show the streamlines in the SAH duct. The flow gets separated from the wall and is reattached before reaching the next obstacle, and this flow structure increases the heat transfer.

CONCLUSION

An attempt has been made to evaluate the performance factor of obstacle mounted SAH. The combine effect of obstacle shape and configuration is considered to be responsible in the increment of heat transfer and friction factor

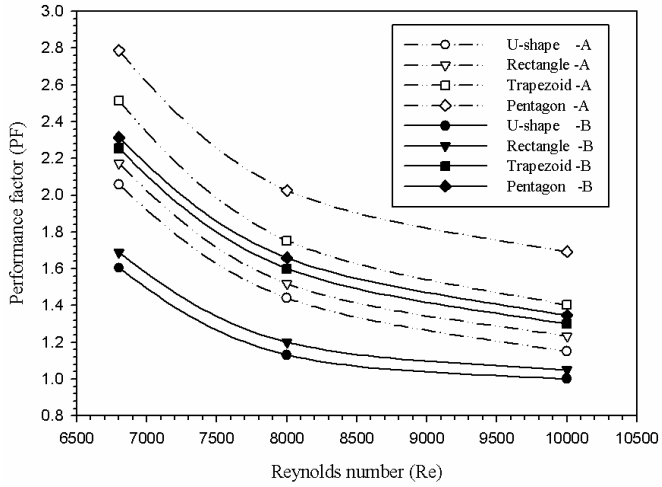

Figure 7 Variation of performance factor (PF) with Reynolds number for different configuration.

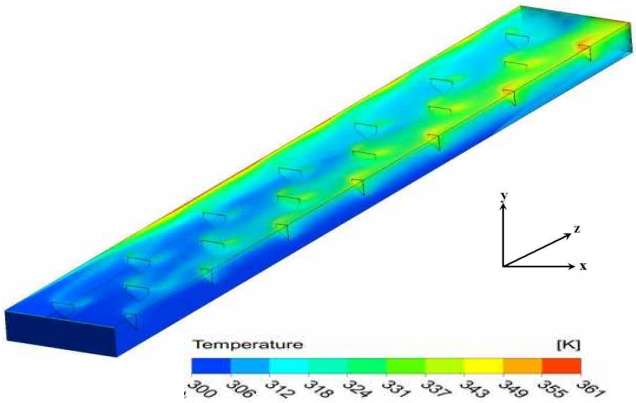

Figure 8 Temperature distribution inside SAH for pentagonal shape obstacles at Re=6800.

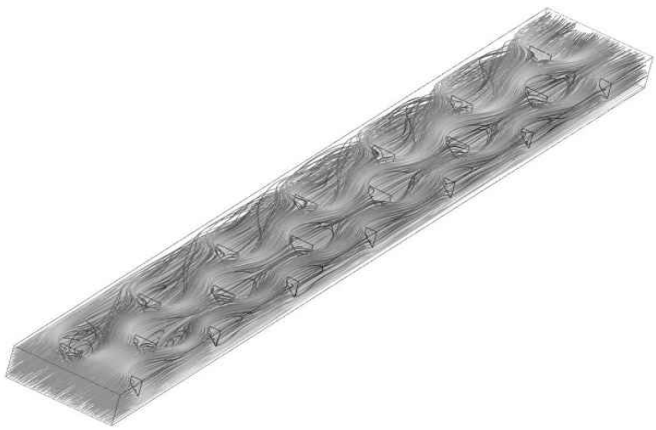

Figure 9 Streamlines for pentagonal obstacles at Re= 6,800.

characteristics. Nusselt number has been found to increase whereas friction factor decreases with increase in Reynolds number for all combinations. Among the tested configuration Type-B shows the highest Nusselt number and Type-A configuration shows the lowest friction factor. A significant enhancement in the value of the thermo-hydraulic performance parameter has been found. The value of the thermo-hydraulic performance parameter varies between 1 and 2.32 for different cases investigated.

ACKNOWLEDGMENT

This work was supported by the National Research Foundation of Korea (NRF) grant funded by the Korean government (MSIP) through the Multi-phenomena CFD Engineering Research Center (No. 2009-0083510).

REFERENCES

[1] Varun, Saini R.P., Singal S.K., "A review on roughness geometry used in solar air heaters", Solar Energy, 81, 1340-1350, 2007.
[2]A.S. Yadav, J.L. Bhagoria, Heat transfer and fluid flow analysis of solar air heater: a review of CFD approach, Renewable Sustainable Energy Rev. 23 (2013) 60–79.
[3] S. Kumar, R.P. Saini, CFD based performance analysis of a solar air heater duct provided with artificial roughness, Renewable Energy 34 (2009) 1285–1291.
[4]A.S. Yadav, J.L. Bhagoria, A CFD based heat transfer and fluid flow analysis of a solar air heater provided with circular transverse wire rib roughness on the absorber plate, Energy 55 (2013) 1127–1142.
[5]A.S. Yadav, J.L. Bhagoria, Numerical investigation of flow through an artificially roughened solar air heater, Int. J. Ambient Energy, 2013. DOI: 10.1080/01430750.2013.823107.
[6] A.S. Yadav, J.L. Bhagoria, A numerical investigation of turbulent flows through an artificially roughened solar air heater, Numerical Heat Transfer, Part A, 65: 679-698, 2013.
[7]A.S. Yadav, J.L. Bhagoria, A CFD based thermo hydraulic performance analysis of an artificially roughened solar air heater having equilateral triangular sectioned rib roughness on the absorber plate. International Journal of Heat and Mass Transfer. 70, 1016-1039, 2014.
[8] Akpinar E. V and Kocyigit F. Energy and exergy analysis of a new flat plat solar air heater having different obstacles on absorber plates. Applied Energy 87 (2010) 3438-3450.
[9] Mi-Ae Moon, Min-Jung Park and K.Y. Kim. Evaluation of heat transfer performance of various rib shapes. International Journal of Heat Mass Transfer 71 (2014) 275–284.
[10] Kim K Y, Lee YM. Design optimization of internal cooling passage with V-shaped ribs. Numerical heat transfer Part A- Application 2007; 11: 1103-16.
[11] CFX-14.5 Solver Theory, Ansys Inc; 2012.[12] Bekele A, Mishra M, Dutta S. Heat transfer augmentation in solar air heater using delta shaped obstacle mounted on the absorber plate. Int J of Sustainable Energy 2013; 32(1):53-69.
[13] Webb RI, Eckert ERG, Application of rough surface to heat exchanger design. International Journal of Heat and Mass Transfer 1972; 15: 1647-58.

MODAL REDUCTION OF LATENT HEAT STORAGE UNIT

Brou S.*, Joly F. and Neveu A.
*Author for correspondence
Laboratoire de Mécanique et d'Energétique d'Evry,
40 rue du Pelvoux CE1455 Courcouronnes
91020 Evry Cédex,
France,
E-mail: s.brou@iut.univ-evry.fr

ABSTRACT

Numerical modeling of latent heat storage unit needs a relatively fine meshing, which leads to large order models. So, for classic simulations in software such as Matlab, C ++ or Fortran, the concept of sparse matrix allows to have good computational time performance. However, in the Simulink environment, in which we develop a numerical simulator of combined heat and power (CHP) system, this notion does not exist. The handling of large-sized matrices leads to inconsistent simulation time with such a decision support tool. To solve this problem, we propose in this paper a reduced model obtained by using branch basis and amalgam method. The integration of this reduced model in the numerical simulator allows reducing simulation times up to a factor 36, for an acceptable precision.

NOMENCLATURE

M		spatial parameter
x_i	[-]	state of the i-eigenmode
V_i	[K or °C]	eigenvector of the i-eigenmode
k	[W/mK]	Thermal conductivity
c	[J/kg.K]	Heat capacity at constant pressure
T	[°C]	Temperature
Re	[-]	Reynolds number
Nu	[-]	Nusselt number
Pr	[-]	Prandtl number
Ra	[-]	Rayleigh number
r	[m]	Node radius, radial coordinate
f_l	[-]	Liquid fraction
u	[m/s]	Velocity
v	[m^3]	Volume
h	[$W/m^2.K$]	Convective heat transfer coefficient
ΔH	[J/kg]	Latent heat of fusion
T_{fus}	[K]	Melting temperature
$f_i(z)$	[-]	hyperbolic or sine function
L	[m]	Length
t	[s]	Time
z	[m]	Axial coordinate

Special characters

δt	[s]	Time step
λ_i	[s^{-1}]	eigenvalue of the i-eigenmode
ρ	[kg/m^3]	Density

Subscripts

eq	Equivalent
in /ef	Inlet
sf	Outlet
s	Solid
l	Liquid
f	HTF
m	PCM
e/env	External

INTRODUCTION

In France, the sector of building is the biggest energy-consuming, with a consumption estimated at 43% of the total consumption of energy, generating 25% of CO2 emissions. Besides, the energy efficiency policies strongly promote the use of renewable energy. It is in this framework that we develop a numerical simulator of CHP system, using renewable energy (Research Program Batimac, in association with the ENS2R Company). This decision support tool must be fast and accurate to dimension and evaluate the performance of the Batimac system.

The thermal storage with phase change material (PCM) is a key component of this system. It is used to provide the balance between energy availability and energy demand.

Generally, the modeling of this type of equipment is performed by finite elements method [1], finite differences method [2] or finite volume method [3], which leads to a numerical resolution where the treated matrices are of large size. Fortunately the concept of sparse matrix allows fast resolution of this high order problem with software such as Matlab, C ++ or Fortran. However, the Simulink environment in which we develop a numerical simulator of Batimac system, does not adapt well to these detailed models (DM), since the concept of sparse matrix does not exist. It is therefore interesting to use the modal reduction methods [4-6] to have a good computational time performance while keeping an acceptable precision.

In this paper, we are looking at the modal reduction of latent heat storage unit. In order to take into account the non-linear thermal problem and its non-homogeneous boundary conditions in the modal representation, the temperature fields of heat transfer fluid (HTF) and PCM are decomposed on a branch basis. The branch basis [6-8], whose specificity is its boundary condition that involves the eigenvalue, is obtained by solving an eigenvalue problem based on the heat equation. The reduction is performed by the amalgam method [10], in which the most influential modes are kept, the remaining modes being aggregated in order to keep a maximum of spatial information. The reduced model (RM) is obtained via the projection of the thermal problems associated with the HTF and the PCM on the corresponding reduced bases.

After being validated by confrontation with the experimental results of [2], this model will be compared with the detailed model in terms of deviations in temperature and computing time gains in Matlab software. Finally, a reduced

model and a detailed model of thermal storage unit will be integrated into the numerical simulator in order to highlight the modal reduction interest in simulation environments such as Simulink.

PHYSICAL PROBLEM

The latent heat storage system planned in Batimac is in the form of a vertical cylinder containing multiple shell-and-tube storage units (Figure 1).

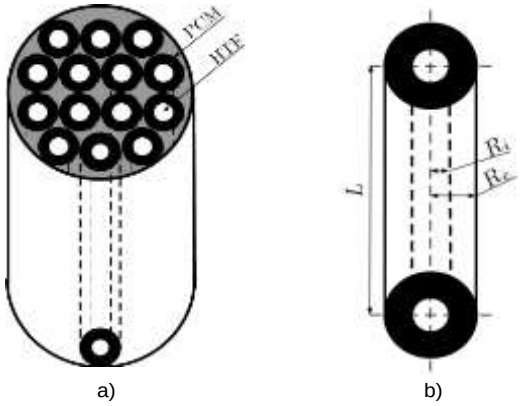

Figure 1 System (a) and unit (b) of PCM heat storage

In this configuration the HTF circulates freely in the inner tube of radius R_i while the PCM is confined in the ring of external diameter R_e. Transient heat transfer and phase change process in the PCM are coupled with the convective heat transfer in HTF.

MATHEMATICAL MODEL

To establish the governing equations, the following assumptions are made :

1) The PCM is isotropic and its thermal conductivity is homogeneous.
2) The thermal resistance of the inner tube is negligible.
3) The thermo-physical properties of the HTF are independent of temperature.
4) The convective heat transfer coefficient between the PCM and HTF is obtained by:

$$h_o = \frac{k_f\, Nu}{2R_i} \quad \text{, where} \qquad Nu = 0.023 R_e^{0.8} P_r^{0.33} \tag{1}$$

5) The effect of natural convection that occurs during melting is taken into account through an equivalent thermal conductivity of the liquid phase [9]:

$$k_{eq} = k_l\, Cr\, R_a^n \left(\frac{\delta}{R_e - R_i}\right)^n \tag{2}$$

6) The thermal conductivity of the PCM depends on the average liquid fraction (and thus of the temperature):

$$k_m = k_{eq} f_{lm} + k_s (1 - f_{lm}) \tag{3}$$

7) The PCM is modelled in 2D - axisymmetric and the HTF is supposed to be 1D.

The computation domain is represented in Fig. 2. With these assumptions, the energy equations write :

- For HTF domain (Ω_f)

$$R_i \rho_f c_f \left(\frac{\partial T_f}{\partial t} + v \frac{\partial T_f}{\partial z}\right) = R_i k_f \frac{\partial^2 T_f}{\partial z^2} + 2h_o \left(T_m|_{\Gamma_p} - T_f\right) \tag{4}$$

with the following boundary conditions:

$$\forall\, M \in\ \Gamma_{ef},\ \ T_f = T_{in} \tag{5}$$

$$\forall\, M \in\ \Gamma_{sf},\ \ k_f \vec{\nabla} T_f \cdot \vec{n} = 0 \tag{6}$$

- For PCM domain (Ω_m)

Following [1-3] or [9], the enthalpy method is used to deal with the problem of phase change in the PCM. The energy equation is therefore :

$$r \rho_m c_m \frac{\partial T_m}{\partial t} = k_m \left(r \frac{\partial^2 T_m}{\partial r^2} + \frac{\partial T_m}{\partial r} + r \frac{\partial^2 T_m}{\partial z^2}\right) - r \rho_m \Delta H \frac{\partial f_l}{\partial t} \tag{7}$$

associated with :

$$\forall\, M \in\ \Gamma_p,\ \ R_i k_m \vec{\nabla} T_m \cdot \vec{n} = R_i h_o \left(T_f - T_m\right) \tag{8}$$

$$\forall\, M \in\ \Gamma_{env},\ \ r k_m \vec{\nabla} T_m \cdot \vec{n} = r h_{env} (T_{env} - T_m) \tag{9}$$

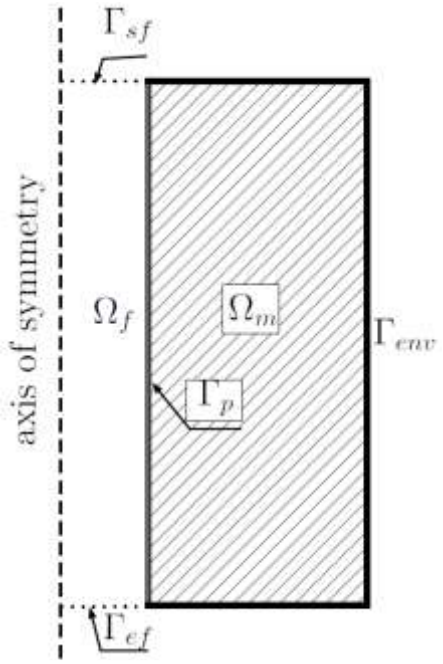

Figure 2 Domains and boundaries

In equation (7), the liquid fraction (f_l) is computed by:

$$f_l(t + \delta t) = f_l(t) + \frac{\rho_m c_m}{\Delta H} \left[T_m(t) - T_{fus}\right] \tag{10}$$

submitted to the conditions :

$$f_l = \begin{cases} 0 & \text{if } f_l \le 0 \\ 1 & \text{if } f_l \ge 1 \end{cases} \tag{11}$$

DETAILED NUMERICAL MODEL (DM)

The detailed numerical model of a heat storage unit is obtained with conventional modeling methods. The finite difference method is used for spatial discretization of Eqs. (4)-(9), leading to the following matrix formulation:

$$\begin{cases} \mathbb{C}_f \dot{T}_f = \left(\mathbb{K}_f + \mathbb{F}\right) T_f + \mathbb{G}_f T_m + \mathbb{B}_f T_{in} \\ \mathbb{C}_m \dot{T}_m = (\mathbb{K}_m + \mathbb{H}) T_m + \mathbb{G}_m T_f + \mathbb{L}_m \dot{f}_l + \mathbb{B}_m U_m \end{cases} \quad (12)$$

Where:

- $\mathbb{C}$: a diagonal matrix of capacities, size [N×N]
- $\mathbb{K}$: matrix of conductivities
- $\mathbb{H}$: matrix containing the boundary condition
- $\mathbb{F}$: advection matrix for the HTF
- $\mathbb{B}$: the solicitation matrix
- $\mathbb{L}$: Latent heat matrix
- $\mathbb{G}$: coupling matrix between HTF and PCM
- $U_m = (T_{in},\ T_{env})^t$ solicitation vector

The time integration of Eq. (12) is performed via an implicit first order Euler scheme.

As the modelisation of PCM requires fine mesh, the detailed model (Eq. (12)) involves tri-diagonal by bloc matrices of large size (N). Thus, due to the sparse function, the numerical solution of this problem in environments such as C++, Fortran or Matlab is fast. However, this notion of sparse matrix does not exist in the Simulink environment. It is therefore necessary to reduce the size of the model while keeping an acceptable accuracy.

REDUCED ORDER MODEL (RM)

Modal analysis methods are used to reduce the unknowns of a system in order to perform a fast calculation. In a modal formulation, the temperature field is expressed as a sum of elementary thermal fields (the modes) weighted by their temporal amplitudes (also named excitation states).

$$T(M,t) = \sum_{i=0}^{N} [x_i(t) \times V_i(M)] \quad (13)$$

Or in matrix form:

$$T(M,t) = \mathbb{P}X \quad (14)$$

where $\mathbb{P}$ is a basis formed by the horizontal concatenation of modes and X is a vector combining the excitation states. The choice of the modes is of course determinant for the quality of the approximation. Several methods exist to chose the modes. The oldest one, used by Fourier, consists in taking the eigenmodes of the Laplace operator associated with the homogeneous boundary conditions of the physical problem. The inhomogeneous part of the boundary conditions is treated separately in a static temperature field [4,10]. This method does not allow temporal variations of the heat transfer coefficient, or of the conductivity. This method have been recently enhanced to take into account such variations. It is the branch eigenmodes reduction method used in this paper [10, 11].

Another solution is to identify the modes from experimental or numerical data. It is the Proper Orthogonal Decomposition (POD) method [12]. Finally, in the Modal Identification Method, the entire reduced model is identify from experimental or numerical data [5].

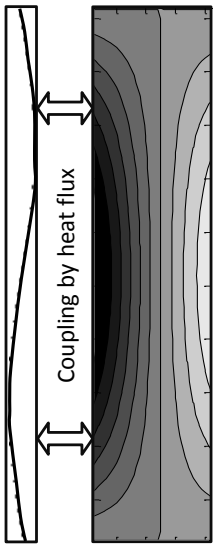

Figure 3 coupling of two modal models

As schematized by Fig. 3, the objective of this paper is to compute separately the modes of the heat transfer fluid and those of the PCM, to build two modal models, one for the HFT and one for the PCM, and then to couple these models to treat simultaneously the heat transfer in both domains.

Branch problem formulation

For a pure diffusion problem, the branch eigenmodes are solutions of following eigenvalues problem:

$$\forall\, M \in \Omega,\ r\vec{\nabla}.\left(k_0 \vec{\nabla} V_i\right) = \lambda_i r \rho_0 c_0 V_i \quad (15)$$

$$\forall\, M \in \Gamma,\ r k_0 \vec{\nabla} V_i . \vec{n} = -\lambda_i r \zeta V_i \quad (16)$$

For an diffusion advection problem in an open system, the branch problem is defined by eqs. (17) to (19).

$$\forall\, M \in \Omega,\ r\vec{\nabla}.\left(k_0 \vec{\nabla} V_i\right) - r\rho_0 c_0 u_0 \vec{\nabla} V_i . \vec{n} = \lambda_i r \rho_0 c_0 V_i \quad (17)$$

$$\forall\, M \in \Gamma_{\text{ef}},\ r k_0 \vec{\nabla} V_i . \vec{n} - r\rho_0 c_0 u_0 \vec{\nabla} V_i . \vec{n} = -\lambda_i r \zeta V_i \quad (18)$$

$$\forall\, M \in \Gamma_{\text{sf}},\ r k_0 \vec{\nabla} V_i . \vec{n} = -\lambda_i r \zeta V_i \quad (19)$$

In contrast to classical eigenmodes problem, the specificity of this eigenvalue problem lies in the boundary condition, named Steklov boundary condition, involving the eigenvalue λ_i. This involves that this modal basis is not linked to any specific boundary condition type. It is also important to emphasize that the branch problem is defined with constant thermo-physical characteristics.

The Steklov parameter ζ is introduced by Steklov boundary condition. It is a numerical coefficient whose purpose is to ensure the dimensional homogeneity of the eigenvalue λ_i in Eqs. (15) and (16) and Eqs. (17) to (19).

Calculation and analysis of branch eigenmodes

Spatial discretization of eqs. (15)-(16) or (17)-(19) allows to write the eigenvalues problem to standard matrix form:

$$\mathbb{K}V_i = -z_i(\mathbb{C}_0 + \mathbb{C}_b)V_i \quad (20)$$

Note that the fact of multiplying Eq. (7) and Eq. (15) by the radius (r) is not harmless. This operation is necessary to ensure the symmetry of the matrix $\mathbb{K}$ during spatial discretization and thus the self-adjoint character of the Laplace operator. $\mathbb{C}_0$ and $\mathbb{C}_b$ respectively represents capacity matrix and Steklov boundary condition matrix. The eigenvalue problem (Eq. (20)) is solved with the suite of Arpack subroutine.

For the HTF domain where the transport problem is considered one-dimensional, the branch basis is computed with a null velocity. Indeed, an analytical study shows that the eigenmodes are of the form:

$$V_i(z) = f_i(z)exp[(z-L)\frac{\rho_0 c_0 v}{2k_0}] \quad (21)$$

For water, the exponential term completely overwrites the function $f_i(z)$. Then, it is not appropriate to compute the modal basis corresponding to the real physical problem. However, as the branch eigenmodes form a basis in Hilbert space, it is possible to decompose the temperature field of the fluid on a basis calculated with a null velocity. The visualization of the first eigenmodes computed this way (see Fig. 4) reveals the interest of this particular basis. Indeed, it is a flat eigenmode and a quasi-linear eigenmode. A linear combination of these two functions allows to approach any stationary solution. Thus, it is no longer necessary to treat separately the inhomogeneous part of the boundary conditions as in the classical modal method.

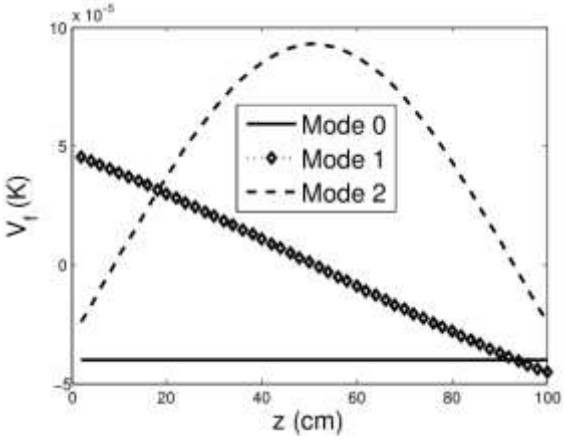

Figure 4 1D eigenmodes in HTF domain

For the domain of the PCM, modelled in 2D, the introduction of the Steklov condition leads to the appearance of two types of eigenmodes:

- Volume eigenmodes whose value is almost zero on the borders but non-zero inside the domain; see Figure 5-b
- Surface eigenmodes whose value is close to zero inside the domain and non-zero on the borders; see Figure 5-a.

The existence of the last kind of eigenmodes allows to reconstruct temperatures and heat flux for any heat exchange coefficient h. This basis is thus suitable for non-linear thermal problems with unsteady parameters. More detailed studies of these eigenmodes were performed in [5] and [8].

Reduction of branch basis using amalgam method

In the amalgam method [10,11], the most influential eigenmodes are kept (they are called major eigenmodes), and the remaining eigenmodes (called minor) are added to them, weighted by a factor. This results in new amalgamated eigenmodes $\widetilde{V}_i$, which are a linear combination of eigenvectors of the original branch basis $\mathbb{P}$.

$$\widetilde{V}_i = \sum_{p=0}^{n_r} \alpha_{i,p} V_{i,p} \quad (22)$$

The determination of factors $\alpha_{i,p}$is performed by minimizing the deviation of energy between a reference model and the reduced model. The modal decomposition of the reduced temperature is then written:

$$\tilde{T}(M,t) = \sum_{i=0}^{\tilde{N}} [x_i(t) \times \tilde{V}_i(M)] \quad (23)$$

Or in matrix form:

$$\tilde{T}(M,t) = \widetilde{\mathbb{P}}X \quad (24)$$

Where $\widetilde{\mathbb{P}}$ is the amalgamated (reduced) branch basis,of size $\tilde{N}$ very small compared to N.

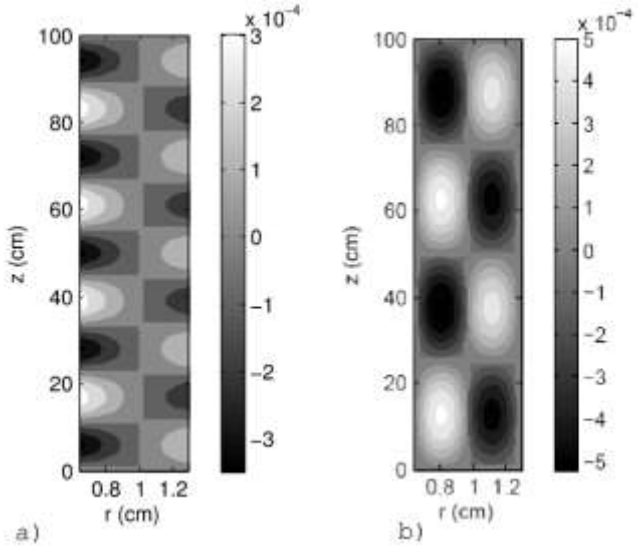

Figure 5 Surface (a) and volume (b) eigenmodes in PCM domain

Formulation of reduced model

Branch eigenmodes are computed for each domains (HTF and PCM). Applying the amalgam method allows to obtain the respective reduced branch basis $\widetilde{\mathbb{P}}_f$ and $\widetilde{\mathbb{P}}_m$. From the set of equations (12), reduced state model Eq. (25) is obtained in two steps :

1. First, the temperature field is decomposed in the modal space (Eq. (24)),
2. Then, each of the equations is projected onto its respective branch basis.

The reduced model is then:

$$\begin{cases} \mathbf{W}_f \dot{X}_f = \mathbf{M}_f X_f + \mathbf{N}_f X_m + \mathbf{P}_f T_{in} \\ \mathbf{W}_m \dot{X}_m = \mathbf{M}_m X_m + \mathbf{N}_m X_f + \mathbf{P}_m U_m + \mathbf{Q}_m \dot{f}_l \end{cases} \quad (25)$$

Where, for $j = \{f, m\}$:

$$\mathbf{W}_j = {}^t\widetilde{\mathbb{P}}_j C_j \widetilde{\mathbb{P}}_j \qquad \mathbf{N}_j = {}^t\widetilde{\mathbb{P}}_j G_j \widetilde{\mathbb{P}}_{\bar{j}}$$
$$\mathbf{M}_f = {}^t\widetilde{\mathbb{P}}_j \left(K_f + F\right)\widetilde{\mathbb{P}}_j \qquad \mathbf{M}_m = {}^t\widetilde{\mathbb{P}}_j (K_m + H)\widetilde{\mathbb{P}}_j$$
$$\mathbf{P}_j = {}^t\widetilde{\mathbb{P}}_j B_j \qquad \mathbf{Q}_m = {}^t\widetilde{\mathbb{P}}_m L_m$$

Compared to the detailed model Eq. (12), the reduced model given by Eq. (25) is of order $\widetilde{N} << N$, but matrices used are full.

Note also that the limitations of this model comes from Eq. (11). Indeed, the need to know the value of the liquid fraction in the whole PCM domain requires to return to the physical space at each temporal iteration, at the cost of vector matrix multiplication. This automatically degrades the performance of the model in terms of computation time.

DETAILED MODEL VALIDATION

In order to ensure that the detailed model (DM) correctly approach the physical phenomena in the thermal storage unit, it is compared to the experimental results of Lacroix [2]. In this experiment, the author used a small storage unit (size: 1 × 0.0123 × 0.00635 m), where the PCM is n-octadecane and HTF is water with a mass flow rate of 0.0315 kg/s.

Figure 6 compares the evolution of PCM temperature at point 1 (z = 0.95, r = 0.001) and point 2 (z = 0.51, r = 0.002) between the detailed model and the experimental results of Lacroix.

$k_{s/l}$	ρ	c_p	T_{fus}	ΔH
0.358/0.148	771	2222	300.7	243500

Table 1: Thermophysical properties of PCM

The mesh size of the detailed model is 51 × 21 (in the axial and radial directions, respectively) and time step is 5s. The agreement between the two models is very good, either at the steady state or during phase change.

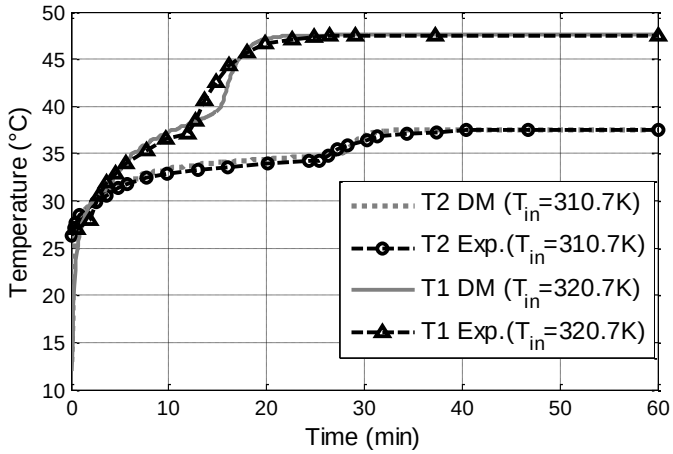

Figure 6: Temporal evolution of the temperature: validation of DM versus [2]

ANALYSIS OF SIMULATIONS WITH REDUCED MODEL

The curves in Figure 5 show a good coherence between the experimental results and the numerical results obtained by the detailed model. In this last part, it will be a question of highlighting the relevance of using a reduced model for numerical simulations in Matlab environment as well as in Simulink environment in which the simulator is modeled.

Comparison of RM to DM under Matlab software

We present here the results in terms of accuracy and computation time (ct) for different reduced model order. The difference at any point and at any time between the reduced model and the detailed model is calculated as:

$$\begin{cases} \epsilon(M,t) = \left|\tilde{T}(M,t) - T(M,t)\right| \\ \epsilon f(M,t) = \left|\tilde{f}(M,t) - f(M,t)\right| \end{cases} \quad (26)$$

CPU time savings between the reduced model and the detailed model is given by:

$$TS_{CPU} = \frac{DM_{ct}}{RM_{ct}} \quad (27)$$

The summary of the results is given in Table 2.

Lines 2-4 show the percentage of temperature difference in three temperature ranges. Thus, we note that although the maximum difference observed between the detailed model and reduced model of order (4 + 11) is 2.76°C, ε (M, t) is over 99% lower than 0.2 °C, which shows good agreement between the two models. This is confirmed by the average difference between the two models which is of 0.014 °C.

It is of course observed that the difference between both models decreases with the increase of the order of the reduced model. For example, for a RM with 30 (4 + 26) eigenmodes, the overall accuracy of the model is comparable to the precision of a thermocouple. The very good agreement between the two models in term of temperature is illustrated by Fig. 7, where the temperature field at t=20 min is represented for detailed model and the (4+11) modes reduced model.

$\epsilon(M,t)$ in °C	Total number of eigenmodes (in $\Omega_f + \Omega_m$)			
	4+11	4+26	4+51	4+201
$\epsilon \leq 0.2$	98.98%	99.97%	99.99%	100%
$\epsilon \in]0.2\text{-}0.5]$	1%	0.02%	0.01%	0%
$\epsilon > 0.5$	0.02%	0.01%	0%	0%
ϵ_{max}	2.76	1.01	0.42	0.034
ϵ_{mean}	14.10^{-3}	5.10^{-3}	2.10^{-3}	2.10^{-4}
ϵf_{max}	0.0898	0.0842	0.0170	8.10^{-4}
ϵf_{mean}	$1.2.10^{-3}$	3.10^{-4}	9.10^{-5}	9.10^{-6}
TS_{CPU}	7.7	7.3	6.6	2.2

Table 2: Synthesis of results of comparison between RM and DM

The precision in term of liquid fraction is a bit more contrasted, with a maximum difference of 0.09 (on a [0-1] scale) for the (4+11) reduced model. This relatively large error must be tempered by the low value of the mean difference, and also by Fig. 8, which represents the liquid fraction field for both models at t=20 min.

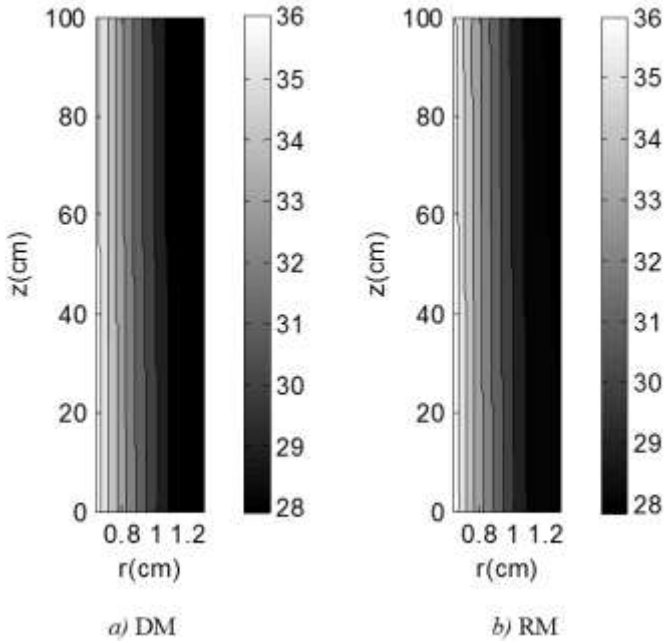

Figure 7: Thermal field of the PCM during phase change at t= 20 min for detailed model (a) and the reduced one with (4+11) modes (b)

The radial position of the solidification front is accurately reproduced, and the little dropping out at z≈0.7 m is found in both simulations. The difference comes from a small discrepancy in the axial position of the dropping out (highlighted by the dashed line in Fig. 7), leading to a relatively large error.

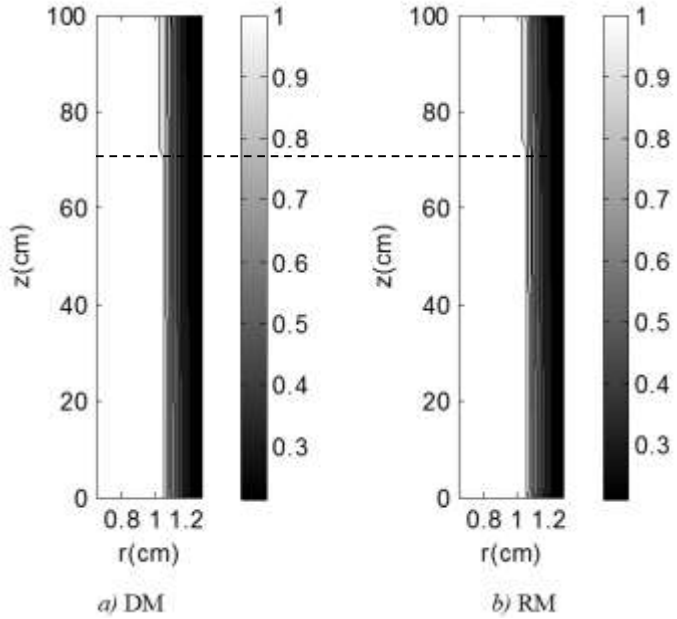

Figure 8: Liquid fraction field in the PCM during phase change at t= 20 min for detailed model (a) and the reduced one with (4+11) modes (b)

Last line of Table 5 shows the time savings due to the use of the reduced model. The gain in computation time is a bit disappointing. For the reduced model with (11+4) modes, the number of unknowns is reduced from a factor 77, but the computation time is only reduced by a factor 7.7. This is due to the fact that the matrices involved in the detailed model are sparse while those of the reduced model are full. This is also due to the fact that the necessary mesh to model the problem is of relatively small size (1071 unknowns).

Impact of RM on the numerical simulator (in Simulink)

As we noted at the beginning of this communication, the purpose of this work is to integrate a model of the component "thermal latent heat storage (TLHS)" in an energy behavior simulator, developed in the Simulink environment.

In Simulink a "MATLAB Function" block is used to simulate the thermal storage unit. Unfortunately, this type of block does not support the "sparse" function and therefore the simulation of detailed model requires manipulation of full matrix.

Knowing that the accuracy of a model chosen is identical whatever the simulation environment (Matlab or Simulink), we present in Table 3 only results in terms of computing time performance between DM and RM (order 30) in the Simulink environment.

$$SimTS_{CPU} = \frac{(DM_{ct} - SimwLTHS_{ct})}{(RM_{ct} - SimwLTHS_{ct})} \quad (28)$$

Simulation real period	Computing time (min)			$SimTS_{CPU}$
	Simulator without LTHS ($SimwLTHS_{ct}$)	Simulator with LTHS		
		DM	RM	
21 days	0.52	26.3	1.75	21
90 days	2.24	108.16	5.17	36
365 days	9.11	453.66	21.47	36

Table 3: Synthesis of results of simulation in Simulink

As might be expected, the implementation of LTHS model lengthens the duration of the simulations by a factor of 48 with MD and of 3 with MR. However, the time saved due to the reduced model is significant because it allows for example a simulation 36 times faster. Table 3 shows that for a simulation of 365 days, it takes about 7 hours and a half with the detailed model, while the waiting time with this reduced model is about 21 minutes only.

CONCLUSION

In this paper, we presented a modal model of a phase change storage system. To be representative of the different physical phenomena, the model is complex, including a variation over time of the physical parameters (heat exchange coefficient, thermal conductivity). Furthermore, the coupling between the HTF and the PCM imposes an inhomogeneity in temperature on the boundary condition.

The proposed modal model is built on amalgamated branch modes. The Steklov boundary condition allows the branch basis to be adapted to this kind of problem, and the above mentioned phenomena have been properly reflected in the reduced model.

A sensitivity study showed that with 4 modes in the fluid and 26 modes in the PCM, the reduced model gives results substantially identical to the detailed model. The integration of this reduced model in the Simulink environment reduces the computation time by a factor of 36, which opens the way for parametric studies.

REFERENCES

[1] Z. Gong, A. S. Mujumdar, Finite-element analysis of cyclic heat transfer in a shell-and-tube latent heat energy storage exchanger, *Applied Thermal Engineering*, Vol.17(6), 1997, pp 583-591.

[2] M. Lacroix, Numerical simulation of a shell-and-tube latent heat thermal energy storage unit, *Solar Energy*, Vol. 50, 1993, 357-367.

[3] Y.B. Tao, Y.L. He, Z.G. Qu, Numerical study on performance of molten salt phase changethermal energy storage system with enhanced tubes, *Solar Energy*, Vol. 86, 2012, 1155-1163.

[4] G. Lefebvre, A. Neveu, K. El Khoury, and J.J. Salgon. Applying the modal method to thermal modelling. *Congres IHTC*, Jerusalem, Israel, 1990, pp 67

[5] D. Petit, R. Hachette, and D. Veyret. A modal identification method to reduce a high-order model: Application to heat conduction modelling. *Journal of Modelling and Simulation*, 17(3), 1997 pp. 242-250.

[6] A. Neveu, K.E. Khoury, and B. Flament, Simulation de la conduction non linéaire en régime variable: Décomposition sur les modes de branches, *Int. J. Thermal Sci*., Vol. 38, 1999, pp. 289-304.

[7] E. Videcoq, M. Girault, A. Neveu, O. Quéméner and D. Petit, Comparison of two non-linear model reduction techniques: the modal identification method and the branch eigenmodes reduction method, *Numerical Heat Transfer*, Vol. B49, pp 537–558, 2006.

[8] F. Joly, O. Quéméner, and A. Neveu, Modal Reduction of an Advection-Diffusion Model using a Branch Basis, *Num. Heat. Transfer* Vol. B53, 2008, pp. 466-485.

[9] Hamid El Qarnia, Numerical analysis of a coupled solar collector latent heat storage unit using various phase change materials for heating the water, *Energy Conversion and Management*, Vol. 50, 2009, pp. 247-254.

[10] O. Quéméner, A. Neveu, and E. Videcoq, A Specific Reduction Method for Branch Modal Formulation: Application to Highly Non Linear Configuration, *Int. J. Thermal Sci.* Vol. 46, 2006, pp. 890-907.

[11] O. Quéméner, F. Joly, and A. Neveu, The generalized amalgam method for modal reduction, *Int. J. Heat and Mass Transfer*, Vol.55, 2012, pp. 1197-1207.

[12] A. Fic, R.A. Bialecki, A.J. Kassab, Solving Transient Non Linear Heat Conduction Problems by Proper Orthogonal Decomposition and the Finite-Element Method; *NHTB*, 48 (2), 2005, pp. 103-124.

Heat Transfer and Hydrodynamics at Natural Circulation of Single and Two-phase Media in Channels with Different Cross-section Configuration .

Sukomel L.A., Kaban'kov O.N.*, Zubov N.O. and Zabirov A.R.
* Author for correspondence
Department of Thermal Physics,
National Research University "Moscow Power Engineering Institute",
111250, Moscow, Krasnokazarmennaya, 14,
Russia
E-mail: kon09.tiger@yandex.ru

ABSTRACT

Experimental natural circulation loop has been designed and put into operation to study heat transfer and hydrodynamics at boiling under low reduced pressures. The paper presents experimental data on wall temperature measurements at natural circulation of water under atmospheric pressure. Various heat and flow regimes in the flow up section of the loop have been studied: pure single-phase convection, pure flow boiling and mixed regimes. Low frequency flow instability has been observed in all mixed regimes. The instability led to temperature and flow rate fluctuations, which amplitudes were very high at some regimes. Wall temperature fluctuations have been also recorded. Joint analysis of flow rate and wall temperature fluctuations is presented. Experimental data on ensemble averaged wall temperature distributions along the heated section are compared with calculated ones according to the 1D and 2D numerical models.

INTRODUCTION

Natural circulation systems, which work at atmospheric pressure meet highly wide practical use. In particular, natural circulation loops are considered as a basic type of passive cooling systems of nuclear reactors under accident conditions [1, 2]. Such systems operate at atmospheric or near atmospheric pressures. As pressure decreases in vapour generating system a specific features of low pressure boiling begin display themselves [3]. Among them are high growth velocities and large departure diameters of vapour bubbles, high wall temperature overheating needed for boiling incipience, irregularity of vapour bubble generation process. Under these conditions the two-phase flow is characterized by instability and fluctuations of flow rate, pressure and temperature. At the same time heat and hydraulic calculations of natural circulation loops for low reduced pressures are accompanied by significant difficulties because at present these circulation regimes are remaining to be poorly studied. Today one still can say about the absence in full extent of knowledge both of theoretical and reliable empirical recommendations to predict integral thermohydraulic characteristics for these regimes. So it remains important to obtain new experimental data on various heat and flow characteristics which will help one to form an adequate insight into the physical processes which take place in natural circulation systems under above considered specific conditions.

The aim of present work is laboratory study of natural circulation characteristic features under boiling conditions at low pressures. The results of flow and temperature measurements at water circulation under atmospheric pressure are presented.

NOMENCLATURE

d	[mm]	Inner diameter of the heated tube
Gr	[-]	Grasgoph number
Pe	[-]	Peclet number
Re	[-]	Reynolds number
P	[kPa]	Pressure
r	[mm]	Current radius
r_0	[mm]	Tube radius
T	[^{o}C]	Temperature
w	[m/s]	Velocity
w_z	[m/s]	Longitudinal velocity component
z	[mm]	Longitudinal coordinate
z/d	[ ]	Nondimensional longitudinal coordinate
Greek symbols		
τ	[s]	Time
ρ	[kg/m^3]	Density

Subscripts	
in	Inlet
w	Wall

EXPERIMENTAL APPARATUS AND PROCEDURE

The designed experimental loop is used as model apparatus to study thermophysical processes at low pressures natural circulation. A schematic diagram of the loop is presented in Figure 1. The flow up (heated) and flow down legs of the loop are joined to the separator-condenser at the top of the loop. One of the structural features of the loop is large aspect ratio between the down leg cross sectional area and that of the heated leg. This detail of construction made it possible to substantially reduce pressure losses in flow down line (down comer). Cooling heat exchanger and two electrical heaters are installed on the down comer. These members are used for maintaining a specified inlet temperature.

Present data have been obtained at water boiling under atmospheric pressure. Two test sections have been used in the experiments. Both were electrically heated stainless steel circular tubes 1300 mm long and differed by inner diameter (5.4 and 9.1 mm). Both test sections were heated along the whole length of the tubes.

The wall temperature of the heated tube was measured by chromium-alumel thermocouples which hot junctions have been point-welded to the outer surface of the tube. The technique afforded to form thermocouple junctions less than 0.2 mm in dimension. Besides the wall thickness of

the heated tubes did not exceed 0.45 mm. Thus the thermal response time of the test section was rather small and we could record temperature fluctuations (which in some regimes were very intensive).

Temperature recordings were realized with data acquisition system, which affords high-frequency sampling of measured quantities. The frequency of thermocouples sample was 100 Hz. It was enough to obtain practically simultaneous temperature records for the whole heated length.

The flow rate in the loop was measured with ultrasonic flow meter FLUXUS F601 with the error of 0.01 m/s. The pressure transducer AIR of 0.2% accuracy class was used for pressure measuring in the separator-condenser chamber. Temperature measurements are in error by 0.2 ^{o}C, heat flux density measuring error is 2%.

Present data have been obtained for the loop fully filled with the working liquid up to outlet of flow up tube section in separator. Measurements have been made within the range of heat flux densities of (1.0–50.0) kWt/m^2 for inlet liquid temperatures of (300–373) K.

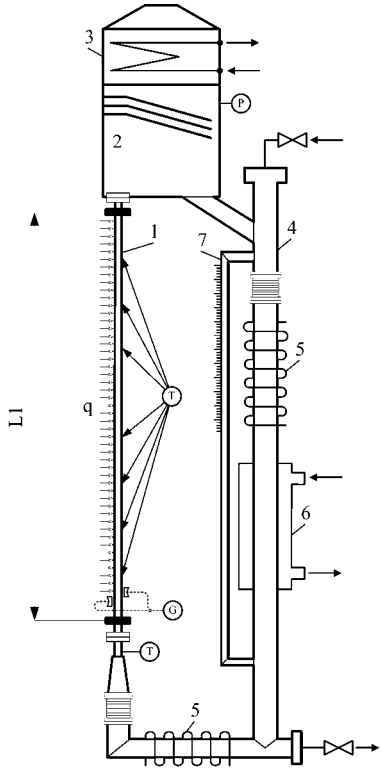

1 – heated section, 2 – separator, 3 – condenser, 4 – down comer, 5 – electrical heaters, 6 – cooling heat exchanger, 7 – level meter

Figure 1 Experimental apparatus

EXPERIMENTAL RESULTS

Different heat transfer regimes have been realized in experiments, namely single phase convection (high liquid subcoolings at the inlet, low heat flux densities), mixed regimes when boiling took place at the part of heated zone and regimes with boiling along the whole heated zone (at inlet liquid subcooling less then 5 K). Typical measured ensemble-averaged longitudinal wall temperature distributions are shown in Figure 2.

It's worth to note, that the length of single-phase zone can be significant even for not so high liquid subcoolings (see the curve for q_w = 22.88 kW/m^2 in figure 2).

Mixed regimes with rather long single-phase zones are typical for low pressures boiling in natural circulation loops. As it is seen from Figure 2 boiling incipience is accompanied

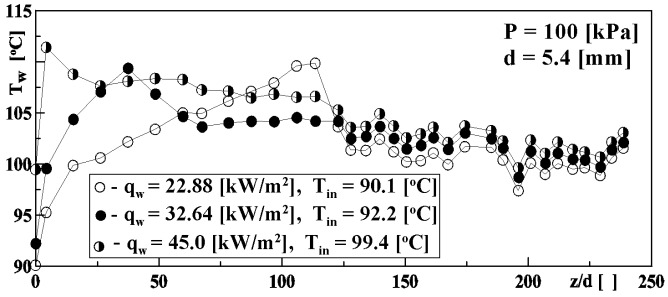

Figure 2 Measured ensemble-averaged wall temperature distributions along the heated section.

by rather sharp wall temperature decrease.

The change of heat transfer regimes along the heated section had an effect on the form of longitudinal temperature distribution curves. Boiling regimes were accompanied by the wall temperature fluctuations of significant amplitude. Temperature curves in Figure 2 are ensemble-averaged data for each cross-section.

Temperature fluctuations were observed not only in boiling zones. Fluctuations were recorded at pure single-phase convection regimes. Typical oscillograms of wall temperature measured at three locations on the heated tube height at different wall heat flux densities for pure single-phase convection are shown in Figure 3. The time dependent liquid temperature records at the inlet to the heated zone are also plotted in Figure 3 [(lines 1 at z/d = 0 in Figure 3 a) – c)]

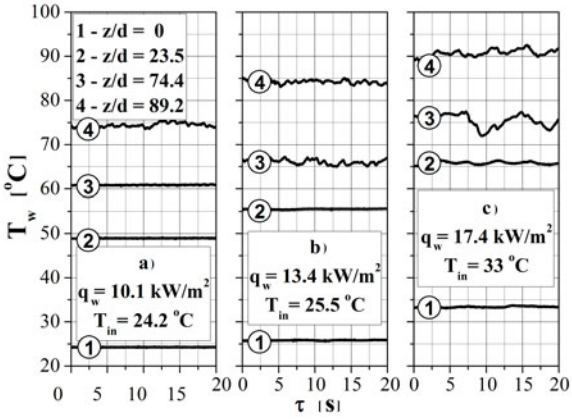

Figure 3 Wall temperature fluctuations at single-phase regime

As it is seen from Figure 3 fluctuation amplitude increases with heat flux density increase. This fact displaces a complex changing of velocity profiles along the tube with vortex formation and occurrence of flow instability.

As heat flux density increases the start section of fluctuation regime displaces towards the inlet to the heated section.

Wall temperature fluctuations, which one can observe for q_w = 10.1 kW/m^2 and T_{in} = 24 ^{o}C at z/d = 89.2 [(line 4 in Figure 3,a)], occurs because of the loss of stability of viscous-gravitation flow at this cross-section. The value of z/d = 89.2 is close to the value of stability loss coordinate $(z/d)_*$ estimated according to [4, 5] correlation. Indeed,

according to [4, 5] the critical adjusted coordinate X_* of stability loss is

$$X_* = \frac{1}{\mathrm{Pe}}\left(\frac{z}{d}\right)_* = 12.9\left(\frac{\mathrm{Gr}}{\mathrm{Re}}\right)^{-0.8} \qquad (1)$$

Sibstituting into (1) the experimental values of Gr and Re numbers gives for conditions of Figure 3,a) the value of $(z/d)_* = 93$.

The adjusted length X_* decreases as Gr/Re increase. The same tendency is observed for our experimental results: as q_w increases the boundary of flow stability loss displaces downstream [data curves 3, 4 in Figure 3 b) and data curves 2, 3, 4 in Figure 3, c].

When it becomes impossible for single-phase natural circulation to remove heat from the wall, its temperature increases and reaches the level, which is enough for boiling incipience. Boiling starts at the outlet section of the heated zone as a rule. The existence of two-phase flow zone leads to circulation instability in the loop. Low-frequency oscillations of flow rate and wall temperature as well as liquid ejections from outlet channel opening into the separator are observed.

Typical wall temperature oscillograms measured at three locations on the heated tube height at different wall heat flux densities for mixed single-phase-boiling circulation are shown in Figure 4. The time dependent liquid temperature records at the inlet to the heated zone are also plotted in Figure 4 [(lines 1 at z/d = 0 in Figure 4 a) – c)]

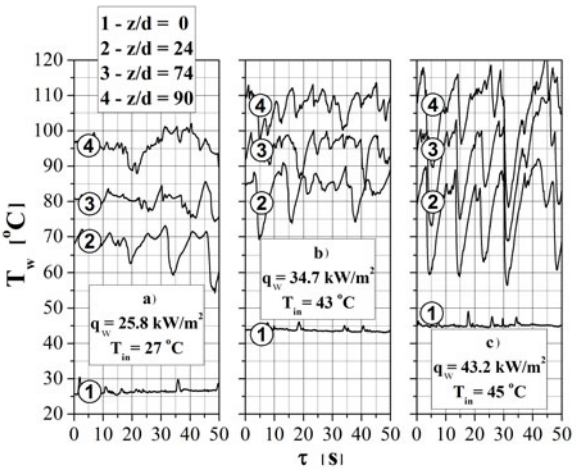

Figure 4 Wall temperature fluctuations at mixed circulation regimes in the tube of 9.1 mm in diameter.

It follows from the analysis of "instantaneous" realizations of temperature time relations (as it was said above, the frequency of thermocouples sample was 100 Hz) that when heat flux density increases or inlet liquid subcooling decreases or both factors take place frequency of temperature and flow rate fluctuations increases and somewhat regularity of the process occurs. This phenomenon can be observed in Figure 5 more clearly. Temperature regime of the heated zone for the conditions of Figure 4,c) is shown in Figure 5 in large scale with more details. It is seen that a trend of temperature time records of thermocouple readings at different locations on the tube is the same. One can say that oscillograms of temperature fluctuations repeat each other but are shifted relative to each other by some time interval. Temperature records include alternating portions of sharp temperature time drops with following time intervals of more fair temperature increasing, the portions of sharp temperature drops and fair temperature increasing alternate quite regularly. Besides, in such regimes a temperature "spikes" are clearly observed on temperature time record of inlet temperature (curves 1 at z/d = 0 in Figures 4, 5). The appearance of these "spikes" corresponds to the time moments of the beginning of wall temperature increase. The time shift between the beginning of wall temperature increase and the appearance of the "spikes" on the inlet time temperature record for different portions of temperature time records is practically the same.

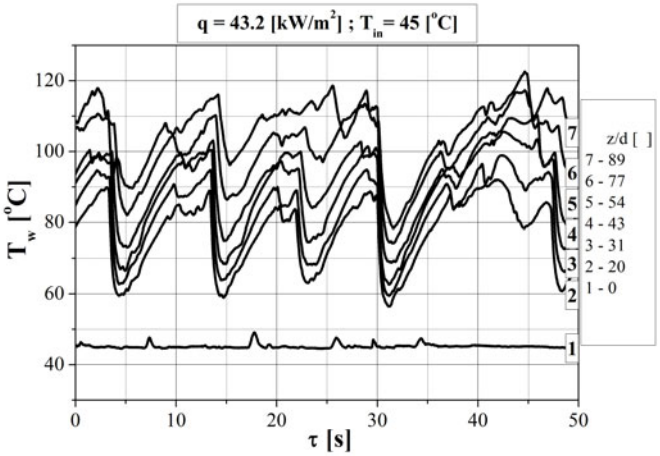

Figure 5 Time temperature records at different locations on the heated wall at q_w = 43.2 kW/m^2

Figure 6 shows oscillograms of circulation velocity in the loop at heat flux density of q_w=25.8 kW/m^2 and at inlet liquid subcooling of T_{in}=27 ^{0}C. This regime has been chosen to demonstrate the existence of reverse flows in the loop. Such a regimes have been usually observed at low heat flux densities and are characterized by rather long recurrence periods.

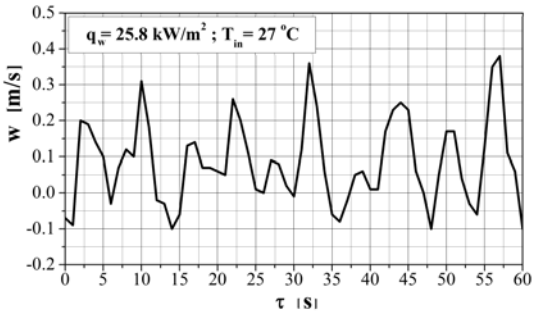

Figure 6 Oscillogramm of circulation velocity fluctuations in the tube of d = 9.1 mm in diameter

Periodic liquid ejections from the tube outlet have been visually observed. The ejection periods correlates with the periods of temperature and flow rate fluctuations in the loop. Low frequency instability has been observed within the frequency range of (0.08 – 0.5) Hz at all realized mixed circulation regimes. The type of instability under observation is caused by boiling incipience and by flow regime change as a consequence. This change is a single-phase two-phase flow transition under the existence of rather long single-phase flow zone.

Vapour bubbles generation at liquid boiling up leads to driving head increase in the loop. So flow rate and correspondently circulation velocity increases. When flow rate increases wall temperature decreases, boiling stops and flow becomes single-phase. This in turn leads to driving head and flow rate decrease. As a result wall temperature rises and liquid starts to boil again. Thus the process replicates itself.

COMPARISON WITH PREDICTING METHOD

Our experimental data have been used for verification of some existing methods for predicting heat and flow regimes in natural circulation loops. First of all we have considered the widely used in engineering practice model based on 1D description of flow and heat transfer in channels. It is assumed according this approach that flow velocity and temperature vary only in streamwise direction. Detailed mathematical formulation of the problem as applied to natural circulation loops one can find elsewhere [for example 6 – 8]. Substantial mathematical simplification of the problem at 1D approach is achieved by introduction of such quantities as heat transfer coefficients and hydraulic loss, which in complex way are connected with the real 3D flow and couldn't be determined from 1D theory in principle. So one needs to get additional information from experimental data, 3D calculations or semiempirical theories to determine the values of heat transfer coefficients and hydraulic loss. As for natural circulation hydraulic loss calculations at flow boiling under low pressures is the most difficult problem. As it was already mentioned in introduction these circulation regimes are remaining to be poorly studied and both of theoretical and reliable empirical recommendations to predict integral thermohydraulic characteristics for these regimes have not been suggested yet. As the first step we consider two main possible flow patterns in two-phase zone of our experimental loop that is bubble flow with large vapour bubbles (we name this regime an intermittent flow) and annular flow. Corresponding hydraulic loss predicting correlations for each regime were got from [3] where one can find one of the most complete generalization of the existing knowledge on the subject. Comparison of experimental data with the results of preliminary calculations showed that some recommendations are needed to be refined. It will be the subject of future work.

In present paper we shall limit ourselves to the analysis of single-phase convection regimes. The predicting friction factor correlations for fully developed isothermal flows are commonly used in literature for this case. These correlations are $\xi = 64/\mathrm{Re}$ for laminar flow regime and Blasius $\xi = 0.3164/\mathrm{Re}^{0.25}$ or Filonenko $\xi = (1.82\lg \mathrm{Re} - 1.64)^{-2}$ formula for turbulent flow. To our point of view this approach is not fully correct because the form of velocity profiles in real gravity driven natural circulation flows differs from fully developed isothermal velocity profiles. Besides the profile configuration can change along the heated zone and it will lead to additional increase of hydrodynamic drag. To our opinion predicting correlations for heat transfer and friction for flows with the same direction of forced and natural convection, suggested by B.S. Petukhov and A.F. Polyakov [4, 5] are more suitable. In present work we used this correlations for prediction of flow and heat transfer in single-phase circulation zones. Besides we took into consideration practically uniform velocity and temperature distribution in the inlet of heated section and concurrent formation of heat and hydrodynamic boundary layers in the entrance region.

Calculated and experimental longitudinal wall temperature distributions are shown in Figure 6. Analysis of the whole massive of temperature measurements showed that 1D model with above corrections underpredicts experimental data at low q_w (that is the model overpredicts circulation velocity) but this discrepancy decreases with heat flux density increasing and in mixed regimes with boiling at the end of the heated zone experimental and calculated temperature curves are in good agreement. The velocity profiles deformation is probably more intensive at low q_w in our loop than under the [4, 5] conditions and hydraulic loss is higher.

To refine this conclusion the numerical 2D simulation of single-phase natural circulation in circular tube for experimental conditions has been carried out. The simulated loop was a closed by liquid ensemble from annular and circular tube. Circular (heated) tube was placed coaxially inside the annular tube. Annular tube was the down comer of the simulated loop. The heated tube height was specified equal to the loop test section height, and cross-sectional area of annular gap was equal to cross sectional area of the experimental loop down leg. Thus the simulated circulation conditions were made more realistic in terms of the circulation in experimental loop. So the axially symmetric 2D problem has been formulated, and the problem was solved as unsteady one.

The expression for buoyancy force vector, which appears in the system of conservation equations and which is the driving force of motion can be written in general case as $\mathbf{F_B}(r,z) = \mathbf{g}[\rho(r,z) - \rho_r(z)]$, where $\mathbf{g}$ is vector of gravity acceleration and ρ_r is local reference density. For inner gravity flows (in closed space bounded by solid walls) the reference density is chosen according to the type of inner flow under consideration. In our calculations $\rho_r(z)$ was considered as cross-section averaged density at local coordinate z in down leg of the loop.

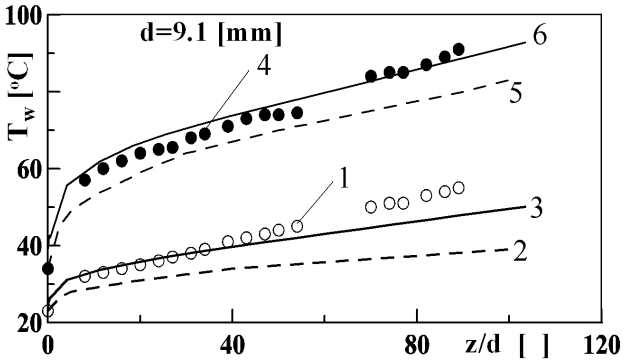

points – experiment: 1 – q_w = 3.7 kW/m^2, T_{in} = 23.0 °C, 4 – q_w = 17.4 kW/m^2, T^i_n = 34.0 °C; lines – calculations: 2 and 5 – 1D calculation, 3 and 6 – 2D numerical simulation

Figure 6 Experimental and calculated longitudinal wall temperature distributions at pure single-phase circulation regimes.

Longitudinal wall temperature distributions calculated numerically for the experiment conditions of Figure 6 (in that experiments flow was laminar) are marked in Figure 6 as curves 3 and 6. As it is seen from Figure 6 numerical results much better agree with the experimental data.

Figures 7 and 8 show typical calculated velocity profiles at different cross sections of the heated zone for tube diameters of 5.4 and 9.1 mm for laminar flow model. Corresponding temperature profiles for the tube of 9.1 mm in diameter are shown in Figure 9. One can see that velocity profiles change along the whole heated zone, the profile deformation being more intensive with tube diameter increasing. For large tube diameters the reverse flows are quite probable [line 3 in Figure 8,b)]. The deformation of velocity profiles is accompanied by velocity gradient increase

at near wall region and hence by the increase of surface tension at the wall.

Single phase convection heat transfer in mixed regimes are predicted with high degree of accuracy by the 1D calculation model based on the B.S. Petukhov and A.F. Polyakov predicting correlations for heat transfer and friction for flows with the same direction of forced and natural convection. In most cases the single phase flows in test sections were laminar. These regimes are characterized by considerably higher hydrodynamic drag in comparison with purely forced convective flows.

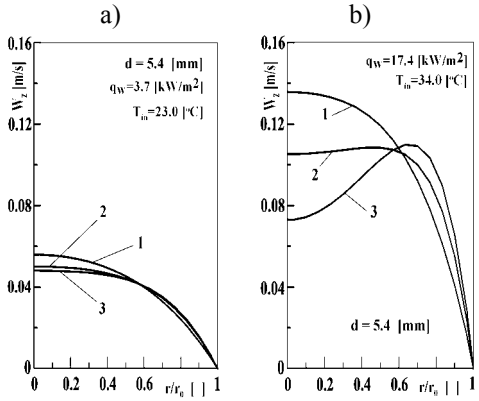

a) : 1 – z/d = 8.4, z/d = 151.7, z/d = 211.4;
b) : z/d = 8.4, z/d = 104.0, z/d = 211.4

Figure 7 Calculated velocity profiles at different distances from the inlet to the heated zone for d = 5.4 mm

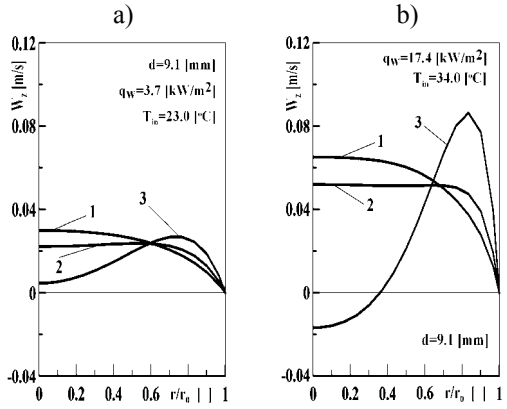

a) : 1 – z/d = 5.0, z/d = 26.2, z/d = 125.5;
b) : z/d = 5.0, z/d = 19.2, z/d = 125.5

Figure 8 Calculated velocity profiles at different distances from the inlet to the heated zone for d = 9.1 mm

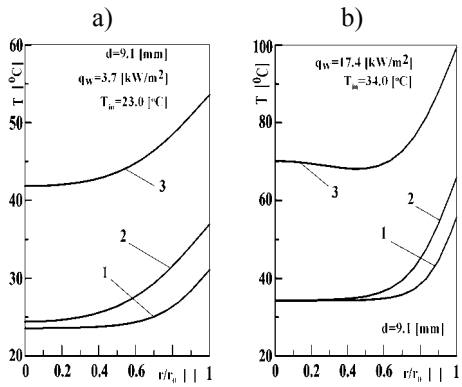

a) : 1 – z/d = 5.0, z/d = 26.2, z/d = 125.5;
b) : z/d = 5.0, z/d = 19.2, z/d = 125.5

Figure 9 Calculated temperature profiles at different distances from the inlet to the heated zone.

The numerical simulation made it possible to perform a parametric study of circulation regimes for arbitrary change of the loop geometry characteristics.

CONCLUSION

Temperature and flow measurements in model experimental natural circulation loop at water flow under atmospheric pressure have been carried out. Single-phase, mixed and boiling circulation regimes have been realized. Low frequency instability of 0.08 to 0.5 Hz was observed at transition from single phase to two-phase flow in mixed regimes. Oscillations frequency increased and its amplitude decreased with heat flux density increase.

In single-phase convection regime 1D thermohydraulic calculations of the loop with the use of formulae [4, 5] for friction factors showed good agreement with the experimental data only for rather high heat flux densities when there is boiling at the upper part of the heated tube that is when circulation velocities are rather high. At lower heat fluxes there exists rather intensive deformation of velocity profiles and essentially higher hydrodynamic drag takes place.

ACNOWLEDGEMENTS

The work was supported by the Russian Foundation of Basic Research grant No. 15-08-05106a.

The work was supported by the grant of the President of Russian Federation for support of leading Scientific Schools of Russia, grant N НШ-3783.2014.8.

REFERENCES

[1] Bakhmet'ev A.M., Bol'shukhin M.A., Vakhrushev V.V., Khizbullin A.M., Makarov O.V., Bezlepkin V.V., Semashko S.E. and Ivkov I.M. Experimental validation of the cooling loop for a passive system for removing heat from the aes-2006 protective envelope design for the leningradskaya nuclear power plant site, *Atomic Energy*, Vol. 106, No3, 2009, pp.185-190.

[2] Lisowski D.D., Omotowa O., Muci M.A., Tokuhiro A, Anderson M.H., Corradini M.L., Influences of boil-off on the behavior of a two-phase natural circulation loop. *Int. Journal of Multiphase Flow* Vol. 60, 2014, pp.135–148

[3] Labuntsov D.A., Yagov V.V. Mechanics of Two-phase Systems. Moscow: MPEI Publishing House, 2007, 384 p (in Russian)

[4] Petukhov B.S. Selected Works. Heat Transfer Problems, Moscow, Nauka, 1987, 278 p. (in Russian).

[5] Petukhov B.S., Polyakov A.F., Strigin B.K. Heat transfer investigation in pipes at viscous-gravitational flow. In collection *Heat and Mass Transfer*, Vol. 1, Moscow, Energia, 1968, 607 p. (in Russian).

[6] Wang J.Y., Chuang T.J., Ferng Y.M. CFD investigating flow and heat transfer characteristics in a natural circulation loop. *Annals of Nuclear Energy*, Vol. 58, 2013, pp. 65-71.

[7] Mousavian S.K., Misale M., D'Auria F., Salehi M.A. Transient and stability analysis in single-phase natural circulation. *Annals of Nuclear Energy*, Vol. 31, 2004, pp. 1177-1198.

[8] Misale M., Garibaldi P., Passos J.C., de Bitencourt G.G. Experiments in a single-phase natural circulation mini-loop. *Experimental Thermal and Fluid Science*, Vol. 31, 2007, pp. 111-1120

STUDY OF HEAT TRANSFER MECHANISM IN QUENCHING PROCESS

Zabirov A., Yagov V. and Leksin M.
Department of Engineering Thermophysics,
National Research University "Moscow Power Engineering Institute",
Moscow,
Russia,
E-mail: zabirov.arslan@gmail.com

ABSTRACT

Film boiling of subcooled liquid as the most available and use-proven way of quick chilling of hardening pieces, ensuring required microstructure of metal is widely used in quenching technology. A vapour explosion is the other important process, in which this boiling regime is surely observed. Under high subcooling of liquid the cooling process of high temperature bodies is featured with very high intensity and can be considered as a particular heat transfer regime. This was revealed first in 1986 by G. Hewitt and D. Kenning, who used for this regime a term "microbubble boiling". Mechanisms of very intensive heat removal from the metal surface to subcooled liquid are not understood till now, because the surface temperature in this process is much higher than the temperature of homogeneous nucleation. Some specialists do not accept even an existence of the problem itself. The present paper gives an analysis of the problem content and of some issues of experimental technique of its investigation. The original experimental study of heat transfer in film boiling of highly subcooled water was carried out at experimental facilities with high frequency induction heating of test samples. Spherical balls made from nickel and stainless steel were equipped with 4 or 5 thermocouples that provide temperature measuring in several points of the cooled body. The experimental results fully confirmed an existence of specific heat transfer process of high intensity during film boiling at large liquid subcooling. It was shown that temperature field in the process is not characterized with spherical symmetry. An approximate method of solution of inverse problem of thermal conductivity was realized to obtain heat flux density and HTC distribution at the ball surface during the intensive cooling.

NOMENCLATURE

T	[K]	Temperature
R	[m]	Radius of the sphere
t	[s]	Time
r	[m]	Radial coordinate
c	[J/kgK]	Specific heat
q	[W/m^2]	Heat flux density

Special characters

α	[W/m^{2}K]	Heat transfer coefficient
λ	[W/mK]	Thermal conductivity
ρ	[kg/m^3]	Density

Subscripts

lim	Homogeneous nucleation
s	Saturated liquid
w	Wall
0	Initial state

INTRODUCTION

Film boiling of subcooled liquid is an unavoidable step in quenching technology; a vapor explosion is the other important process, in which this boiling regime is surely observed. For the first of these applications boiling of subcooled liquid is the most available and use-proven way of quick chilling of hardening pieces, ensuring required microstructure of metal. Certainly, the mechanisms, which induce intensive heat removal from the pieces surface, were of no special interest for technologist. With respect to the vapor explosion, there are serious grounds to believe that just film boiling of subcooled liquid is the main appropriating precondition of dispersion of molten metal and catastrophically rapid vapor generation. Here appeal to the internal mechanisms is quite natural.

The publications analysis shows that experts in any case oriented to the two mentioned applications in small scales allow for each other results. In their publications we can find references on the same basic papers, but there is no mutual quoting.

Judging by monograph [1] and journal papers, the Russian specialists in quenching directly or indirectly take into consideration that quenching process undergoes in nucleate boiling regime. A value of heat transfer coefficient (HTC), which exceeds one- two orders of magnitude the typical HTC at film boiling of saturated liquid, is a main argument for such point of view. At the same time this view does not take into account that at temperatures exceeded not only the temperature of limit superheating (close to the spinodal temperature), T_{lim}, but even the critical one, a direct contact of a liquid with the surface is not possible. Moreover, at such great surface superheat (in comparison with saturation temperature) it should be observed fantastic high heat fluxes and HTC at nucleate boiling. For the sake of justice, note that the author of [1] in one of his further papers denoted impossibility of nucleate boiling in initial stage of quenching.

The second edition of comprehensive book [2] published recently contains important data about heat transfer processes in quenching metal balls and cylinders from initial temperature near 900°C in water and other quenching mediums. This book is structured like a collective monograph, individual chapters

have been written by experts from various countries; six from the seventeen chapters dedicate to heat transfer. The authors have no doubt that at immersion of a very hot piece in a quenching medium a vapor blanket appears on the solid surface, it being perfectly stable, if the cooling liquid is at saturated condition. In a subcooled liquid the vapor film could lose stability when the surface temperature exceeds greatly T_{lim}.

The German specialists (R. Jeschar, E. Specht, Chr. Kohler, Ch. 6 [2]) show that the metal bodies instability of the vapor film increases at quenching with rise of liquid subcooling and of velocity of liquid. On the cylindrical pieces the film collapse started from the bottom end, while on the spherical ones video filming registered symmetrical cooling. The temperature of film distortion measured by thermocouple placed at 0.5 mm from the south pole is as higher as less the sphere diameter. The authors call this temperature as "Leidenfrost temperature", which seems to be ambiguously. In fact, it is a question about the temperature, at which a rate of cooling sharply increases, i.e. the temperature of breaking off stable film boiling; but the authors do not discuss what a boiling regime is established at the cooled surface. Usually with the Leidenfrost temperature one connect a possibility of direct contact a liquid with a hot surface, i.e. it is identified with the film boiling minimal temperature. Usually the Leidenfrost temperature refers to the possibility of direct liquid contact with hot surface, i.e. It is identified with film boiling minimal temperature. Obviously, this temperature cannot exceed the spinodal temperature at predetermined pressure as a substance exists only in vapor phase on spinodal. (Papers, reporting about experiments in which the values of the film boiling minimal temperature exceed even the critical temperature of a substance, q.v.[3], raise doubts in quality of measuring or in validity of interpretation of their results but, of course, they cannot disprove the fundamentals thermodynamic laws).

In Jeschar et al. [2] experiments at immersing nickel spheres in water with temperature 20°C the intensive cooling started when the temperature of the surface was higher than 400°C that exclude a possibility of direct liquid contact with the hot surface. The calculated rates of maximal ("critical") heat flux was approximately typical for boiling water at the atmospheric pressure (near 1,5MW/м^2), whereas heat flux at the nucleate boiling with value ΔT near 200K should be 300 times higher. Obviously, the intensive cooling of high-temperature surface in subcooled water is controlled by some special mechanism which is different from any known kind of boiling (nucleate, transient, film). The authors of ch.10 [2] (F. Moreaux, G. Beck, and P. Archambault) are more prudent in description of the metal pieces quenching in subcooled liquid, and they do not use "Leidenfrost temperature" term. The most part of the presented experiments were conducted on the standard for quenching examination silver cylindrical sample (diameter 16mm, length 48mm, thermocouple is in a centre). Vapor film becomes unstable upon cooling in subcooled liquid (with the temperature of water less than 60°C), however the authors point a very bad data reproducibility. At the same conditions (initial temperature of piece is 850°C, motionless water at 40°C) instability of film boiling starts at the temperature range 450-800°C, but vapor film can restore itself. Only at near 300°C the quenching process reproducibly passes in transient boiling and then in the nucleate boiling regime. A water jet injected from a syringe with the inner diameter 0.5mm at 2mm distance from the cooled surface of a hemispherical head of the hot cylinder leads to good reproducibility of the conditions of the film boiling stability loss. With the water jet velocity increasing the instability of the film boiling observes at higher temperature of a cooled piece, and at 2 m/s this process could be explosive. Increase of water subcooling greatly raises the surface temperature corresponding to film boiling stability loss. In water at 30°C film boiling instability is observed at very low jet velocity – 0.1m/s, practically at the sample initial temperature (850°C). The authors refer to their research [4] where destabilization of vapor film and direct water contact with the surface were detected at the surface temperature higher than the temperature of the homogeneous nucleation (i.e. T_{lim}). In our opinion, these observations do not dispute that at $T > T_{lim}$ liquid state is impossible. The paper [5] basing on the analysis of video frame and electro conductivity of water drop/plate system also reported on direct contact of the surface roughness elements with liquid at the temperature of the plate higher 300°C; the author discusses a possible influence of capillary waves at the drop surface on these contacts. It is really possible that discrete asperities could be chilled to $T < T_{lim}$ and contact with water.

To our opinion papers [6-8] published in 1986-90 gave the rise to a new approach in studying film boiling of subcooled liquid. The studies were directed to accomplish better understanding mechanisms of the vapor explosion. The authors first clearly formulated that film boiling of water subcooled higher 22K presents a specific regime of heat transfer, which they defined as microbubble boiling. This regime was observed at the surface of the copper ball at temperature higher than 400°C that excludes a possibility of direct liquid–surface contact. Near the surface of the sphere the plurality of microscopically small steam bubbles was observed. Heat transfer coefficient (HTC) referred to the saturation temperature of water under these conditions were unusually high for film boiling - above 10 kW/m^{2}K, that is almost two orders higher than the values characteristic for the saturated liquid. In [6] qualitative experiments are described where a free falling ball in subcooled water in the event of microbubble boiling deviates sharply in the horizontal direction, which indicates significant increase of pressure at some areas of the hot surface. In [8] the results of study of cooling of molten brass droplet suspended in a magnetic field in subcooled water are presented; on the surface of the solidified droplet "craters" were remarked indicating the pressure impulse under the intensive cooling. Although in the discussed papers any theoretical results which explain the mechanisms of phenomena were not obtained, these unique researches stimulated the similar experiments begun by the authors of this article [9-11]. Our investigations were carried out mainly with a 45mm diameter nickel ball. In contrast to the known work in this field, there were 4 or 5 thermocouples placed in the ball, one in the center and the rest in the various points of the surface. This revealed that spherical symmetry of the temperature field in the cooling process occurs only at a stable film boiling, which is typical for cooling in

saturated or weakly subcooled water, as well as in isopropanol. In the intensive cooling regime (microbubble boiling) stability of film boiling initially is disturbed at the bottom part of the sphere surface (near the south pole), and the front of intensive cooling extends from the bottom up to the whole surface usually for 2-4 seconds. Thus the Jeschar's et al. [2] conclusion on symmetric cooling nickel ball in subcooled water based on the temperature measurements at one point raises doubts. The completed studies have clearly formulated questions about the mechanisms of the intense heat transfer during film boiling of subcooled liquids. The research program devoted to finding the answers to them, currently being implemented at the Department of Engineering Thermophysics NRU "MPEI" and supported by a grant from the Russian Science Foundation.

It should be noted that in the recent years the studies of film boiling in subcooled liquid are carried out in several research teams. More than 10 years colleagues from High Temperatures Institute of RAS [12-14] work in this direction. Accent (as in [6-8]) is made on a "trigger mechanism" of the vapor explosion. The important and useful in terms of the objective results have been obtained, but the quantitative models of heat transfer under the considered conditions have not offered yet.

It's interesting that papers [15], [16] dedicated to film boiling of subcooled water do not mentioned the predecessors' studies, including the all English-language publications cited above. At the same time in [15] the experimental results related to the water with subcooling higher 40K, were not analyzed because according to the authors film boiling at high subcooling is not observed. It should be mentioned that the Japanese scientists (see, Eg, [17]) introduced the term very similar to the proposed in [6 - 8], microbubble emission boiling. In this case boiling of water and water-alcohol mixtures is considered at subcooling to the saturation temperature about 40K, which is accompanied by the emission of microbubbles; this leads to significant increase of critical heat flux. This process is nothing but the same names is not similar to those discussed the intensive film boiling regime of subcooled liquid.

Thus, despite rather large interest to the problem, this regime doesn't have a clear explanation and some researchers do not actually recognize its existence as a specific phenomenon.

Experimental Facility

Our research program includes experiments using spheres with different diameters, various metals and various cooling media. Experimental stand "High Temperature Surfaces Cooling Regimes," was created in 2013 under the program of development of the material base of the NRU "MPEI".

Schematic of the stand is shown in Fig. 1. Sealed housing of experimental camera is made of stainless steel tube 219 mm outer diameter with a wall thickness of 10mm. In its upper part a coil (2) of a high frequency induction heater (3) is placed; the lower part is filled with the cooling liquid, the temperature of which is maintained at a predetermined level by means of the thermostat (8) and the coil pipe (7) immersed in the liquid. The heating zone is separated from the liquid volume by thin metal diaphragm (5), which protects the cooling medium against heat radiation. The metal sphere (1) at the beginning of the experiment is mounted inside the coil (2) by system for moving the working piece (4). Heating is controlled by the thermocouples placed inside the sphere. Power of the high frequency inductor allows obtaining high heating rate; in a moderate mode providing controlled uniform heating sphere is heated to 800°C less than for 5 minutes. There is a possibility of heating a specimen in inert gas incoming from the gas balloon (9). The heated ball moves into the cooling liquid at the level of viewing windows. During cooling signal from thermocouples (11) is transmitted through the connector NI SCXI-1303 to the measuring module NI SCXI-1102 (12), which is part of the system NI SCXI-1001. Signal detection is carried out from each thermocouple at 100 Hz. The measurement results through USB-interface are transmitted to the personal computer (13), wherein in the Lab View program temperature versus time relation is built. In some runs video filming the processes occurring at the surface of cooled sphere is conducted with a digital video camera (14) in transmitted light from a halogen lamp (15). Video is saved at the PC hard disk.

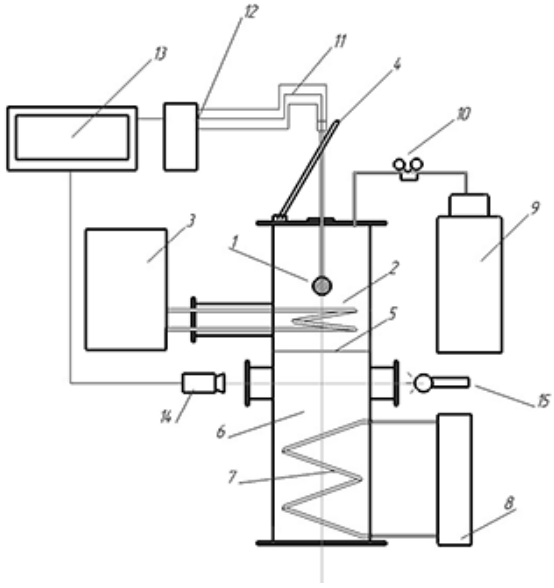

Figure 1 Schematic of experimental stand

Test samples are metal balls of 30 to 51mm diameter. In a ball through holes with a diameter of about 1 mm were drilled to accommodate the cable with thermoelectrodes. One variant of the thermocouples arrangement is shown in Figure 2; in this case 4 thermocouples are mounted in metal ball: three are located on the surface at the points with polar angle of 90, 135 and 180º, and one is placed in the center. In other cases a ball can be equipped with 5 thermocouples, 4 of them are on the surface. All the drillings are made from the top of sphere. Chromel-alumel thermocouple stretched inside the ball through the holes and welded by laser welding flush with the surface. Electrodes of thermocouples were collected in a tube-holder of 5 mm O.D., which is attached to the ball first on thread at a depth of 5 mm, and then the coupling place is sealed with laser welding. This technique of thermocouples embedding is

definitely time-consuming, but it provides obtaining information on actual temperature field at rapid cooling of the ball without its significant distortion with measuring devices.

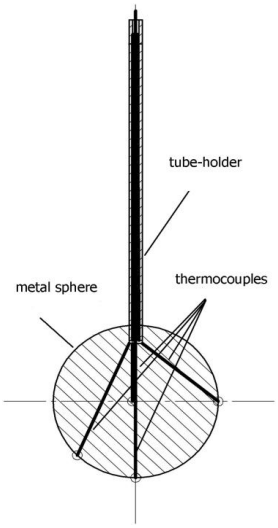

Figure 2 Thermocouples disposition scheme in a sample.

In [1] to simulate the quenching process a cylindrical sample was used with a thermocouple welded at its outer surface and thermoelectrodes coming out directly through the volume of water. We had no doubt that in this case the measuring device would inevitably influence on the studied process. But a temptation to obtain a simple and inexpensive measurement scheme pushed us to the direct verification of quantitative effect of external mounting the thermocouples.

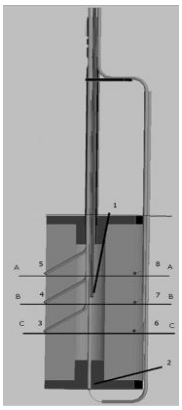

Figure 3 Schematic of thermocouples arrangement in a cylindrical sample.

Methodical experiments were performed with simultaneous temperature measurement with the outer thermocouples and with the ones embedded inside the sample. Fig. 3 depicts a sketch of a test sample as a thick-walled stainless steel pipe, 30 mm O.D., 10 mm I.D., and 60 mm long. The inner volume of the tube was sealed with the welded top and bottom covers from the same material. Besides thermocouples 1 and 2 welded at the inner surface, three pairs of thermocouples were mounted at the equal distances from the lower end of the tube (in the cross sections CC, BB, and AA), the thermocouples 3, 4, and 5 being inserted in the bores of the wall and welded flush the tube surface, the thermocouples 6, 7, and 8 being welded outside the tube surface. The thermocouple wire was 150 μm, their junctions were about 250 μm; this is significantly less than in the experiments of [1] .

For simplicity in further discussion we use the term "external" for thermocouples 6, 7, and 8 and the term "internal" for thermocouples 3, 4, and 5. The experimental thermograms obtained in the cylindrical sample cooling are shown in Fig. 4.

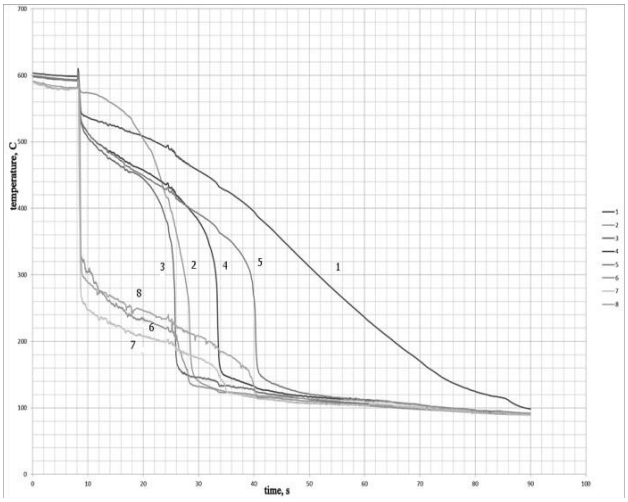

Figure 4 Cooling of the cylinder with different ways of the thermocouples embedding: 1-central, 2-inner bottom, 3, 4, and 5 - the internal; 6, 7, and 8- external.

It can be seen that the thermograms of the internal and external thermocouples differ each other even qualitatively. Thus, the temperature measured with the external thermocouples falls from 580-600 to 300-320°C factually instantaneously, while this decrease takes 13 seconds for the lowest internal thermocouple 3 (section CC) and 30 seconds for the upper one 5 (section AA). The video filming showed that the front of the intense cooling moves upward in the same manner as described in experiments [2] on a cylindrical nickel specimen. Shift of start time of intensive cooling is clearly visible from the thermograms of the internal thermocouples, but the external thermocouples show almost simultaneous cooling the cylinder surface in places of their mounting. Obviously, these thermocouple junctions and thermoelectrodes act as a sort of a fin, which is intensively cooled in liquid. When the front of intensive cooling of the sample surface reaches the level of the external thermocouples, some natural differences appear in their readings, but they are substantially lower than the actual temperature measured with the internal thermocouples. Probably, for samples with higher thermal conductivity the observed effect can be quantitatively less striking. But the described methodological experiments remove any doubts on impossibility of using external thermocouples welding in studies of quenching process in subcooled liquids.

At high cooling rates recovering conditions at the body surface requires solving the inverse problem of thermal conductivity. This type of problems is related to ill-posed ones; their solution is ordinarily achieved by means of approximate

methods. In this study factually a direct numerical solution of nonsteady heat conduction problem consistent with the measured results was found to recover the conditions at the surface of a cooled ball. The program «Rteta» developed at the Department of Engineering Thermophysics MPEI was used in solving; the temperature field in the ball was calculated by the control volume approach.

An assumption on axis symmetry of the problem seems to be quite natural, if one accounts for region geometry and video filming results on development of cooling process along the ball surface. So the following energy equation is valid:

$$\rho c \frac{\partial T}{\partial t} = \frac{1}{r^2}\frac{\partial}{\partial r}\left(r^2 \lambda \frac{\partial T}{\partial r}\right) + \frac{1}{r^2 \sin\theta}\frac{\partial}{\partial \theta}(\sin\theta \lambda \frac{\partial T}{\partial \theta}) \quad (1)$$

This 2D equation is solved for description of those experimental runs, where intensive cooling front spreads along the ball surface upward beginning from the south pole. In the modes with a small rate of cooling, when the process can be considered with good accuracy as spherically symmetric, one-dimensional approximation is successfully used. In this case the 2nd term of RHS of Eq. (2) is omitted and the third kind boundary condition is used:

$$t = 0,\ 0 \le r \le R : T = T_w = T_0;\ r = 0 : \frac{\partial T}{\partial r} = 0;$$
$$r = R : -\lambda \frac{\partial T}{\partial r} = \alpha(t)(T_w - T_s). \quad (2)$$

The program «Rteta» allows determining heat transfer coefficient during cooling interactively. First, Eq. (1) is decided at predetermined HTC and (1) for a certain time period. The temperature field inside the ball is calculated, and temperature at the control points is compared with the measured values for the corresponding thermocouples.

As the result of comparisons, either the HTC value is adjusted or solution moves to the next time step. For each subsequent step the solving result at the previous time step is used as the initial temperature distribution. This method gives good results in the modes with a small rate of cooling, i.e. at the steady film boiling or at small subcooling to saturation. It is revealed that it can be used also under the intensive cooling of a small diameter sphere, when deviation between the experimental thermograms is small, and the process can be considered approximately as spherically symmetric.

Experimental results

In the most cases the experiments with each new test sample are started with cooling in saturated or weakly subcooled liquid. Fig. 5 shows the typical thermograms of cooling of a ball of AISI316 stainless steel, 30 mm in diameter, in water at 90°C. The experiments were carried out with the new experimental facility described above.

As it was expected the most part of the cooling process was held at stable film boiling regime, which is replaced by a transition, and then nucleate boiling. Transition boiling always began at about the same temperature close to temperature of liquid superheat limit. Thermograms show that film boiling regime proceeds about 70 seconds; at t = 75-80s temperature at center sphere was lower than temperature registered by the surface thermocouples (135º and 180º), but higher than temperature registered by the equatorial thermocouple (90º). This is because the development of the transition and nucleate boiling regions begins at the upper part of the ball due to heat removal through the tube-holder. Its influence on breaking symmetry of cooling process of small diameter sphere with less thermal conductance is much stronger than in earlier experiments with nickel ball, 45mm diameter [9, 10]. In the stable film boiling regime, as is clear from Fig. 5, the surface thermocouples readings differ from each other insignificantly that allowed averaging temperature over the whole surface of the ball.

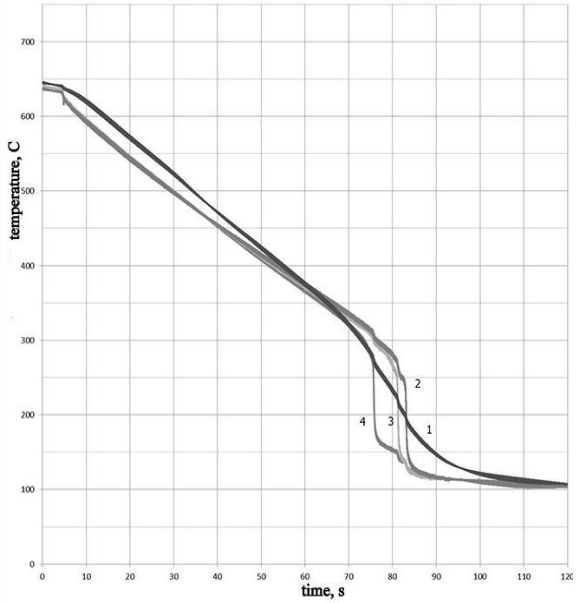

Figure 5 Cooling of the stainless steel ball, 30mm in diameter, in water with a temperature of 90°C. Location of thermocouples: 1-central; 2, 3, and 4 at the surface at θ=180°, 135°, and 90° correspondingly.

Basing on the averaged thermograms heat flux and HTC were calculated. The calculated dependence *q(ΔT)* is in good agreement with the recommendations [3] for stationary film boiling and [18] for subcooled film boiling. Spherical symmetry of the temperature field approximately conserved for the whole period of cooling. This allowed to obtain the curves *q*(*ΔT*) for transition and nucleate boiling regimes; they appeared to be in reasonable agreement with the recommendations of [19,20] for heat transfer in the corresponding steady regimes.

The main part of researches was carried out with subcooled water. At subcooling more than 30K the regimes of intense heat transfer are always observed under the conditions when the ball surface temperature significantly exceeds the critical one for water (374°C). Fig. 6 presents the thermograms of the ball cooling in water with temperature 30°C; for better understanding the thermograms shape in the beginning of the intensive cooling the different scales of time were used. For 1s the surface temperature in the points of thermocouples positions decreased by 470-500K, whereas in the center of the

sphere only by 50K. At the end of this time interval the temperature difference between the ball center and the surface was 420-450K. It is clear that under these conditions assessment of surface heat flux on basis of a lumped heat capacity is impossible.

More attentive analysis reveals a difference in cooling rates at various points of the surface. As in other similar regimes front of intensive cooling moves upward; the thermocouples 3 and 4 located on the lower half of the ball surface show that for the first 0.3s the temperature lapse rate is about 1000 K/s. The cooling rate at the sphere equator (θ = 90°) fixed with the thermocouple 2 significantly lower. Strictly speaking, in these circumstances using 1D energy equation is not correct. At the same time comparison with the previously obtained cooling thermograms for the nickel ball of 45mm in diameter [8] shows that in the discussed cooling regime deviation is much smaller. The main thing is that the regime of intense heat transfer (microbubble boiling) starts simultaneously in the all points of the surface equipped with thermocouples, i.e. a qualitative homogeneity of the process is observed.

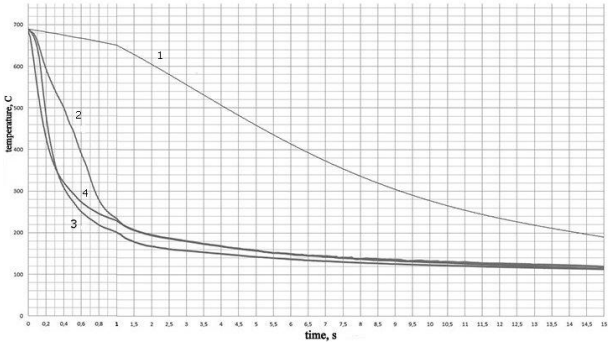

Figure 6 Cooling of the stainless steel ball, 30mm diameter, in water at 90°C. Location of thermocouples: 1-central, 2, 3, and 4 at the surface at θ=180°, 135°, and 90° correspondingly.

Therefore, for an approximate estimate of heat flux at the surface for the cooling regime shown in Fig. 6 the process can be considered as spherically symmetric one. For the averaged surface temperature at each time step HTC is calculated as it is described in the previous section. A comparison of the calculated and the measured thermograms for the ball center was used as an independent criterion of the solution reliability. For the most important period of intense cooling (t ≤ 1s) the calculated value of the ball center temperature exceeds the measured one at this point by 35K maximum, that is about 5% of ΔT. Probably, the main reason of advancing cooling rate of the ball in comparison with the calculated one is the discussed above influence of the tube-holder.

Fig. 7 shows variation of heat flux density at the ball surface in dependence on the wall superheat $\Delta T = T_w - T_s$. In the real process ΔT decreases with time, i.e. the process occurs from right to left in the coordinates of Fig. 7. As can be seen, heat flux density in intensive cooling regime reaches 5 MW/m^2 that is almost four times higher than characteristic value of CHF in pool nucleate boiling of saturated water.

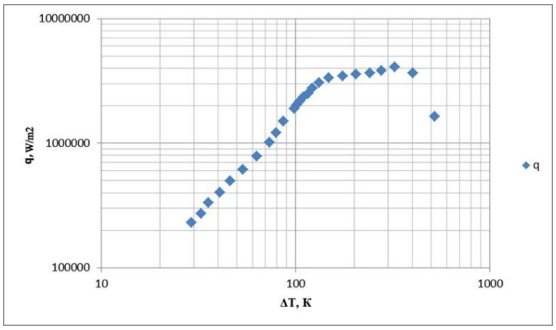

Figure 7 Dependence $q(\Delta T)$ for the 30mm stainless steel ball cooling in subcooled water, ΔT_{sub} = 70K.

Fig. 8 presents comparison of the thermograms for the surface thermocouple at θ = 90° for different values of coolant temperature. With increasing of water subcooling stability of vapor film is lost at the higher wall temperature and in shorter period of time after immersion of the ball. This general trend in some experimental runs is disrupted by random disturbances, probably, due to influence of the holder. The most notable deviation is obtained for water at temperature T_1 = 55°C. But in all cases presented in the figure there is a regime with a very high rate of surface cooling (up to 1000 K/s). Thus, the study has shown that during the stainless steel ball quenching in subcooled water the regime of intensive heat transfer in film boiling (microbubble boiling) is also observed.

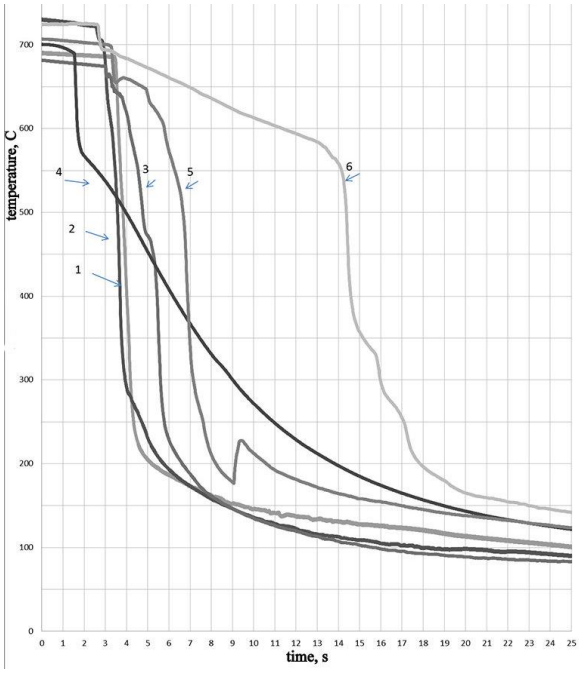

Figure 8 Thermograms of cooling at different temperatures of cooling water: 1-30º, 2-40º, 3-50º, 4-55º, 5-60º, 6-65ºC. Data are referred to the lateral thermocouple (θ=90°).

Thus, the existence of a specific regime of high heat transfer intensity in subcooled water film boiling, which was named the microbubble boiling by G. Hewitt and D. Kenning, is now confirmed for metals with thermal conductivity divergent more than 20 times: from about 400W/(m·K) for argentum and

copper to approximately 18W/(m·K) for stainless steel. It is revealed that for a spherical sample of low thermal conductivity even at small size cooling process loses spherical symmetry.

Since there is currently no physical model for heat transfer during microbubble boiling, experimental studies using different cooling media and various metals have to be continued. Revealing the quantitative regularities of influence of liquids subcooling, their thermal properties, of properties and size of the cooled object on the process should lead to understanding the mechanisms of this boiling regime.

The study was performed at the expense of Russian Science Foundation (project №14-19-00991).

REFERENCES

[1] Kobasko N.I Steel quenching in liquid medium under pressure, *Kiev: Naukova dumka.(In Russian)*, 1980.

[2] B. Liscic and H.M. Tensi, Quenching Theory and Technology, Second Edition, *Published in 2010 by CRC Press Book.*

[3] Ametistov E.V., Klimenko V.V., Pavlov Y.M., Boiling of cryogenic liquids, *Energoatomizdat*, 1995, 400p.

[4] Flament G., Moreaux F., et Beck G., Instabilite de la calefaction a haute temperature sur an cylinder vertical trempe dans up liquide sousrefroidi, *Int. J. Heat Mass Transfer*, vol. 22 (1979) 1059-1067.

[5] Bradfield W.S., Solid-liquid contact in stable film boiling, *Ind. Eng. Chem. Fundam*, Vol. 5, 1966, pp. 200-204

[6] Aziz S., Hewitt G.F., Kenning D.B.R., Heat transfer regimes in forced-convection film boiling on spheres, *Proc. 8th Int. Heat Transfer Conf., San Francisco*, Vol. 5, 1986, pp. 2149-2154

[7] Zvirin Y., Hewitt G.F., Kenning D.B.R., oiling on free falling spheres: drag and heat transfer coefficient., *Exp. Heat Transfer*, Vol. 3, 1990, pp. 185-214

[8] Corell S.J., Kenning D.B.R., Hewitt G.F., Film boiling on a molten brass spheres in flowing water., *UK Nat. Conf. on Heat Transfer*, Glasgow. 1988. P. 1557-1564

[9] Lexin M.A., Yagov V.V., Varava A.N, Experimental study of heat transfer in the intensive cooling metal ball, *Vestnik MPEI (In Russian).* 2009, №2, с. 28-34.

[10] Lexin, M.A., Yagov, V.V., Pavlov, P.A., Zabirov, A.R., Experimental study of heat transfer at cooling of high-temperature bodies in subcooled liquids, *Proc. of 6th Int. Conf. on Transport Phenomena in Multiphase Systems*, . 2011. Ryn, Poland. pp. 301-306

[11] Victor V. Yagov., In *"Heat Pipes and Solid Sorption Transformations. Fundamentals and Practical Applications"*, edited by L.L. Vasiliev and Sadik Kakac. CRC Press, Taylor & Francis Group. 2013. P. 109-143. [7] Zvirin Y., Hewitt G.F., Kenning D.B.R., oiling on free falling spheres: drag and heat transfer coefficient., *Exp. Heat Transfer*, Vol. 3, 1990, pp. 185-214

[12] V. S. Grigor'ev, V. G. Zhilin, Yu. A. Zeigarnik, Yu. P. Ivochkin, V. V. Glazkov, and O. A. Sinkevich, The behavior of a vapor film on a highly superheated surface immersed in subcooled water, *Teplofizika Vysokikh Temperatur*, Vol. 43, No. 1, 2005, pp. 100–114.

[13] V.G. Zhilin, Yu.A. Zeigarnik, Yu.P. Ivochkin, A.A. Oksman, K.I. Belov. An experimental investigation of the characteristics of explosive boiling of subcooled water on a hot surface under conditions of change of boiling modes, *Teplofizika Vysokikh Temperatur*, 2009, Vol. 47, No. 6, pp. 891–898.

[14] Yu.A. Zeigarnik, Yu.P. Ivochkin, V.S. Grigor'ev, A.A. Oksman., Notes concerning some aspects of vapor explosion, *Teplofizika Vysokikh Temperatur*, Vol. 46, No. 5, 2008, pp. 797–800.

[15] Bolukbasi A., Ciloglu D. Investigation of heat transfer by means of pool film boiling on vertical cylinders in gravity. *J. Heat Mass Transfer.* 44 (2007) 141-148.

[16] Sher I., Harari R., Reshef R., Sher E., Film boiling collapse in solid spheres immersed in a sub-cooled liquid, *Appl. Therm. Engng.* 36 (2012), 219-226..

[17] Suzuki K. Microbubble emission and high heat flux observed in subcooled boiling. *ECI Int. Conf. on Boiling Heat Transfer*, Spoleto, Italy. 7-12 May 2006.

[18] Yagov V.V. ,Lexin M.A., approximate model of heat transfer in the steady film boiling, *Proceedings NCHM-5. T.* 4 Moscow : MPEI publishing house 2010, 177-180.(in Russian).

[19] Labuntsov D.A., Yagov V.V.. Mechanics of two-phase media Moscow : MPEI publishing house 2010.(in Russian).

[20] Yagov, V.V. 1993. Mechanism of transition boiling of liquids. *J. Eng Phys Thermophys.* 64: 740–751 (in Russian).

Flow Visualization and Thermal Measurements on Pulsating Gravity Assisted Heat Pipes

De Paul, I*., Piera, R., Hoyos D.
Facultad de Ciencias Exactas
Universidad Nacional de Salta
Av. Bolivia 5150 - 4400 Salta - Argentina
E-mail: depaul.irene@gmail.com

ABSTRACT

A gravity assisted heat pipe (GAHP) was employed as an efficient heat transfer device in passive cooling by IR nocturnal radiation. Experiences were performed to compare the functioning of two GAHPs, one constructed in copper and other one in glass for flow visualization. Both have similar dimensions, use distilled water as transport fluid and have similar fill ratio using the environment as the cold source. Flow visualization experiments showed a pulsating behavior, the heat absorbed at the evaporator generates bubbles that rise very quickly, displacing sometimes an important volume of water. The rise velocity was measured during the pulsating interval giving values in the range 1.2 to 5.7 m/s and a mean period of pulsations of 0.14 s. The use of digital image processing allowed to detect the presence of ascending vapor masses inside the tube, that were not visible at a glance. Experiences of variable and constant power supply were performed. Temperature measurements of the warm source, the environment, the evaporator, a midpoint along the tube and the condenser were performed allowing to establish a clear correlation between the thermal measurements and the pulsation observed in the glass GAHP, verifying that the copper GAHP in which the visualization was not possible also pulsate. The global thermal transfer coefficient and thermal resistance were calculated giving good correlations with the power supplied, in the tested range of 3W to 60W, with a determination coefficient bigger than 0.9.

INTRODUCTION

Gravity assisted heat pipes (GAHP) are a particular case of heat pipes that operate in vertical position, often without a wick, so the return of the working liquid from the condenser towards the evaporator is realized by gravity and therefore behave as a thermosiphon [1,2,3]. GAHPs are very efficient devices and their use is spreading to different areas of the technology such as electronics, solar collectors, etc [4,5,6,7]. A GAHP without wick was employed as a heat transfer device in passive cooling by IR nocturnal radiation [8]. For having a better knowledge of its functioning experiences were performed to compare the operation of two GAHPs, one constructed in copper and other one in glass for flow visualization [9]. Both have similar dimensions, use distilled water as transport fluid and have similar fill ratios. The observations showed a pulsating character in the fluid dynamics and heat transfer [10] associated with the geyser effect [11,12,13,14]. The comparative study of the thermo-fluiddynamic behavior of these pipes showed that under the same working conditions both pipes had a pulsanting behavior, each one with its own characteristics that could be inferred from thermal measures. These experiences were realized at first supplying thermal variable power, carrying the temperature of the water of a thermos to a maximum specified value and analyzing the cooling towards the environment produced by the GAHP, the following experiences were realized with a constant power source, a cylinder of isolated aluminum warmed with an electrical resistance and a variable transformer.

NOMENCLATURE

T	[ºC]	Temperature
T'	[-]	Dimensionless temperature
C	[-]	Condenser
E	[-]	Evaporator
M	[-]	Midpoint
S	[-]	Heat source
Q	[W]	Thermal power supplied
V	[V]	Voltage
I	[A]	Current
UA	[W/ºC]	Global thermal coefficient
R	[ºC/W]	Global thermal resistance

Subscripts

a	ambient
c	condenser
e	evaporator
m	midpoint
s	source
w	water

FLOW VISUALIZATION

For flow visualization experiences a glass GAHP was constructed with a burette of 67cm length, 1,45cm internal diameter, 1,73cm external diameter, with a scale that allows to realize a precise measure of the volume of liquid in its interior and of the position of the water menisci. The length of the evaporator was 12cm; the adiabatic zone was 5cm and the condenser 50cm, evacuating heat to the environment. The copper GAHP built for comparison had 71cm of total length, external diameter 1,5cm and internal diameter 1,3cm. The evaporator measured 12cm, the adiabatic section 5cm and the condenser 54cm. The working liquid for both was distilled water with a filling fraction of 12 %. The heat source employed was thermalized water placed in a thermos shield with high density expanded polyurethane that allows to introduce the pipe

and the thermocouples. The evaporator E (T_e), midpoint M (T_m), condenser C (T_c), water (T_w) and ambient (T_a) temperatures were measured with T thermocouples using a datalogger Omega, with sample rates of 2 sec and 1min. The evacuated heat was calculated by measuring the cooling rate of the water in the flask. The general layout is shown in Figure 1a. A video camera Panasonic and a digital photographic camera Sony with a period of 1/30s between captures were used in flow visualization experiences. A non disturbing method was employed to measure the speed of the fluid inside the pipe, for which a camera Sparklan controlled by a computer was arranged, taking images at a rate of 10 images per second and processing them with a specific program [10].

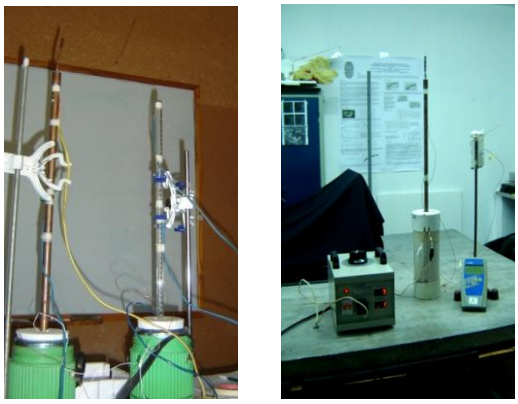

Figure 1. Experimental layout for a) variable heat power supply b) constant power supply.

The flow inside the glass GAHP develops in the following way: at the beginning the top meniscus of the water contained in the pipe is observed practically at the same height of the flask cover (Figure 2a); later a rapid vaporization takes place (Figure 2b) and vapor rises along the pipe; sometimes during the ascent vapor condenses forming a drop. When the steam or liquid water reaches the end of the pipe the impact is listened as a shot. The water condensed at the top slips down forming a film that breaks slowly until the initial level of the water is recovered and the pulsation begins again. Everything is very rapid; this process could be kept for hours, until the temperature of the water descends below the certain value.

(a) (b)

Figure 2. Visualization of flow inside the glass GAHP a) Top meniscus of water in the pipe. b) Vaporization.

Sometimes a bubble is formed inside the liquid at the evaporator and a slug is formed that rises very fast (geyser effect), as can be seen in Figure 3, loses part of the water on the glass, reaching the end of the pipe and producing also a shot.

Figure 3. Visualization of a slug rising inside the GAHP.

VELOCITY MEASUREMENTS

In one of the experiences in which the maximum temperature of the water was 89ºC a sequence of 16 images was taken at a rate of 30 images per second that allowed to follow the evolution of four consecutive slugs, to measure their velocities, the variation of the water volume displaced that diminishes during the ascent generating a film on the glass of the pipe, and to measure the period of the pulsation. The position of the top meniscus as function of time was fitted with a degree two polynomial that allows to know the speed and acceleration of each of the four sequences of images; the range of velocities measured was 1.22m/s to 5.72m/s, that of acceleration was -2.57m/s^2 to -6.75m/s^2, the periods ranging from 0.14s to 0.16s. The water volumes displaced diminish because of adherence in the glass surface of the pipe.

In an experience in which the maximum temperature of the water was 70ºC, two images were taken with a camera controlled by a computer with a difference of 0.116s recording the position of a drop in that interval. The images were digitally processed extracting the first from the second and defining better the edges.

Figure 4a shows one of the images taken by the camera, while Figure 4b shows the result of the processing. It can be seen the position of the water drop marked on the photograph and something that was not possible to see at a glance: the presence of other pulses of steam inside the pipe, besides the drop that is condensed. Measuring the position of the drop along the pipe it was possible to calculate the average speed obtaining the value of 3,79 m/s that agrees with the range of values obtained with the previous method.

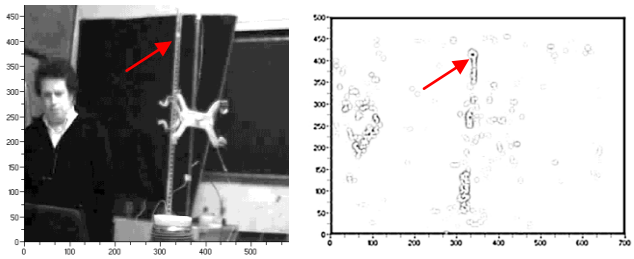

(a) (b)

Figure 4. a) Image recorded by the camera. b) Processed images showing steam pulses inside the pipe.

THERMAL MEASUREMENTS

The thermal measurements performed simultaneously on the glass and copper GAHPs under similar thermal conditions showed oscillations of temperatures of both GAHPs associated

with the pulsations observed in that of glass, so it was conclude that the copper GAHP also pulsates. During the pulsations the thermos water and the evaporator temperatures went down while the condenser temperature went up; this means that heat is absorbed at the evaporator and create inside the pipe conditions that allowed the nucleation and growth of bubbles that can be expelled as a water slug or exploited forming a pulse of vapor rising very fast. Pulsation depends on the maximum water temperature: at 89 ºC the pulsation is immediate, whereas at less than 50ºC no slugs pulsations were observed. This behavior is kept for more short periods in the copper GAHP than in the glass one. In the same measurements different ranges of functioning associated with different thermo-hydrodynamic behaviors in the fluid were observed. Figure 5 shows a typical measure of temperatures on the glass and copper GAHP under similar thermal conditions.

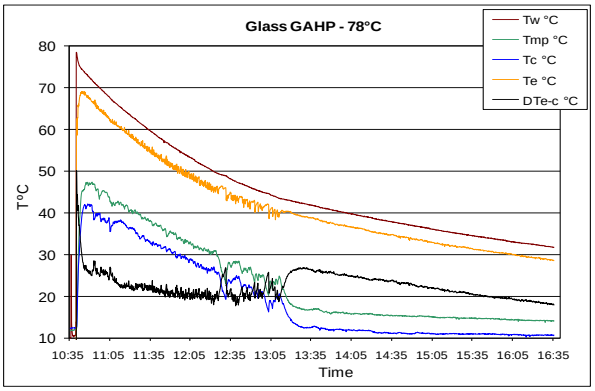

(a)

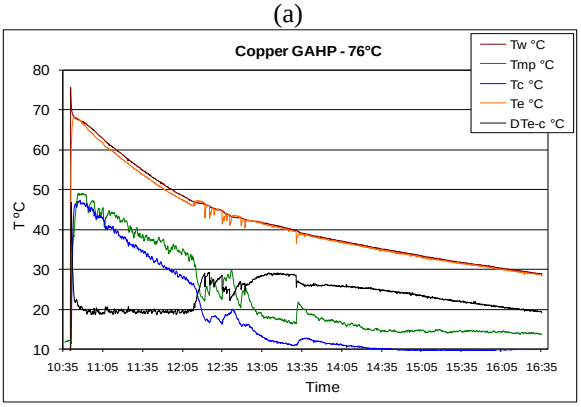

(b)

Figure 5. Temperature measurements a) on the glass GAHP and b) on the copper GAHP.

The global thermal coefficient UA as function of the thermal power supplied shows a linear trend for both the copper and the glass GAHPs, with a slope slightly minor for that of glass, while the thermal resistance as function of power can be fitted with good precision with a potential curve $R = aP^b$, the parameters a and b ranging from 12 to 27 ºC/W and -0,75 to -1,03 respectively.

Tests on the copper GAHP

For constant power experiences the heater was an aluminum bar of 20cm length and 5cm diameter with a perforation of 2,2cm of diameter where the GAHP was placed. An 18Ω resistance was wounded around the bar connected to a variable transformer. The bar was placed in a support of PVC, wrapped in 5cm of mineral wool that assures that thermal losses were less than 0,3 %, so it was assumed that all the electrical power that is used in warming the cylinder is evacuated towards the environment by the GAHP (Figure 1b).

Temperatures of the evaporator E (T_e), the condenser C (T_c), in the midpoint of the pipe M (T_m), on the heat source S (T_s) and the ambient (T_a), were measured with T thermocouples with a sample rate of 10 seconds. Many experiences were realized changing the power supplied between 3,7W and 60,2W evacuating the heat towards the environment in conditions in which the temperature of the laboratory was practically constant.

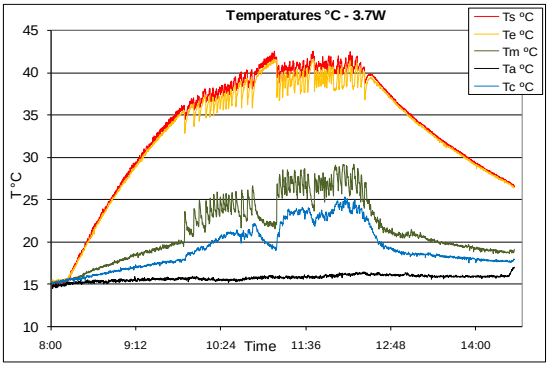

(a)

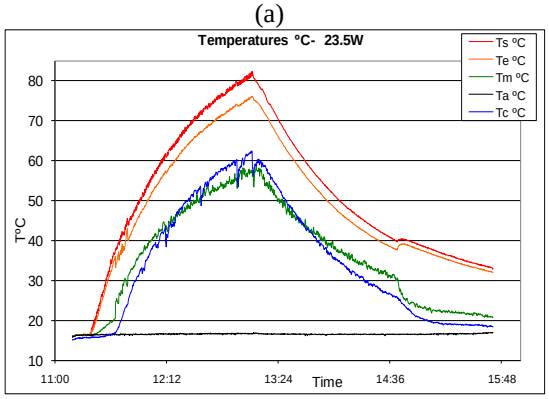

(b)

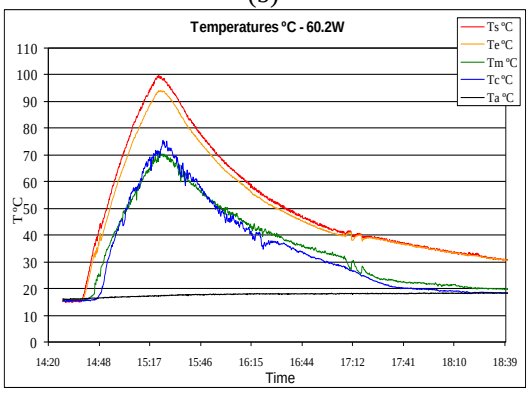

(c)

Figure 6. Temperatures at the different measurement points corresponding to three power supplies: 3.7W, 23.5W and 60.2W.

Figures 6 a, b, and c show the temperatures corresponding to three power supplies: 3,7W, 23,5W and 60,2W at the different measurement points. The changes that they show are evidence of different thermo-hidrodynamic flows inside the GAHP.

At the beginning the temperature rises regularly, almost linearly at the midpoint M and the condenser C, until the first pulsation takes place. At this stage the thermal conduction realizes by conduction in the copper wall of the pipe and by convection of the steam from the evaporator in agreement with the usual description. Later very regular oscillations are observed in which the heat source S and the evaporator temperatures diminish in phase whereas the midpoint temperature M increases in opposition of phase in a pulsating way, and the temperature of the condenser C increases with less marked oscillations. This suggests the formation of bubbles in the liquid that absorb heat and detach as a steam pulse or water slug as was described previously (geyser effect). At 3,7W two intervals in which there were no pulsations but a systematic increase of the temperatures of the source and the evaporator and a decrease of those of the midpoint and condenser are observed. This suggests that bubbles were not formed, the warming of S and E comes from the heater whereas M and C cool towards the environment; the heat supply is low and the cooling is dominated by the transfer towards the environment. In this experience an equilibrium temperature seems to be reached at the source, about 40°C. When the warming ends a last pulsation takes place that cools S and E, and warms M and C. Later the evaporator E and the average point M disconnect from C, increasing a bit the temperature and then cooling slowly without pulsations. At this stage the heat would be transmitted by conduction in the copper towards the environment, and in minor measure by convection in the interior.

At mean power supplies pulsations in phase of great extent take place between S and E and in opposition of phase in M, whereas C increases softly without big oscillations. The temperatures rise systematically and a transition takes place to a regime of rapid oscillations of minor extent and major frequency (small oscillations), until an anomalous pulsation takes place: S and E increase their values whereas M diminishes sharply; later the warming continues regularly with small oscillations. When the warming ends the small oscillations stop and all the points cool slowly. Another anomalous pulsation can appear and the disconnection between E and M takes place as in the previous case.

A question rises about how an anomalous pulsation could be provoked. A possibility is that a water slug at mid height absorbs heat from the pipe, breaks and generates a steam wave that propagates down increasing the temperature of S and E; another possibility is that a bubble was formed in the liquid film returning from the condenser lowering the temperature in M, exploding and generating also a steam wave that warms suddenly S and E.

At powers over 25W the temperature of C overcomes that of M during a certain interval, suggesting that the heat is transported by an intense convective process which prevails on the copper conduction. When the warming finished the disconnection between E and M takes place and, sometimes, a last pulsation is observed.

At powers ranging from 35 to 60W approximately the general behavior is similar to the observed at medium powers except that after the disconnection some big oscillations take place before following a monotonous cooling.

Difference of temperature analysis

The oscillations observed were analyzed by performing a Fourier analysis of the time series of the differences of temperatures between E and C at different power supplies, that showed a spectrum dominated by low frequencies corresponding to periods ranging from 24.4min to 113.8min, but they also showed the presence of higher frequencies associated to the small oscillations observed that could be produced by steam pulses rather than water slugs (Figure 7).

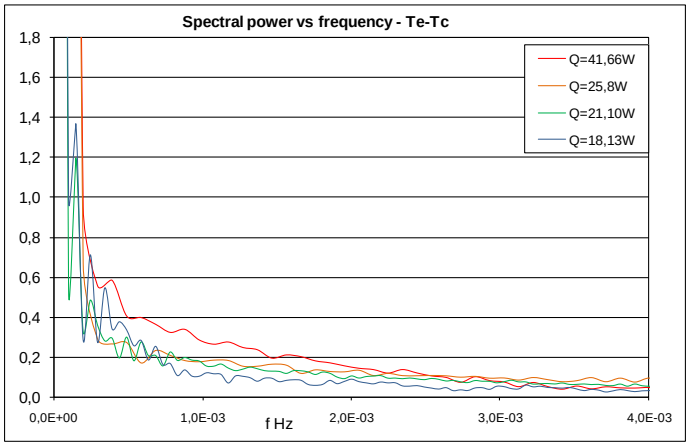

Figure 7. Fourier spectrum of the temperature difference between evaporator and condenser at different Q.

The difference of temperature between the evaporator and the condenser is an indicative of the thermal transfer inside the GAHP, whereas the difference of temperature between the condenser and the environment is a measure of how much heat is liberated to the cold source. Since the transfer depends on the average temperature of the environment during every experience, in order to compare the heat transfer, dimensionless temperatures were defined in the following way:

$$T' = \frac{\left(T - \overline{T_a}\right)}{\overline{T_a}} \qquad (1)$$

Figure 8 shows the differences T'e - T'c whereas Figure 9 shows the differences T'c - T'a as function of time from the beginning of the warming; the parameter is the electrical power supplied by the heater. They show a pulsanting behavior even after disconnection between evaporator and the midpoint occurred, that is, it persisted after the warming has stopped.

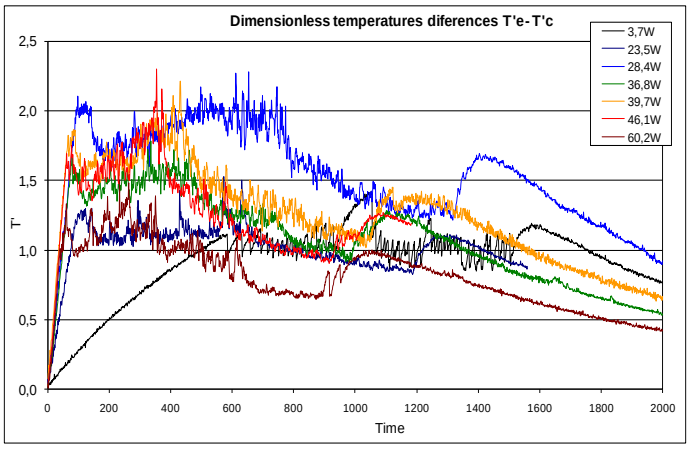

Figure 8. Dimensionless temperature difference between evaporator and condenser.

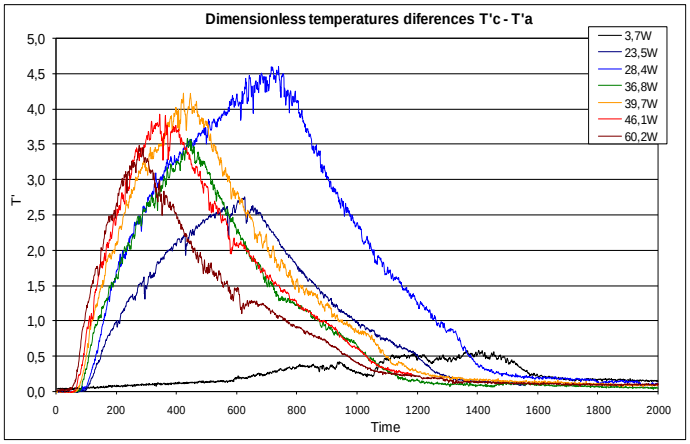

Figure 9. Dimensionless temperature difference between condenser and ambient.

Coefficients UA and R

Following the bibliography the global thermal transfer coefficient UA and thermal resistance R of the GAHP were calculated with the following expressions: supplied power: $Q = VI$, global thermal transfer coefficient: $UA = Q / (Te-Tc)$ thermal resistance: $R = 1/UA$. Figures 10a and 10b show the mean values of UA and R during the pulsating period as function of the power supplied Q. The linear fitting of UA and the potential fitting of R have a good determination as can be seen on the figures.

Something wrong happened at high powers: the thermal power evacuated by the GAHP was greater than the electrical power supplied. This occurred when the condenser temperature was greater than that of the midpoint as can be seen in Figure 11. This suggested that the condenser extracted heat not only from the source but also from the ambient through the copper wall of the GAHP. To test this observation a second coefficient UA1 was calculated in the following way: $UA1 = Q/(T_m-T_c)$.

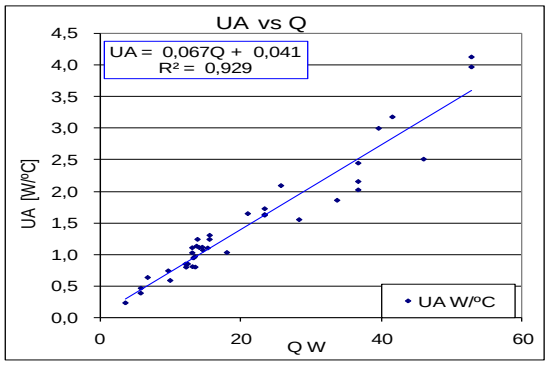

(a)

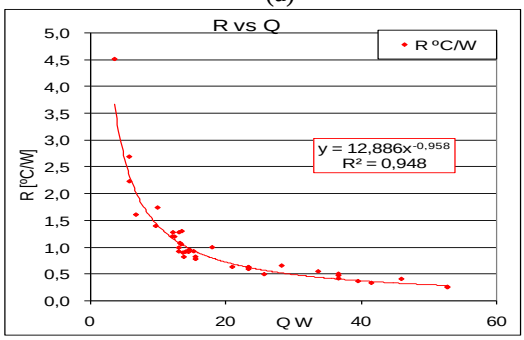

(b)

Figure 10. Mean values of UA (a) and of R (b) as function of Q, pulsating period.

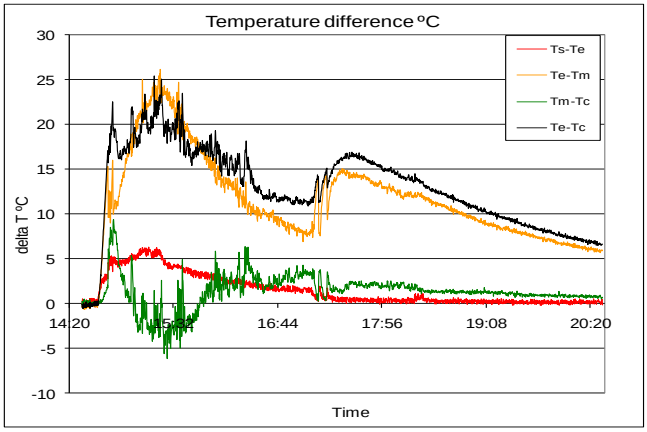

Figure 11. Temperature differences at Q = 60.2W.

Figure 12 shows that UA1 as function of time presents rapid oscillations. When an inversion of the temperatures occurred between the midpoint and the condenser the coefficient UA1 is negative. This suggest that bubbles detached from the liquid film at the midpoint, extract heat from the ambient, rise very quickly, warm the condenser and produce strong oscillations in UA1; in this way the evacuated thermal power dissipated is greater than that supplied by the source.

To confirm this interpretation new experiences were performed isolating the pipe with mineral wool and reducing the length of the condenser to 15cm. In these cases the condenser temperature was always less than that of the midpoint and the evacuated thermal power was less than the electrical power supplied.

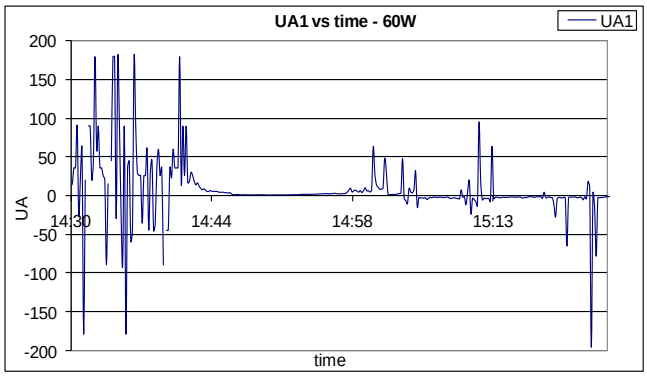

Figure 12. Coefficient UA1 between de midpoint and the condenser as function of time.

A conclusion that can be obtained from these results is that at sufficient high powers the convective flow inside the pipe is so strong that can create conditions for bubble generation at the middle length of the pipe, extracting heat not only from the source that is wanted to cool but from the environment, if the condenser is too long. A longer condenser means more capacity for heat transfer but it could be inefficient; so it is important to determine the optimum length of the condenser according to the requirements. Excluding these anomalous results the thermal behaviour of the copper GAHP can be characterized with the following relations in the range 3W < P < 60W:

$UA = 0.067Q+0.041$ W/ºC $\quad R^2 = 0.93$

$R = 12.886Q^{-0.958}$ ºC/W $\quad R^2 = 0.95$

CONCLUSIONS

Flow visualization experiments performed with a glass GAHP showed that in the range of thermal power supplied the heat transfer was not only through evaporation of the working fluid at the evaporator but also through strong pulsations of steam or water slugs that detach from the evaporator. The thermal measurements showed these pulsations as strong oscillations of the temperature recorded along the pipe that give information about the characteristics of the flow inside the GAHP; this fact becomes a tool for analyzing what happen inside a copper GAHP through thermal measurements. The ascent velocities measured were high, 1.22 to 5.73 m/s. Thermal measurements performed on the copper GAHP showed different thermo-hidrodynamic flows, pulsations of different intensity were always present, some anomalous that suggest that steam waves form at mid way along the pipe. Pulsation periods range from 24.4min to 113.8min. Another unexpected result allows to know that at high powers bubbles can be formed from de returning film of liquid extracting heat not only from the source but also from the ambient. This remarks the importance of adjust correctly the length of the condenser to the requirements for having an efficient performance.

In the range 3W < P < 60W the copper GAHP can be characterized in the following way: the global thermal coefficient is $UA = 0.067Q+0.041$W/ºC with a determination coefficient $R^2 = 0.93$, while the thermal resistance is $R = 12.886Q^{-0.958}$ ºC/W with $R^2 = 0.95$.

Acknowledgements

We want to acknowledge the financial support of the Consejo de Investigación de la Universidad Nacional de Salta, and the invaluable work of Dr. Erico Frigerio who collaborated with this project until his last days of live.

REFERENCES

[1] Joudi, K.A., Witwit, A.M. Improvements of gravity assisted wickless heat pipes, *Energy Conversion and Management*, 2000, **41**, 2041-2061.

[2] Anwarul Hasan, Chowdhury MD Feroz, Sadrul Islam, A.K.M. Performance of gravity assisted heat pipe *Proceedings of the International Conference on Mechanical Engineering* 2003, Dhaka, Bangladesh.

[3] Filippeschi, S., On periodic two-phase thermosyphons operating against gravity, *Int. Journal of Thermal Science*, 2009, 45, 124-137,

[4] Khandekar, Sameer. Thermo-Hydrodynamics Of Closed Loop Pulsating Heat Pipes, Doctoral Thesis, Institut für Kernenergetik und Energiesysteme der Universität Stuttgart, 2004.

[5] Khandekar, S., Dollinger, N., Groll, M. Understanding operational regimes of closed loop pulsating heat pipes: an experimental study, *Applied Thermal Engineering*, 2003, 23,707-719.

[6] Tang, X., Quan, Z., Zhao, Y. Experimental investigation of solar panel cooling by a novel micro heat pipe array, *Energy and Power Engineering*, 2010, 2, 171-174

[7] Rittidech, S., Wannapakne, S., Experimental study of the performance of a solar collector by closed-end oscillating heat pipe (CEOHO), *Applied Thermal Engineering*, 2007, **27**,11-12, pp.1978-1985.

[8] Frigerio, E. La radiación nocturna como fuente fría, su caracterización y uso. Doctoral Thesis, Universidad Nacional de Salta, Argentina, 2000.

[9] Frigerio, E. De Paul, I. Quintana J. Estudio comparativo del funcionamiento de tubos de calor en cobre y vidrio *Actas 33ª Reunión de Trabajo de ASADES AVERMA*, 2010. **Vol. 14**, pp.03.177-03.183.

[10] De Paul, I., Frigerio, E., Hoyos, D., Quintana,J. Visualización de flujos en un tubo de calor asistido por la gravedad. *Actas 32ª Reunión de Trabajo de ASADES AVERMA*,2009,**Vol. 13**, pp.03.09-03.15.

[11] Lin, T.F., Lin, W.T., Tsay, Y.L., Wu, J.C. Experimental investigation of geyser boiling in an anular two-phase closed thermosyphon, *Int. J. Of Heat and Mass Transfer*, 1995, 38 (2) 295-307.

[12] Khazaeea, I., Hosseinib, R., Noie, S.H. Experimental investigation of effective parameters and correlation of geyser boiling in a two phase closed thermosyphon, *Applied Thermal Engineering* 2010, 30 (5) 406-412.

[13] Lips, S., Bensalem, A., Bertin, Y, Ayel, V., Romestant, C. Experimental evidences of distinct heat transfer regimes in pulsating heat pipes (PHP) *Applied Thermal Engineering* 2010, 30, 900-907

[14] Sarmasti Emami, M.R., Noie, S.H., Khooshnoodi, M.K., Hamed Mosavian, M.T., Kianifar, A. Investigation of geyser boiling phenomenon in a two-phase closed thermosyphon Heat Transfer Engineering, 2009, 30(5), 408-415.

PHASE-LOCKED AVERAGING OF VELOCITY FIELDS WITHIN AN AXIAL FAN OPERATING UNDER ROTATING STALL CONDITIONS

Hribernik A.*, Bombek G. and Fike M.
*Author for correspondence
Faculty of Mechanical Engineering,
University of Maribor,
Smetanova 17,
SI 2000 Maribor
Slovenia,
E-mail: ales.hribernik@um.si

ABSTRACT

In state-of-the-art research of the flow within the turbo-machinery, numerical simulations are performed time-dependently and in three dimensions. The availability of quantitative measurement data is crucial for the validation of such simulations. In this study angle-resolved flow-fields within the rotor passage of an axial fan operating under rotating stall conditions were measured with the use of particle image velocimetry (PIV). PIV triggering was synchronised with the observed blades' passing, and over 1000 PIV images were obtained. These were then phase-locked averaged, and a sequence of 36 images was composed. The successive images represented the evolution of a flow field within the blade passage with 10° angular steps and made it possible for the structure and behaviour of the flow within the rotor blade passage to be analysed under rotating stall conditions. This paper reports on phase-locked averaging procedure. The influence of the reference signal, i.e. dynamic pressure time-history ahead of the rotor, on composed flow-fields and their measurement uncertainty was studied. Three averaging procedures were developed and compared using the criteria of minimal velocity variation along the selected flow path. Measurement uncertainty improved substantially when the characteristic shape and not the frequency of the reference signal was used for the phase shift averaging.

INTRODUCTION

Rotating stall is a characteristic flow instability of axial and centrifugal compressors and fans at reduced flow rates. This instability leads to a reduction in a compressor's performance (efficiency, pressure ratio, etc.) and plays a prominent role as a precursory phenomenon of a surge [1, 2]. As shown by Day [3] and Cumpsty [4], rotating stall originates in the instability of a local structure within the compressor's cascade-flow, and rotates in a circumferential direction as one or more rotating stall cells at a fraction of the rotor speed.

Rotating stall has been investigated over several decades via both analytical and experimental methods. Most of the experimental investigations based on velocity and pressure measurements have used hot-wire or multi-hole probes, and high response pressure transducers. Measurement signals were then processed with the periodical multisampling technique, and the double phase-locked averaging technique, which allowed for predicting the velocity and pressure fields at the compressor's inflow and outflow cross-sections, respectively, [5] and made the capture of a rotating stall cell and its propagation possible in an axial compressor. However, these averaged results were limited to the non-rotating section of the compressor, and the flow structures within the rotor blade rows (passages) remained hidden. Bearing in mind that the rotating stall phenomenon originates from the instability of local structure within the rotor's cascade flow, it is reasonable to focus the investigations of flow field into the rotating blade passage. Wernet [6] was one of the first who tried to investigate the rotor flow instabilities by applying the Particle Imaging Velocimetry (PIV) system. However, he failed to perform systematic investigation of the reverse flow due to the inability of correct system timing with the flow phenomenon. Krause et al. [7] applied the fast PIV system, which allowed for the capturing of each rotor blade passage per rotor revolution. However, even this was not enough for resolving the flow field evolution within the rotor cascade influenced by the rotating stall cell. All this calls for seeking the new ways for possible improvements in time-resolved visualisation of the described and similar flow phenomena. The purpose of this investigation was to check whether this can be achieved by the double phase-locked averaging technique which has been already successfully applied for time resolving the flow ahead of the rotor. The PIV method was applied in order to capture 2-D velocity flow-fields within the rotor blade passage at 80% of the rotor blade span, and ahead of the rotor. Exact PIV camera triggering was achieved by a signal from an optical encoder mounted on a motor shaft. The stall cell propagation was followed by a dynamic pressure signal ahead of the rotor. The dynamic pressure and trigger signals were acquired simultaneously, thus enabling phase-locked averaging to be used, and animations to be made of the velocity flow-field within the rotor blade passages. Three different averaging procedures were developed. In the first, the characteristic frequency of the reference signal was applied. However, it was stated during the tests, that there were some oscillations in the

reference signal frequency, thus an improved averaging procedure was developed which took frequency oscillations into account. Although this improved the accuracy, the third procedure based on the characteristic shape of reference signal was developed and showed even better results. This paper aims to provide the comparisons between all three averaging procedures and focuses on parameters influencing their accuracies.

EXPERIMENTAL SET-UP

Fan geometry and instrumentation

Experimental investigations were performed on a test rig, as shown in Figure 1. The test rig was built according to ISO 5801:2007 [8] and comprised an inflow section, an axial fan and an outflow section. A transparent duct (D_{in} = 290 mm) formed the fan's outer casing and extended 1000 mm into the inflow section. Coaxially, an inner cylinder, the diameter of which corresponded to the fan's hub diameter, was inserted so as to straighten the flow-field ahead of the fan in the axial direction. An axial flow fan was used without a stator and inlet guide vane. The rotor comprised 10 blades with a NACA 65 profile. The chord length and stagger angle were constant and did not change with the span. The rotor drive was hub-mounted, and the three-phase electromotor rotated the rotor at 1470 rpm. Detailed fan geometry specifications are summarized in Table 1. The outflow section was made of a 2000 mm long duct (D_{in} = 290 mm). It ended with a movable lattice that was used as a flow throttle.

Table 1: Design parameters of the test fan

No. of blades	10
Casing radius	145 mm
Hub radius	92.5 mm
Chord length	80 mm
Tip clearance	2.5 mm (constant)
Blade profile	NACA 6508
Stagger angle	45°
Hub/Tip ratio	0.65
Rotation speed	1470 rpm

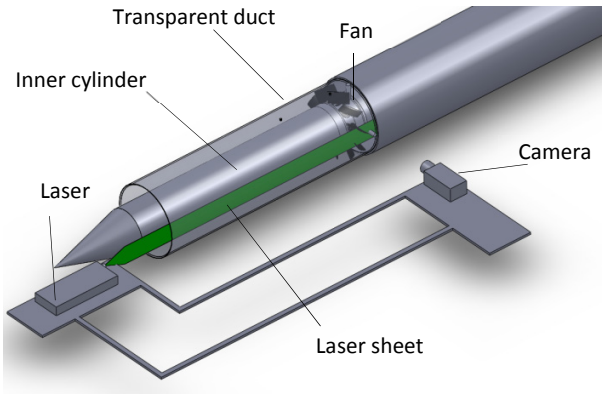

Figure 1 Schematic view of the test rig

PIV system

The Dantec low-speed PIV (Particle Image Velocimetry) system was used to capture the flow-field within the blade passage and at the rotor entry (Figure 1). The maximum system operating frequency was 4.5 Hz. A camera and laser were placed on a lightweight traverse system originally used for LDA measurements. A two-cavity Nd: YAG laser was used, operating at high power with 50 mJ pulse energy. A fog-generator was used for seeding in order to produce seeding particles with average diameters of 1 μm. The laser was placed upstream at ca. 1000 mm from the rotor. A CCD camera with 1280×1024 pixels resolution was used, and the area covered was ca. 81×65 mm. The time-interval between the laser pulses was 20 μs, and 32×32 pixel-size interrogation areas were used for velocity calculation. Cross-correlation and adaptive correlation were used, both with 25% overlaps.

The blade passage velocity fields were measured within the axial-circumferential plane (x–y plane) at 80% of the rotor blade span (Figure 2). The captured area covered the whole blade passage and extended approximately 20 mm into the fan entry.

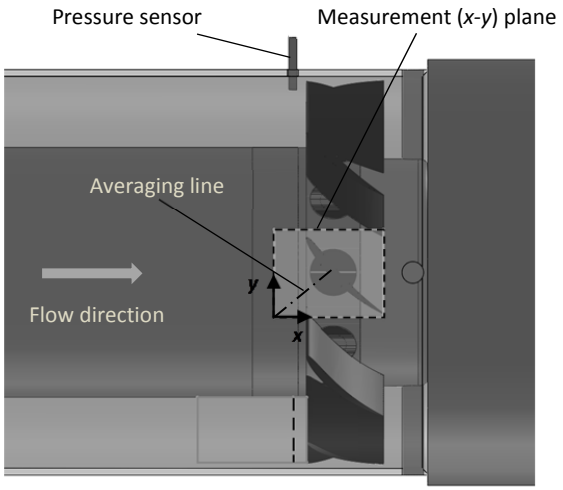

Figure 2 PIV measurement plane

A signal relating to the stall cell propagation was needed in order to utilise the phase-locked averaging technique. A signal from the pressure transducer measuring the dynamic pressure 10 mm upstream of the rotor's leading edge (Figure 2) was used for this purpose. The output of the photo-encoder mounted on the rotor shaft was used to trigger the PIV system, and the 2-D velocity-field was, therefore, always captured within the same blade passage. The triggering accuracy was approximately ± 0.05 degrees. The generated trigger signal and the rotating stall reference signal (dynamic pressure ahead of the rotor) were both acquired by the DAQ card based data acquisition system with a 100 kHz sampling frequency.

RESULTS

Overall characteristics of the test fan

The overall fan performance was measured and is presented in Figure 3. It was obtained by moving the exit lattice from fully opened to almost closed, and measuring the pressure rise and fan flow rate. The fan design point D was located in the middle of the stable region at flow coefficient φ = 0.32 and pressure rise coefficient ψ = 0.325. When the flow was reduced below the design point, the pressure rise coefficient ψ increased until reaching the stall point S_{in}. Below this point, a discontinuity occurs, and the operating point is suddenly moved to point S_1. Further flow reduction is accompanied by continuous pressure rise decrease towards points S_2 and SP, where the fan surge starts. With the increase of the exit lattice opening, the flow and pressure rise increased, and the fan's performance characteristic started moving back, crossed points S_2 and S_1 and reached point S_3, where the second discontinuity occurred, and the operating point moved suddenly into a stable region (point S_{out}). Characteristic hysteresis was formed in this way, as reported by [9]. The region between the operating points S_{in} and S_2 formed the rotating stall region, which was experimentally investigated. In this paper, we focus on operating point S_3, while the reference data on flow under other conditions may be found in [10]. One thousand PIV images of the same blade passage were made for the operational point S_3 and the results were phase-locked averaged.

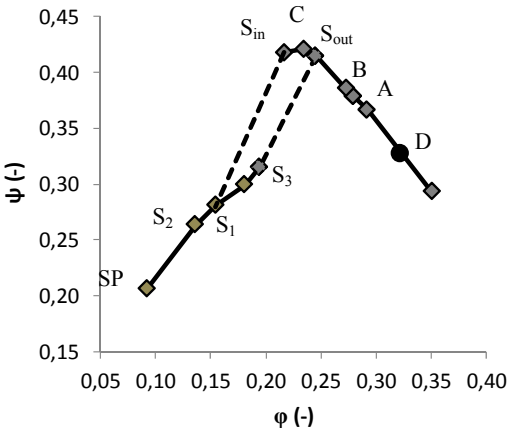

Figure 3 Fan performance curve

Rotating stall

When rotating stall occurs, the flow pattern within a blade passage alternates between a through flow and a backflow. If only one rotating stall cell exists, two domains can be observed: normal-flow and rotating stall cell. Whilst in the normal-flow domain the through flow prevails, the back flow is locally present in a domain of the rotating stall cell. This alternation between the through flow and back flow may simply be observed as a dynamic pressure variation ahead of the rotor which can be used as a rotating stall reference signal when performing phase-locked averaging. Thus a small twin-tube probe with a total pressure tap in front and a static pressure tap at the back was inserted 10 mm from the fan tip and 20 mm deep from the outer casing (Figure 2). Its circumferential position was shifted by 90° from the PIV measurement plane.

Figure 4 shows the dynamic pressure signal from the twin-tube probe. Its periodic shape allowed for the assumption that the rotating cell propagates at a constant speed (see also [5]). The characteristic reference signal frequency was obtained by the FFT procedure and equals 15.8 Hz which is 65% of rotor rotational frequency.

Phase-locked averaging

Three different averaging procedures were developed and tested. In the first procedure, a simple sine-wave signal was used instead of the raw rotating stall reference signal. A sine-wave signal with amplitude of 0.5 V was generated using the characteristic frequency f_{ref} of the raw rotating stall reference signal. It can be represented by a simple time-dependent function as:

$$f_{sw}(t) = 0.5 \cdot \left[\sin\left(2\pi f_{ref} t\right) + 1\right] \qquad (1)$$

The generated sine-wave signal is presented in Figure 4. It fits the general periodic form of the reference rotating stall signal well. The PIV trigger signal is also presented in the Figure 4. The PIV system operated at a 2.7 Hz frequency, thus approximately every sixth passing of the rotating stall cell was captured; however, the captures were not synchronised with the rotating cell position.

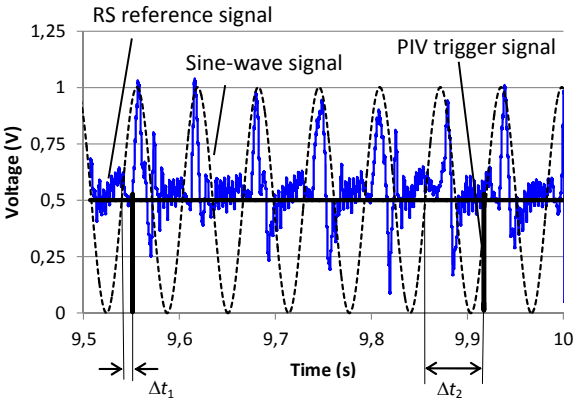

Figure 4 Raw rotating stall reference signal, generated sine-wave signal, and the PIV system trigger signal – OP S_3

In order to obtain phase-locked averaging, every single PIV image had to be correctly sorted according to the rotating stall cell position. This sorting was performed by a simple procedure (AP 1). The time-delay (Δt_i) between the trigger point and the nearest point, in a positive time direction, where the increasing sine-wave crossing the 0.5 value (Figure 4) was first found for each PIV image. Then the angular position of the PIV image in respect to the rotating stall cell position was assigned, and finally the images were sorted in respect of their angular positions from the minimum to maximum values.

A simple test was made to check the effectiveness of the sorting procedure. An averaging line was drawn in the measurement plane perpendicular to the blade chord (Figure 2), and the average velocity along this line was calculated, for each

PIV image. Figure 5 presents the sequence of averaged velocities before and after sorting thus proving that the images had been successfully sorted. The domains of normal-flow and rotating stall cell (RSC) are clearly distinctive. The rotating stall cell occupied approximately 40% of the rotor circumference. The averaged velocities dropped significantly within this region, and their fluctuations were extremely high. In contrast, normal-flow prevailed in 60% of the rotor circumference; the averaged velocities were almost constant here and the fluctuations were smaller. However, there is a possibility that a part of the velocity fluctuations is a consequence of phase-locked averaging and may not be ascribed to the flow phenomenon. Thus the first phase-shift averaging procedure was checked for possible improvements. In the first step the reference pressure signal was carefully inspected in order to find any disturbance which may influence the calculated phase shift Δt_i. It was found that in some cases there were small oscillations in the reference signal frequency, thus the sine wave function (equation (1)), did not represented the reference signal adequately which caused inaccurate prediction of phase shift Δt_i corresponding to the i-th PIV image.

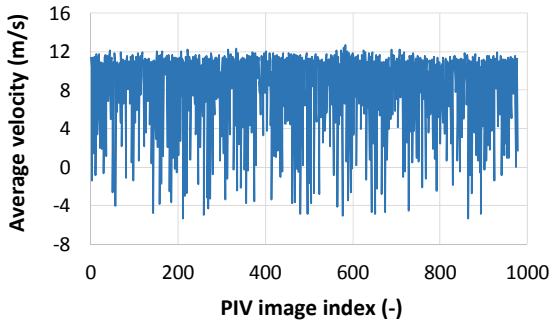

a) before sorting

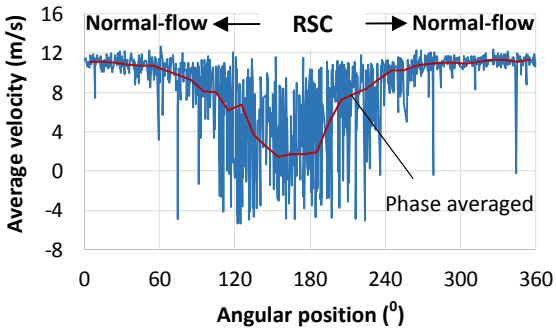

b) after sorting

Figure 5 The sequence of averaged velocities along the averaging line - AP1

In order to overcome the problem with oscillations of reference signal frequency, the averaging procedure was changed. Instead of using constant reference signal frequency instantaneous signal frequency was applied. The signal was first split into 1000 intervals each corresponding to the particular PIV image and extending between two successive PIV triggering and then the characteristic interval frequencies were computed. These were used in equation (1) to generate a sine wave signal for each single PIV image and finally to predict its phase shift Δt_i. This new averaging procedure (AP 2) has increased the computational time substantially, however, it has significantly improved the results. As shown in Figure 6, the velocity fluctuations reduced, especially within the region of the normal flow, while severe velocity fluctuations remained within the region influenced by the rotating stall cell. In order to further reduce these oscillations, a third averaging procedure (AP3) has been proposed.

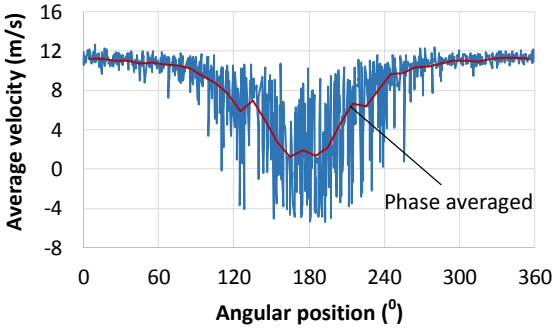

Figure 6 The sequence of averaged velocities along the averaging line – AP2

The third averaging procedure is based on the morphology of the reference signal. An abrupt signal change is observed when the rotating stall cell passes the pressure sensor (Figure 4). The first peak in the reference signal may, therefore, be used as an indicator of rotating stall cell passage and used to predict the phase shift Δt_i of a particular PIV image. However, high frequency disturbances in the signal made a correct determination of the peak difficult. Thus the signal was first processed by a moving average algorithm. The selected moving average interval was set to a time period which corresponded to the frequency of the highest disturbance. Figure 7 presents both, the raw and processed reference signals. It is obvious that the local peak position of the processed signal may be determined more precisely simply by searching the point where the signal gradient equals zero. Once the position of the local peak is determined the phase shift Δt_i of the particular PIV image was calculated from its distance to the trigger point as shown in Figure 8. The final sorting of all PIV images was then performed in the same way as already explained for the first averaging procedure AP1.

The results of third averaging procedure are presented in Figure 8. Velocity fluctuations reduced significantly both within the normal-flow as well as the rotating stall cell domains. Relative standard deviation of velocity within normal-flow domain is less than 4 %, whilst it increases to 50 % in the middle of the domain affected by the rotating stall cell. This indicates very unstable flow conditions taking place within the blade passage under rotating stall conditions, which are demonstrated in Figure 9.

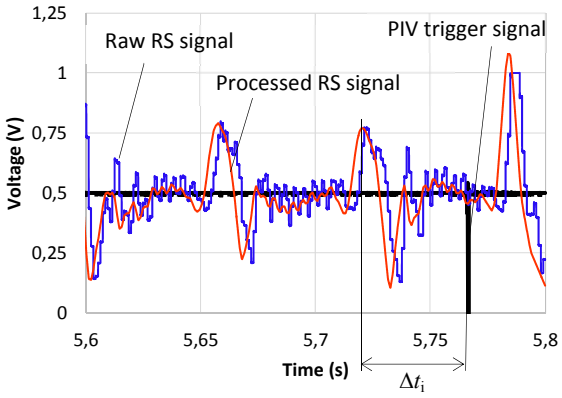

Figure 7 Raw and processed reference signal (AP3)

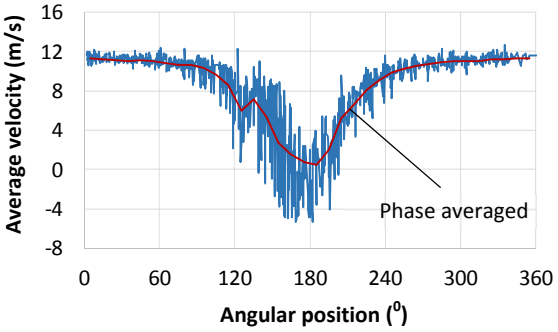

Figure 8 The sequence of averaged velocities along the averaging line – AP3

The last step of phase-locked averaging is the averaging of sorted PIV images. It was performed within constant 10° angular steps, and resulted in 36 consecutively averaged PIV images. A particular sequence of 36 consecutively averaged PIV images may be used for flow animation within the observed measurement plane. The successive relative velocity fields within the blade passage at 80% span are presented in Figure 9. Only a selection of angles is shown, in order to observe the main flow phenomena within the blade passage. The first image (0°) represents the blade passage flow under normal-flow conditions. The flow entirely follows the shape of the suction side of the rotor blade and no swirls are shown within the flow-field. The first changes occur at 100°. The axial velocity component changes the direction in the upper part of the flow field, and some of the fluid flows around the leading edge from the pressure to the suction side of the aerofoil and, since the overall velocity is slightly reduced, the flow still follows the suction side of the aerofoil. The fluid flow around the leading edge starts increasing and pushing the incoming intake flow away from the leading edge of the aerofoil. The overall flow velocity reduces, and at 140° flow separation from the suction side of the aerofoil occurs near the trailing edge. The flow separation point moves then very quickly toward the leading edge, reaching 30% of a chord length at 160° persists here at 170°, whilst the whole intake domain remains blocked (axial flow velocity component is 0). At 180°, the back flow around the leading edge stops, the flow separation point starts moving back towards the trailing edge and the intake flow starts filling the blade passage (image at 210°), until the flow conditions normalise and slowly change to normal flow.

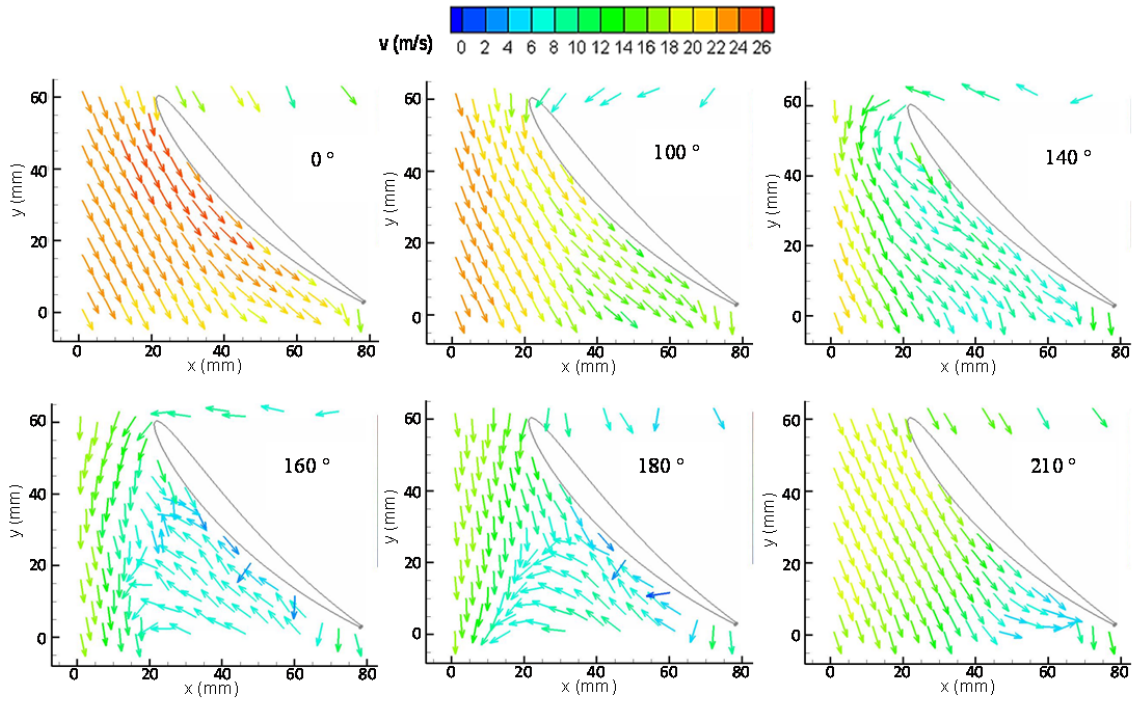

Figure 9 The sequence of averaged relative velocity fields within the blade passage at 80% span (every fifth vector is shown)

CONCLUSION

This paper has presented the visualisation of a blade passage flow within an axial flow fan operating under rotating stall conditions. Dynamic pressure measurements at the rotor tip proved that the rotating cell propagated at approximately 65% of the rotor speed. This made possible the phase-locked averaging of PIV measured velocity fields within the rotor blade passage using the dynamic pressure time history as the reference signal. Three averaging procedures (AP1 to AP3) were developed and compared. The first averaging procedure based on the assumption of constant rotating stall speed. It was simple to execute, however, it lacked on precision which caused unreasonable fluctuations of predicted velocity. With the second procedure, which considers rotating stall cell speed oscillations, some high fluctuations of predicted velocity still remained. These were satisfactorily reduced with the third averaging procedure which is based on the morphology of the reference signal and thus predict the phase shift of particular PIV image more precisely.

Using phased-locked averaging it was possible to build an animation of flow within the blade passage. A sequence of images was composed, presenting a flow-field changing over 10° steps. It showed that the first flow disturbance was induced by a reverse flow from the pressure side around the leading edge to the suction side of the aerofoil. Increasing the reverse flow slowly blocked and separated the blade from the intake air and flow separation suddenly occurred near the trailing edge. The flow separation moved extremely quickly in front to the leading edge and was then swept back to the trailing edge when the reverse flow around the leading edge declined, and normal-flow restoration took place. It was interesting that the blade passage was totally blocked for only a short 50° interval, although the whole flow distortion covered almost 150°. This showed that the blockage induction and especially the normal-flow restoration comprised the prevailing part of the phenomenon caused by the rotating stall cell passing the observed blade passage.

This paper proves that even a low frequency PIV system may be successfully applied for the time resolved visualisation of periodic flow phenomena such as rotating stall which occurs within compressors and fans. Although, some complex local flow structures vanish due to the averaging the obtained results faithfully mimic the global time depended flow field variation and the way of spreading flow disturbance caused by rotating stall cell through the rotor blade passage. As such, these, time-resolved flow visualisation results may be applied for quantitative and qualitative validations of flow simulations performed time-dependently in order to test their reliability and applicability.

REFERENCES

[1] Hara, T., Morita, D., Ohta, Y., Outa, E., Unsteady flow field under surge and rotating stall in a three-stage axial flow compressor, *Journal of Thermal Science,* Vol. 20, No. 1, 2011, pp. 6-12.

[2] Guardain, N., Burguburu, S., Leboeuf, F., Michon, G.J., Simulation of rotating stall in a whole stage of an axial compressor, *Computers & Fluids*, Vol. 39, 2010, pp. 1644-1655.

[3] Day, I.J., Cumpsty, N.A., The measurement and interpretation of flow within rotating stall cells in axial compressors, *Journal of Mech. Engineering Sci.*, IMechE, Vol. 20, No. 2, 1978, pp. 101-114.

[4] Cumpsty, N.A., Greitzer, E.M., A simple model for compressor stall cell propagation, *Trans. ASME, J. Engineering Power*, Vol. 104, 1982, pp. 170-176.

[5] Shiomi, N., Cai, W.X., Muraoka, A., Kaneko, K., Setoguchi, T., Internal flow of a high specific-speed diagonal-flow fan (Rotor outlet flow fields with rotating stall), *Int. Journal of Rotating Machinery*, Vol. 9, 2003, pp. 337-344.

[6] Wernet, M.P., Application of DPIV to study both steady state and transient turbomachinery flows, *Optics & Laser Technology*, Vol. 32, 2000, pp. 497-525

[7] Katz, M., Zaehringer, K., Pap, E., Time-resolved particle imaging velocimetry for the investigation of rotating stall in a radial pump, *Experiments in Fluids*, Vol. 39, 2005, pp. 192-209

[8] ISO. European Standard, Industrial fans – Performance testing using standardized airways, ISO 5801:2007 including Cor 1:2008, CEN, 2008, pp. 88-95.

[9] Shuey, M.G.E., Numerical near-stall performance prediction for a low speed single stage compressor, M.Sc. Thesis, University of Cincinnati, Cincinnati, OH, 2005, pp. 7-11.

[10] Fike, M., Bombek, G., Hriberšek, M., Hribernik, A., Visualisation of rotating stall in an axial flow fan, *Experimental Thermal and Fluid Science,* Vol. 53, 2014, pp. 269-276.

A SEQUENTIAL APPROACH FOR THE SYNTHESIS OF FLEXIBLE HEAT EXCHANGER NETWORKS

Miranda C. B[(1)]., Ravagnani M. A. S. S.[(1)*], Costa C. B. B.[(2)]
*Author for correspondence
(1) Av. Colombo 5790, State University of Maringá
87020900 – Maringá – PR - Brazil
(2) Rod. Washington Luís, km 235
13565905 - São Carlos – SP - Brazil
e-mail : ravag@deq.uem.br, mauro.ravagnani@hotmail.com

ABSTRACT

Heat exchanger network (HEN) synthesis is a very important field research in the process industry. It is possible to reduce the utilities usage as well as pollutant emissions by an optimal HEN synthesis. In industrial process, sometimes, it is mandatory to work with multiple products. It means that multiple operation conditions occur and the HEN must be flexible to operate with the same equipment under different operating conditions. The synthesis of flexible HEN is not a trivial task and can be formulated as an optimization problem. In the present paper it is presented a sequential approach to synthesize flexible HEN, considering thermal capacities and stream temperatures variations into different operation periods. The developed model decomposes the problem into three steps, considering three different objective functions: i) the minimization of the utilities cost for each operation period, in a Linear Programming (LP) problem formulation; ii) the minimization of the number of heat exchangers in a Mixed Integer Linear Programming (MILP) problem formulation; iii) the minimization of the global cost in a Non Linear Programming (NLP) problem formulation. An additional algorithm is developed to achieve automatically the flexible HEN. A multiperiodic superstructure is proposed and a literature example is used to test the developed model. Results prove the model applicability, with better results than the ones published in the literature.

INTRODUCTION

A flexible heat exchanger network (HEN) is formed by a set of heat transfer pieces of equipment able to accept changes in the operating conditions (inlet and outlet streams temperatures and flowrates).

Mathematical Programming has been used as a tool to solve the problem of flexible HEN synthesis, formulated as an optimization problem. In general, the objective function to be minimized consists of the global cost of the industrial process.

Floudas and Grossmann (1986) developed a sequential method to synthesize flexible HEN considering variations in the flowrates and in the inlet and outlet streams temperatures in finite periods. Two period duration independent criteria were developed, achieving the minimum utilities cost for each operating period as well as the minimum number of heat exchangers.

The first criterion is achieved with the extension of the Linear Programming (LP) model of Papoulias and Grossmann (1983), solved separately for each period. The second criterion is achieved by using a multi-periodic version of the Mixed Integer Linear Programming (MILP) model of Papoulias and Grossmann (1983), considering the variations in the utilities demand in each period and in the pinch point.

Floudas and Grossmann (1987) presented an improved version of the previous model, generating automatically the multi-periodic HEN configurations. They used the Non Linear Programming (NLP) model of Floudas *et al.* (1986). Floudas and Grossmann (1987) proposed a superstructure that includes several possible alternatives for a set of pre-established matches for the different periods. The authors also presented a graphical representation aiming to reduce the NLP problem considering changes in the pinch point.

El-Temtamy and Gabr (2012) presented a multiperiodic MILP model to synthesize flexible HEN with the minimum number of heat exchangers and utilities demand, able to adapt to changes in the streams flowrates and inlet and outlet temperatures.

In the present paper it is proposed a sequential approach with three steps to synthesize flexible HEN: a LP model to calculate the minimum utilities demand, a MILP model to achieve the minimum number of heat exchangers and a NLP model to obtain the minimum global cost.

DEVELOPED MODEL

The developed model is comprised of three steps.

First step: LP model

In the first step it is calculated the minimum utilities demand as well as the pinch point temperature in each period of operation by a LP model. The objective function to be minimized is the summation of the hot and cold utilities cost, and the constraints are mass and energy balances in the temperature intervals generated by the inlet and outlet streams temperatures, as presented in Floudas and Grossmann (1986).

Second step: MILP model

In the second step a MILP model is used to achieve the minimum number of heat exchangers. The model must be simultaneously solved for all periods and for all sub-networks, since it is possible to have different pinch points for the different periods. The MILP solution determines streams matches and the heat amount exchanged in each piece of equipment in each period. Some remarks are important:

i) Each heat exchanger must be able to exchange variable heat duty;

ii) In all periods of operation for each heat exchanger the same hot and cold stream match must be fixed in order to avoid excessive piping costs;

iii) If, in a specific period, a pair of streams is necessary in several sub-networks, different pieces of equipment are necessary for each sub-network, so as to avoid increasing heat exchange area.

Binary variables $y_{i,j}$ (i is the hot stream or hot utility and j is the cold stream or cold utility) are used to indicate if a match between two streams exists (1 means the match exists while 0 expresses the opposite) Due to the large number of possible matches, the number of binary variables can be large. To escape from this disadvantage, Floudas and Grossmann (1986) suggested that the pairs of streams can satisfy just one of the following conditions or do not satisfy any of them: A: the match between the hot stream or utility with the cold stream or utility is possible in only one sub-network and in each period of operation. The pair (i,j) that satisfies this condition belongs to the set Pa;

B: the match (i,j) is possible in different sub-networks in only one period of operation, named dominant period. In the other periods the match is possible in only one sub-network. Match (i,j) that satisfies this condition belongs to the set Pb.

Variables that satisfies conditions A and B are $ya_{i,j}$ and $yb_{i,j}$ respectively, and s is the sub-network index. In the non-dominant periods in the B condition, it is attributed the summation of the variables defined in the dominant period, making possible one or more matches in the sub-networks in the other periods. To the pairs that not satisfy conditions A and B it must be attributed a binary variable $y_{i,j,s,t}$ for each period, in which t stands for the period index.

The model also uses other sets, to know, Hq is the set of hot streams and utilities; Cf is the set of cold streams and utilities; Ha is the set of hot streams that can exchange heat in the interval k of a period; Ca is the set of cold streams and utilities that can exchange heat in the interval k in a period; IS are the sub-networks in the period of operation; IT is the set of temperature intervals belonging to a specific sub-network; d is the dominant period of a pair of streams.

Model parameters are as follows: $QHa_{i,k,t}$ is the heat exchanged by the hot streams and utilities; $QCa_{j,k,t}$ is the heat exchanged by the cold streams and utilities; $U_{i,j,s,t}$ is the upper limit of heat exchange for a pair of streams.

Positive variables are $Q_{i,j,k,s,t}$ (the amount of heat exchanged for the pair of streams (i,j)), $R_{i,k,s,t}$ (the residual heat), $u_{i,j}$ (the number of heat exchangers for the pair of streams (i,j)).

The objective function to be minimized is the number of pieces of equipment for N periods of operation in K temperature interval. The model constraints are energy balance in each temperature interval and in each period of operation.

Model formulation:

$$\min Z = \sum_{i \in Hq} \sum_{j \in Cf} u_{i,j} \tag{1}$$

Subject to:

Constraints for the number of units:

$$u_{i,j} = ya_{i,j} \quad \forall\, (i,j) \in Pa \tag{2}$$

$$u_{i,j} = \sum_{s \in IS} yb_{i,j,s} \quad \forall\, (i,j) \in Pb;\ t \in d \tag{3}$$

$$u_{i,j} \geq \sum_{s \in IS} y_{i,j,s,t} \quad \forall\, t = 1, \cdots, N;\ (i,j) \notin Pa, Pb \tag{4}$$

Energy balance:

$$R_{i,k,s,t} - R_{i,k-1,s,t} + \sum_{j \in Ca} Q_{i,j,k,s,t} = QHa_{i,k,t} \quad \forall\, i \in Ha;\ k \in IT;\ s \in IS;\ t = 1, \cdots, N \tag{5}$$

$$\sum_{i \in Ha} Q_{i,j,k,s,t} = QCa_{j,k,t} \quad \forall\, j \in Ca;\ k \in IT;\ s \in IS;\ t = 1, \cdots, N \tag{6}$$

$$R_{i,K,s,t} = 0 \tag{7}$$

Logical constraints:

$$\sum_{K\in IT} Q_{i,j,k,s,t} - U_{i,j,s,t}\cdot ya_{i,j} \le 0 \quad \forall\,(i,j) \in Pa;\ s\in IS;\ t = 1,\cdots,N \tag{8}$$

$$\sum_{K\in IT} Q_{i,j,k,s,t} - U_{i,j,s,t}\cdot yb_{i,j,s} \le 0 \quad \forall\,(i,j) \in Pb;\ s\in IS;\ t\in d \tag{9}$$

$$\sum_{K\in IT} Q_{i,j,k,s,t} - U_{i,j,s,t}\cdot \sum_{tt\in d}\sum_{s\in IS} yb_{i,j,s} \le 0 \quad \forall\,(i,j)\in Pb;\ s\in IS;\ t\notin d \tag{10}$$

$$\sum_{K\in IT} Q_{i,j,k,s,t} - U_{i,j,s,t}\cdot y_{i,j,s,t} \le 0 \quad \forall\,(i,j) \notin Pa,Pb;\ s\in IS;\ t = 1,\cdots,N \tag{11}$$

In the previous equations *tt* is the index that represents the same operating periods *t*.

Third step: NLP model

In the third step, the minimum global cost is obtained by using a NLP model. It provides automatically the viable configuration of a HEN with the minimum cost, minimum number of equipment and minimum utilities demand for each period of operation. Heat exchangers heat transfer area is also calculated. Individual superstructures for each stream are proposed, considering all the possible match connections including parallel and series arrangements and stream splitting.

The developed superstructure for a hot stream H1 that can match with two cold streams C1 and C2 in the units U1 and U2 in period T1 is presented in Figure 1.

Other multi-periodic superstructures for the other hot and cold streams can be easily generated.

In the superstructures for the cold streams, variables are: $Fcsplit1_{i,j,u,t}$, $Fcmix1_{i,j,u,t}$, $Tcmix1_{i,j,u,t}$, $Fcsplit2_{i,j,ii,u,uu,t}$, $Tcsplit2_{i,j,ii,u,uu,t}$, $Fcsplit3_{i,j,u,t}$, $Tcsplit3_{i,j,u,t}$, $Fcinu_{i,j,u,t}$, $Tcinu_{i,j,u,t}$, $Fcoutu_{i,j,u,t}$, $Tcoutu_{i,j,u,t}$, $Fcmix2_{i,j,u,t}$, $Tcmix2_{i,j,u,t}$, $Fcsplit4_{i,j,u,t}$, $Tcsplit4_{i,j,u,t}$, $Fcsplit5_{i,j,ii,u,uu,t}$ and $Tcsplit5_{i,j,ii,u,uu,t}$. i and ii represent hot streams and hot utilities, j and jj represent cold streams and cold utilities and u and uu represent the piece of equipment and t represents the period.

The positive variables include: $d1_{u,t}$ and $d2_{u,t}$ are the hot and cold heat exchangers terminals temperature difference; $LMTD_{u,t}$ is the logarithmic mean temperature difference, calculated by Chen approximation (Chen, 1987); $Area_{u,t}$ is the heat transfer area in a period of operation; $AreaM_u$ is the maximum value for the heat exchanger area among the periods; $Qu_{u,t}$ is the heat exchanged; $CustoTotal$ is the total cost; $CustoTotal1$ is the cost calculated with the maximum area for each heat transfer unit. Parameters are Co_u (the global heat transfer coefficient), and a, b, c (coefficients in the cost equation). The set Pl indicate the pairs of streams that have only one heat transfer unit in the network in all the periods, the set Pm indicate the pairs of streams that have different pieces of equipment in the sub-network in at least one period and the set Un indicate the match in a specific piece of equipment.

The information of each period in the sub-networks can reduce the number of variables and constraints in the NLP, simplifying the problem. Here two sets, Nh and Nc, are proposed to indicate if hot and cold streams exchange heat in successive sub-networks. Units that use utilities are not included in these sets. It is also proposed a parameter Sub that indicates the sub-network of the period of operation in which the unit is present.

The objective function to be minimized is the total cost for *N* periods of operation. Constraints are mass and energy balances in mixers and splitters of the superstructure.

$$\min Custo = CustoTotal \tag{12}$$

Subject to:
Mass balance in the first splitter (1):

$$Fh_{i,t} = \sum_{j}\sum_{u\in Un} Fhsplit1_{i,j,u,t} \tag{13}$$

Mass balance in splitter (2):

$$Fhmix1_{i,j,u,t} = Fhsplit3_{i,j,u,t} + Fhinu_{i,j,u,t} + \sum_{jj}\sum_{\substack{uu\in Un\\ \forall uu\neq u}} Fhsplit2_{i,j,jj,u,uu,t} \quad \forall\, u \in Un \tag{14}$$

$$Thmix1_{i,j,u,t} = Thsplit3_{i,j,u,t} = Thinu_{i,j,u,t} = Thsplit2_{i,j,jj,u,uu,t} \quad \forall\, u \in Un; uu \in Un; u \neq uu \tag{15}$$

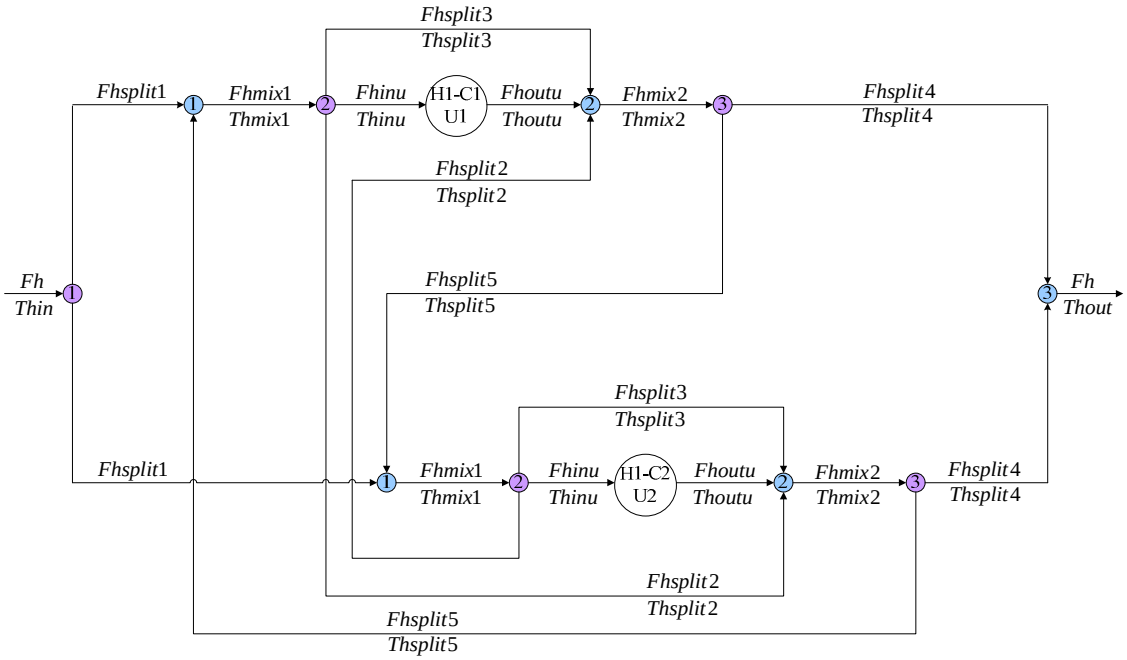

Figure 1: Multi periodic superstructure for a hot stream

Mass balance in splitter (3):

$$Fhmix2_{i,j,u,t} = Fhsplit4_{i,j,u,t} + \sum_{jj} \sum_{\substack{uu \in Un \\ \forall uu \neq u}} Fhsplit5_{i,j,jj,u,uu,t} \quad \forall u \in Un \tag{16}$$

$$Thmix2_{i,j,u,t} = Thsplit4_{i,j,u,t} = Thsplit5_{i,j,jj,u,uu,t} \quad \forall u \in Un; uu \in Un; u \neq uu \tag{17}$$

Mass balance in mixer (1):

$$Fhsplit1_{i,j,u,t} + \sum_{jj} \sum_{\substack{uu \in Un \\ \forall uu \neq u}} Fhsplit5_{i,jj,j,uu,u,t} = Fhmix1_{i,j,u,t} \quad \forall u \in Un \tag{18}$$

Energy balance in mixer (1):

$$Fhsplit1_{i,j,u,t} \cdot Thin_{i,t} + \sum_{jj} \sum_{\substack{uu \in Un \\ \forall uu \neq u}} \left(Fhsplit5_{i,jj,j,uu,u,t} \cdot Thsplit5_{i,jj,j,uu,u,t}\right) = Fhmix1_{i,j,u,t} \cdot Thmix1_{i,j,u,t} \quad \forall u \in Un \tag{19}$$

Energy balance in mixer (2):

$$Fhoutu_{i,j,u,t} + Fhsplit3_{i,j,u,t} + \sum_{jj} \sum_{\substack{uu \in Un \\ \forall uu \neq u}} Fhsplit2_{i,jj,j,uu,u,t} = Fhmix2_{i,j,u,t} \quad \forall u \in Un \tag{20}$$

$$Fhoutu_{i,j,u,t} \cdot Thoutu_{i,j,u,t} + Fhsplit3_{i,j,u,t} \cdot Thsplit3_{i,j,u,t} + \sum_{jj} \sum_{\substack{uu \in Un \\ \forall uu \neq u}} \left(Fhsplit2_{i,jj,j,uu,u,t} \cdot Thsplit2_{i,jj,j,uu,u,t}\right) = Fhmix2_{i,j,u,t} \cdot Thmix2_{i,j,u,t} \quad \forall u \in Un \tag{21}$$

Mass balance in mixer (3):

$$\sum_{j} \sum_{u \in Un} Fhsplit4_{i,j,u,t} = Fh_{i,t} \tag{22}$$

Energy balance in mixer (3):

$$\sum_{j} \sum_{u \in Un} \left(Fhsplit4_{i,j,u,t} \cdot Thsplit4_{i,j,u,t}\right) = Fh_{i,t} \cdot Thout_{i,t} \tag{23}$$

Temperatures feasibility:

$$Thoutu_{i,j,u,t} \geq Thoutu_{i,jj,uu,t} \quad \forall u \in Un;\ uu \in Un; i \in Nh; Sub_{u,t} < Sub_{uu,t} \tag{24}$$

$$Tcoutu_{i,j,u,t} \geq Tcoutu_{ii,j,uu,t} \quad \forall\, u \in Un;\ uu \in Un; j \in Nc; Sub_{u,t} < Sub_{uu,t} \tag{25}$$

Heat capacities feasibility:

$$\sum_{\substack{uu \in Un \\ \forall Sub_{uu,t}=2}} \sum_{\substack{u \in Un \\ \forall Sub_{u,t}=1}} \sum_{jj \notin n} \sum_{j} Fhsplit5_{i,j,jj,u,uu,t} \leq \sum_{\substack{uu \in Un \\ \forall Sub_{uu,t}=2}} \sum_{jj \notin n} Fhmix1_{i,jj,uu,t} \quad \forall\, i \notin m \tag{26}$$

$$\sum_{\substack{uu \in Un \\ \forall Sub_{uu,t}=1}} \sum_{\substack{u \in Un \\ \forall Sub_{u,t}=2}} \sum_{ii \notin m} \sum_{i} Fcsplit5_{i,j,ii,u,uu,t} \leq \sum_{\substack{uu \in Un \\ \forall Sub_{uu,t}=1}} \sum_{ii \notin m} Fcmix1_{ii,j,uu,t} \quad \forall\, j \notin n \tag{27}$$

Minimum temperature approach (ΔT_{min}):

$$d1_{u,t}, d2_{u,t} \geq \Delta T_{min} \tag{28}$$

Mass and energy balance in each equipment:

$$Fhinu_{i,j,u,t} = Fhoutu_{i,j,u,t} \text{ e } Fcinu_{i,j,u,t} = Fcoutu_{i,j,u,t} \quad \forall\, u \in Un \tag{29}$$

$$Qu_{u,t} = Fhinu_{i,j,u,t} \cdot \left(Thinu_{i,j,u,t} - Thoutu_{i,j,u,t}\right) \quad \forall\, u \in Un \tag{30}$$

$$Qu_{u,t} = Fcinu_{i,j,u,t} \cdot \left(Tcoutu_{i,j,u,t} - Tcinu_{i,j,u,t}\right) \quad \forall\, u \in Un \tag{31}$$

Where:

$$Qu_{u,t} = Qij_{u,t} \quad \forall\, u \in Un; (i,j) \in Pl \tag{32}$$

$$Qu_{u,t} = Qij_{u,t} \quad \forall\, u \in Un; (i,j) \in Pm;\ t \in d \tag{33}$$

$$\sum_{u \in Un} Qu_{u,t} = Qij_{u,t} \quad \forall\, (i,j) \in Pm; t \notin d \tag{34}$$

Heat exchanger design:

$$d1_{u,t} = Thinu_{i,j,u,t} - Tcoutu_{i,j,u,t} \quad \forall\, u \in Un \tag{35}$$

$$d2_{u,t} = Thoutu_{i,j,u,t} - Tcinu_{i,j,u,t} \quad \forall\, u \in Un \tag{36}$$

$$Qu_{u,t} = Co_u \cdot Area_{u,t} \cdot LMTD_{u,t} \tag{37}$$

$$CustoTotal = \sum_{u} \sum_{t} \left(a + b \cdot {Area_{u,t}}^{c}\right) \tag{38}$$

Finally, with the largest heat transfer area among all calculated areas for the same piece of equipment in all periods of operation ($AreaM_u$), the cost of that unit can be calculated:

$$CustoTotal1 = \sum_{u} \left(a + b \cdot {AreaM_u}^{c}\right) \tag{39}$$

CASE STUDY

An example proposed by Floudas and Grossmann (1987) was used to evaluate the developed model. There are one cold and six hot streams, one hot utility (fuel - CM) and one cold utility (water - W), in three periods of operation. Table 1 presents temperatures and flowrates for the process. The minimum approach temperature is 10 K.

First of all, the LP model is used for each period of operation and the values obtained are the same as those published by Floudas and Grossman (1987) for the utilities demand and pinch point location.

Table 1: Data example

Stream	Period 1			Period 2			Period 3		
	Tin (K)	$Tout$ (K)	F (kW/K)	Tin (K)	$Tout$ (K)	F (kW/K)	Tin (K)	$Tout$ (K)	F (kW/K)
H1	640	460	9.9	620	460	9.9	620	460	8.1
H2	560	480	7.15	540	480	7.15	540	480	5.85
H3	540	480	3.3	520	480	3.3	520	480	2.7
H4	480	400	39.6	460	400	39.6	460	400	32.4
H5	460	310	7.7	440	310	7.7	440	310	6.3
H6	420	350	79.2	400	350	79.2	400	350	64.8
C1	300	650	29.7	300	650	29.7	300	650	24.3

With the results obtained in the LP model, the MILP model is used and the matches are calculated in less than 1 second, using CPLEX solver, in GAMS. Matches: $H1$ - W, $H2$ - $C1$, $H3$ - $C1$, $H4$ - $C1$, $H4$ - W, $H5$ - $C1$, $H5$ - W, $H6$ - $C1$, $H6$ - W and CM - $C1$ satisfy the condition A and the match $H1$ - $C1$ satisfies condition B. Considering that all possible matches are in accordance with one of the conditions, the MILP model can be formulated using just the binary variables $ya_{i,j}$ and $yb_{i,j,s}$, adding up 12 binary variables. The HEN has 9 units and is presented in Table 2. Floudas and Grossmann (1987) also found 9 units, but with different matches and heat exchanged.

With the results from the MILP model, it is possible to identify that the parameter $Sub_{u,t}$ receives value 1 for units $U1$, $U2$, $U3$ and $U4$ in all the periods, value 2 for units $U6$, $U7$, $U8$ and $U9$ in all periods, and for unit $U5$, the value is 1 for period 1 and 2 for periods 2 and 3. It is necessary to rename the cold utility ($W1$ and $W2$), because it is used in $U7$ and $U9$. Also the matches are divided in two sets: Pl is formed by the matches $H2$ - $C1$, $H3$ - $C1$, $H4$ - $C1$, $H5$ - $W1$, $H6$ - $C1$, $H6$ - $W2$ and CM - $C1$; and Pm is formed by the match $H1$ - $C1$; period 1 is dominant for this match.

It is also possible to generate the sets Nh and Nc to simplify the superstructures. The matches $H1$ - $U2$ - $U5$ - $T1$ belong to the set Nh, because in period 1 the hot stream $H1$ exchange heat in equipment $U2$ as well in $U5$ and these equipment are in successive sub-networks. The set Nc is comprised of the matches $C1$ - $U2$ - $U5$ - $T1$, $C1$ - $U2$ - $U6$ - $T1$, $C1$ - $U2$ - $U6$ - $T2$, $C1$ - $U2$ - $U6$ - $T3$, $C1$ - $U2$ - $U8$ - $T1$, $C1$ - $U2$ - $U8$ - $T2$, $C1$ - $U2$ - $U8$ - $T3$, $C1$ - $U3$ - $U5$ - $T1$, $C1$ - $U3$ - $U6$ - $T1$, $C1$ - $U3$ - $U6$ - $T2$, $C1$ - $U3$ - $U6$ - $T3$, $C1$ - $U3$ - $U8$ - $T1$, $C1$ - $U3$ - $U8$ - $T2$, $C1$ - $U3$ - $U8$ - $T3$, $C1$ - $U4$ - $U5$ - $T1$, $C1$ - $U4$ - $U6$ - $T1$, $C1$ - $U4$ - $U6$ - $T2$, $C1$ - $U4$ - $U6$ - $T3$, $C1$ - $U4$ - $U8$ - $T1$, $C1$ - $U4$ - $U8$ - $T2$, $C1$ - $U4$ - $U8$ - $T3$.

The global heat transfer coefficients and the cost data, as presented by Floudas and Grossmann (1987) are presented in Table 3. The NLP model is used to solve the optimization problem using the solver CONOPT3, in GAMS, in less than one second.

Table 2: Matches and heat exchanged (kW) in each period

Unit	Match	Period 1	Period 2	Period 3
1	CM-C1	2992	3795	3105
2	H1-C1	1584	1584	1296
3	H2-C1	572	429	351
4	H3-C1	198	132	108
5	H1-C1	198	0	0 *
6	H4-C1	3168	2376	1944
7	H5-W	1155	1001	819
8	H6-C1	1683	2079	1701
9	H6-W	3861	1881	1539

* The line indicates division into sub-networks

Table 3: Heat transfer coefficients and areas

Unit	Match	$Co_u\ (kW/(m^2.K))$	$AreaM\ (m^2)$
1	CM-C1	----	----
2	H1-C1	0,6	95,936
3	H2-C1	0,4	72,882
4	H3-C1	0,3	35,596
5	H1-C1	0,6	8,498
6	H4-C1	0,4	350,317
7	H5-CW	0,3	85,595
8	H6-C1	0,3	142,6
9	H6-CW	0,4	163,942

$Cost = 4333 \cdot Area^{0.6}$, $Area$ [=] m^2.

$Furnace\ cost = 1.5246 \cdot Qs^{0,7}$, Qs [=] W.

Fuel cost (700-680 K) = 204.732×10^{-4} \$/kWh.

Water cost (300-330 K) = 60.576×10^{-4} \$/kWh.

The final network configuration is presented in Figure 2, for the 3 periods. It is possible to note that stream $C1$ is splited. There is a by-pass of stream $H1$ in unit 5, because in periods 2 and 3 there are no matches in it. The proposed network is feasible in all the three periods of operation. The utilities costs are the same as presented by Floudas and Grossmann (1987), but the final cost is lower, as presented in Table 4. The HEN configuration in Figure 2 has a lower number of stream splitting than the solution presented by Floudas and Grossmann (1987), decreasing the costs in the network implementation, reducing the number of accessories in piping.

CONCLUSIONS

The synthesis of flexible HEN can be formulated as an optimization problem. In the present paper a sequential approach was proposed to solve the problem, with three steps, a LP model, a MILP model and a NLP model, to achieve the minimum global cost with the minimal number of heat transfer units and utilities demand. A case study was used to test the applicability of the developed methodology and the results were better when compared to the literature. The major differences are in the network configuration, with less stream splitting and the possibility of by-pass.

REFERENCES

Chen, J. J. J. Letters to the editors: comments on improvements on a replacement for the logarithmic mean. *Chem. Eng. Sci.*, v. 42, n.10, p. 2488-2489, 1987.

El-Temtamy, S. A.; Gabr, E. M. Design of optimum flexible heat exchanger networks for multiperiod process. *Egyptian Journal of Petroleum*, v. 21, p. 109-117, 2012.

Floudas, C. A.; Ciric, A. R.; Grossmann, I. E. Authomatic synthesis of optimum heat exchanger network configurations. *AIChE J.*, v. 32, n. 2, p. 276-290, 1986.

Floudas, C. A.; Grossmann, I. E. Synthesis of flexible heat exchanger networks for multiperiod operation. *Comput. Chem. Eng.*, v. 10, n. 2, p. 153-168, 1986.

Floudas, C. A.; Grossmann, I. E. Automatic generation of multiperiod heat exchanger network configuration. *Comput. Chem. Eng.*, v. 11, n. 2, p. 123-142, 1987.

GAMS Development Corporation. *GAMS - The Solver Manuals*. Washington: 2008.

Papoulias, S. A.; Grossmann, I. E. A structural optimization approach in process synthesis. Part II: Heat recovery networks. *Comput. Chem. Eng.*, v. 7, n. 6, p. 707-721, 1983.

Table 4: Costs comparison ($)

	Area cost	Furnace cost	Total cost
Floudas and Grossmann (1987)	571,368.36	61,461.64	632,830.00
Present paper	561,994.05	61,461.64	623,455.69

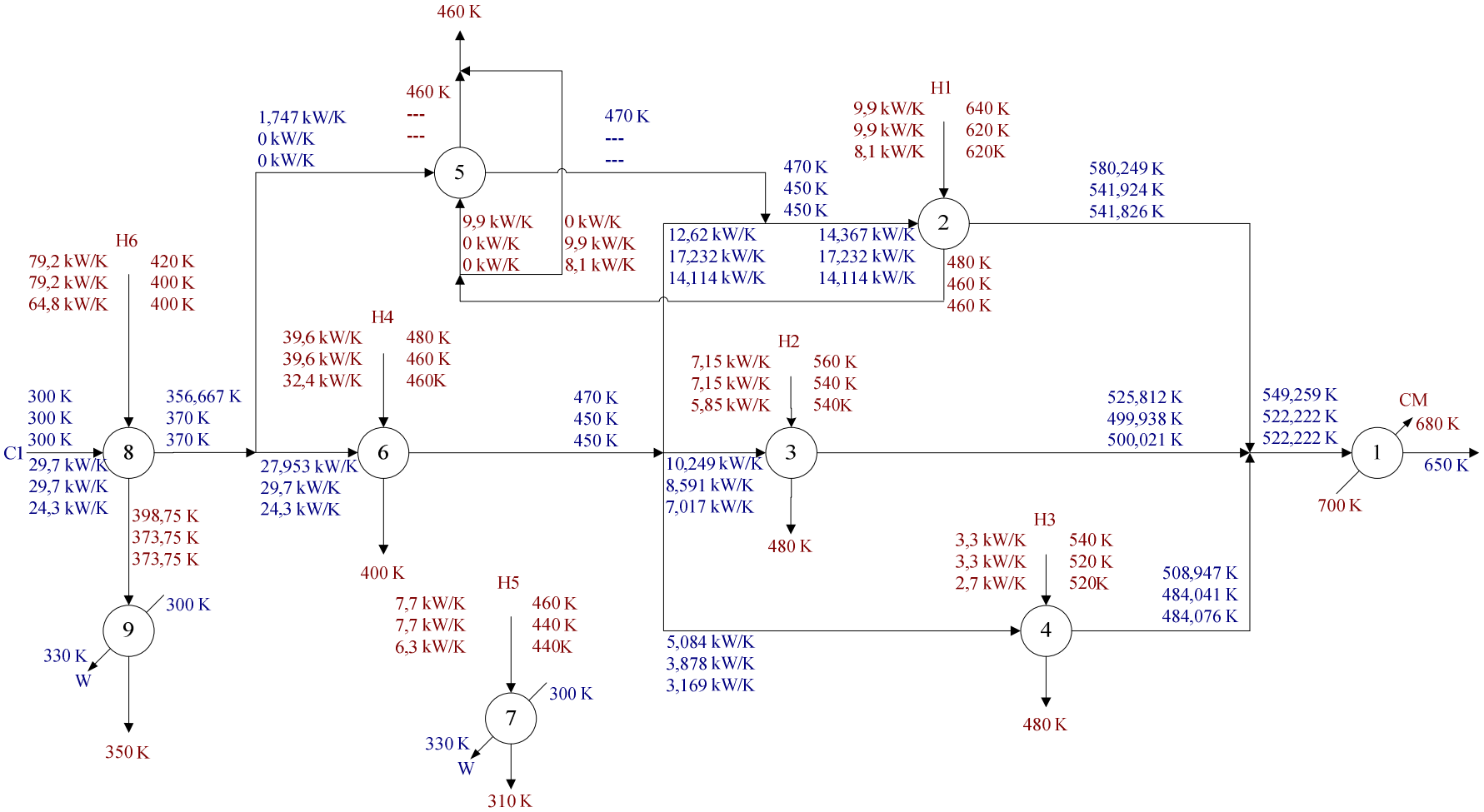

Figure 2: Final HEN

DYNAMIC SIMULATION OF TUBULAR HEAT EXCHANGERS

Ravagnani M. A. S. S[(1)*]., Mano T. B[(1)]., Carvalho E. P[(1)]., Costa C. B. B[(2)].
*Author for correspondence
(1) Av. Colombo 5790, State University of Maringá, 87020-900 – Maringá – PR - Brazil
(2) Rod. Washington Luís, km 235, 13565905 - São Carlos – SP – Brazil
e-mail : ravag@deq.uem.br, mauro.ravagnani@hotmail.com

ABSTRACT

The process of heat exchange between two fluids at different temperatures and separated by a solid wall occurs in many engineering applications. Heat exchangers are the equipment used to implement this heat exchange. Dynamic models for the simulation of tubular heat exchangers are very rare in the literature and few papers have been published in this area. In this paper a tubular heat exchanger dynamic simulation is carried out using a distributed parameters model. Three different cases were studied: unsteady state with heat transfer in the radial direction, conjugated problem with both uniform velocity profile and velocity with parabolic profile. Numerical and analytical solutions were provided. Analytical and numerical solutions have shown a very good agreement. The influence of the number of Peclet on the heat transfer process was evaluated and results showed that the temperature variation decreases when the number of Peclet increases.

INTRODUCTION

The process of heat exchange between two fluids at different temperatures and separated by a solid wall occurs in many engineering applications. Heat exchangers are the equipment used to implement this heat exchange. Dynamic models for the simulation of tubular heat exchangers are very rare in the literature and few papers have been published in this area. Ho et al.[1] investigated how to improve the efficiency of heat and mass transfer in a parallel plate channel with recycle. A waterproof sheet with thermal resistance and negligible thickness was inserted between the parallel plates. The orthogonal expansion technique was used to obtain the solution. Results showed significant improvement in the heat transferred when compared to plates without recycle. The efficiency of heat transfer in the conjugated Graetz problem with laminar countercurrent flow in a double tube concentric circular heat exchanger has also been investigated[2]. Also, a waterproof sheet was inserted parallel to the fluid flow. This study showed the improvement in the efficiency of heat transfer when compared to single pass without recycle.

Another work[3] developed a model to evaluate the dynamic response of a countercurrent heat exchanger, in which temperature and mass flow variations are applied in the exchanger entrance. The used method consists in dividing the tubes into N cells and the hot and cold fluid and the elements of the tube wall are included in each cell. The coefficients of the energy equation and the physical properties were considered constant. The solution of the energy equation is analytical in each cell, but the authors extended it to the whole exchanger using a numerical algorithm.

In the present paper three case studies were simulated using a dynamic model for the design of tubular heat exchangers. Analytical and numerical solutions (obtained by the finite difference method available in Maple software) for the three case studies were provided as well as qualitative and quantitative analysis of the solutions.

NOMENCLATURE

c_p	[J/kg·K]	Heat capacity
k	[W/m·K]	thermal conductivity
L	[m]	Tube length
Pe	[-]	Peclet number
R	[m]	Radius of tube
t	[s]	Time
T	[K or °C]	Temperature
T_0	[K or °C]	Inlet temperature
T_p	[K or °C]	Tube wall temperature
T_L	[K or °C]	Outlet temperature
V	[m/s]	Fluid velocity
x	[-]	Dimensionless tube length
α	[m^2/s]	Thermal diffusivity
η	[-]	Dimensionless radius
λ	[-]	Constant
μ	[N·s/m^2]	Viscosity
ρ	[kg/m^3]	Density
τ	[-]	Fourier number (Dimensionless time)
φ	[-]	Dimensionless temperature

SIMULATION MODEL

The general equation of energy balance in cylindrical coordinates[4] is expressed by Eq. (1)

$$\rho c_p\left(\frac{\partial T}{\partial t}+v_r\frac{\partial T}{\partial r}+\frac{v_\theta}{r}\frac{\partial T}{\partial \theta}+v_v\frac{\partial T}{\partial z}\right)=k\left[\frac{1}{r}\frac{\partial}{\partial r}\left(r\frac{\partial T}{\partial r}\right)+\frac{1}{r^2}\frac{\partial^2 T}{\partial \theta^2}+\frac{\partial^2 T}{\partial z^2}\right]+\mu\theta \quad (1)$$

where

$$\theta = 2\left[\left(\frac{\partial v_r}{\partial r}\right)^2 + \left(\frac{1}{r}\frac{\partial v_\theta}{\partial \theta} + \frac{v_r}{r}\right)^2 + \left(\frac{\partial v_r}{\partial z}\right)^2\right] + \left[r\frac{\partial}{\partial r}\left(\frac{v_\theta}{r}\right) + \frac{1}{r}\left(\frac{\partial v_r}{\partial \theta}\right)\right]^2 + \left[\frac{1}{r}\frac{\partial v_z}{\partial \theta} + \frac{\partial v_\theta}{\partial z}\right]^2 + \left[\frac{\partial v_r}{\partial z} + \frac{\partial v_z}{\partial r}\right]^2 - \frac{2}{3}\left[\frac{1}{r}\frac{\partial}{\partial z}\left(r v_r\right) + \frac{1}{r}\frac{\partial v_\theta}{\partial \theta} + \frac{\partial v_z}{\partial z}\right]^2 \quad (2)$$

Case 1) Distributed parameters model considering heat transfer in the radial direction

Assume that a fluid flows slowly through a cylindrical tube of radius R (Fig. 1). The fluid in $z = 0$ is at temperature T_0 and the tube wall is maintained at a constant temperature T_p. The flow is axisymmetric ($V_\theta = V_r = 0$). Transient regime is considered, viscous dissipation is considered negligible and the velocity profile is supposed to be plug flow. Therefore, Eq. (1) and Eq. (2) reduce to:

$$\frac{\partial T}{\partial t} = \alpha\left[\frac{1}{r}\frac{\partial}{\partial r}\left(r\frac{\partial T}{\partial r}\right)\right] \quad (3)$$

The boundary and initial conditions are:

$$r = R \rightarrow T\left(R,t\right) = T_p \quad (4)$$

$$r = 0 \rightarrow \frac{\partial T}{\partial r} = 0 \quad (5)$$

$$t = 0 \rightarrow T\left(x,0\right) = F\left(r\right) = T_o \quad (6)$$

Eq. (5) is known as symmetry condition. The dimensionless form of Eq. (3) is Eq.(7) and the boundary and initial conditions are in Eq. (8)-(10):

$$\frac{\partial \varphi}{\partial \tau} = \frac{1}{\eta}\frac{\partial \varphi}{\partial \eta} + \frac{\partial^2 \varphi}{\partial \eta^2} \quad (7)$$

$$\eta = 1 \rightarrow \varphi\left(1,\tau\right) = 0 \quad (8)$$

$$\eta = 0 \rightarrow \frac{\partial \varphi}{\partial \eta} = 0 \quad (9)$$

$$\tau = 0 \rightarrow \varphi\left(\eta,0\right) = 1 \quad (10)$$

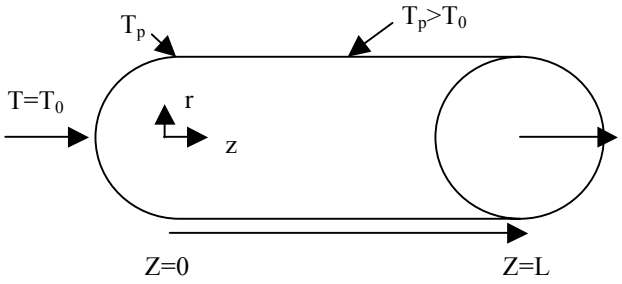

Figure. 1: Representation of a tube of a tubular heat exchanger.

The solution is obtained using the separation of variables method. Therefore, it is assumed that the constant of separation ($-\lambda^2$, $\lambda > 0$) has only negative values, to avoid trivial solutions. Accepting the error that ranges from -2.39% for (i = 1) to 2.34% for (i = 30) between the exact and approximate solutions, the following approximation is considered:

$$\lambda \cong \frac{50}{21} + \pi\left(i-1\right) \quad (11)$$

Hence, the solution is:

$$\varphi\left(\eta,\tau\right) = \sum_{i=1}^{\infty} C_i J_0\left\{\left[\frac{50}{21} + \pi\left(i-1\right)\right]\eta\right\} e^{-\left[\frac{50}{21} + \pi\left(i-1\right)\right]\tau} \quad (12)$$

where:

$$C_i = \frac{\int_0^1 \eta J_0\left\{\left[\frac{50}{21} + \pi\left(i-1\right)\right]\eta\right\} d\eta}{\int_0^1 \eta J_0\left\{\left[\frac{50}{21} + \pi\left(i-1\right)\right]\eta\right\}^2 d\eta} \quad (13)$$

where J_0 is a Bessel function of the first kind, zero order.

Case 2) Distributed parameters model in two spatial directions

Considering the previous case, but steady state and temperature as a function of radial and axial directions, Eq. (1) and Eq. (2) reduce to:

$$v_z\frac{\partial T}{\partial z} = \alpha\left[\frac{1}{r}\frac{\partial}{\partial r}\left(r\frac{\partial T}{\partial r}\right)\right] \quad (14)$$

This problem is known as the Graetz problem. The boundary conditions are:

$$r = R \rightarrow T\left(z,R\right) = T_p \quad (15)$$

$$r = 0 \rightarrow \frac{\partial T}{\partial r} = 0 \quad (16)$$

$$z = 0 \rightarrow T\left(0,r\right) = F\left(r\right) = T_0 \quad (17)$$

In the dimensionless form:

$$Pe\frac{\partial \varphi}{\partial x} = \frac{1}{\eta}\frac{\partial \varphi}{\partial \eta} + \frac{\partial^2 \varphi}{\partial \eta^2} \quad (18)$$

$$\eta = 1 \rightarrow \varphi(x,1) = 0 \tag{19}$$

$$\eta = 0 \rightarrow \frac{\partial \varphi}{\partial \eta} = 0 \tag{20}$$

$$\tau = 0 \rightarrow \varphi(0,\eta) = 1 \tag{21}$$

In the solution, the values of the roots (λ) of the Bessel function of the first kind and zero order are obtained considering that, in this case, there are no trivial solutions. Consequently, accepting the error between the approximate and exact root of -2.35% with i = 1 to 2.34% with i = 30, the result is:

$$\varphi(x,\eta) = \sum_{i=1}^{\infty} C_i J_0\left\{\left[\frac{50}{21} + \pi(i-1)\right]\eta\right\} e^{-\frac{\left[\frac{50}{21} + \pi(i-1)\right]^2}{Pe} x} \tag{22}$$

where C_i is given by Eq. (13).

Case 3) Distributed parameters model in two spatial directions with a parabolic velocity profile

Considering the parabolic velocity profile as:

$$v_z(r) = v_{\max}\left[1 - \left(\frac{r}{R}\right)^2\right] \tag{23}$$

Due to the axisymmetric flow and the transport of heat by the movement of the fluid, the heat conduction in the axial direction can be neglected. Then:

$$v_z(r)\frac{\partial T}{\partial z} = \alpha\left[\frac{1}{r}\frac{\partial}{\partial r}\left(r\frac{\partial T}{\partial r}\right)\right] \tag{24}$$

The boundary and initial conditions are the same as given by Eqs. (15), (16) and (17). Furthermore,

$$V(\eta) = \frac{v_z}{v_{\max}} = 1 - \eta^2$$

The dimensionless form of Eq. (24) is:

$$PeV(\eta)\frac{\partial \varphi}{\partial x} = \frac{1}{\eta}\frac{\partial \varphi}{\partial \eta} + \frac{\partial^2 \varphi}{\partial \eta^2} \tag{25}$$

or:

$$Pe\frac{\partial \varphi}{\partial x} = \frac{1}{\eta(1-\eta^2)}\frac{\partial \varphi}{\partial \eta} + \frac{1}{(1-\eta^2)}\frac{\partial^2 \varphi}{\partial \eta^2} \tag{26}$$

The boundary and initial conditions are the same as given by Eqs. (19), (20) and (21). The solution is also obtained in series of Kummer and roots (λ) with no trivial solution, given by:

$$\lambda \cong \frac{27}{10} + \frac{70}{55}\pi(i-1) \tag{27}$$

Therefore:

$$\varphi(x,\eta) = \sum_{i=1}^{\infty} C_i \Phi \times e^{\left\{-\frac{1}{2}\left[\frac{27}{10} + \frac{70}{55}\pi(i-1)\right]\eta^2 - \frac{\left[\frac{27}{10} + \frac{70}{50}\pi(i-1)\right]^2}{Pe}\right\}} \tag{28}$$

Where:

$$C_i = \frac{\int_0^1 \eta(1-\eta^2)\Phi e^{-\frac{1}{2}\left[\frac{27}{10} + \frac{70}{55}\pi(i-1)\right]\eta^2} d\eta}{\int_0^1 \eta(1-\eta^2)\left\{\Phi e^{-\frac{1}{2}\left[\frac{27}{10} + \frac{70}{55}\pi(i-1)\right]\eta^2}\right\}^2 d\eta} \tag{29}$$

The Kummer function is given by:

$$\Phi\left\{\frac{1}{2} - \frac{1}{4}\left[\frac{27}{10} + \frac{70}{55}\eta(i-1)\right], 1, \left[\frac{27}{10} + \frac{70}{55}\eta(i-1)\right]\eta^2\right\} \tag{30}$$

RESULTS AND DISCUSSION

Case 1) Distributed parameters model considering heat transfer in the radial direction

Figures 2 to 4 show the temperature profile given by Eq. (12). In the quantitative analysis, two relatively large errors are found. Error of about 99% at η = 1 and τ = 0 and an error of about 12.9% at η = 0 and τ = 0. For the other coordinates, the maximum error is approximately 7.2% and the minimum error is approximately zero. This shows that there is a good agreement between the solutions within a range of error. However, since the largest errors are at τ = 0 it is desirable not to use the numerical method at this point. Also, there is a symmetrical temperature profile.

In the qualitative analysis, in Figures 2 and 3, there are some ripples at $\tau = 0$ and $\eta = 0$ (or -1) to $\eta = 1$. These ripples are caused by the Gibbs phenomenon, in which the sine and cosine series partial sums tend to go beyond the values of an exact possible analytical solution.

Case 2) Distributed parameters model in two spatial directions

Figures 5 to 10 show the temperature profile given by Eq. (22). The first analysis is focused on comparing Eq. (18) and Eq. (7). In the case in focus, as it is for Eq.(7), the temperature variation increases with *x*. Therefore, it is observed that the variable *x* behaves as a time variable. Since Peclet number is present in the solution, Eq. (22), it is possible to evaluate its influence on heat transfer in two spatial directions.

The major influence of the Peclet number is on the temperature variation as the flow velocity is changed. If the velocity variation is very large, the contact time between the fluid and the tube wall is small and, consequently, the heat exchange will be low. Therefore, the change in temperature may become too small and can be considered negligible.

In a qualitative analysis, there is a good agreement between the results of the numerical method and the results of the analytical solution. However, the quantitative analysis shows that the largest differences are at the points $x = 0$ or $\eta = 0$ for $Pe = 1$ and $Pe = 10$. Therefore, the numerical solutions at these points are not feasible.

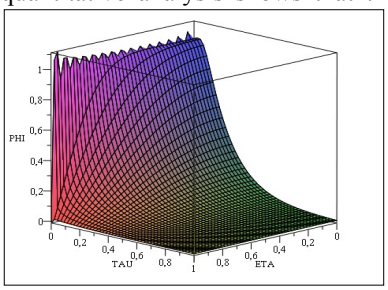

Fig. 2: Dimensionless temperature profile (φ) in dimensionless radial direction (η) and time (τ), analytical solution (Case 1).

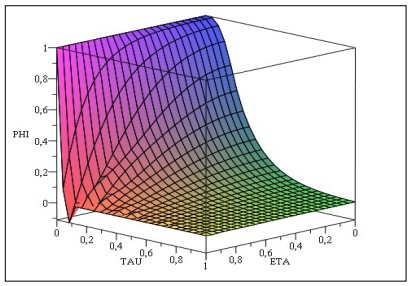

Fig. 3: Dimensionless temperature profile (φ) in dimensionless radial direction (η) and time (τ), numerical solution (Case 1).

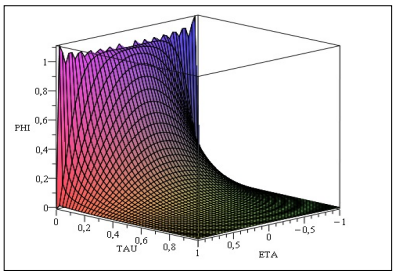

Fig. 4: Symmetric analytical solution of dimensionless temperature profile (φ) in dimensionless radial direction (η) and time (τ) (Case 1).

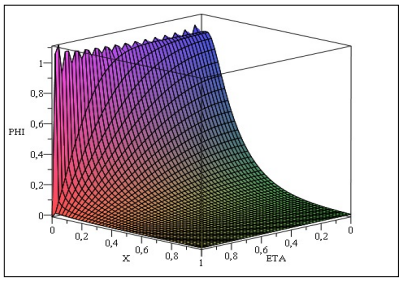

Fig. 5: Dimensionless temperature profile (φ) in dimensionless radial direction (η) and time (τ), analytical solution for $Pe = 1$ (Case 2).

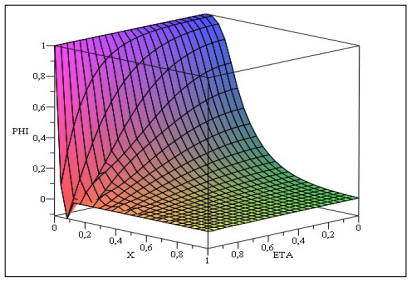

Fig. 6: Dimensionless temperature profile (φ) in dimensionless radial direction (η) and time (τ), numerical solution for $Pe = 1$ (Case 2).

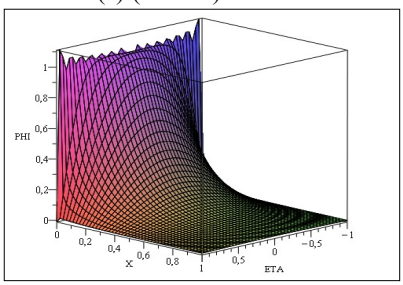

Fig. 7**:** Symmetric analytical solution of dimensionless temperature profile (φ) in dimensionless radial direction (η) and time (τ) for Pe = 1 (Case 2).

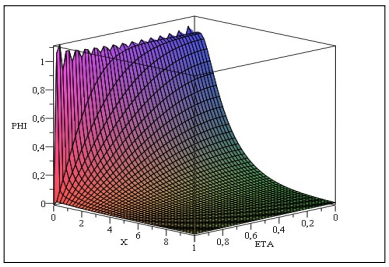

Fig. 8: Dimensionless temperature profile (φ) in dimensionless radial direction (η) and time (τ), analytical solution for $Pe = 10$ (Case 2).

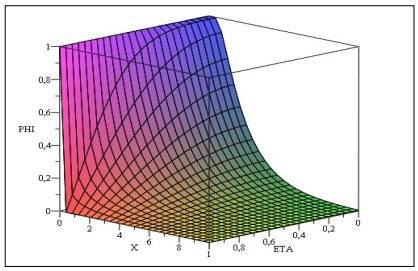

Fig. 9: Dimensionless temperature profile (φ) in dimensionless radial direction (η) and time (τ), numerical solution for $Pe = 10$ (Case 2).

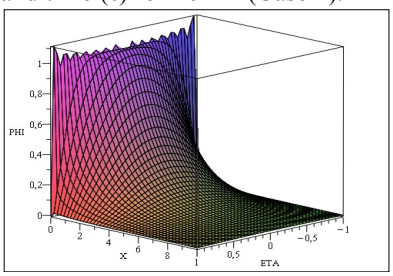

Fig. 10: Symmetric analytical solution of dimensionless temperature profile (φ) in dimensionless radial direction (η) and time (τ) for Pe = 10 (Case 2).

Case3) Distributed parameters model in two spatial directions with a parabolic velocity profile

Figures 11 to 16 show the temperature profile given by Eq. (28). It can be seen in these figures a resemblance to the figures of the previous case. However, there is a parabolic velocity profile (laminar flow). Accordingly, the temperature is slightly lower than in the plug flow profile case (turbulent flow). Just as in the previous case, the effect of the Gibbs phenomenon is also observed. There is a particularly strong influence of the Peclet number on the reduction of temperature variation.

In the quantitative analysis it appears that the greatest deviation of η is between 0 and 0.2. For other values of η, the deviations are less than 2%. The largest deviations between the analytical and numerical solutions is approximately 97.7% in $\eta = 1$ and $x = 0$.

CONCLUSIONS

Three models were studied to describe the temperature profile of a fluid flowing in a tube whose wall temperature was kept constant. In all cases, the numerical solutions were obtained by the finite difference method available in Maple software.

It was possible to observe the influence of Peclet number on the temperature variation. Also, it was found that the model of plug flow velocity profile (Case2)

showed a change in temperature slightly faster than the parabolic profile model (Case 3). Finally, as the largest errors were found in the end points, then it is recommended to use numerical methods in these points.

In addition to the aforementioned conclusions, this study showed an advantage of obtaining the transient model. This model allowed us to analyze the behavior of the temperature profile in all points of the heat exchanger.

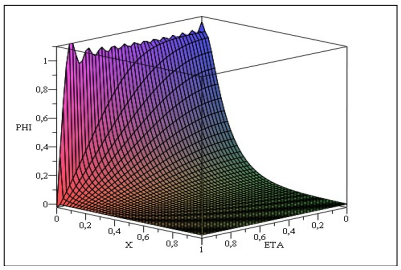

Fig. 11: Dimensionless temperature profile (φ) in dimensionless radial direction (η) and time (τ), analytical solution for *Pe* = 1 (Case 3).

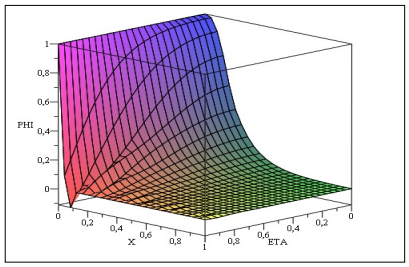

Fig. 12: Dimensionless temperature profile (φ) in dimensionless radial direction (η) and time (τ), numerical solution for *Pe* = 1 (Case 3).

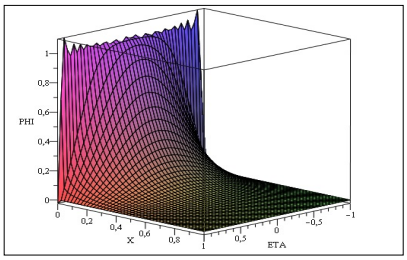

Fig. 13: Symmetric analytical solution of dimensionless temperature profile (φ) in dimensionless radial direction (η) and time (τ) for Pe = 1 (Case 3).

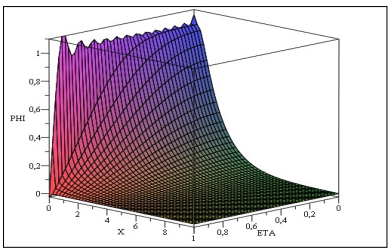

Fig. 14: Dimensionless temperature profile (φ) in dimensionless radial direction (η) and time (τ), analytical solution for *Pe* = 10 (Case 3).

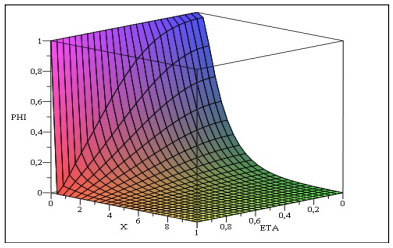

Fig. 15: Dimensionless temperature profile (φ) in dimensionless radial direction (η) and time (τ), numerical solution for *Pe* = 10 (Case 3).

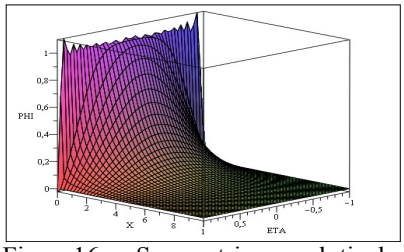

Fig. 16: Symmetric analytical solution of dimensionless temperature profile (φ) in dimensionless radial direction (η) and time (τ) for Pe = 10 (Case 3).

REFERENCES

[1] Ho, C.D., Yeh, H.M., Sheu, W.S., 1998, An analytical study of heat and mass transfer through a parallel-plate channel with recycle. *Int. J. Heat Mass Transfer 41*, pp. 2589– 2599.

[2] Ho, C.D., Yang, W.Y., 2003, Heat transfer of conjugated Graetz problems with laminar counterflow in double-pass concentric circular heat exchangers, *International Journal of Heat and Mass Transfer*, vol. 48, pp. 4474-4480.

[3] Dolezal, A. R., Rolf, M. K., Riemenschneider, G., 1983, Solution of the heat-exchanger equation system, in: *Proc. 1st IFAC Workshop Modeling and Control of Electric Power Plants*, Como, Italy, pp. 69–75.

[4] Bird, R. B., Stewart, W. E., Lightfoot, E. N., 1960, *Transport Phenomena*.

Sensitive Approach To Thermodynamic Analysis Of Chemically Reacting Systems: Combustion Gaseous Evaluation

Sohret Y.*, Kaya N., and Karakoc T.H.
*Author for correspondence
Department of Airframe and Powerplant Maintenance,
Anadolu University,
Eskisehir, TR-26470
Turkey,
E-mail: ysohret@anadolu.edu.tr

ABSTRACT

In this study, it is aimed to present a sensitive approach for exergy analysis of chemically reacting systems. In many studies previously performed, a generalized formulation to calculate thermophysical properties of the combustion gaseous was used. It is possible to gain approximate results by using that well-accepted formula, but not certain. In fact, mathematical formulations and models never meets the real cases but enable us to understand the phenomena. In this case, a more sensitive mathematical method to obtain more approximate results is presented. The method explained in this paper, enable us to calculate heat capacity (under constant pressure), specific physical exergy, energy capacity of the combustion gases with respect to the mixture and ideal gas laws. For better understanding, thermophysical properties of the combustion gaseous are calculated for a temperature and pressure range by asserted methods. As a result of the study, sensitivity and benefits of the asserted method are discussed.

INTRODUCTION

Thermodynamic analysis and optimization methods are commonly used in thermal engineering nowadays. Especially determination of thermophysical properties of working fluids in power cycles occupies an important position. Cause, it has a great impact on calculating the enthalpy, internal energy, flow exergy and many more. So, the specific heat capacity is the most remarkable thermophysical property as a well-known fact. Different approaches are presented to the literature for calculation of the specific heat capacity until today. In basic considerations, temperature dependent specific heat capacity is disregarded and a more simple evaluation is performed. But, the certainty is too low in this approach. Thus, temperature dependent approach is mostly preferred in thermodynamic analysis.

Two different temperature dependent approach is developed for specific heat capacity calculations. First of them focuses on the average temperature and calculates the specific heat capacity with dependence on average temperature of the working fluids. Result obtained in this approach is closer to the actual value than temperature independent approach but not exactly correct Details of the mentioned approaches may be found in many text [1-4].

In the present study, third approach is aimed to explain in details dependence of the specific heat capacity on the temperature and is intended to evaluate for combustion gaseous. Differently from previously performed studies, composition of the combustion gaseous is regarded in addition to temperature dependence according to authors' best of knowledge.

METHODOLOGY

Differently from commonly used methodology, regarding composition of the combustion gaseous can enhance sensitivity of the thermophysical property calculations. As a well-known fact, combustion gaseous is a mixture of burned gaseous such as carbon dioxide, carbon monoxide, nitrogen oxides, hydrocarbons and more. For this reason, thermophysical properties of the ingredient gaseous should be found firstly. Then, thermopyhsical properties of the mixture may be considered. Within this scope, calculation of the specific heat capacity, specific enthalpy and standard entropy calculation methodologies are explained in details below.

Specific Heat Capacity Calculation

This approach is developed on the basis of former NASA researches [5]. Firstly specific heat capacity of combustion gaseous ingredients under constant pressure should be found. Specific heat capacity (constant pressure) of carbon dioxide, water vapour, carbon monoxide, hydrogen, oxygen and nitrogen are respectively expressed as [5]:

$$\bar{c}_{p,CO_2} = \bar{R}_{CO_2}[2.4008 + 0.0087351T - \frac{0.66071}{10^5}T^2 + \frac{0.20022}{10^8}T^3 + \frac{0.63274}{10^{15}}T^4] \quad (1)$$

$$\bar{c}_{p,H_2O} = \bar{R}_{H_2O}[4.0701 - 0.0011084T + \frac{0.41521}{10^5}T^2 - \frac{0.29637}{10^8}T^3 + \frac{0.80702}{10^{12}}T^4] \quad (2)$$

$$\bar{c}_{p,CO} = \bar{R}_{CO}[3.7101 - 0.0016191T + \frac{0.36924}{10^5}T^2 - \frac{0.20320}{10^8}T^3 + \frac{0.23953}{10^{12}}T^4] \quad (3)$$

$$\bar{c}_{p,H_2} = \bar{R}_{H_2}[3.0574 + 0.0026765T - \frac{0.58099}{10^5}T^2 + \frac{0.55210}{10^8}T^3 - \frac{0.18123}{10^{11}}T^4] \quad (4)$$

$$\bar{c}_{p,O_2} = \bar{R}_{O_2}[3.6256 - 0.0018782T + \frac{0.70555}{10^5}T^2 - \frac{0.67635}{10^8}T^3 - \frac{0.21556}{10^{11}}T^4] \quad (5)$$

$$\bar{c}_{p,N_2} = \bar{R}_{N_2}[3.6748 - 0.0012082T + \frac{0.23240}{10^5}T^2 - \frac{0.63128}{10^9}T^3 - \frac{0.22577}{10^{12}}T^4] \quad (6)$$

Eqs. 1-6 are applicable in the temperature range of 300-1000 K. At temperatures over 1000 K following formulations are used to calculate specific heat capacity under constant pressure [5]:

$$\bar{c}_{p,CO_2} = \bar{R}_{CO_2}[4.4608 + 0.0030982T - \frac{0.12393}{10^5}T^2 + \frac{0.22741}{10^9}T^3 - \frac{0.15526}{10^{13}}T^4] \quad (7)$$

$$\bar{c}_{p,H_2O} = \bar{R}_{H_2O}[2.7168 + 0.0029451T - \frac{0.80224}{10^6}T^2 + \frac{0.10227}{10^9}T^3 - \frac{0.48472}{10^{14}}T^4] \quad (8)$$

$$\bar{c}_{p,CO} = \bar{R}_{CO}[2.9841 + 0.0014891T - \frac{0.57900}{10^6}T^2 + \frac{0.10365}{10^9}T^3 - \frac{0.69354}{10^{14}}T^4] \quad (9)$$

$$\bar{c}_{p,H_2} = \bar{R}_{H_2}[3.1002 + 0.00051119T + \frac{0.52644}{10^7}T^2 - \frac{0.34910}{10^{10}}T^3 + \frac{0.36945}{10^{14}}T^4] \quad (10)$$

$$\bar{c}_{p,O_2} = \bar{R}_{O_2}[3.6220 + 0.00073618T - \frac{0.19652}{10^6}T^2 + \frac{0.36202}{10^{10}}T^3 - \frac{0.28946}{10^{14}}T^4] \quad (11)$$

$$\bar{c}_{p,N_2} = \bar{R}_{N_2}[2.8963 + 0.0015155T - \frac{0.57235}{10^6}T^2 + \frac{0.99807}{10^{10}}T^3 - \frac{0.65224}{10^{14}}T^4] \quad (12)$$

$$\bar{c}_{p,NO} = \bar{R}_{NO}[3.189 + 0.0013382T - \frac{0.52899}{10^6}T^2 + \frac{0.95919}{10^{10}}T^3 - \frac{0.64848}{10^{14}}T^4] \quad (13)$$

After calculating heat capacity of each ingredient, according to perfect gas law heat capacity of the combustion gaseous mixture under constant pressure can be found by [1-2]:

$$\bar{c}_{p,cg} = \sum_i \bar{c}_{p,i}x_i \quad (14)$$

Herein, x_i is the mole fraction of combustion gaseous ingredient i and may be expressed as [1-2]:

$$x_i = \frac{n_i}{\sum n_i} \quad (15)$$

Specific Enthalpy Calculation

A similar approach is derived for specific enthalpy of the combustion gaseous mixture. Thus, following equations may be written for specific enthalpy of each combustion gaseous ingredient [5]:

$$\bar{h}_{CO_2} = \bar{R}_{CO_2}[2.4008T + 0.00436755T^2 - \frac{0.220236}{10^5}T^3 + \frac{0.050055}{10^8}T^4 + \frac{0.126548}{10^{15}}T^5 - 48378] \quad (16)$$

$$\bar{h}_{H_2O} = \bar{R}_{H_2O}[4.0701T - 0.0005542T^2 + \frac{0.138403}{10^5}T^3 - \frac{0.0740925}{10^8}T^4 + \frac{0.161404}{10^{12}}T^5 - 30280] \quad (17)$$

$$\bar{h}_{CO} = \bar{R}_{CO}[3.7101T - 0.00080955T^2 + \frac{0.12308}{10^5}T^3 - \frac{0.0508}{10^8}T^4 + \frac{0.047906}{10^{12}}T^5 - 14356] \quad (18)$$

$$\bar{h}_{H_2} = \bar{R}_{H_2}[3.0574T + 0.00133825T^2 - \frac{0.193663}{10^5}T^3 + \frac{0.138025}{10^8}T^4 - \frac{0.036246}{10^{11}}T^5 - 988.9] \quad (19)$$

$$\bar{h}_{O_2} = \bar{R}_{O_2}[3.6256T - 0.0009391T^2 + \frac{0.235183}{10^5}T^3 - \frac{0.1690875}{10^8}T^4 - \frac{0.043112}{10^{11}}T^5 - 1047.5] \quad (20)$$

$$\bar{h}_{N_2} = \bar{R}_{N_2}[3.6748T - 0.0006041T^2 + \frac{0.07746}{10^5}T^3 - \frac{0.15782}{10^9}T^4 - \frac{0.045154}{10^{12}}T^5 - 1061.2] \quad (21)$$

Eqs. 16-21 can be used in the temperature range of 300-1000 K. Over 1000 K specific enthalpy of each combustion gaseous ingredient may be stated as following [5]:

$$\bar{h}_{CO_2} = \bar{R}_{CO_2}[4.4608T + 0.0015491T^2 - \frac{0.04131}{10^5}T^3 + \frac{0.0568525}{10^9}T^4 - \frac{0.031052}{10^{13}}T^5 - 48961] \quad (22)$$

$$\bar{h}_{H_2O} = \bar{R}_{H_2O}[2.7168T + 0.00147255T^2 - \frac{0.267413}{10^6}T^3 + \frac{0.0255675}{10^9}T^4 - \frac{0.096944}{10^{14}}T^5 - 29906] \quad (23)$$

$$\bar{h}_{CO} = \bar{R}_{CO}[2.9841T + 0.00074455T^2 - \frac{0.193}{10^6}T^3 + \frac{0.0259125}{10^9}T^4 - \frac{0.138708}{10^{14}}T^5 - 14245] \quad (24)$$

$$\bar{h}_{H_2} = \bar{R}_{H_2}[3.1002T + 0.000255595T^2 + \frac{0.17548}{10^7}T^3 - \frac{0.04387}{10^{10}}T^4 + \frac{0.07389}{10^{14}}T^5 - 877.38] \quad (25)$$

$$\bar{h}_{O_2} = \bar{R}_{O_2}[3.6220T + 0.00036809T^2 - \frac{0.065506}{10^6}T^3 + \frac{0.090505}{10^{10}}T^4 - \frac{0.057892}{10^{14}}T^5 - 1202] \quad (26)$$

$$\bar{h}_{N_2} = \bar{R}_{N_2}[2.8963T + 0.00075775T^2 - \frac{0.190783}{10^6}T^3 + \frac{0.2495175}{10^{10}}T^4 - \frac{0.130448}{10^{14}}T^5 - 905.86] \quad (27)$$

$$\bar{h}_{NO} = \bar{R}_{NO}[3.189T + 0.0006691T^2 - \frac{0.17633}{10^6}T^3 + \frac{0.2397975}{10^{10}}T^4 - \frac{0.129696}{10^{14}}T^5 + 9828.3] \quad (28)$$

By using calculated specific enthalpy of each combustion gaseous ingredient, specific enthalpy of the combustion gaseous mixture can be determined by [1-2]:

$$\bar{h}_{cg} = \sum_i \bar{h}_i x_i \quad (29)$$

Standard Entropy Calculation

To find standard entropy of a gaseous mixture, firstly standard entropy of each ingredient should be obtained similar to previously explained approaches. For this purpose following equations can be beneficial from 300 K to 1000 K [5]:

$$\bar{s}_{CO_2} = \bar{R}_{CO_2}[2.4008\ln T + 0.0087351T - \frac{0.330355}{10^5}T^2 + \frac{0.06674}{10^8}T^3 + \frac{0.158185}{10^{15}}T^4 + 9.6951] \quad (30)$$

$$\bar{s}_{H_2O} = \bar{R}_{H_2O}[4.0701\ln T - 0.0011084T + \frac{0.207605}{10^5}T^2 - \frac{0.09879}{10^8}T^3 + \frac{0.201755}{10^{12}}T^4 - 0.3227] \quad (31)$$

$$\bar{s}_{CO} = \bar{R}_{CO}[3.7101\ln T - 0.0016191T + \frac{0.18462}{10^5}T^2 - \frac{0.06773}{10^8}T^3 + \frac{0.05988}{10^{12}}T^4 + 2.9555] \quad (32)$$

$$\bar{s}_{H_2} = \bar{R}_{H_2}[3.0574\ln T + 0.0026765T - \frac{0.29046}{10^5}T^2 + \frac{0.18403}{10^8}T^3 - \frac{0.04530}{10^{11}}T^4 - 2.2997] \quad (33)$$

$$\bar{s}_{O_2} = \bar{R}_{O_2}[3.6256\ln T - 0.0018782T + \frac{0.352775}{10^5}T^2 - \frac{0.22545}{10^8}T^3 - \frac{0.05389}{10^{11}}T^4 + 4.3053] \quad (34)$$

$$\bar{s}_{N_2} = \bar{R}_{N_2}[3.6748\ln T - 0.0012082T + \frac{0.1162}{10^5}T^2 - \frac{0.210426}{10^9}T^3 - \frac{0.0564425}{10^{12}}T^4 + 2.358] \quad (35)$$

For gaseous mixture ingredients over the 1000 K temperature, standard entropy can be found by following equations [5]:

$$\bar{s}_{CO_2} = \bar{R}_{CO_2}[4.4608\ln T + 0.0030982T - \frac{0.061965}{10^5}T^2 + \frac{0.113705}{10^9}T^3 - \frac{0.038815}{10^{13}}T^4 - 0.98636] \quad (36)$$

$$\bar{s}_{H_2O} = \bar{R}_{H_2O}[2.7168\ln T - 0.0029451T - \frac{0.40112}{10^6}T^2 + \frac{0.03409}{10^9}T^3 - \frac{0.12118}{10^{14}}T^4 + 6.6306] \quad (37)$$

$$\bar{s}_{CO} = \bar{R}_{CO}[2.9841 \ln T - 0.0014891T - \frac{0.2895}{10^6}T^2 + \frac{0.03455}{10^9}T^3 - \frac{0.173385}{10^{14}}T^4 + 6.3479] \quad (38)$$

$$\bar{s}_{H_2} = \bar{R}_{H_2}[3.1002 \ln T + 0.0026765T + \frac{0.26322}{10^7}T^2 - \frac{0.11636}{10^{10}}T^3 + \frac{0.0923625}{10^{14}}T^4 - 1.9629] \quad (39)$$

$$\bar{s}_{O_2} = \bar{R}_{O_2}[3.622 \ln T - 0.00073618T - \frac{0.09826}{10^6}T^2 + \frac{0.120673}{10^{10}}T^3 - \frac{0.0572365}{10^{14}}T^4 + 3.6151] \quad (40)$$

$$\bar{s}_{N_2} = \bar{R}_{N_2}[2.8963 \ln T + 0.0015155T - \frac{0.286175}{10^6}T^2 + \frac{0.33269}{10^{10}}T^3 - \frac{0.16306}{10^{14}}T^4 + 6.1615] \quad (41)$$

$$\bar{s}_{NO} = \bar{R}_{NO}[3.189 \ln T + 0.0013382T - \frac{0.264495}{10^6}T^2 + \frac{0.31973}{10^{10}}T^3 - \frac{0.16212}{10^{14}}T^4 + 6.7458] \quad (42)$$

By using standard entropy of each combustion gaseous ingredient, standard entropy of the combustion gaseous mixture may be found by [1-2]:

$$\bar{s}_{cg} = \sum_i \bar{s}_i x_i \quad (43)$$

RESULTS AND DISCUSSION

In this study, thermophysical properties of combustion gaseous as product of kerosene reaction with air are found by explained methodology. Stoichiometric combustion reaction for kerosene is written as:

$$(C_{11}H_{21}) + 79.854\begin{bmatrix} 0.7567\ N_2 \\ 0.2035\ O_2 \\ 0.0303\ H_2O \\ 0.000345\ CO_2 \\ 0.000007\ CO \end{bmatrix} \rightarrow 11.028\ CO_2 + 12.92\ H_2O + 60.425 N_2 \quad (44)$$

In Figure 1, variation of specific heat capacities of combustion gaseous and ingredients are graphed. As indicated in the figure, specific heat capacity of each ingredient is logarithmically proportional to the temperature. It is clearly stated in Eq. 14, variation of combustion gaseous specific heat capacity is dependent to ingredients' specific heat capacity. Thus, specific heat capacity of the combustion gaseous is also logarithmically proportional to the temperature.

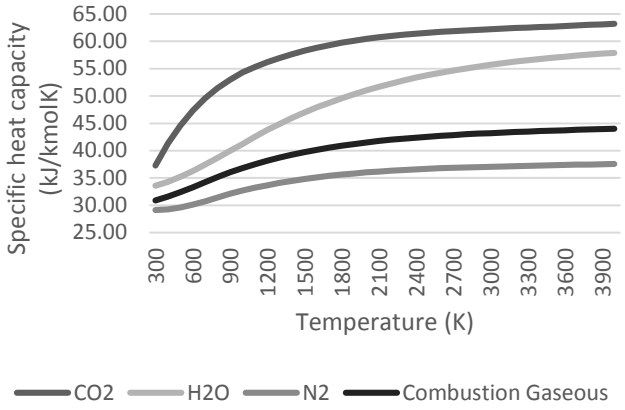

Figure 1 Variation of specific heat capacity with temperature

Same graph can be illustrated for specific heat capacity and standard entropy variations of combustion gaseous ingredients. Heat capacity variation of combustion gaseous and its ingredients are plotted in Figure 2. Similar situation of the specific heat capacity dependence to temperature van be noted for specific enthalpy. It is clearly indicated in the graph, specific enthalpy of combustion gaseous and its ingredients increase depending on temperature rise.

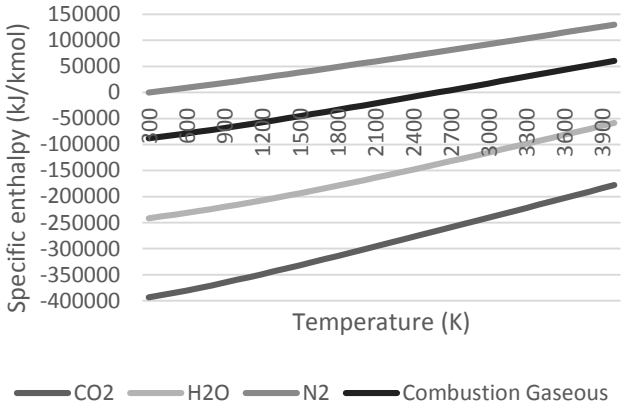

Figure 2 Variation of specific enthalpy with temperature

CONCLUSIONS

As a result of this study, following assertions are concluded by authors:

- Calculating thermophysical properties of gaseous mixtures with regard to mixture composition enables to achieve more sensitive results.
- Specific heat capacity of a gaseous mixture varies logarithmic proportionally with temperature.
- Specific enthalpy of a gaseous mixture varies direct proportionally with temperature.

For a future, application of explained methodology to numerous gaseous mixtures is intended by the authors.

ACKNOWLEDGEMENT

The authors would like to gratefully thank Anadolu University located in Eskisehir city of Turkey.

REFERENCES

[1] Cengel Y.A. and Boles M., Thermodynamics: an Engineering Approach, McGraw-Hill, 2014.
[2] Moran, M.J., Shapiro, H.N., Fundamentals of Engineering Thermodynamics, Wiley and Sons, 2014.
[3] Turan, O., Effect of reference altitudes for a turbofan engine with the aid of specific-exergy based method, *Int. J. Exergy*, vol. 11, no. 2, 2012, pp.252–270.
[4] Aydin, H., Turan, O., Karakoc, T.H., Midilli, A., Component-based exergetic measures of an experimental turboprop/turboshaft engine for propeller aircrafts and helicopters, Int. J. Exergy, Vol.11, No.3, 2012, pp.322–348.
[5] Svehla, R.A., McBride B.J., Fortran IV computer program for calculation of thermodynamic and transport properties of complex chemical systems, NASA, 1973.

HEAT AND MASS TRANSFER AT NANOPARTICLES SYNTHESIS IN A JET PLASMACHEMICAL REACTOR: MODELLING AND EXPERIMENT

Samokhin[1] A. V. *, Polyakov[1] S., Alekseev[1] N.V., Kolesnikov[2] A., Astashov[1] A., Tsvetkov[1] Yu.
*Author for correspondence
[1]Baikov Institute of Metallurgy and Material Sciences, Russian Academy of Sciences,
Leninskii pr. 49, Moscow, 119991, Russia
[2]Department of Chemical, Metallurgical and Materials Engineering,
Tshwane University of Technology,
Pretoria, 0001, South Africa,
E-mail: samokhin@imet.ac.ru

ABSTRACT

Embedded 3D CFD model of nanoparticles formation by coagulation in a confined plasma jet reactor is developed and implemented using ANSYS/CFX 12.1 software. The results of calculations of steady-state thermal regime of plasma jet reactor are in a good agreement with the experimental data on the heat flux distribution along the reactor wall.

INTRODUCTION

Nanopowders are used in manufacturing of various nanostructured materials such as functional ceramics, carbide materials with increased wear resistance and toughness, dispersion-strengthened and modified structural alloys with high performance, protective thermal coatings, corrosion and wear-resistant coatings, polymer composites, and others [1-5]. Thermal plasma synthesis is still the most versatile method for producing nanopowders. In this method the nanopowders are formed via condensation from the gaseous phase in controlled inert, reducing or oxidizing atmospheres.

DC arc and high-frequency microwave discharge generators are used for thermal plasma generation [6-8] in power range 1 kW – 100 MW.

Broad spectrum of gases and gas mixtures can be used in plasma torches if proper gas protection and appropriate cathode materials are used. Thermal plasma streams with mean mass temperatures up to 12000 K are confidently generated.

A cylindrical reactor with confined DC arc jet was successfully applied for the synthesis of nanopowders [9-10]. In such reactor the plasma jet was generated by a DC arc generator and discharged into the cooled cylindrical reactor along its axis. The ratio of the plasma jet diameter to the reactor diameter was above 10.

Inside reactor the plasma jet is rapidly cooled due to heat transfer with cooled walls of reactor providing sharp temperature decrease and formation of supersaturated vapour. Fast condensation of the supersaturated vapour leads to formation of nanoparticles. In this process particles size distribution is determined by condensation and coagulation growth mechanisms [11-15].

This paper focuses on the model development for characterisation of temperature and velocity fields in plasma reactor for nanoparticles synthesis and aims to provide some information on model predictive capabilities.

NOMENCLATURE

C_{s1}	[-]	Coefficients of k-ε turbulence model
C_{s2}		
D_m	[m^2/s]	Diffusivity
D	[m]	Diameter
d_1	[m]	Diameter of monomer particle
$E\{\}$	[-]	Operator of mathematical expectation
h	[J/kg]	Enthalpy
I	[-]	Integer random variable
k_B	[m^2 kg /s^2 /K]	Boltzmann constant
L	[m]	Length
M	[-]	Moment of particle size distribution function
N	[1/m^3]	Number concentration
Pr	[-]	Prandtl number
p'	[Pa]	Turbulent analogue of static pressure
r	[-]	Order of moment
S_E	[W/m^3]	Inner heat sources power
S_m	[N]	Sum of mass forces
S_Φ	[kg/m^3/s]	Inner mass sources power
t	[s]	time
T	[K]	Temperature
$\mathbf{U}$	[m/s]	Velocity vector
x	[m]	Cartesian axis direction
y	[m]	Cartesian axis direction
z	[m]	Cartesian axis direction

Special characters

β	[-]	Collision coefficient
Γ	[m^2/s]	Molecular diffusivity of scalar substance
δ	[-]	Kroneker symbol
λ	[W/m/K]	Thermal conductivity
λ_{FP}	[m]	Free path length
μ	[Pa.s]	Dynamic viscosity coefficient
v	[m^3]	Volume of i-mer
σ_ζ	[-]	Constant of k- ε turbulence model
σ_ε	[-]	Constant of k- ε turbulence model
ρ	[kg/m^3]	Density
Φ	[-]	Scalar substance
τ	[kg/m^2/s^2]	Viscous stress tensor
$\otimes$	[-]	Dyadic vector product

Subscripts

i	Index for random variable I
m	molecular
th	thermophoretic
t	turbulent

MODEL EQUATIONS

The mathematical description of nanoparticles coagulation growth inside the DC thermal plasma reactor with confined flow includes:

- Reynolds-averaged Navier-Stokes equations, with two additional closing equations, modelling parameters for calculation of turbulent viscosity coefficient;
- Thermal energy transport equation, containing an additional term source, taking into account the radiation heat transfer in optically thin media;
- Four equations for zeroth, first, second and third moments of the particle size distribution function;
- Initial and boundary conditions.

In general case, total system of equations consists of:

- Continuity equation

$$\frac{\partial \rho}{\partial t} + \nabla(\rho \boldsymbol{U}) = 0 \qquad (1)$$

- Momentum transport equation

$$\frac{\partial \rho \boldsymbol{U}}{\partial t} + \nabla \cdot (\rho \boldsymbol{U} \otimes \boldsymbol{U}) = \\ = -\nabla p' + \nabla \cdot (\tau - \rho \overline{\boldsymbol{u} \otimes \boldsymbol{u}}) + S_m \qquad (2)$$

- Energy transport equation

$$\frac{\partial \rho h_{tot}}{\partial t} - \frac{\partial p'}{\partial t} + \nabla \cdot (\rho U h_{tot}) = \\ = \nabla \cdot \left(\lambda \nabla \mathrm{T} - \rho \overline{uh}\right) + \nabla \cdot (\boldsymbol{U} \cdot \tau) + \boldsymbol{S}_E \qquad (3)$$

Where

$$h_{tot} = h + \frac{\boldsymbol{U}^2}{2} + k; \qquad k = \frac{1}{2}\overline{\boldsymbol{u}^2} \qquad (4)$$

- Scalar transport equations

$$\frac{\partial \rho \Phi}{\partial t} + \nabla \cdot (\rho \boldsymbol{U} \Phi) = \nabla \cdot (\Gamma \nabla \Phi - \rho \overline{\boldsymbol{u} \Phi}) + S_\Phi \qquad (5)$$

and closing equations for the turbulent stress

$$-\rho \overline{\mathrm{u} \otimes \mathbf{u}} = \mu_t \left[\nabla \boldsymbol{U} + (\nabla \boldsymbol{U})^T - \frac{2}{3}\delta \nabla \cdot \mathbf{U}\right] \qquad (6)$$

Turbulent energy transport equation

$$-\rho \overline{\mathbf{u} h} = \frac{\mu_t}{Pr_t} \nabla h \qquad (7)$$

Equation for turbulent flux of a substance

$$-\rho \overline{\mathbf{u} \Phi} = \frac{\mu_t}{Pr_\Phi} \nabla \Phi = \Gamma_t \nabla \Phi \qquad (8)$$

In the framework of k-ε turbulence model, the coefficient of eddy viscosity μ_t is determined by using two model parameters k (kinetic energy of pulsation motion) and ε (the rate of dissipation of turbulent fluctuations)[6-8].

$$\mu_t = C_\mu \rho \frac{k^2}{\varepsilon} \qquad (9)$$

Transport equations for parameters k and ε:

$$\frac{\partial (\rho k)}{\partial t} + \nabla \cdot (\rho U k) = \\ = \nabla \cdot \left[\left(\mu + \frac{\mu_t}{\sigma_k}\right) \nabla \mathrm{k}\right] + P_k - \rho \varepsilon \qquad (10)$$

and

$$\frac{\partial (\rho \varepsilon)}{\partial t} + \nabla \cdot (\rho U \varepsilon) = \nabla \cdot \left[\left(\mu + \frac{\mu_t}{\sigma_\varepsilon}\right) \nabla \varepsilon\right] + \\ + \frac{\varepsilon}{k}(C_{s1} P_k - C_{s2} \rho \varepsilon) \qquad (11)$$

In current work, the momentum source term S_M in the Equation (2) was assumed to be equal to zero because the volumetric fraction of solid raw material particles was small (of order of 0.01). The same refers to the energy source term S_E in the Equation (3). The temperature, pressure and velocity fields obtained from solution of Equations (1-11) were used for the simulation of the nanoparticle growth in the plasma flow.

COAGULATION GROWTH KINETICS

To describe the process of coagulation growth the simplified model was used [4] where collision coefficient β was assumed to be independent of particle size.

In this case, the value of β could be calculated from simple correlation $\beta = <\beta> = C <b>$.

The parameter C at Knudsen number $Kn >> 1$ can be calculated as

$$C = \sqrt{\frac{8\pi k_B T}{m_1}} \left(\frac{3 m_1}{4\pi \rho_1}\right)^{2/3}$$

where m_1 is the mass of the initial particle, ρ_1 is density of material; k_B is Boltzmann constant.

Parameter $<b>$ depends on the ratio $\mu_2'/\mu_1'^2 = D$, where μ_2' and μ_1' are the second and first initial normalized moments, D is dimensionless dispersion parameter.

Parameter $<b>$ is defined as

$$< b > = \begin{cases} \left(5.67 + \dfrac{0.589}{\mu^2}\right)\mu^{\frac{1}{6}} \\ at\ \ D \to 1 \\ (3.138 + 3.108D - 0.589D^2)\mu^{\frac{1}{6}} \\ at\ \ 1 \le D \le 2 \\ \left(8.339 - \dfrac{2.682}{D}\right)\mu^{\frac{1}{6}} \\ at\ \ D > 2 \end{cases} \qquad (12)$$

In Lagrange coordinate system the coagulation growth of nanoparticles can be described as evolution of four initial moments of the particle size distribution function (M_0, M_1, M_2, M_3) [4]:

$$\frac{dM_0}{dt} = -\frac{1}{2}\beta M_0^2, \quad (13)$$

$$\frac{dM_1}{dt} = 0, \quad (14)$$

$$\frac{dM_2}{dt} = \beta M_1^2, \quad (15)$$

$$\frac{dM_3}{dt} = 3\beta M_1 M_2. \quad (16)$$

The initial moments of order n are introduced for an integer random variable I, taking discrete values i = 1, 2, 3, ... ∞.

Introduced random variable I represents the number of monomer volumes in the growing nanoparticle which has been formed after the merger of i monomers. Here $v_i = i * v_1$ where v_i is the volume of the growing nanoparticle and v_1 is the volume of monomer. Mass of growing particle is expressed as $m_i = im_1 = iv_1\rho_1 = i\pi d_1^3\rho_1/6$, where d_1 is the diameter of a single particle (monomer).

The initial moments of the random variable I of order r are defined as

$$M_r = \sum_{i=1}^{\infty} i^r N_i$$

where $r = 0,1,2 \ldots, N_i$ is number concentration of particles with dimension i.

The normalized initial moments are expressed as $\mu_r' = E\{I^r\} = M_r/M_0$.

In 3-dimesional framework when particle concentrations are determined by collisions in moving flow, the coagulation growth of nanoparticles can be described as temporal and spatial evolution of the first four initial moments [17-18]. Transport of each moment can be described as scalar substance transport in the fixed (Eulerian) coordinate system.

The system of transport equations includes four partial differential equations:

$$\frac{\partial(\rho M_0)}{\partial t} + \nabla(\rho \mathbf{U} M_0) = -\nabla(\rho \mathbf{U}_{th} M_0) + \nabla(\rho D_m \nabla M_0) - \frac{\rho}{2}\beta M_0^2, \quad (17)$$

$$\frac{\partial(\rho M_1)}{\partial t} + \nabla(\rho \mathbf{U} M_1) = -\nabla(\rho \mathbf{U}_{th} M_1) + \nabla(\rho D_m \nabla M_1), \quad (18)$$

$$\frac{\partial(\rho M_2)}{\partial t} + \nabla(\rho \mathbf{U} M_2) = -\nabla(\rho \mathbf{U}_{th} M_2) + \nabla(\rho D_m \nabla M_2) + \rho\beta M_1^2, \quad (19)$$

$$\frac{\partial(\rho M_3)}{\partial t} + \nabla(\rho \mathbf{U} M_3) = -\nabla(\rho \mathbf{U}_{th} M_3) + \nabla(\rho D_m \nabla M_3) + 3\rho\beta M_1 M_2. \quad (20)$$

It is assumed that the time of the nucleus formation is significantly shorter than their coagulation growth time in the reactor .

In this approach, the beginning of nucleation is not considered as starting point the particle growth. But particle size evolution starts from the moment when ensemble of particles with the size of 1 nm appears in the zone determined by the condensation isotherm. Condensation temperature is determined by the material properties of nanoparticles.

The first and second terms on the left side of the equations describe the accumulation and convective transport of substance under consideration, respectively. The first term on the right hand side describes the source of additional substance flux through termoforetic effect with the migration velocity:

$$\mathbf{U}_{th} = -0,55\nu(\nabla T/T)$$

The second term describes the particles Brownian motion with diffusion coefficient D_m:

$$D_m = \frac{k_B T}{3\pi\mu d}\left(1 + \frac{3,314\lambda_{fp}}{d}\right)$$

Where λ_{fp} is mean free path of the gas molecules [19]. The last term on the right side (not in the equation (18)) is the source term, describing coagulation growth of nanoparticles expressed via moments of particle size distribution function. These moments are considered as scalars obeying scalar transport Equation (5) in general form, but in current work the evolution of each of the four moments is described by corresponding Equations (17-20).

PLASMA REACTOR

Simulated plasma reactor (Figure 1 and Table 1) is a cylinder with a conical bottom.

Dimensions of the plasma reactor are given in the Table 1.

Table 1. Plasma reactor dimensions

Parameter	D1	D2	D3	D4	L1	L2	L3	L4
Value, mm	200	10	2	40	600	900	10	40

In the upper part of the reactor there are a thermal plasma discharge channel and thin oblique channels for raw material feed by carrier gas. The synthesized nanoparticles are removed from the reactor through the side outlet together with gas

mixture. Plasma generation occurs inside the volume of the plasma torch (channel length L_4 and diameter D_2). Plasma jet is discharged from the torch channel into the volume of reactor. The plasma jet formation was simulated by introducing of heat source uniformly distributed inside volume of the plasma torch. Axial and/or tangential plasma gas injection into the channel was used.

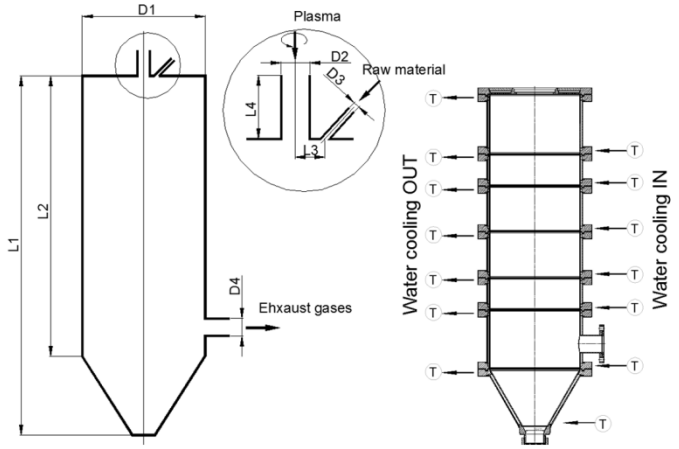

Figure 1 Plasma reactor geometry and configuration of water-cooled sections.

Standard velocity, pressure, concentrations and temperature boundary conditions were applied. The temperature of the water-cooled walls was assumed to be constant and equal to a predetermined value of 30 °C.

Thermophysical properties of the gaseous medium were determined in the approximation of local thermodynamic equilibrium (LTE). The LTE calculations were carried out by TERRA software. The software is used for modelling of phase and chemical equilibria in multicomponent systems [20].

The presented model of nanoparticles growth in the plasma reactor was implemented in software package ANSYS CFX 12.1 using ANSYS Workbench platform.

EXPERIMENTAL

Model validation was done by comparison of the measured and calculated heat flux density distribution along the length of the plasma reactor wall.

The cylindrical plasma reactor consisted of 6 sections with inner diameter 200 mm. Each section had a water-cooling jacket with water-swept inner surface. Total length of the reactor was equal to 600 mm. Cooling water was supplied to the connected in series sections of the reactor and water temperature was measured at the inlet and the outlet of each section by resistance thermometer DTS174-50M.V3.120/2 (Figure 1.). The temperature values were recorded using an 8-channel data logger OWEN-UKT38 SCH4.TS and software Owen Process Manager. Plasma flow was generated in DC plasma torch of nominal capacity of 25 kW with vortex discharge stabilization [16].

RESULTS AND DISCUSSION

The simulations were performed in two stages:

Stage I: Simulation of heat and momentum transfer in the reactor's volume in the absence of the dispersed phase;

Stage II: Simulation of particle formation via coagulation in the pre-calculated at Stage I velocity and temperature field

Stage I simulation results

In calculating the temperature, pressure and velocity fields at Stage I two cases were considered:

Case (a): Initial spinning of plasma jet and radiative heat transfer were not considered;

Case (b): Initial spinning of plasma jet and radiative heat transfer were taken into consideration. Effective two-phase mixture absorptivity was adopted in radiation calculations

Results obtained by calculation without accounting for initial spin of the plasma gas and radiant heat transfer component were in poor agreement with the experimental data (Figure 2). The calculated values of the heat flux density have lower values, especially in the upper part of the reactor as compared with those obtained in experiments.

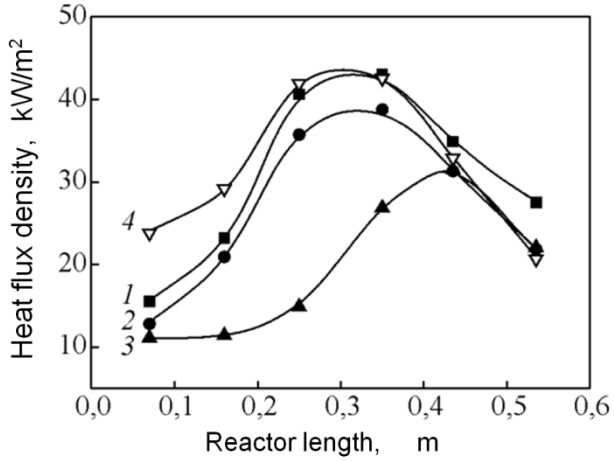

Figure 2 Density distribution of the heat flux (kW/m^2) along the length of reactor (m): 1 - plasma gas flowrate 1.7 m^3/h, enthalpy 25.6 MJ/m^3, experiment; 2 - plasma gas flowrate 1.6 m^3/h, enthalpy 23.8 MJ/m^3, experiment; 3 - plasma gas flowrate 2.0 m^3/h, enthalpy 25.2 MJ/m^3, calculation without initial gas spinning and radiation; 4 - plasma gas flowrate 2.0 m^3/h, enthalpy 25.2 MJ/m^3, calculated taking into account the initial gas spinning and radiation heat transfer.

To obtain better agreement with experimental data, gas spinning and radiative heat transfer were taken into consideration (Case (b)). When cold plasma-forming gas enters into the plasma torch via tangentially positioned openings, the gas is spinned and retains tangential velocity component during movement in the heating section until the entrance into reactor. The radiative heat transfer in ultraviolet part of spectrum was modelled using effective absorptivity equal to 0.25.

Including gas spinning and radiative heat transfer in simulations allowed obtaining better agreement between measured and calculated heat flux density values (Figure 2.).

CFD calculations revealed the temperature distribution and flow pattern in the plasma reactor (Figure 3.). Further simulations of nanoparticles growth via solution of transport

equations for the moments of size distribution function were based on the calculated gas temperature and velocity fields.

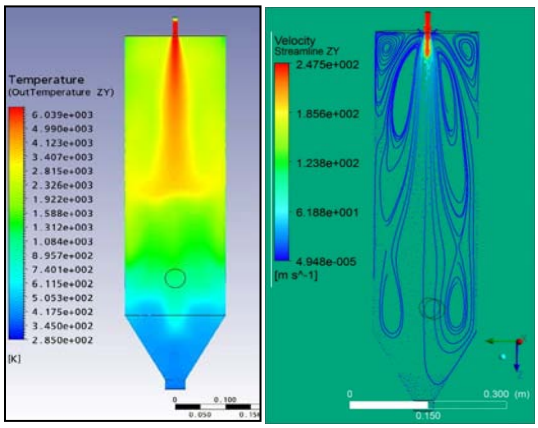

Figure 3 Temperature distribution (a) and flow streamlines (b) in axial cut planes. Nitrogen plasma gas flowrate 2.0 m^3/h; nitrogen carrier gas flowrate 0.3 m^3/h, enthalpy 25.2 MJ/m^3.

Some difference between experimental and calculated values of heat flux density is observed in the initial zone of the reactor. This could be attributed to the assumption of the constant radiation absorption coefficient, while this coefficient is a function of the temperature. At high temperatures diatomic nitrogen molecules dissociate into atoms and thermophysical properties of the gas change.

The plasma gas spinning results in the increase of the plasma jet opening angle at the reactor inlet and leads to reduction of the plasma jet propagation length. However, the intensity of heat transfer to the reactor wall rises with increase of the initial gas spin.

As it follows from calculations of the velocity profiles, the flow pattern within the reactor is characterized by existence of stationary vortices in different temperature zones (Figure 3). The presence of vortices could be explained by sudden expansion of plasma flow into the reactor volume, and by location of gas outlet pipe on the side of reactor. The implication of vortexes existence in reactor is that some nanoparticles will be involved into motion inside the eddy currents, and therefore will have increased residence time in respective temperature zones. In this case the nanoparticles properties (and especially geometric dimensions) could significantly change.

Stage II simulations results

Formation of W, Cu and Al_2O_3 nanoparticles was simulated using the developed model. These materials were selected because they have very different phase transformation temperatures. The calculations were performed for the parameters of the reactor presented in the Table 2.

The simulated and experimental values of average size d_{32} for the reaching the reactor wall nanoparticles were compared. The average particle size d_{32} was calculated as the ratio of corresponding moments of the particle size distribution function. The value obtained was compared with an experimental particle size, defined as

$$d_{32} = \frac{6}{\rho_{pat} S_{spec}}$$

where S_{spec} is experimentally measured specific surface of the nanopowder, ρ_{pat} – nanoparticle material density.

Table 2 Plasma reactor operating conditions

Material	W	Al_2O_3	Cu
Plasma gas	N_2+30% vol. H_2	Air	N_2
Plasma gas flowrate, st. m^3/s	5.5e-04	5.5e-04	5.5e-04
Carrying N_2 flowrate, st. m^3/s	8.33e-05	8.33e-05	8.33e-05
Material flowrate, g/min	4-10	3-15	2-8
Plasma enthalpy, MJ/kg	33.2	13.4	20.2

W nanopowders were obtained by reduction of 40 micron tungsten oxide WO_3 particles in nitrogen-hydrogen plasma (30 vol.% H_2), Cu nanopowders were produced by evaporation and condensation of 20 microns copper powder in a nitrogen plasma and Al_2O_3 nanopowders - by oxidation of 30 microns aluminium particles in air plasma.

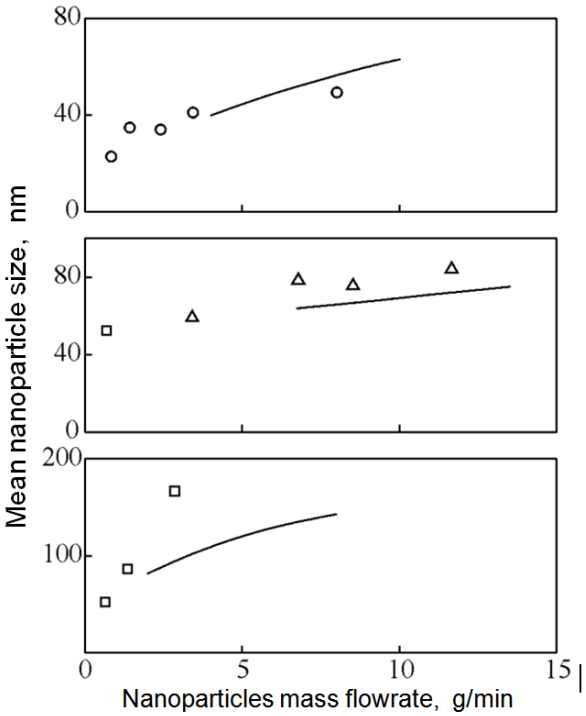

Figure 4 Average sizes of the nanoparticles (nm) vs. mass flowrate of condensing components (g/min): top - tungsten; middle - alumina; bottom - copper. Line – calculations; points - experiment.

Average size of nanoparticles increases with growth of the condensed phase mass concentration in the gas (Figure 4), which is predetermined by coagulation particle growth model. Simulated average diameter of W nanoparticles gives very good agreement with experiment. For Al_2O_3 the calculated values of mean diameter are a bit lower than the experimental values, and calculated values for Cu differ significantly from experiment, especially at high condensed phase mass flowrates. In case of aluminium oxide the discrepancy with experiment can be due to the fact that the model does not takes into account

thermal effect of the oxidation reaction. The difference of experimental and calculated mean size of copper nanoparticles could be explained by thermal processes occurring in the layer of nanoparticles deposited on the reactor wall.

This layer is exposed to the heat flux from high temperature gas-particles mixture that leads to an increase in temperature at the boundary between the layer and gas-particles mixture. Since copper has the lowest melting point amongst all used materials, sintering of Cu nanoparticles could take place. At constant time of experiments the increase in the material mass flowrate could lead to the growth of layer thickness followed by its temperature rise, which causes sintering of nanoparticles and average size increase.

CONCLUSIONS

Three-dimensional model of nanoparticle formation via coagulation mechanism in a DC plasma reactor with confined jet flow was developed and implemented in ANSYS CFX 12.1 software. The solution of mass, momentum, and energy conservation equations in 3D turbulent flow enabled to evaluate temperature and velocity distributions in the confined plasma jet reactor under assumption of negligible momentum and heat exchange between raw material and plasma flow due to small volumetric concentration of solid materials in plasma flow. The calculations of stationary heat transfer in the reactor demonstrated good agreement with experimental values of heat flux distribution along the wall of the reactor. The solution of transport equations for the first four moments of nanoparticles size distribution function made it possible to evaluate the influence of condensed phase mass concentration on the mean nanoparticle size. The experimental and simulated trends in mean size changes were in qualitative agreement i.e. mean size of nanoparticles increased with rise of the condensed phase mass concentration in the gas. Predicted mean nanoparticle size was closest to the experimental value for the material with high phase transition temperature (W).The calculated values of mean diameter for Cu nanoparticles (material with lowest phase transition temperature) differed significantly from experiment.

ACKNOWLEDMENTS

This research was conducted with financial support of Russian Ministry of Education and Science (Federal Target Program “Research and development on priority directions of Russian scientific-technological complex for 2014 – 2020”, project “Development of plasmachemical technologies foundations for production of titanium anoxic compounds as nanosized powders (nitrides, carbides and carbonitrides) to manufacture new structural and functional materials”, agreement №14.607.21.0103, unique code RFMEFI60714X0103).

REFERENCES

[1] Nanotechnology in Aerospace. Ed. I. Malsch. *9th Nanoforum Report*, 2007. http://ru.scribd.com/doc/ 36082496/Aerospace.

[2] Shiju N.R., Guliants V.V. Recent developments in catalysis using nanostructured materials. *App. Catalys., A: General*, 2009, v.356, iss.1, p.1-17.

[3] Zak F. Z., Xu W., Taegong R., Kyu S. H., Sohn H.Y. Synthesis, sintering, and mechanical properties of nanocrystalline cemented tungsten carbide. - A review. *Int. J. Refract. Met. Hard Mater.*, 2009, v.27, iss.2, pp.288-299.

[4] McWilliams A. Advanced ceramics and nanoceramic powders. *BCC Research LLC, Report code: NAN015F*, 2011.

[5] Encyclopedia of low-temperature plasma. Ed. V.E. Fortov. Introduction volume, IV, Moscow, Nauka, 2000, 509 p.

[6] Zhukov M.F., Zasipkin I.M., Timoshevsky A.N., Mikhailov, B.I., Desyatkov G.A. *Arc thermal plasma generators*. Nauka, Novosibirsk 1999, Ser . Low-temperature plasma, vol.17, 712 p.

[7] Dresvin S.V., Bobrov A.A., Lelevkin V.M., Lysov G.M., Sorokin L.M. *RF and microwave plasma torches*. Novosibirsk, Nauka, 1992, Ser. Low-temperature plasma, Volume 6, 317 p.

[8] Samokhin A.V., Tsvetkov J.V., Alekseev N.V. Plasma setup for nanodispersive powders manufacturing. *RF patent №2311225*, 2007. Publ. 27.11.2007, Bull. No. 33.

[9] Kolesnikov A.V., Alexeev N., Samokhin A. Controlled synthesis of alumina nanoparticles in a reactor with self-impinging plasma jets. *Int. J. Chem. React. Eng.*, 2007, v.5, iss.1. DOI: 10.2202 / 1542-6580.1521.

[10] Samokhin A.V., Alexeev N.V., Kornev S.A., Tsvetkov Yu.V. WC nanosized composition synthesis and characterization. *Proc. 19 Int. Symp. on Plasma Chemistry (ISPC- 19).* July 26-31, 2009. Bochum, Germany. http://www.ispc-onference.org/ispcproc/ispc19/652.pdf.

[11] Alekseev N.V., Samokhin A.V., Tsvetkov Y.V. Synthesis of titanium carbonitride nanoparticles via interaction of titanium tetrachloride and air hydrocarbons plasma. *High Energy Chemistry*, 1999, vol.33, №3. pp.238-242.

[12] Alekseev N.V., Samokhin A.V., Grechikov M.I., Tsvetkov Y. Dispersity control of metal powders produced by plasma reduction. *Physics and chemistry of material processing*, 1997, No. 6, pp.54-60.

[13] Gonzalez N.Ya.M., El Morsli M., Proulx P. Production of nanoparticles in thermal plasmas: A model including evaporation, nucleation, condensation, and fractal aggregation. *J.Therm.Spray Technol.*, 2008, v.17, iss.4, pp.533-550.

[14] Gherardi M., Colombo V., Ghedini E., Sanibondi P., Shigeta M. 2-D nodal model with turbulent effects for the synthesis of Si nanoparticles in RF thermal plasmas. *Proc. 20 Int. symp. on Plasma Chemistry (ISPC-20)*. July 24- 29, 2011. Philadelphia, USA, ID 20, 2011. http://www.ispc-conference.org/ispcproc/ispc20/309.pdf.

[15] Colombo V., Concetti A., Deschenaux C., Ghedini E., Gherardi M., Jaeggi C., Leparoux M., Sanibondi P. Validation of 3D modeling of an inductively coupled thermal plasma reactor through enthalpy probe measurements. *Ibid*.

[16] A. G. Astashov, A. V. Samokhin, Yu. V. Tsvetkov, and N. V. Alekseev. Heat-and-Mass Transfer in a Confined-Jet Flow Plasma Reactor during Nanopowder Manufacturing Processes. ISSN 0018-1439, High Energy Chemistry, 2012, Vol. 46, No. 4, pp. 279–282.

[17] Roach P. *Computational Fluid Dynamics*. Mir, 1980, 618 p.

[18] Poinsot T., Veynante D. *Theoretical and numerical combustion.* R.T.Edwards, Inc. Philadelphia, PA, USA, 2005, 527 p.

[19] Phanse G.M., Pratsinis S.E. Theory for aerosol generation in laminar flow condensers. *Aerosol Sci. Technol*., 1989 v.11. iss.2, pp.100-119.

[20] Trusov B.G. TERRA software for modeling of phase and chemical equilibria at high temperatures. *Proc. III Intern. Symp. "Combustion and plasma chemistry."* August 24-26, 2005, Almaty, Kazahkstan. Almaty: Kazahk University, 2005, pp.52-57

CALCULATION OF THERMO-HYDRAULIC EFFECTIVENESS OF POROUS CYLINDRICAL EVAPORATORS AT LAMINAR REGIME FLOW AND UNDER BOUNDARY CONDITIONS OF THE FIRST KIND

Lukisha A.P.

Department of Mine Energy Complexes,
Institute of Geotechnical Mechanics, National Academy Sciences of Ukraine
Simferopol'skaya Str. 2a, Dnipropetrovsk, 49005, Ukraine
E-mail: lukisha@ukr.net

ABSTRACT

Presented thermal-hydraulic calculations of the efficiency of steam-generating porous channels with using water as a coolant. As a parameter of the thermo - hydraulic efficiency used the ratio Q / N, where Q - the quantity of heat that consumed to evaporate of the liquid, N - power required to pump of the coolant. The calculation was performed for the boundary conditions of the first kind. In the calculation of the thermal characteristics was performed recalculation of known relations for the boundary conditions of the second kind for the case of their use under the boundary conditions of the first kind. As comparison surface was used pipe with smooth wall. Flow rate of coolant for compared channels (as well as the Reynolds number at the channel inlet) was taken to be equal. During calculations were used the following ranges of the regime - design parameters. The porous material - copper felt with porosity Θ = 0,5 ÷ 0,9; Reynolds number at the channel inlet Re = 100 ÷ 2300; diameter of channels d = 0,006 ÷ 0,05 m; temperature difference $t_w - t_{s\ in}$ = 1 ÷ 5 ^{0}C liquid temperature on saturated line at the inlet to channel $t_{s\ in}$ = 250 ÷ 300 ^{0}C. During calculations was found that for these conditions porous channels may have significantly shorter length compared to channels with smooth wall.

INTRODUCTION

The limitations of the world's energy resources requires a search for energy-saving technologies. One way in this direction is to study the possibility of using energy-efficient porous heat exchange elements. An earlier digitally simulated study of thermal-hydraulic efficiency of porous heat exchange channels with a single phase liquid coolant flow [1] - [4] showed the presence of domains of both, regime and design dependent parameters where possible energy gain in comparison to the smooth-wall heat exchanger channels. However, the biggest interest would be to investigate thermal-hydraulic efficiency of the highly porous channels in the phase transition of coolant evaporation. As a reference surface for comparison let's choose a smooth pipe, working as a once-through steam generator.

It should be noted that the analysis of the literature [5] - [7] showed that most of the researches of thermal phase transition from boiling to evaporation (in the smooth-walled and porous channels) was carried out for the boundary conditions of the second kind, i.e. at a constant heat flux on channel wall. However, as shown by a study on the effectiveness of porous thermal-hydraulic channels for single-phase heat transfer medium, the energy effect can be achieved with the boundary conditions of the first or third kind, i.e. when specifying the channel wall either a constant temperature, or with a known law of heat at ambient temperature.

Let's consider the problem of finding thermal-hydraulic efficiency of porous cylindrical channels at the phase transition temperature to the evaporation of the boundary conditions of the first kind.

NOMENCLATURE

d	[m]	Diameter of the channel
Fcs	[m^2]	Cross-sectional area of the channel
G	[kg/m^{2}s]	Specific mass rate of flux of a coolant
h_v	[W/m^{3}K]	Intensity volumetric heat exchange Inside of porous material
K	[-]	Slide factor
K_F	[-]	Geometric efficiency coefficient
L	[m]	Length
$\dot{m}$	[kg/s]	Mass flow rate
N	[W]	Power consumed for press (pumping) heat transfer medium through the channel
Nu	[-]	Nusselt number
P	[N/m^2]	Pressure
ΔP	[N/m^2]	Pressure drop
Pe	[-]	Peclet number
Pr	[-]	Prandtl number
Q	[W]	Quantity of heat that enters inside of the channel in unit of time
Q	[W/m^2]	Specific heat flux
Re	[-]	Reynolds number
T,t	[K]	Temperature
V	[m^3/kg]	Specific volume
W	[m/s]	Speed
X	[-]	Parameter of Lockart and Martinelli
X	[-]	Mass content of steam in the flow
x_{bound}		Boundary mass content of steam in the flow

Special characters

α	[m^{-2}]	Viscous coefficient of resistance of a porous material
α	[W/m^{2}K]	Heat transfer coefficient in zone of the nucleate boiling
$\alpha_к$	[W/m^{2}K]	Heat transfer coefficient in the water flow phase within a pipe or channel
α_0	[W/m^{2}K]	Heat transfer coefficient at boiling in a large volume
α_V	[W/m^{3}K]	Volumetric heat exchange coefficient at motion of two-phase vapor-liquid flow through the porous material
α_{VLO}	[W/m^{3}K]	Volumetric heat exchange coefficient inside of the porous material at moving of the liquid at a rate equal to the total rate of the mixture

β	[m^{-1}]	Inertial coefficient of resistance of a porous material
γ	[-]	Parameter, which characterizes intensity of heat exchange inside of porous material
θ	[-]	Porosity
λ_l	[W/mK]	Thermal conductivity of a fluid
λ_p	[W/mK]	Thermal conductivity of porous material
μ	[kgm/s]	Coefficient of dynamic viscosity
ν	[m^2/s]	Coefficient of cinematic viscosity
ξ	[-]	Pipe resistance coefficient
ρ	[kg/m^3]	Density
σ	[N/m]	Coefficient of surface tension of the liquid

Subscripts

cs	Cross section
G	Gas
in	Inlet
L,l	Liquid
p	Porous
sm	Smooth-wall
tw. ph.	Two phase
w	Wall
′	Relation to the liquid on the saturation line
″	Relation to the vapor on the saturation line

BOILING INTO SMOOTH-WALLED CYLINDRICAL CHANNELS (PIPES)

Zone of nucleate boiling

At creation of methodology for calculating thermal characteristics of smooth and porous channels, we assume that the liquid at the inlet to the channel is on the saturation line. According to [5], in the zone of the nucleate boiling heat transfer coefficient is defined by the formula

$$\alpha = \alpha_1 \sqrt{1 + 7 \cdot 10^{-9} (\rho w_{mix} r / q)^{3/2} (0{,}7\alpha_o / \alpha_1)^2}, \quad (1)$$

where $\alpha_1 = \sqrt{\alpha_\kappa^{\,2} + (0{,}7\alpha_o)^2}$, (2)

here α_κ – heat transfer coefficient in the water flow phase within a pipe or channel, which is calculated by the formula

$$Nu_d = \frac{\alpha_\kappa d}{\lambda} = \frac{(\xi/8) Re \cdot Pr \cdot C_t}{k + 4{,}5\sqrt{\xi}\ (Pr^{2/3} - 1)}, \quad (3)$$

where $k = 1 + 900/Re$; (4)

$$\xi = (1{,}82\ lg\ Re - 1{,}64) \quad (5)$$

C_t – adjustment for nonisothermality flow.

For liquid drops at $\mu_w/\mu_t = 0{,}08 \div 40$

$$C_t = (\mu_f/\mu_w)^n, \quad (6)$$

where $n = 0{,}11$ – while heating the liquid;

$n = 0{,}25$ – while cooling the liquid.

In formula (6) μ - coefficient of dynamic viscosity, indices *f* and *w* means relating to the mean temperature and the wall temperature, respectively.

Value α_o in formula (1) – boiling heat transfer coefficient in a large volume. Calculating value α_o using formula

$$\alpha_o = 4{,}34 q^{0{,}7} (p^{0{,}14} + 1{,}35 \cdot 10^{-2} p^2), \quad (7)$$

where q - value of the specific heat flux in W/m^2;

p – pressure in MPa;

α_o - heat transfer coefficient in W/(m^2K).

Value w_{mix} in formula (1) - the average speed of the water-steam mixture, m/s. Calculated by formula

$$w_{mix} = w_o[1 + x(\rho'/\rho'' - 1)], \quad (8)$$

where w_o - flow speed, m/s;

ρ' и ρ'' - respectively, the density of the liquid and vapor on the saturation line;

x - expendable mass vapor content.

As can be seen, in the formula (1) to determine the heat transfer coefficient entered α the value of heat flux q. When substituted in equation (1) of value $q = \alpha(t_w - t_s)$ can be seen that in this case the value of α included in the left and right sides of the equation. It means, the equation (1) is non-linear algebraic equations for the heat flux α, which can not be solved analytically in an explicit form. For calculating the value of α for equation (1) the method of consecutive approximations have to be used.

Calculation of boiling heat transfer in cylindrical smooth wall channels at dryout zone

As it is known [5] - [7] at boiling liquid in the smooth-walled pipe, with an increase in the value of mass consumable steam content, starting with a certain value, called the boundary vapor content, dispersed flow regime occurs, when starting the drying of the liquid film on the wall. Vapor-liquid stream begins to move in a vaporized mixture of steam and liquid droplets. Thus there is a significant deterioration in the heat exchange channel. According to [5], [6] a generalization of data on the boundary vapor content has led to the expression

$$x_{bound} = 1 - 0{,}86 \exp\left(-\frac{19}{\rho w \sqrt{d/\rho'\sigma}}\right) \pm 20\%, \quad (9)$$

where σ - coefficient of surface tension.

The heat transfer coefficient in the dryout zone was calculated from the equation proposed by Z. L. Miropol'skii [7]:

$$Nu'' = 0{,}028 Re''^{0{,}8} Pr''^{0{,}4} (\rho'/\rho'')^{1{,}15}, \quad (10)$$

where $Nu'' = \alpha d/\lambda''$; $Re'' = w'' d/\nu''$ - the Reynolds number is calculated using the reduced speed of steam $w_r = (\overline{\rho w})x/\rho''$. Here

d –diameter of the channel;

λ'' - thermal conductivity of a vapour.

CALCULATION OF HEAT TRANSFER IN THE MOVEMENT OF TWO-PHASE FLOW IN POROUS MATERIALS

The problem of experimental study of heat transfer at moving steam mixture through porous media addressed in dissertation of Kalmykov I. V. [9]. Based on the generalization of experimental data the author has received of the following generalized relationship characterizing heat exchange when moving steam-water mixture through porous media

$$\alpha_V / \alpha_{VLO} = 1 + 810x \sqrt{(\rho w)_0 \frac{\nu'}{\sigma} \cdot \frac{1-x}{x}}, \quad (11)$$

where α_V - volumetric heat exchange coefficient at motion of two-phase vapor-liquid flow through the porous material, W/m^{3}K;

α_{VLO} – volumetric heat exchange coefficient inside of the porous material at moving of the liquid at a rate equal to the total rate of the mixture (the amount of heat absorbed by the fluid per unit time per unit volume of the porous body), W/m^{3}K.

$(\rho w)_0 = \dot{m}/F_{II}$ – filtration rate of the mixture (mass flow rate, kg/m^{2}s;

$\dot{m}$ - full mass flow rate of mixture, kg/s;

$F_{cs} = \pi d^2/4$ – cross-sectional area of the channel, m^2;

ν' - coefficient of cinematic viscosity of the fluid on the saturation line, m^2/s;

σ - coefficient of surface tension of the liquid, N/m;

x – mass content of steam in the flow.

To find value of α_{VLO} was used recommended by Kostornov A.G. [10] relationship to calculate the heat transfer inside the porous metal-fiber material when moving through a single-phase coolant.

$$Nu_V = 0{,}007 Re^{1,2} \qquad (12)$$

where $Nu_V = \alpha_V(\beta/\alpha)^2/\lambda_l$, $Re = \dfrac{(\rho w)_0(\beta/\alpha)}{\mu_l}$, index l refers to the parameters of fluid.

As seen from the expression (11) it does not include in explicit form of the porous structure characteristic parameters, such as particle size, or flow resistance coefficients α и β. This makes it possible to use these expressions for virtually any porous materials.

One of the minor flaws of the formula (11) is that, as the author [9] indicates, in the course of the experiments at high steam content occurred thermal nonequilibrium flow. Therefore, the generalization of the experimental data was conducted only for values α_v, corresponding to $x \le 0{,}8$. Application of the formula (11) with steam content greater than 0.8 are not recommended, as this could lead to significant error. Estimation of the value α_v in the interval $x \approx 0{,}8 \div 1{,}0$ recommended exercise by interpolation calculated by (11), values α_v for x = 0.8 and expressions characterizing the convective heat transfer in a porous material with steam coolant flow (x = 1).

$$Nu'' = 0{,}007 Re''^{\,1,2}, \qquad (13)$$

where $Nu'' = \dfrac{h(\beta/\alpha)^2}{\lambda''}$; $Re'' = \dfrac{G\ (\beta/\alpha)}{\mu''}$, (14)

Here Nu″ and Re″ respectively Nusselt number and Reynolds number calculated by the thermal properties of steam at saturation line

$G = (\rho w)_0$ – full mass flow rate of the coolant, kg/m^{2}s.

In calculating the specific heat flux, which is absorbed by the coolant during evaporation in a porous cylindrical channel, we used the expression obtained in [12]

$$q = (\lambda h_V)^{1/2} \frac{I_1(\gamma)}{I_0(\gamma)} \vartheta(1), \qquad (15)$$

where $I_0(\gamma)$ and $I_1(\gamma)$ – modified Bessel functions of the first kind of zero and first order, respectively;

λ – coefficient of thermal conductivity of the porous material. For it's calculation the material of the frame of the wick, the thermal conductivity of liquid and vapor at saturation line have to be taken in to consideration;

h_V - the intensity of the volume of the intraporous heat transfer;

$\gamma^2 = \dfrac{h_V (d/2)^2}{\lambda}$ - parameter characterizing the intensity of the of the intraporous heat exchange;

d – diameter of channel;

$\vartheta = T - t_s$, where T – the temperature of the porous structure, t_s - the coolant temperature at the saturation line;

$\vartheta(1) = T_w - t_s$, - temperature difference of the porous frame and on the cooler inner surface of the wall.

CALCULATION OF HYDRAULIC RESISTANCE AT THE MOTION OF TWO-PHASE VAPOUR-LIQUID FLOW IN SMOOTH-WALL CHANNELS

When calculating the hydraulic resistance at the motion of two-phase vapour-liquid flow in the pipes and channels, the method developed by Lockhart and Martinelli [12] and particularized in [13], is commonly used. The essence of it is that the pressure gradient due to friction in the two-phase flow is usually expressed in terms of coefficients, which are multiplied by the respective gradients in the single-phase flows, i.e

$$\left(\frac{dp}{dz}\right)_{tw.ph.} = \Phi_L^2 \left(\frac{dp}{dz}\right)_L \qquad (16)$$

or $$\left(\frac{dp}{dz}\right)_{tw.ph.} = \Phi_G^2 \left(\frac{dp}{dz}\right)_G, \qquad (17)$$

where $\left(\dfrac{dp}{dz}\right)_{tw.ph.}$ is pressure drop due to friction in the two-phase flow;

x is a coordinate;

$\left(\dfrac{dp}{dz}\right)_L$ and $\left(\dfrac{dp}{dz}\right)_G$ are respectively, the pressure drop for a liquid or gas, if a liquid or gas occupied the entire cross section of the pipe;

Φ_L^2 and Φ_G^2 - empirically determined coefficients;

z is a coordinate.

Lockhart and Martinelli [12] found that the coefficients Φ_L^2 and Φ_G^2 are the function of the parameter X^2, which is determined as follows

$$X^2 = \left(\frac{dp}{dz}\right)_L \Big/ \left(\frac{dp}{dz}\right)_G \quad . \tag{18}$$

Chisholm and Sutherland [14] proposed an analytical expression for the dependences $\Phi^2_{L,G} = f(x)$ in the following form

$$\Phi_L^2 = 1 + \frac{C}{X} + \frac{1}{X^2} \ , \tag{19}$$

$$\Phi_G^2 = 1 + CX + X^2 \ , \tag{20}$$

where $$C = \frac{1}{K}\sqrt{\frac{\rho_L}{\rho_G}} + K\sqrt{\frac{\rho_G}{\rho_L}} \quad . \tag{21}$$

Herein K is the slide factor.

Basing on a simple model, Zivi [15] found that for the vapour-water flow

$$K = (\rho_L/\rho_G)^{1/3} \quad . \tag{22}$$

After the analysis of the correlations (16) - (22) it becomes apparent that the system of equations allows us to calculate the pressure drop in the channels and pipes at the motion of two-phase vapour-liquid flow.

To calculate the parameter $X^2 = \left(\frac{dp}{dz}\right)_L \Big/ \left(\frac{dp}{dz}\right)_G$, we use the correlations that characterize the pressure drop in a single-phase flow at different velocities (Reynolds numbers) of motion of the cooler [16].

In the general case, the pressure drop across the pipe at the motion of a single-phase liquid or gas (vapour) heat carrying agent is calculated as per the formula [16]

$$\Delta P = \xi \cdot \frac{l}{d} \cdot \frac{\rho u_{av}^2}{2} \ , \tag{23}$$

where ξ is the pipe resistance coefficient;

l, d are, correspondingly, the length and the diameter of the pipe, m;

ρ is the density of the liquid (gas), kg/m^3;

u_{av} is the average velocity of liquid along the cross section in the pipe, m/s.

Taking into consideration that the Reynolds number is calculated from the correlation $\mathrm{Re} = \frac{\rho u_{av} d}{\mu'}$, the expression (23) can be transformed into

$$\Delta P = \xi \cdot \frac{l}{d} \cdot \frac{\rho\left(\frac{Re\mu'}{\rho d}\right)^2}{2} \quad . \tag{24}$$

For laminar flow at Reynolds number Re ≤ 2300, the coefficient of resistance is determined from the correlation [16]

$$\xi = 64/Re_o \tag{25}$$

To calculate the coefficients of hydraulic resistance for transitional and turbulent areas of the flow in smooth-wall pipe S. S. Kutateladze correlations were used [17],

$$\xi \approx 6{,}3 \cdot 10^{-4}\ \mathrm{Re}^{0{,}5} \tag{26}$$

Blasius [16]

$$\xi = 0{,}3164\ \mathrm{Re}^{-1/4} \tag{27}$$

and Nikuradze [16]

$$\xi = 0{,}0032 + 0{,}221/\mathrm{Re}^{0{,}237} \tag{28}$$

When calculating values $\left(\frac{dp}{dz}\right)_L$ and $\left(\frac{dp}{dz}\right)_G$ in formulas (16) and (17), the following values of Reynolds numbers have to be used:

$$Re_L = Re_o\,(1 - x) \ , \tag{29}$$

$$Re_G = Re_o\, x\, (\mu'/\mu'') \ , \tag{30}$$

where $\mathrm{Re_o}$ is Reynolds number at the channel inlet;

x is the mass expendable vapour content of the flow;

μ' and μ'' are , correspondingly, coefficients of dynamic viscosity of liquid and vapour at saturation line.

CALCULATION OF HYDRAULIC RESISTANCE IN POROUS CHANNELS WITH HIGH HEAT CONDUCTIVITY AT TWO-PHASE VAPOUR-LIQUID MOTION OF HEAT CARRYING AGENT

Calculation of hydraulic resistance in porous channels with high heat conductivity at two-phase vapour-liquid motion of heat carrying agent will be performed as per the method similar to Lockhart-Martinelli's method [12], [13]. According to this method, which Yu. A. Zeigarnik and I.V. Kalmykov applied to the motion of two-phase vapour-liquid adiabatic flows in porous media [9], [18], the calculation of the frictional resistance of adiabatic two-phase mixture in porous channels is performed as per the formulas:

$$\left(\frac{\Delta P}{\ell}\right)_{tw.ph.\ por.} = (\Delta P/\ell)_L \cdot \Phi_L^2 \quad , \tag{31}$$

or

$$\left(\frac{\Delta P}{\ell}\right)_{tw.ph.\ por.} = (\Delta P/\ell)_G \cdot \Phi_G^2 \ , \tag{32}$$

where $(\Delta P/\ell)_L$ and $(\Delta P/\ell)_G$ are pressure drops at the flow through a porous structure of a liquid phase only in the quantity that the mixture contains, or of steam phase only. These values are calculated as per the equation (33), in which corresponding mass filtration velocities of each phase are used as mass filtration velocities $\rho w = G$.

$$\frac{-dP}{dZ} = \alpha\mu\upsilon G + \beta\upsilon G^2 \tag{33}$$

where α and β –are inertial and viscosity coefficients of a porous material resistance;

μ and υ are dynamic viscosity coefficient and specific volume of liquid;

G is mass flow rate of liquid through a porous material.

According to [12], parameters Φ_L and Φ_G are the function of Martinelli parameter $X = \sqrt{(\Delta P/\ell)_L/(\Delta P/\ell)_G}$. The following formula can be written for X^2 parameter [18] :

$$X^2 = (\frac{1-x}{x})(\frac{\mu'}{\mu''})(\frac{\rho''}{\rho'})\frac{1+(\beta/\alpha)[G(1-x)]/\mu'}{1+(\beta/\alpha)[G\cdot x]/\mu''} =$$

$$= (\frac{1-x}{x})(\frac{\mu'}{\mu''})(\frac{\rho''}{\rho'})\frac{1+Re'}{1+Re''} \quad (34)$$

The connection between parameter X and Φ_L and Φ_G can be expressed analytically [14]:

$$\Phi_L^2 = 1 + C/X + 1/X^2, \quad (35)$$

$$\Phi_G^2 = 1 + CX + X^2. \quad (36)$$

After processing test data, Zeigarnik Yu. A and Kalmykov I.V. [18] concluded that coefficient C is the function of mass filtration velocity $(\rho w)_0 = G$, physical characteristics (ρ' and μ') and hydraulic characteristics of porous structure (coefficients α and β)

$$C = 4{,}0(\frac{\beta/\alpha}{G}\cdot\frac{\rho'}{\mu'})^{0{,}4}. \quad (37)$$

THE ANALYTICAL MODEL FOR CALCULATING THERMO PHYSICAL AND HYDRAULIC PARAMETERS OF TWO-PHASE FLOW UNDER BOUNDARY CONDITIONS OF THE FIRST TYPE

The full description of re-calculation of the original equations from boundary conditions of the second type to the boundary conditions of the first type will include a fairly large amount of material and can be the subject of a separate article. In essence, the method can be summarized as follows. A cylindrical channel is divided into separate 1 mm long sections, within which calculation is performed for fixed values of specific heat flow rate. The specific heat flow rate in the inlet section is calculated as per the known heat hydraulic characteristics. Further, taking into consideration the lateral surface area of the sector, total amount of heat absorbed in this sector is calculated. After that, the increment of steam content at the sector and the value of steam content in the final section of the sector are calculated. Based on average thermo physical properties of the flow at the sector, pressure drop within 1 mm long sector and the power to pump the heat carrying agent within the sector are calculated. Further, based on the existing calculated data, specific heat flow rate in the final section of the sector, the average value of the specific heat flow rate at the sector and the total amount of absorbed heat at the sector on the second iteration step are determined. Calculation within a 1 mm long sector continues as long as the total values of heat absorbed at the sector that were calculated in two consecutive iteration steps do not coincide with the desired accuracy. Further, the calculation is made for the next sector. The initial calculated values of thermo physical characteristics for the subsequent sector are to be taken equal to the calculated values in the final section of the previous sector. Calculation of the length of the evaporation channel is performed until the value of steam content takes the value of 1. It should be noted that with the same mass flow rates of cooler, the total quantity of heat that is used for evaporation of the flow in both cases are the same.

THE RESULTS OF RESEARCHES

As a result of executed researches the calculations of efficiency of cylindrical porous channels during evaporation of a water flow (once-through steam generator) were carried out. A smooth-wall pipe was used as a reference surface for comparison.

As the calculation base were taken following regime-design parameters: temperature of the liquid at the saturation line at the channel inlet: $T_{so(in)}$=260 ^{o}C, 270 ^{o}C, 280 ^{o}C, 290 ^{o}C, 300 ^{o}C; difference between temperature of the channel's wall and a liquid inlet temperature $\Delta T = T_w - T_{in}$ = 1, 2, 3, 4, and 5 ^{0}C; the Reynolds number at the channel inlet Re_0 = 100, 200, 500, 1000, 2000, 2300; porosity of a channel θ = 0,5, 0,6, 0,7, 0,8, 0,9; the porous material - copper felt with diameter of fibers 200 microns mkm; diameter of a channel $d = 6\cdot10^{-3}$, $1\cdot10^{-2}$, $2\cdot10^{-2}$, $5\cdot10^{-2}$ m. Total was calculated 3000 regime-design points that characterize the structural parameters of the model. Example (fragment) of calculation's results for $T_{so(in)}$ = 270 ^{0}C, d = 0,006 m, $\Delta T = T_w - T_{in}$=4 ^{0}C are shown in Table. 1-7.

Table 1 The length of the smooth wall vapor generator, l_{sm},m

	Reynolds number Re_0					
	100	200	500	1000	2000	2300
Length l, m	28,2	56,4	139,7	265,4	445,2	479,3

Table 2 The length of the porous vapor generator, l_p , m

Poro-sity, Θ	Reynolds number Re_0					
	100	200	500	1000	2000	2300
0,9	17.56	16.37	16.45	16.16	14.73	14.28
0,8	16.1	13.27	12.17	11.49	10.12	9.75
0,7	16.59	12.42	10.13	8.99	7.52	7.18
0,6	17.54	12.19	8.70	7.11	5.58	5.27
0,5	18.0	11.78	7.32	5.42	3.94	3.66

Table 3 Geometric efficiency coefficient $k_F = l_{sm}/l_p = f(\Theta, Re)$

Poro-sity ,Θ	Reynolds number Re_0					
	100	200	500	1000	2000	2300
0,9	1.61	3.44	8.5	16.42	30.23	33.56
0,8	1.75	4.25	11.49	23.1	43.98	49.14
0,7	1.7	4.54	13.79	29.51	59.18	66.72
0,6	1.61	4.62	16.07	37.35	79.83	91.04
0,5	1.57	4.79	19.09	49.01	113.1	131.0

Table 4 Pressure drop in smooth-wall channel ΔP_{sm}, N/m^2

	Reynolds number Re_0					
	100	200	500	1000	2000	2300
ΔP_{sm}, N/m^2	99,51	397,8	2,5·10^3	12,67·10^3	57,5·10^3	74,7·10^3

Table 5 Pressure drop in porous channel ΔP_p, N/m^2

ΔP_p, N/m^2	Reynolds number Re_0					
	100	200	500	1000	2000	2300
0,9	22,23·10^3	38,06·10^3	98,39·10^3	226,5·10^3	537,51·10^3	638,85·10^3
0,8	34,14·10^3	52,37·10^3	127,1·10^3	285,9·10^3	663,04·10^3	784,71·10^3
0,7	63,75·10^3	89,73·10^3	198,9·10^3	426,4·10^3	947,19·10^3	1113,9·10^3
0,6	135,4·10^3	177,4·10^3	352,3·10^3	705,4·10^3	1496,2·10^3	1749,2·10^3
0,5	310,8·10^3	391,4·10^3	694,0·10^3	1289,8·10^3	2639,6·10^3	3079,4·10^3

Table 6 The ratio Q / N for smooth-wall vapor generator

	Reynolds number Re_0					
	100	200	500	1000	2000	2300
Q/N	2,33·10^{10}	5,82·10^9	9,1·10^8	1,64·10^8	3,64·10^7	2,83·10^7

Table 7 The ratio Q / N for porous vapor generator

Poro-sity, Θ	Reynolds number Re_0					
	100	200	500	1000	2000	2300
0,9	1,03·10^8	5,78·10^7	2,10·10^7	8,71·10^6	3,50·10^6	2,91·10^6
0,8	6,77·10^7	4,2·10^7	1,62·10^7	6,9·10^6	2,82·10^6	2,35·10^6
0,7	3,65·10^7	2,46·10^7	1,04·10^7	4,64·10^6	1,95·10^6	1,62·10^6
0,6	1,75·10^7	1,26·10^7	5,91·10^6	2,79·10^6	1,17·10^6	9,63·10^5
0,5	7,73·10^6	5,78·10^6	2,99·10^6	1,46·10^6	5,61·10^5	4,37·10^5

Graphs of geometric efficiency coefficient $K_f=l_{sm}/l_p$ on porosity θ, Reynolds number Re of flow at inlet, the channel's diameter d, the temperature difference $\Delta T= T_w-T_{in}$ and the fluid temperature on the saturation line at the inlet channel $T_{so(in)}$, built in the Excel application programme, for a set of design parameters θ = 0.9; Re = 2000; d = 0,006 m; T_w = 274 ^{0}C; T_{in} = 270 ^{0}C are shown in Fig. 1-5.

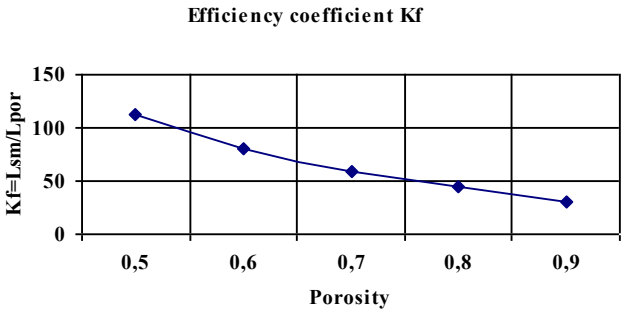

Figure 1 The dependence of the geometrical efficiency coefficient on the porosity of the channel

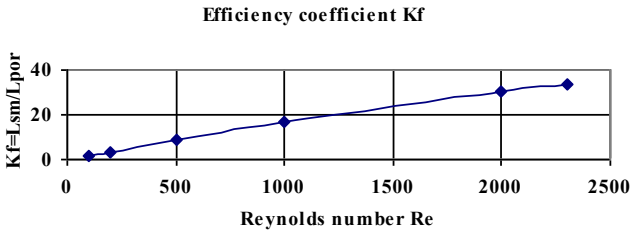

Figure 2 The dependence of the geometrical efficiency coefficient on the Reynolds number

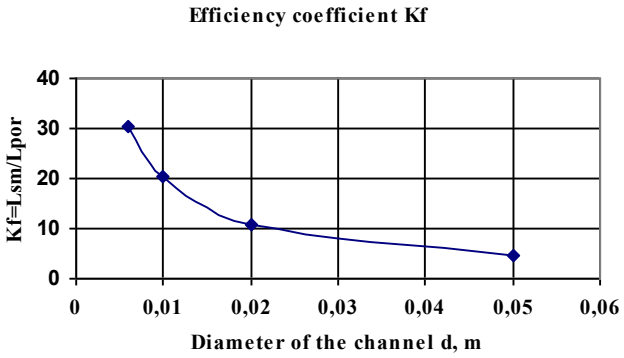

Figure 3 The dependence of the geometrical efficiency coefficient on the diameter of the channel

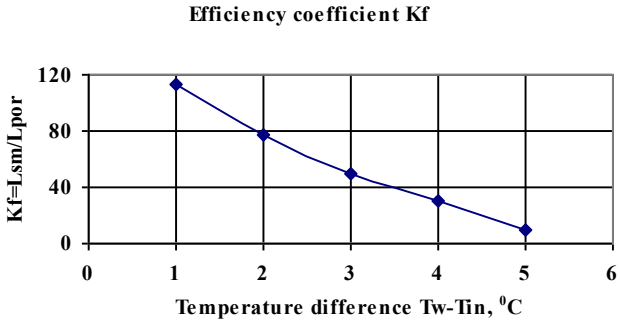

Figure 4 The dependence of the geometrical efficiency coefficient on the temperature difference $\Delta T= T_{in}-T_w$, ^{0}C

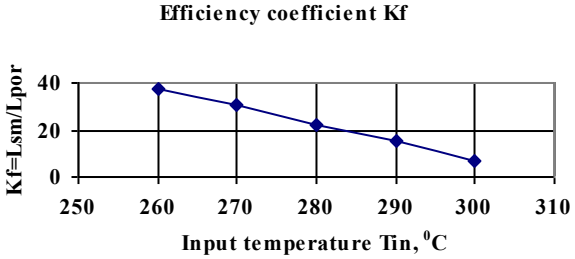

Figure 5 The dependence of the geometrical efficiency coefficient on the fluid temperature on the saturation line at the inlet channel $T_{in(so)}$, ^{0}C

CONCLUSIONS

1. At laminar regime motion of evaporating liquid and for the conditions of equal mass flow rate and the same diameter of channels it is possible to achieve a significant reduction (up to several tens of times and more) length of porous once-through steam generator compared to the length of a smooth - wall once-through steam generator.

2. At the given set of calculating parameters and in the context of significantly shorter length of porous once-through steam generators it is not possible to reach reduction of a pressure drop in them and accordingly power reduction to pump coolant in comparison with smooth-wall once-through steam generators.

3. The dependences of the geometrical efficiency factor of the porous steam generator on the porosity, the channel diameter, the temperature difference and the saturation temperature (pressure) at the channel inlet are inversely proportional.

4. Dependence of the geometric efficiency factor of the porous steam generator on the Reynolds number of flow at the channel inlet is directly proportional.

5.Performed calculations demonstrate necessity of realization of further researches.

REFERENCES

[1] Prisnyakov V.F., Lukisha A. P. Computation of efficiency of porous heat exchangers with high heat conductivity applied in the structure of power plants *Proceedings of the 6th International Conference on Heat Transfer, Fluid Mechanics and Thermo-dynamics. (HEFAT 2008)*– 30 June to 2 July 2008, Pretoria, South Africa Paper number: PV2.

[2] Lukisha A. P., Prisnyakov V. F. The efficiency of round channels fitted with porous, highly heat-conducting insert in a laminar fluid coolant flow at boundary conditions of the third kind *International Journal of Heat and Mass Transfer*, № 53, 2010,. pp.2469-2476.

[3] Lukisha, A. P. Calculation of efficiency of porous channels of round cross section at a transition regime of a motion of a liquid coolant in compared canals with smooth wall and under the boundary conditions of the first type, *Proceedings of the VIII Minsk International Seminar on Heat Pipes, Heat Pumps, Refrigerators, Power Sources*, Vol. 2, Minsk, Belarus, 12–15 September, 2011, pp. 35-42.

[4] Lukisha A. P. Calculation of the efficiency of circular porous channels by the modified Guhman method, *Journal of Engineering Physics and Thermophysics. Springer, New York*, Vol. 85, No 6, 2012, pp. 1266–1277.

[5] Handbook of thermal-hydraulic calculation (nuclear reactors, heat exchangers, steam generators). *Edited by. P. L. Kirilov*, M.: Energoatomizdat, 1990, 360 pp. (rus.)

[6] Heat transfer in nuclear power plants. *Edited by B.S. Petuhov*, M.: Energoatomizdat, 1986, 472 pp. (rus.)

[7] Kutepov, A.M., Sterman L.S., Stjushin N.G. Hydrodynamics and heat transfer in steam generation, M.:Vysshaja skola, 1986, 448 pp.(rus.)

[8] Miropolsky, Z.L. Heat transfer to the superheated steam with the input and output of heat, *Teploenergetika*, 1975, № 3, p. 75.(rus.)

[9] Kalmykov I.V. Heat transfer and hydrodynamics at motion of the steam-liquid flow in porous media, *The dissertation on competition for the degree of candidate of technical sciences*, M.: 1987, 224 pp. (rus.)

[10] Poljaev V.M., Majorov V.A., Vasiliev L.L. Hydrodynamics and heat transfer in porous design elements of aircraft, M.: Mashinostoenije, 1988, 168 pp. (rus.)

[11] Lukisha A.P. Heat exchange at evaporating of flow in the cylindrical porous channel, *Visnyk Dnipropetrvskogo universitety*, 2014, V. 22, № 3, Series mechanics, Issue 16, V.1, pp. 107-114. (rus.)

[12] Lockart R. W., Martinelli R.C. Proposed correlation of data for isothermal two-phase, two-component flow in pipes, *Chemical Engineering Progress*, 1949, Vol. 45(1), pp. 39-48.

[13] Two-phase flow and heat transfer. *Edited by D. Batterworth and G.F. Hewwit*, Oxford University Press, 1977, 326 pp.

[14] Chisholm, D., L. A. Sutherland L.A. Prediction of pressure gradient in pipeline system during two-phase flow / D. Chisholm , L. A. Sutherland, *Proceedings of the Institute of Mechanical Engineers*, 1969, Vol. 184, Pt. 3c, pp. 24-32.

[15] Zivi S. M. Estimation of steady state steam void fraction by means of the principle of minimum entropy production, *Yournal Heat Transfer*, 1964, 86, pp. 247-252.

[16] Dejch M.E., A.E. Zarjankin A.E. Hydrodynamics: A manual for highschools, M.:Energoatomizdat, 1984, 384 pp.(rus.)

[17] Kutateladze, S. S. Heat transfer and flow resistance: A Reference Guide, M.: Energoatomizdat, 1990, 367 pp. (rus.)

[18] Zeigarnik Yu. A., Kalmykov I.V. Experimental study of the hydraulic resistance of porous structures at adiabatic motion steam-water mixture, *Teplofizika vysokih temperatur*, 1985, T. 23, № 5, pp. 934-940.(rus.)

[19] N. B. Vargaftik Handbook on thermophysical properties of gases and liquids, M.: Nauka, 1972, 720 pp.(rus.)

NUMERICAL STUDY OF PUMP-JET PERFORMANCE WITH A RING ROTOR USING AN UNSTRUCTURED MESH TECHNIQUE

Ahn S.J. and Kwon O.J.*
Department of Aerospace Engineering,
Korea Advanced Institute of Science and Technology,
Daejeon, 305-701,
Korea,
E-mail: ojkwon@kaist.ac.kr

ABSTRACT

In the present study, the hydrodynamic characteristics of a pump-jet have been numerically investigated using an incompressible RANS flow solver based on pseudo-compressibility. For this purpose, a vertex-centered finite-volume method on unstructured meshes was utilized. For the unsteady time integration, a dual-time stepping method and the Gauss-Seidel iteration were used. An unstructured overset mesh technique was adopted to treat the relative motion between the rotor and the main body of the pump-jet. To validate the flow solver, the calculations were initially made for the High-Reynolds-Number-Pump (HIREP) configuration at several advancing ratios. To investigate the effect of the ring on the flow characteristics and the propulsion performance of the pump-jet, additional calculations were made for the HIREP configuration installed with the circumferential ring at the rotor blade tip, and the results were compared with those of the original HIREP configuration. It was found that the addition of the ring at the blade tip helps reducing the tip vortex strength, which might be beneficial to suppress the formation of water vapor. With the addition of the ring, the efficiency of the pump-jet is well maintained, even though the blade loading is slight reduced.

INTRODUCTION

Recently the pump-jets have been widely used as an alternative propulsion system of modern underwater vehicles. Pump-jets are typically composed of rotating rotor, stator, and duct. They usually exhibit relatively high propulsive efficiency, and maintain good balance of the rotating moment on the body. The duct surrounding the rotor helps prevent the noise radiating outside. However, the flow field inside the pump-jets are very complicated, accompanying those features, such as the interaction between the rotor and the stator, horseshoe vortex at the hub, rotor blade tip leakage flow, and flow separation. Therefore, physical understanding of the hydrodynamic characteristics is important to design pump-jets with an improved performance.

In the past, several researches were carried out regarding the performance and the flow characteristics of the pump-jets. Furuya and Chiang [1] presented a design methodology and various related issues about the pump-jets. Zierke et al. [2] conducted an experimental study of the High-Reynolds-Number-Pump (HIREP) for physically understanding the complex flow fields and for acquiring a data base for the validation of numerical predictions. Several other researchers, such as Dreyer and Zierke [3], Yang [4], Yu et al.[5], and Lee et al. [6], have also conducted numerical simulations of the HIREP configuration to validate their RANS flow solvers. Vosper and Brown [7] reported the cases where pump-jets are adopted as a submarine propulsive system. Das et al. [8] presented the computational fluid dynamics (CFD) validations of the drag force of an axisymmetric underwater body with a pump-jet using a commercial software package. Suryanarayana et al. [9] presented a technique for experimentally evaluating pump-jet propulsors. Ivanell [10] also used a commercial software package and performed CFD simulations of a torpedo with a pump-jet, and the calculated results were compared with experiments.

In spite of the favorable features of the pump-jets as a propulsive system for underwater vehicles, the formation of vortex cavitation at the rotor blade tip and along the tip clearance gap is usually unavoidable. Cavitation on marine propulsors is an undesirable phenomenon that causes asymmetric load, performance breakdown, vibration, noise and erosion. In order to remedy the problems related to cavitation, and to further improve the performance of pump-jet propulsors, the concept of pump jet with ring rotors was suggested by Lee et al. [11]. In the proposed pump-jet configuration, a circumferential ring is attached at the tip of the rotor blades, and the blades are interconnected by the ring. The ring presumably helps prevent the generation of the strong tip vortex, and thus delays the cavitation inception. However, the effect of the ring rotor on the overall flow characteristics and the performance of the pump-jet propulsor has not been assessed and validated in detail yet for practical applications.

In the present study, the propulsion performance and the flow characteristics of a pump-jet with ring rotor was numerically evaluated using an incompressible Navier-Stokes flow solver on unstructured meshes. For this purpose, the HIREP configuration tested by Zierke et al. [2] was adopted, and the original rotor configuration was modified by attaching a ring at the rotor blade tip. To validate the flow solver, calculations were initially made for the original HIREP configuration, and the predicted results were compared with the experimental data. Then additional calculations were made for the configuration with the ring rotor, and the results were

compared with those of the original configuration without ring, and the effect of the ring was investigated.

NUMERICAL METHOD

In the present calculations, an unstructured mesh CFD flow solver [12] was used to simulate the time-accurate viscous flows around the pump-jet with and without the ring. The fluid motion was modeled by using the incompressible Reynolds averaged Navier-Stokes equations in conjunction with an artificial compressibility method.

The governing equations were discretized using a vertex-centered finite-volume method. The inviscid flux terms were computed using Roe's flux-difference splitting scheme, while the viscous flux terms were computed by adopting a modified central difference method. The implicit time integration was performed based on a linearized Euler backward difference scheme of second order. The Spalart-Allmaras one-equation turbulence model [13] was used to estimate the eddy viscosity, and the flow was assumed to be fully turbulent. An unstructured overset mesh technique [14] was adopted for the simulation of the relative motion between the rotor and the other components of the pump-jet in a fully unsteady manner.

To reduce the large computational time, a parallel algorithm based on a domain decomposition strategy was adopted. The load balancing between the processors was achieved by partitioning the global computational domain into local subdomains using the MeTiS libraries. The Message Passing Interface was used to transfer the flow variables across the subdomain boundaries. All calculations were performed on PC-based Linux clusters.

PUMP-JET CONFIGURATION

The basic pump-jet configuration adopted in the present study is the High-Reynolds-Number-Pump (HIREP) configuration. The experimental test was made by Zierke et al. [2] at the Garfield Thomas water tunnel at the Pennsylvania State University, and a large quantity of data was acquired for the validation of numerical prediction tools. The HIREP configuration consists of a row of 13 inlet guide vanes (IGV), a row of seven rotor blades with significant circumferential blade skew, and a casing. The inlet guide vanes have a chord length of 17.53cm and a solidity ranging from 1.36 at the hub to 0.68 at the tip. The rotor blades have a chord length of 28.50cm and a solidity of 1.19 at the hub, and a chord length of 26.64cm and a solidity of 0.56 at the tip. The diameters of the hub and the casing are 0.53m and 1.07m, respectively. The gap clearance between the casing endwall and the rotor blade tip is 3.3mm.

At the design operating condition, the inlet flow velocity is 10.63m/s, and the rotor blades rotate at 260rpm with a blade tip speed of 14.52m/sec. The Reynolds number based on the chord length of the IGV and the inlet flow velocity is 2.3milions. Even though most of the data were obtained for the design operating condition, two off-design conditions of 236rpm and 290rpm were also tested in the experiment. The measured data were given in terms of the time-averaged static pressure on both the IGV and the rotor blade surface, the circumferentially averaged velocity components inside the flow field, and the integrated thrust and torque of the rotor.

To investigate the effect of the ring on the pump-jet performance, a circumferential ring was attached at the rotor blade tip of the original HIREP configuration. The ring covers the whole chord length of the rotor blade tip, and the leading edge and the trailing edge of the sectional geometry of the ring are semicircular. The thickness of the ring is 3.33% of the span of the rotor blade. The HIREP configurations with and without the ring are presented in Fig. 1.

COMPUTATIONAL MESH & BOUNDARY CONDITIONS

The computational meshes were constructed for both pump-jet configurations with and without the ring using an unstructured mesh topology. For the present overset mesh topology to handle the relative motion between the IGV and the rotor, the meshes are composed of multiple independent mesh blocks. The main block mesh represents the complete computational domain, including the IGV, and the sub block mesh covers the rotating rotor. To resolve the boundary layer accurately on surface of the IGV, casing end wall and the rotor, 30 layers of prismatic cells were packed in the direction normal to the surface. The grid spacing of the first layer was selected such that the y^+ coordinate is approximately one. The remainder of the computational domain was populated by using tetrahedral elements.

Figure 2 shows the computational meshes for both configurations. The main block meshes contain 4,730,688 nodes and 14,977,734 cells. The sub block meshes around the rotor contain 3,749,819 nodes and 11,688,808 cells for the configuration without the ring, and 4,824,147 nodes and 13,618,568 cells with the ring. The parallel calculations were made using 180 processors.

At the solid wall, the no-slip boundary condition was applied for viscous flow such that all components of velocity and the normal gradient of static pressure vanish. At the inlet boundary plane, the velocity components were specified and the static pressure was extrapolated from the interior. At the outlet boundary, the static pressure was specified, and the velocity components were extrapolated from the interior.

VARIDATION FOR CONFIGURATION WITHOUT RING

For the validation of the present flow solver, simulations of the original configuration without the ring were initially performed, and the results were compared with the experiment at the design condition.

The time-averaged static pressure coefficient distributions at five spanwise locations of the IGV are compared with the experimental data in Fig. 3. The static pressure coefficient is defined as

$$C_P = \frac{P - P_{ref}}{\frac{1}{2}\rho U_{tip}^2} \tag{1}$$

where P is the static pressure, P_{ref} is the averaged static pressure at the inlet plane, and U_{tip} is the velocity of the rotor blade tip. It is shown that good agreement was obtained between the present calculation and the experiment at all spanwise

locations.

The circumferentially-averaged velocity components are compared with the experimental data in Fig. 4. The measuring plane is at 49.7% chord axially downstream of the IGV tailing edge. Each velocity component was normalized by the rotor blade tip velocity. It is shown that the agreement between the measurement and the computation is good for all velocity components. The boundary layers were also well captured at the hub and at the casing endwall.

Figure 5 shows the time-averaged static pressure coefficient at the five spanwise locations of the rotor blade. Again, the agreement between the predicted results and the experimental data is good.

The circumferentially-averaged velocity components at the plane 32.2% chord axially downstream of the trailing edge of the rotor blades are compared with the experimental data in Fig. 6. Near the hub surface, while the axial velocity is decreased, the tangential velocity is increased due to the viscous effect on the rotating hub. Near the casing endwall, the axial velocity is decreased, and the magnitude of the tangential velocity is decreased due to the effect of the tip vortex. The agreement between the computation and the experiment is reasonable for all velocity components.

Figure 7 shows the torque and thrust coefficients in terms of the flow coefficient, which is defined as the ratio of the inlet velocity and the rotor blade tip velocity. In this definition, the flow coefficients are a design value of 0.74 and off-design values of 0.66 and 0.81. The thrust and torque coefficients are defined as

$$K_T = \frac{T}{\rho n^2 D_{tip}^4} \tag{2}$$

$$K_Q = \frac{Q}{\rho n^2 D_{tip}^5} \tag{3}$$

where T and Q are the thrust and the torque, respectively, ρ is the density of the water, n is the revolutions per second, and D_{tip} is the rotor blade diameter. Good agreement was obtained between the present calculation and the experiment.

EFFECT OF RING

To investigate the hydrodynamic characteristics of the pump-jet with a ring rotor, the results for the configuration with ring were compared with those of the configuration without ring.

Figure 8 shows the flow visualization near the gap clearance between the rotor blade tip and the casing endwall. The tip vortex is formed and shedded from the pressure side to the suction side on the configuration without ring. On the other hand, the ring attached at rotor blade tip helps prevents the generation of tip vortex on the configuration with ring, and the tangential velocity near the rotor blade tip is increased by the rotating ring.

Figure 9 shows instantaneous axial velocity contours at a sectional plane of 50% chord of the rotor blades. Because the flow passage for the configuration with ring is decreased by the attached ring, the flow near the rotor blades is accelerated so as to conserve the mass flow. It is expected that the accelerated velocity reduces the effective angle of attack of the rotor blades, and affects the thrust of the rotor blades.

Circumferentially averaged velocity components on the plane of 49.7% chord axially downstream of the IGV trailing edge are compared for two configurations in Fig. 10. Two results are almost same. It means that rotor blades surrounded ring don't affect this region.

The circumferentially-averaged velocity components on the plane of 32.2% chord axially downstream of the rotor tip tailing edge are compared in Fig. 11. While the axial velocity patterns are almost same, the tangential velocity shows different phenomenon. Above 90% span, the magnitude of the tangential velocity for the configuration without ring is increased by the tip vortex, and the magnitude of the tangential velocity for the configuration with ring is decreased in the opposite direction due to the rotating ring.

The time-averaged static pressure coefficients on the IGV and the rotor blade surfaces are shown in Figs. 12 and 13. The static pressure on the IGV surface is almost same, regardless of the existence of the ring. On the other hand, the static pressure on the rotor blade surface for the configuration with ring is lower than the other, except at the leading edge of the suction side. Especially, at 90% span, the static pressure on the pressure side of the rotor blade for the configuration with ring is significantly lower than the other. This is presumably due to the increased velocity by the rounded ring section.

The time-averaged thrust distribution on the rotor blade is shown in Fig. 14. The thrust on the blade of the configuration with ring is decreased at all spanwise locations, and the decreasing rate gets larger at the rotor blade tip.

The thrust and torque coefficients at several conditions of the advancing ratio are shown in Fig. 15. It is shown that relatively small thrust is generated for the configuration with ring at all advancing ratios. However, the torque is also decreased, and the efficiency, defined by the ratio of thrust to torque, is maintained.

CONCLUSIONS

In the present study, numerical simulations were carried out to investigate the propulsion performance and the flow characteristics of the pump-jet with a ring rotor by using an unstructured mesh Navier-Stokes flow solver. For this purpose, the HIREP configuration was adopted for the simulations, and the original rotor configuration was modified by attaching a ring at the rotor blade tip.

To validate the flow solver, calculations were initially made for the original HIREP configuration, and the predicted results were compared with the experimental data. Good agreements were obtained for the static pressure coefficients on the blades of the IGV and the rotor, for the velocity distributions behind the IGV and the rotor, and for the rotor blade loading.

Then, additional calculations were made for the configuration with ring, and the results were compared with those of the configuration without ring, and the effect of the ring was examined. It was found that addition of the ring at the blade tip helps reducing the tip vortex strength, and the effect might be beneficial to suppress the formation of water vapor. With the addition of the ring, the efficiency of the pump-jet is well maintained, even though the blade loading is slight reduced.

ACKNOWLEDGEMENT

The authors also would like to acknowledge the support from the NRF of Korea, Grant No. 2009-0083510, funded by the Korean government MSIP through the Multi-phenomena CFD Engineering Research Center.

REFERENCES

[1] Furuya, O., Chiang, W. L., 1988, A new pumpjet design theory. DTIC Report No. N00014-85-C-0050, 30 June.

[2] Zierke, W. C., Straka, W. A., Taylor, P. D., 1993, An experimental investigation of the flow through an axial-flow pump. Journal of Fluids Engineering 117(3), 485-490.

[3] Dreyer, J. J., Zierke, W. C., 1994, Solution of the averaged-passage equations for the incompressible flow through multiple-blade-row turbomachinery. The Pennsylvania State University, Applied Research Laboratory Technical Report No. TR 94-05.

[4] Yang, C, I., 1995, A simulation of viscous incompressible flow through a multiple-blade-row turbomachinery with a high-resolution upwind finite-differencing scheme. Numerical Simulation in Turbomachinery, ASME FED 227, 11-18.

[5] Yu, W. S., Lakshminarayana, B., Thompson, D. E., 1996, Computation of three-dimensional viscous flow in high Reynolds Number Pump Guide Vane. Journal of Fluids Engineering 118(3), 698-705.

[6] Lee, Y. T., Hah, C., Loellbach, J., 1996, Flow analyses in a single-stage propulsion pump. Journal of Turbomachinery 118(2), 240-248.

[7] Vosfer, P.L., Brown, A. J., 1996, Pumpjet propulsion – a british splendid achievement. Journal of Naval Engineering 36(2).

[8] Das, H. N., Jayakumar, P., Saji, V. F., 2006. CFD examination of interaction of flow on high speed submerged body with pump-jet propulsor. 5th International Conference on High Performance Marine Vehicles, Australia, 8-10 Nov.

[9] Suryanarayana, Ch., Satyanarayana, B., Ramji, K.., Saiju, A., 2010, Experimental evaluation of pumpjet propulsor for an axisymmetric body in wind tunnel. International Journal of Naval Architecture and Ocean Engineering 2(1), 24-33.

[10] Ivanell, S., 2011, Hydrodynamic simulation of a torpedo with pumpjet propulsion system. Master thesis, Royal Institute of Technology, Stockholm, Sweden.

[11] Lee, H. K., Park, E. D., Shin, K. K., Kim, C. K., Lee, K. C., 2004, Ring rotor-type pump-jet propulsion device of underwater moving mass. Korean Patent, Publication Number : 1020040026906.

[12] Kang, H. J., Kwon, O. J., 2002, Unstructured mesh Navier-Stokes calculations of the flow field of a helicopter rotor in hover. Journal of American Helicopter Society 47(2), 90-99.

[13] Spalart, P.R., Allmaras, S.R., 1992, A one-equation turbulence model for aerodynamic flows. AIAA Paper 92-0439, Jan.

[14] Jung, M. S., Kwon, O. J., 2007, A parallel unstructured hybrid overset mesh technique for unsteady viscous flow simulations. International Conference on Parallel Computational Fluid Dynamics, Antalya, Turkey.

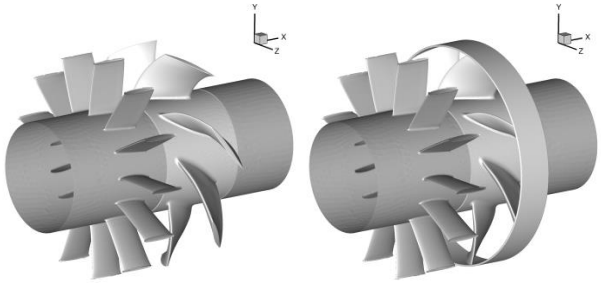

(a) Without ring (b) With ring

Figure 1 Geometry of the HIREP configurations.

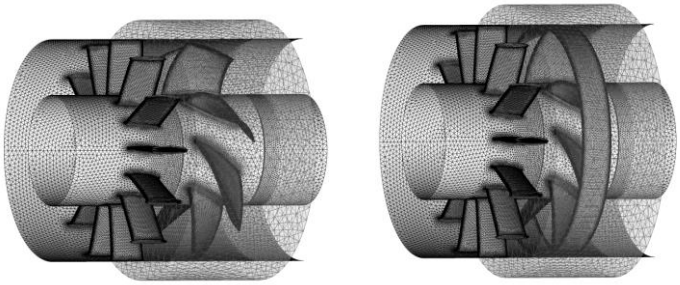

(a)Without ring (b) With ring

Figure 2 Computational meshes for the HIREP configurations.

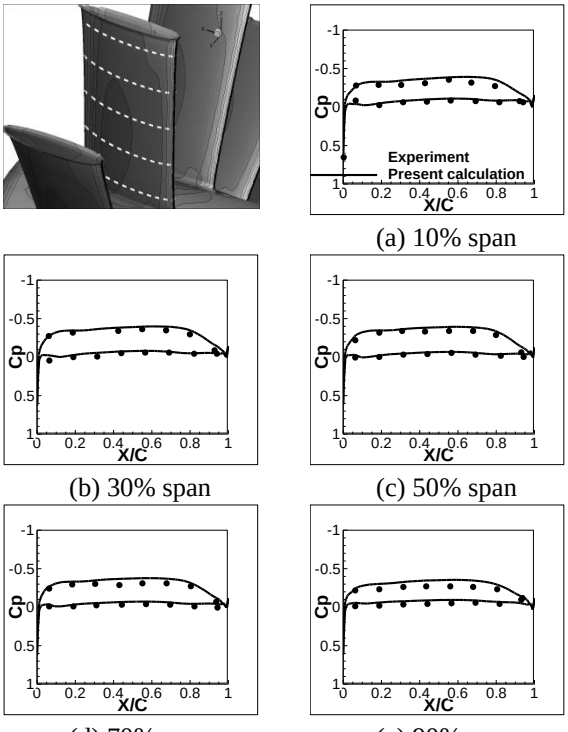

(a) 10% span

(b) 30% span (c) 50% span

(d) 70% span (e) 90% span

Figure 3 Pressure coefficient distribution at selected spanwise sections of the IGV surface.

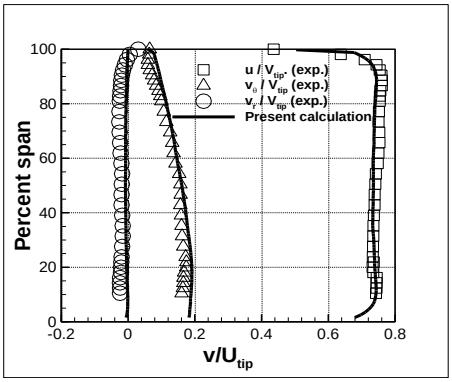

Figure 4 Circumferentially averaged velocity components at 49.7% chord downstream of the IGV trailing edge.

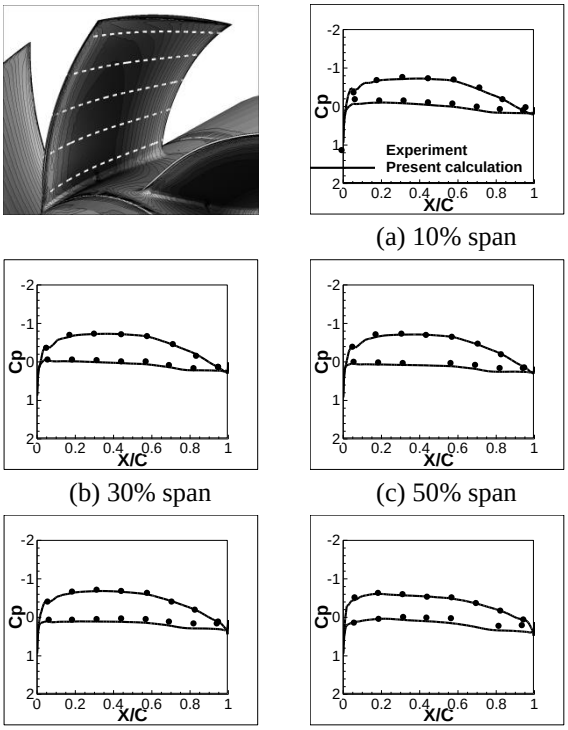

(a) 10% span

(b) 30% span (c) 50% span

(d) 70% span (e) 90% span

Figure 5 Pressure coefficient on the rotor blade surface.

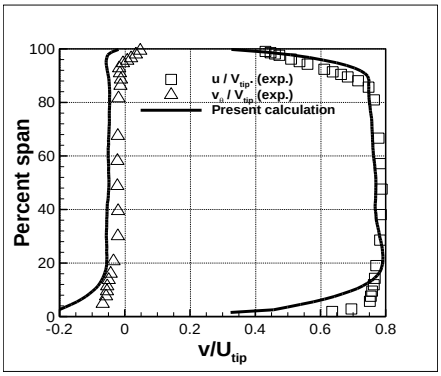

Figure 6 Circumferentially averaged velocity components at 32.2% chord downstream of the rotor trailing edge.

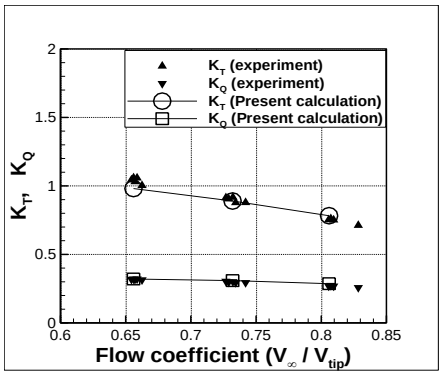

Figure 7 Thrust and torque coefficient at different flow coefficients.

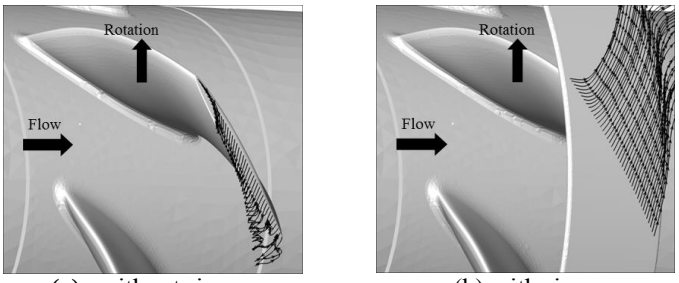

(a) without ring (b) with ring

Figure 8 Streamlines at gap clearance between the rotor blades and casing endwall.

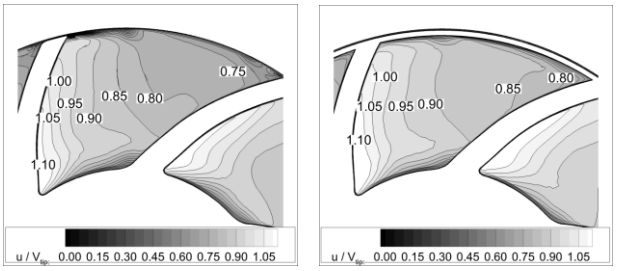

(a) without ring (b) with ring

Figure 9 Axial velocity contours on a sectional plane of 50% chord of the rotor.

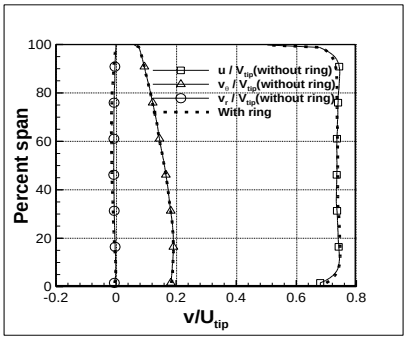

Figure 10 Circumferentially averaged velocity components at 49.7% chord downstream of the IGV trailing edge.

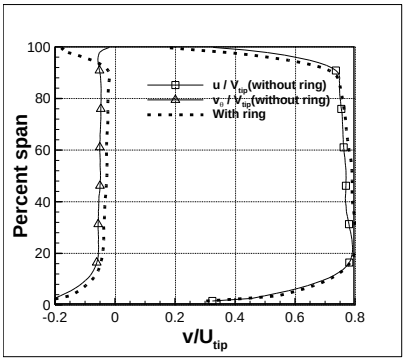

Figure 11 Circumferentially averaged velocity components at 32.2% chord downstream of the rotor trailing edge.

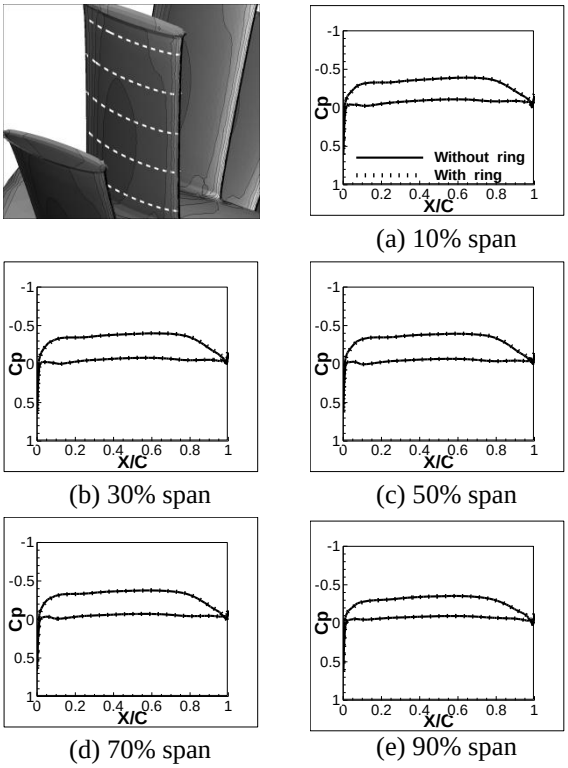

(a) 10% span (b) 30% span (c) 50% span (d) 70% span (e) 90% span

Figure 12 Pressure coefficient on the IGV blade surface.

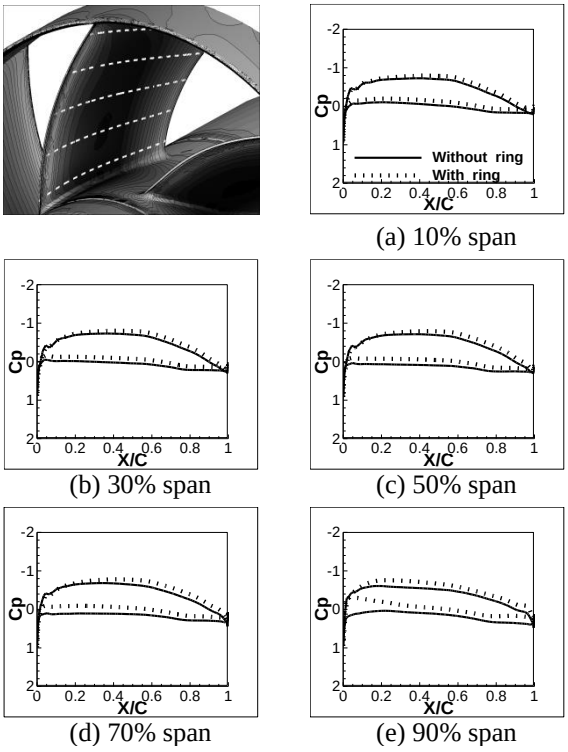

(a) 10% span (b) 30% span (c) 50% span (d) 70% span (e) 90% span

Figure 13 Pressure coefficient on the rotor blade surface.

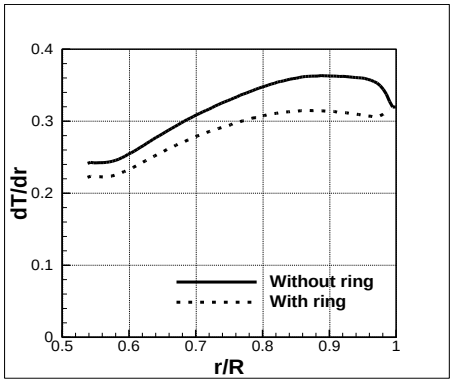

Figure 14 Time-averaged spanwise thrust distribution on the rotor blade.

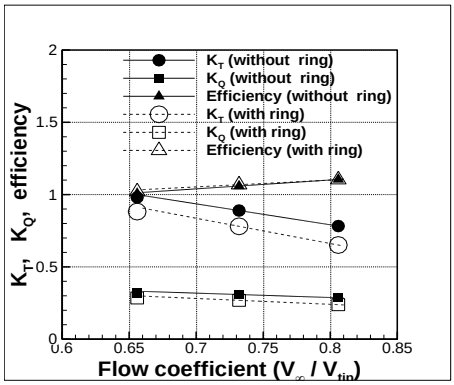

Figure 15 Thrust and torque coefficient at different flow coefficients.

FLAT PLATE BOUNDARY LAYER UNDER NEGATIVE PRESSURE GRADIENT

Antoš P.*, Jonáš P., Procházka P., Skála V.
*Author for correspondence
Institute of Thermomechanics, Academy of Sciences of the Czech Republic,
Dolejškova 5, 182 00 Prague, Czech Republic,
Europe,
E-mail: antos@it.cas.cz

ABSTRACT

Preliminary results of experimental investigation of the boundary layer in decelerating flow are presented. The decelerating flow was simulated in the closed circuit wind tunnel 0.9 m × 0.5 m at IT AS CR. Characteristics inside the boundary layer under negative pressure gradient were studied by means of constant temperature anemometer. The free stream turbulence was risen up by square mesh plane grid. The details of experimental settings and measurement procedures are described. The distributions of the shape factor and the skin friction coefficient of the boundary layer are presented.

INTRODUCTION

Regions with decelerating flow frequently occur in industrial machinery flows. Thus understanding the effect of an adverse pressure gradient on the by-pass transition seems very important. Experimental investigation of the transition in zero pressure gradient boundary layers has been done for many years at IT AS CR. The results and conclusions were presented in e.g. Antoš *at al.* (2014). A diffuser has been placed in the test section in order to extend the boundary layer research on decelerated flow. The experiments were carried out in the closed type wind tunnel and the investigated boundary layers were developing on the smooth flat plate. In fig. 1, the scheme of the wind tunnel setup is shown and orthogonal coordinate system is introduced.

The wind tunnel has a cross section of 0.9 m x 0.5 m. The length of a flat plate was of 2.65 m. The flat plate was made of laminated wood board and the surface was aerodynamically smooth. The streamwise pressure gradient is imposed on the flat plate boundary layer by a confusor/diffuser body fastened to the upper wall. The flow acceleration begins about 1.2 m upstream the flat plate. The deceleration starts at a leading edge (x=0) where the flow velocity is U_0 = 10 m/s. The plane diffuser has a length of 1.4 m and opening angle is 11°. It was checked carefully that there was no flow separation on the deflected wall.

NOMENCLATURE

x, y	[m]	Cartesian coordinates
u, v	[m/s]	fluctuations of fluid velocity in direction x, y
U_e	[m/s]	free-stream velocity
U_0	[m/s]	incoming free-stream velocity at x=0
Iu_e	[-]	free-stream intensity of turbulence
K	[-]	dimensionless pressure gradient parameter
τ_w	[Pa]	wall shear stress
ν	[m^2/s]	kinematic viscosity
δ_{99}	[m]	customary boundary layer thickness
δ_1	[m]	displacement thickness
δ_2	[m]	momentum thickness
H_{12}	[-]	shape factor
Re_2	[-]	Reynolds number based on a momentum thickness
C_f	[-]	skin friction coefficient
C_{fBl}	[-]	skin friction coefficient from the Blasius solution
C_{fLT}	[-]	Ludwig and Tilmann skin friction coefficient

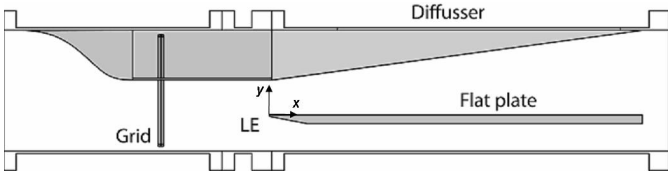

Figure 1 Experimental setup of the flat plate

The leading edge of the plate has a super-ellipse shape. This leading edge (MSE6) was used also in previous experiments in zero pressure gradient and is described in Antoš *at al.* (2014).

The free stream turbulence intensity at the leading edge was either Iu_e = 0.01 or Iu_e = 0.03. The level was manipulated by grids being placed upstream the plate. The CTA measurements in the free stream proved that the grid generates homogenous and close to isotropy turbulence.

MEASUREMENT TECHNIQUE

The mean flow characteristics were measured by a Prandtl tube at the inlet of test section. Measurement of the velocity profiles and turbulence characteristics was carried out by hot-wire probe operated in CTA system - Dantec Streamline. Measurement time was set to 20 s.

The hot-wire probe was put into defined positions by the traversing system. The distance y from the wall is measured by cathetometer with accuracy ±0.02 mm.

The reference value of the free stream velocity was measured by Prandtl probe (dia 6 mm) connected to pressure transducer Druck DPI 145 (range 7 kPa, accuracy ±0.005% FS). Barometric pressure was measured also by Druck DPI 145. The differential pressure between the barometric and the local static pressure was measured by pressure transducers Omega PX653-0.5D5V (range 125 Pa, repeatability 0.05% FS).

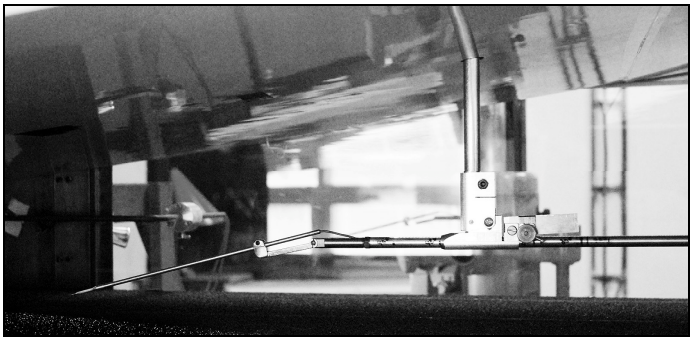

Figure 2 Hot wire probe and traversing system

The flow temperature was measured by thermometer Pt100. Output voltage from the transducers were read by Data acquisition unit HP 34970A.

A single hot-wire probe was used for HWA measurement. A sensor of the probe has tungsten wire of the diameter of d_w=5e-06 m and the length of l_w=1.25e-03 m. Operating wire temperature during measurement was of T_w=493 K. The output anemometer signal was digitalized using the A/D transducer (National Instruments data acquisition system) and recorded in the PC using the LabVIEW scripts (sampling frequency 75 kHz, 16 bit, 2.25e6 samples).

A cooling law of Koch and Gartshore (1972), was used for hot-wire measurements:

$$Nu \left(\frac{T_m}{T}\right)^m = A_w + B_w \, Re^n \quad , \qquad (1)$$

where the Nusselt and the Reynolds numbers are defined by equations:

$$Nu = \frac{R_w E^2}{\pi l_w \lambda_m \left(R_A + R_w\right)^2 \left(T_w - T_a\right)} \quad ; \quad Re = \frac{d_w u \rho_m}{\mu_m} \quad . \qquad (2)$$

The output voltage of the anemometer is denoted E, T_m=0,5(T_w+T_a) is a film temperature, ρ is density, λ is thermal conductivity, μ is molecular viscosity, l_w and d_w are length and diameter of the wire, R_w is operating resistance and R_A is a sum of leads resistance, which is connected in series with R_w.

The hot-wire probe was calibrated in the calibration rig with variable flow velocity. The constants in eq. (1) A, B, n, m were evaluated from calibration data in the range U=(2−20) m/s at operating temperatures within the range of T_w=(450−510) K.

MEASUREMENT UNCERTAINITIES

The experimental uncertainties are estimated based on calculated root mean square errors of interpolations and observed repeatability. The upper limits of relative errors of evaluated quantities depend mainly on precision of the height adjustment of the probe y, accuracy of hot-wire local velocity U and reference dynamic pressure q_r measurement: $\Delta U/U$=±0.005; $\Delta q_r/q_r$=±0.02 (U_e=10 m/s); $\Delta\delta_1/\delta_1$=$\Delta\delta_2/\delta_2$=±0.015; $\Delta H_{12}/H_{12}$=±0.03. The estimated accuracy of evaluation of skin friction τ_w is about 4%.

TURBULENT FREE STREAM FLOW

The free stream velocity decreases with the distance x in the diffuser from the value of U_0. Dimensionless velocity is shown in figure 3.

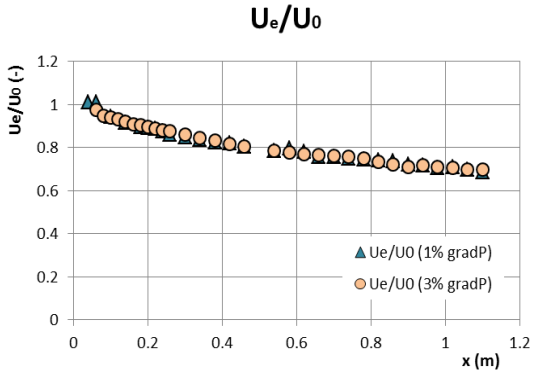

Figure 3 Dimensionless free stream mean velocity $U_e/U_0=f(x)$.

The course can be described in the set up with both levels of free stream turbulence by the empirical formulae:

$$\frac{U_e}{U_0} = 1 - 0.523x + 0.234x^2 \pm 0.02 \quad , [x] = \text{m} \qquad (3)$$

The intensity of the longitudinal component of turbulent velocity fluctuations in the free stream Iu_e is defined:

$$Iu = \frac{\sqrt{u^2}}{U_e} \qquad (4)$$

The intensity increases downstream the diffuser, as one can see in figure 4.

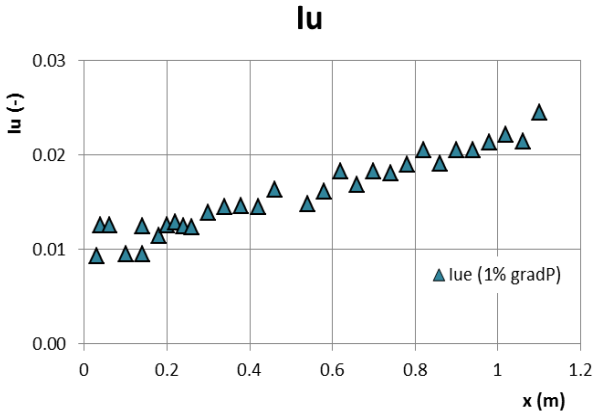

Figure 4 Intensity of free stream velocity fluctuations $Iu_e=f(x)$.

The definition of commonly used dimensionless pressure gradient parameter K is as follows:

$$K = \frac{\nu}{U_e^2} \frac{dU_e}{dx} \quad , \qquad (5)$$

where ν is a kinematic viscosity. Measured distribution of K along the x-coordinate is plotted in figure 5.

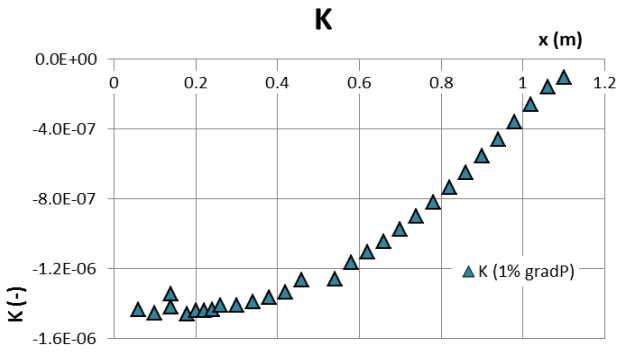

Figure 5 Pressure gradient parameter $K=f(x)$.

The absolute value of negative pressure gradient parameter K in free stream decreases namely due to forming shear layers on upper wall of diffuser and the flat plate.

BOUNDARY LAYER CHARACTERISTICS

The main characteristics evaluated from the measurement are: the customary boundary layer thickness $\delta_{99}=y(U=0.99U_e)$, the displacement thickness δ_1, the momentum thickness δ_2, the wall shear stress τ_w, the shape factor H_{12}, and the skin friction coefficient C_f.

Current setup of decelerated flow with: U_0=10 m/s, Iu_0=0.01 and with diffuser angle of 11° is denoted (1% gradP). The configuration without diffuser (zero pressure gradient): U_0=10 m/s, Iu_0=0.03 is denoted (3% constP). One of previously performed measurements on smooth flat plate with zero pressure gradient: U_0=5 m/s, Iu_0=0.03, denoted (3% T3A+), is also plotted for comparison. Details of that setup are described in Jonáš *et al.* (2000).

Following two graphs show developments of the skin friction coefficient and the shape factor along the x-coordinate.

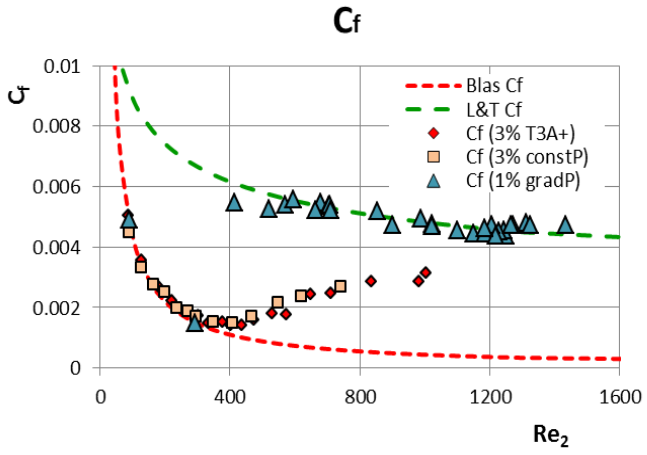

Figure 6 Skin friction coefficient $C_f=f(Re_2)$. Decelerated flow: C_f (1% gradP), zero pressure gradient: C_f (3% constP) and C_f (3% T3A+), $C_{f\,Bl}$, $C_{f\,LT}$.

The graph in fig. 6 shows the skin friction coefficient vs. the momentum Reynolds number. One can see that the transition process is more rapid and ends at lower values of Re_2 in case of adverse pressure gradient (C_f gradP) then at zero pressure gradient (C_f constP). Both zero gradient setups (3% constP) and (3% T3A+) have very similar pattern. Distributions of C_f correspond with the distributions of the shape factor H_{12}, shown in fig. 7.

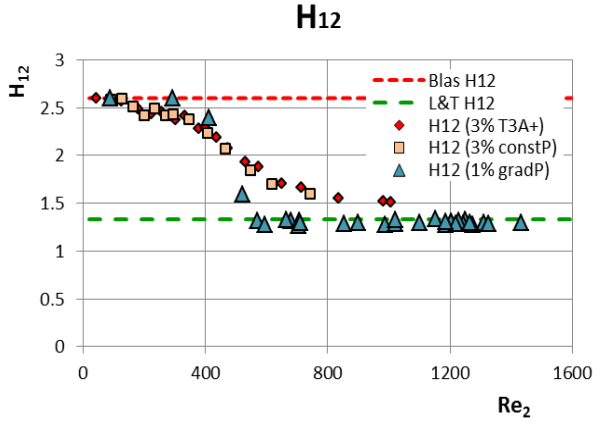

Figure 7 Shape factor $H_{12}=f(Re_2)$. Decelerated flow: H_{12} (1% gradP), zero pressure gradient: H_{12} (3% constP) and H_{12} (3% T3A+), $H_{12\,Bl}$, $H_{12\,LT}$.

The shape factor in case of pressure gradient (H_{12} gradP) decreases quickly to the limit given by Ludwig and Tilmann relationship. It can be seen that transition (1% gradP) finishes at Re_2≈600, where the turbulent boundary layer is observed. Data available for zero pressure gradient are up to Re_2≈1000 and boundary layer is not yet fully turbulent there. Established pressure gradient K=1.4e-6 has quite a strong effect on the transition process.

CONCLUSION

Distributions of the skin friction coefficient C_f and the shape factor H_{12} are presented. The setup of decelerated flow with diffuser angle of 11° was compared with the configuration without diffuser. Preliminary results of experiments on the smooth flat plate transition under negative pressure gradient shows that the transition process is more rapid in case of adverse pressure gradient. Fully developed turbulent boundary layer occurs at lower values of Re_2 under pressure gradient then at zero pressure gradient.

REFERENCES

[1] P. Jonáš, O. Mazur and V. Uruba, On the receptivity of the by-pass transition to the length scale of the outer stream turbulence. Eur. J. Mech. B – Fluids 19, pp. 707-722. (2000)

[2] P. Antoš, P. Jonáš, Reynolds number effect on the transition on a flat plate. HEFAT2014, Proceedings of 10th International Conference on Heat Transfer, Fluid Mechanics and Thermodynamics, pp. 709-711. (2014)

[3] P. Jonáš, ZAMM Z. angew. Math. Mech. 77, S1, pp. 145-146. (1997)

[4] L.U. Schrader, L. Brandt, C. Mavriplis, D. S. Henningson, Receptivity to free-stream vorticity of flow past a flat plate with elliptic leading edge, J. Fluid Mech. Vol. 653, pp. 245–271. (2010)

[5] J.C. Rotta, Turbulent boundary layers in incompressible flow. Progress in Aeronautical Sciences, Vol. 2, Oxford. (1962)
[6] F.A. Koch, J.S. Gastshore, Temperature effects on hot-wire anemometer calibrations. J. Phys. E: Sci. Inst. 5, pp. 58-61. (1972)
[7] P. Spalart, J. Watmuff, Experimental and numerical study of a turbulent boundary layer with pressure gradients, J. Fluid Mech. Vol. 249, pp. 337-371. (1993)
[8] A.E. Samuel, P.N. Joubert, A boundary layer developing in an increasingly adverse pressure gradient. J. Fluid Mech.Vol. 66, pp. 481-505. (1974)
[9] A.G. Gungor, Y. Maciel, M.P. Simens, J. Soria, Analysis of a turbulent boundary layer subjected to a strong adverse pressure gradient, J. of Physics: Conf. Series, 506. (2014)

ACKNOWLEDGEMENT

This work has been supported by the Grant Agency of the Czech Republic GACR GAP101/12/127. Support is gratefully acknowledged.

ANALOGY BETWEEN MOMENTUM AND HEAT TRANSFER IN VERTICAL LIQUID-SOLID FLOW

Garić-Grulović R,[1]*, Jaćimovski D.[1], Bošković-Vragolović N.[2], Pjanović R.[2] and Grbavčić Ž.[†2]
*Author for correspondence
[1] Institute of Chemistry, Technology and Metallurgy, Department of Catalysis and Chemical Engineering, University of Belgrade, Njegoševa 12, Belgrade, Serbia
[2] Faculty of Technology and Metallurgy, University of Belgrade, Karnegijeva 4, Belgrade, Serbia
E-mail: garic@tmf.bg.ac.rs

ABSTRACT

Wall-to-bed heat transfer in hydraulic transport of spherical particles was studied. Experiments were performed by spherical glass particles of 1.20, 1.94 and 2.98 mm in diameter with water in a 25.4 mm I.D. cooper tube equipped with a steam jacket.

The influence of different parameters as liquid velocity, particles size and voidage on heat transfer in hydraulic transport is presented. In the hydraulic transport experiments the Reynolds number varied between 3300 and 20150. The loading ratio (G_p/G_f) was between 0.009 and 0.328, and the fluid superficial velocity was from $0.30 \cdot U_t$ to $2.86 \cdot U_t$, where U_t represents the single particle terminal velocity. For these ratios, the voidage ranged from 0.711 to 0.901.

The data for wall-to-bed momentum and heat transfer, in the hydraulic transport of particles, show that an analogy between these two phenomena exists. The data were correlated by treating the flowing fluid–particle suspension as a pseudofluid, by introducing a mixture-wall friction coefficient (f_w) and a modified Reynolds number (Re_m).

In the hydraulic transport two characteristic flow regimes were observed: turbulent and parallel particle flow regime. The transition between two characteristic regimes occurs at a critical voidage $\varepsilon \approx 0.85$.

INTRODUCTION

Wall-to-bed heat transfer in vertical fluid-solids flow plays an important role in some industrial processes. Numerous industrial applications of fluid-solid systems require transfer determination of transfer characteristics, such as heat transfer in liquid-solid systems. Note that, much industrial continuous processing equipment use a two-phase mixture of solids and fluid such as water treatment, polymerization, biotechnology, food processing etc.

For single-phase flow, there is large number of wall-to-fluid investigations. The most important result, in single-phase flow, is known Chilton-Colburn analogy [1]. For turbulent flow conditions, these authors found:

$$j_H = \frac{f_f}{2} \qquad (1)$$

where j_H is heat transfer factor and f_f is fluid-wall friction coefficient.

[†] Dedicated to the memory of Emeritus Prof. Dr Željko Grbavčić

The literature is lack of experimental data of momentum and heat transfer in fluid-particles systems, which could be used for establishing analogy of these phenomena [2]. The most of knowing papers investigate heat transfer in vertical flow of suspensions of smaller or bigger particles of fruits and vegetables in food industry [3, 4]. The correlations we obtained in our previous research for large particles [5, 6] are:

NOMENCLATURE

A_t	[m^2]	Cross-sectional area of the transport tube
c_p	[J/kg K]	Specific heat
c_s	[m/s]	particle superficial velocity in the transport tube, $=G_p/\rho_p A_t$
d_p	[m]	Particle diameter
Dt	[m]	Diameter of the transport tube
f	[-]	Friction coefficient
f_w	[-]	Mixture-wall friction coefficient
g	[m/s^2]	Gravitational acceleration
G	[kg/s]	Mass flowrate in the transport tube
j_H	[-]	heat transfer factor, $=Nu/\mathrm{RePr}^{1/3}$
L_H	[m]	Length of the heating zone
Nu	[-]	Nusselt number, $\alpha D_t/\lambda$
Pr	[-]	Prandtl number, $=\mu C_{pf}/\lambda$
Re	[-]	Reynolds number, $=D_t\rho_f U/\mu$
Re_m	[-]	Modified mixture Reynolds number, $=D_t\rho_m U_m/\mu_m$
T	[K]	Temperature
u	[m/s]	Mean interstitial fluid velocity in the transp. tube, $=U/\varepsilon$
U	[m/s]	Superficial fluid velocity in the transport tube
U_m	[m/s]	Superficial mixture velocity, $=U+G_p/\rho_p A_t$
U_t	[m/s]	Particle terminal velocity in an infinite medium
W_p	[kg/m^2 s]	Particle mass flux, $=G_p/A_t$

Special characters

α	[kW/m^2 K]	heat transfer coefficient
β		
γ_*	[-]	Defined by eqn.(15)
γ^*	[-]	Criterion for regime transition
ε	[-]	Averaged voidage in the transport tube
λ	[W/m·K]	Water thermal conductivity
ρ	[kg/m^3]	Density
ρ_m	[kg/m^3]	Mean mixture density, $=\varepsilon\rho_f+(1-\varepsilon)\rho_p$
μ	[Ns/m^2]	Viscosity of the fluid
μ_m	[Ns/m^2]	Viscosity of the fluid-particle mixture
δ	[%]	$100 \cdot \frac{1}{n}\sum_1^n \left\lvert \Gamma_{\exp.} - \Gamma_{calc.} \right\rvert / \Gamma_{\exp.}$

Subscripts

mF	Minimum fluidization
f	Fluid
p	Particle

$$j_H = \frac{6565}{\mathrm{Re}_m^{1.5}} \quad for \quad 2800 < \mathrm{Re}_m < 15000 \tag{2}$$

$$j_H = \frac{0.0395}{\mathrm{Re}_m^{0.25}} \quad for \quad 15000 < \mathrm{Re}_m < 32000 \tag{3}$$

where the Re_m is modified mixture Reynolds number.

The aim of the present investigation was to study the simultaneous momentum and heat transfer in vertical liquid-solid flow i.e. hydraulic transport, and to confirm the analogy between these two phenomena obtained in our previous research [5].

EXPERIMENTAL

Simultaneous wall-to-bed momentum and heat transfer in vertical liquid-solids flow of spherical glass particles 1.20, 1.94 and 2.98 mm in diameter was investigated. An outline of the experimental apparatus is shown in Figure 1.

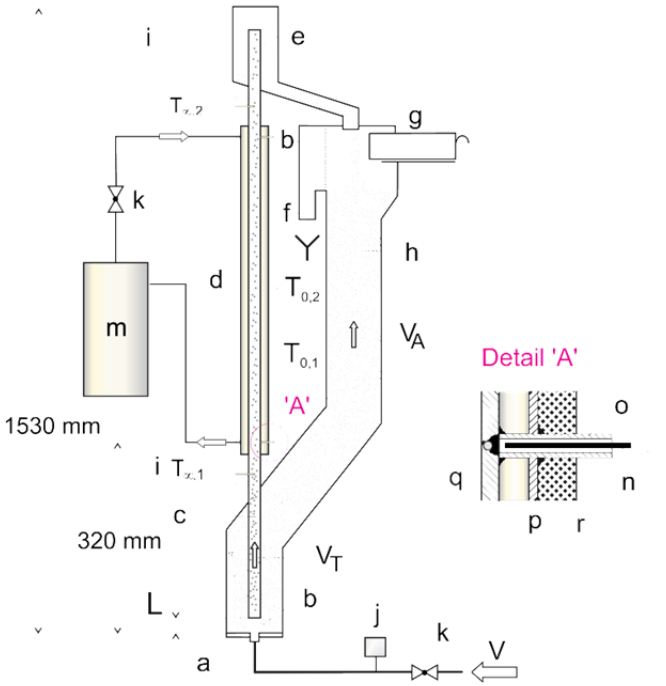

Figure 1. Schematic diagram of experimental systems: Vertical transport setup;

a – inlet nozzle, 20 mm I.D.,
b – screen,
c – transport tube, 25.4 mm I.D.,
d – heating section, 700 mm in length,
e – overflow,
f – water overflow,
g – box,
h – modified spouted bed, 70x70 mm in ross-section,
i – pressure taps,
j – flowmeter,
k – valve,
L – distance of 20mm,
m – steam generator, 30 kW,
T – temperature,
V – water flowrate at the column inlet.

Detail 'A'

n – Ni-Cr thermocouple,
o – cooper tube 8/6 mm,
p – jacket wall,
q – transport tube wall,
r – thermoisolation.

The transport line (c) was a copper tube 27.4/25.4 mm in diameter and 1360 mm long equipped with a 700 mm long steam jacket (d, Figure 1). The heating section (d) was located far enough (320 mm) above the inlet to the transport line for the flow there to be non-accelerating.

At the bottom of the bed the water is introduced through a nozzle (a). The separation distance between the bed bottom and the transport tube inlet (L, Figure 1) was 20 mm. The tube was mounted in a modified spouted bed in order to obtain non-fluctuating controlled flow of particles (h, Figure 1). The inlet flowrate (V, Figure 1) is divided into the tube flow (V_T) and annular flow (V_A). In our experiments, the ratio V_A/V varies between 0.07 and 0.52, so that heated particles falling into the annulus region have enough time to approach inlet water temperature. The particle residence time in the heating section of the transport tube varied between 0.9 and 60 s.

The fluid and particle flowrates are measured using a specially designed box (g), which allows all of the flow (fluid and particles) to be collected, separated and weighed. When the fluid and particle flowrates are to be measured the box (g) is moved to the left to collect the entire flow for a short period of time (10 s to 1 min). The water is then separated from the particles. The particles are weighed dry and the volume of water recorded. The pressure gradient was measured using piezometers.

Saturated steam at atmospheric pressure was supplied to the steam jacket. The inlet water temperature was maintained constant during each experimental run. It ranged from 14 to 16°C. Temperatures were measured with Ni-Cr thermocouples. The wall temperature was measured at two points (inlet and exit) on a such way that junction point was filled with tin at about 0.2 mm from the inside tube wall, as shown schematically on Figure 1 (detail 'A'). The exit temperature of the fluid-particle mixture was measured by a thermocouple located in the tube axis. It was assumed that at the inlet and at the exit of the heating zone, the particles and fluid have the same temperature. Assuming that the particles and fluid have the same temperature at exit, the heat transfer coefficient is [7, 8]:

$$\alpha = \frac{(G_f c_{pf} + G_p c_{pp}) \cdot (T_{\infty,2} - T_{\infty,1})}{(D_t \pi L_H) \Delta T_{lm}} \tag{4}$$

The mean logarithmic temperature difference is defined as:

$$\Delta T_{lm} = \frac{(T_{0,2} - T_{\infty,2}) - (T_{0,1} - T_{\infty,1})}{\ln \dfrac{(T_{0,2} - T_{\infty,2})}{(T_{0,1} - T_{\infty,1})}} \tag{5}$$

Particle characteristics as well as the range of experimental conditions are summarized in Table 1. As a transport medium water was used. The physical parameters of water were determined at mean water temperature [9].

Table 1. Particle characteristics and range of experimental conditions

d_p (mm)	1.20	1.94	2.98
ρ_p (kg/m3)	2641	2507	2509
U_t (m/s) /8/	0.188	0.2878	0.3698
U/U_t	0.435-2.208	0.303-2.863	0.295-2.112
W_p (kg/m2s)	6.5-87.0	0.8-226.1	5.9-239.2
G_p/G_f	0.080-0.237	0.009-0.302	0.055-0.328
ε	0.794-0.901	0.748-0.882	0.711-0.862

RESULTS AND DISCUSSION

Momentum transfer in vertical liquid-solids flow

The one-dimensional momentum equation for the mixture outside of acceleration zone for the transport tube is:

$$-\frac{dP}{dz}=\left(\rho_p-\rho_f\right)g\left(1-\varepsilon\right)+F_w \tag{6}$$

The individual momentum balances for the fluid and particles [10, 11] are:

$$\varepsilon\left(-\frac{dP}{dz}\right)=\beta\left(u-v\right)^2+F_f \tag{7}$$

$$\left(1-\varepsilon\right)\left(-\frac{dP}{dz}\right)=-\beta\left(u-v\right)^2+\left(\rho_p-\rho_f\right)g\left(1-\varepsilon\right)+F_p \tag{8}$$

where $\beta\cdot(u-v)^2$ is the hydrodynamic drag force per volume unit of suspension. F_f and F_p are pressure losses due to fluid-wall and particle-wall friction written in terms of friction coefficient f_f and f_p:

$$F_f=2f_f\ \rho_f\frac{U^2}{D_t} \tag{9}$$

$$F_p=2f_p\rho_p\frac{\left(1-\varepsilon\right)v^2}{D_t} \tag{10}$$

Fluid-wall friction term (F_f) was determined using equation (9) and a standard friction coefficient correlation [7]:

$$f_f=\frac{0.0791}{\mathrm{Re}^{0.25}} \tag{11}$$

where Reynolds number is based on superficial fluid velocity ($Re=D_t\rho_f U/\mu$).

A particle-wall friction coefficient f_p, in particle-wall friction term F_p (equation 10), was correlated in our previous work [11] as:

$$f_p=7.33\cdot10^{-3}\cdot v^{-2},\quad v\ in\ m/s \tag{12}$$

As seen above, from the individual momentum balances for the fluid and particles phases (equations 7 and 8), could be concluded that the overall friction of the flowing mixture with the wall, have additive character, i.e.

$$F_w=F_f+F_p \tag{13}$$

Flow regime in vertical liquid-solids flow

In our previous works [5, 11] we found that the choking criterion for vertical pneumatic transport lines [12], can also be applied as a criterion for the determination of flow regimes in vertical liquid-solids flow of coarse particles.

For the non-steady flow at the transport tube inlet, the one-dimensional momentum equation in the accelerating region of the transport tube [11, 13] is:

$$\gamma\frac{d\varepsilon}{dz}=-\frac{dP}{dz}-(\rho_p-\rho_f)g(1-\varepsilon)-F_w \tag{14}$$

where

$$\gamma=\rho_p v^2-\rho_f u^2 \tag{15}$$

For the steady state conditions, dε/dz=0 (equation 14) and equation (14) resulting to equation (6).

The criterion γ (equation 15), together with a semi-theoretical relationship for the slip velocity at the inlet, leads to an equation for prediction of the choking velocity in vertical gas-particle flow. Our visual observations indicate that γ=0 in hydraulic transport corresponds to the transition from turbulent to the parallel flow. Figure 2, shows the relationship between dimensionless parameter γ^* and transport line voidage, where

$$\gamma^*=\frac{\rho_p v^2-\rho_f u^2}{\rho_f U_t^2} \tag{16}$$

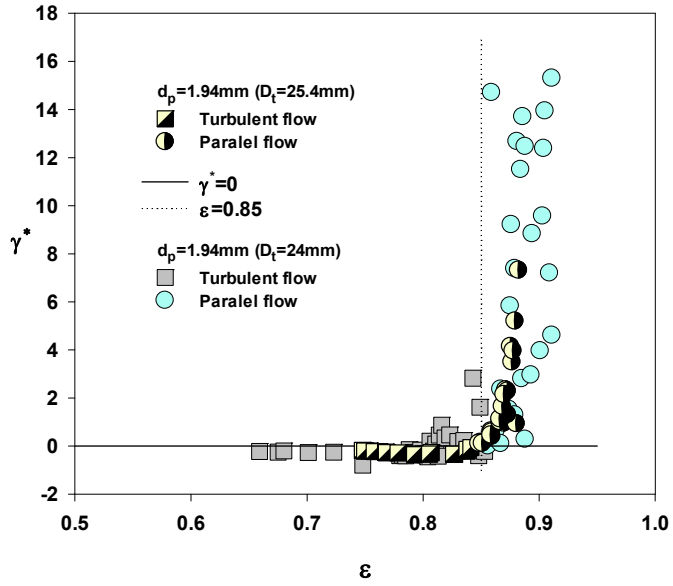

Figure 2. Relationship γ^* vs. ε for vertical liquid solid flow.

Voidage in the transport line, in our investigation, was calculated using measured values of particle mass flowrate (G_p), fluid mass flowrate (G_f) and pressure gradient (-dP/dz) and the model was described in detail in our previous work [11], i.e. based on equation (6÷13) voidage is:

$$\varepsilon=1-\left(\frac{\left(-\frac{dP}{dz}\right)-F_f-F_p}{(\rho_p-\rho_f)\cdot g}\right) \tag{17}$$

We have assumed that the particle wall friction coefficient f_p (equation 12) is unaffected by the transport tube material and water temperature, so that correlation (12) for calculating ε (equation 17) was used. This correlation was developed using the same spherical glass particles and a glass transport tube of the similar diameter, but operated with cold water (14÷16°C).

Figure 2 shows correlation $\gamma^*=f(\varepsilon)$, where the porosity was experimentally measured in the transport tube with diameter D_t = 24 mm [11]. As can be seen, on the same plots, the critical voidage for regime transition is about $\varepsilon \approx 0.85$.

Another way to determine flow regime in liquid-solid flow is the dependence-dP/dz = f (U/U_t). Also, the loading ratio method G_p/G_f can be used for liquid-solids systems.

Figure 3 the experimental data of -dP/dz and G_p/G_f were presented as well as data for ε. In this figure can be noticed that there is a change in the functions G_p/G_f and -dP/dz at the $\varepsilon \approx 0.85$ and $U/Ut \approx 1$. On a plot of -dP/dz vs. U/U_t the change point is close to the pressure minimum.

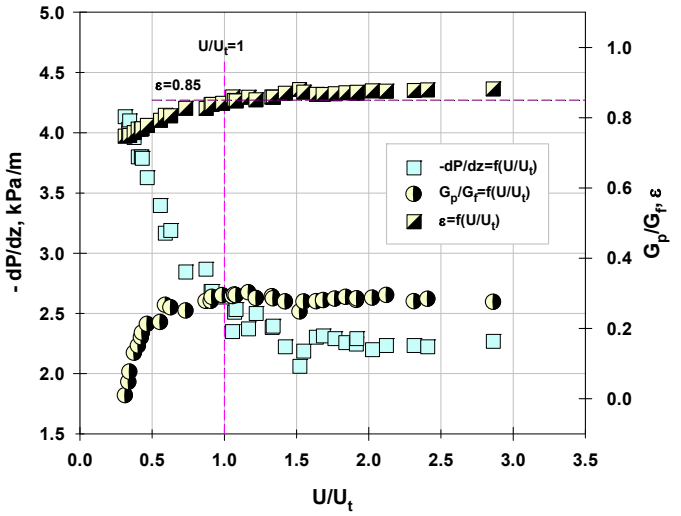

Figure 3. Variation of –dP/dz, G_p/G_f and ε with U/U_t (d_p=1.94 mm).

Concept of pseudofluid

From the overall pressure gradient (equation 6) the sum of fluid-wall friction and particle-wall friction represents mixture overall friction with tube walls (equation 13), i.e.

$$F_w = -\frac{dP}{dz} - \left(\rho_p - \rho_f\right) g \left(1-\varepsilon\right) \qquad (18)$$

Treating a flowing mixture as a pseudofluid with the mean density:

$$\rho_m = \varepsilon \rho_f + (1-\varepsilon)\rho_p \qquad (19)$$

by the analogy with the Fanning friction factor for single phase flow (equation 9), a mixture-wall friction coefficient can be defined [14]:

$$f_w = \frac{F_w D_t}{2 \rho_m U_m^2} \qquad (20)$$

where the mean mixture superficial velocity is:

$$U_m = U + c_s = \frac{G_f}{\rho_f A_t} + \frac{G_p}{\rho_p A_t} \qquad (21)$$

Figure 4 gives the variation of the ratio f_w/f_f, with the U/U_t. As one can expected, the ratio of the friction coefficients f_w/f_f is monotonically decreasing function of fluid superficial velocity. With increase in U/U_t, the ratio f_w/f_f asymptotically tends to 1.

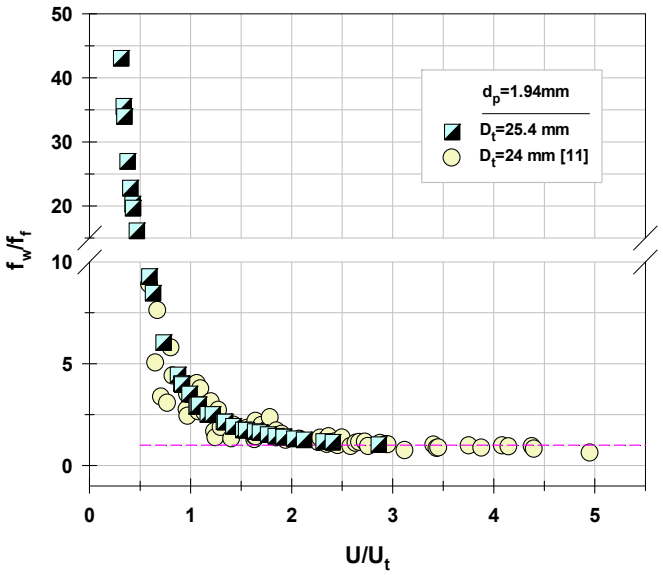

Figure 4. Variation of f_w/f_f with superficial fluid velocity.

Heat transfer in vertical liquid-solids flow

Values of heat transfer coefficient α, are determined from heat balances:

$$\bar{m} \cdot c_p \cdot \left(T_{\infty,2} - T_{\infty,1}\right) = \alpha \cdot D_t \cdot \pi \cdot L_H \cdot \Delta T_{lm} \qquad (22)$$

where $\bar{m} \cdot c_p = (G_f c_{pf} + G_p c_{pp})$, as it use in equation (4).

Effect of the fluid velocities and particle concentration, on the heat transfer coefficients, in our investigation is shown in Figure 5.

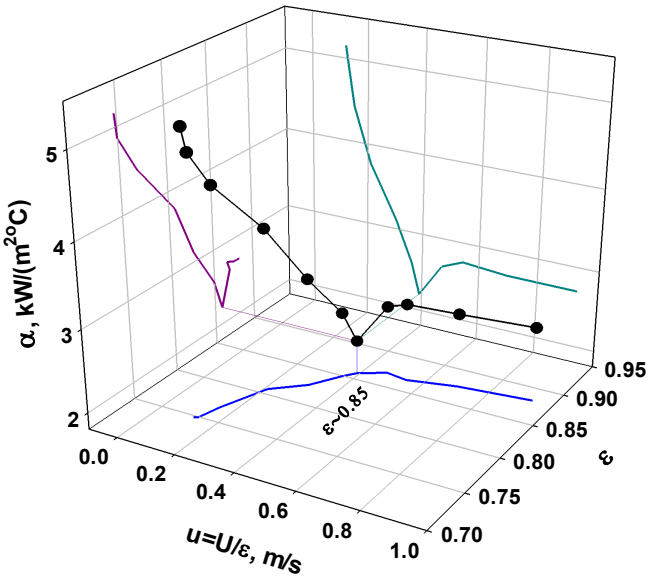

Figure 5. Interdependence fluid velocity, porosity and heat transfer coefficient in a vertical liquid-solids flow (d_p=1.94mm).

The presence of particles improves the heat transfer for lower fluid velocities, where the particle concentration in flowing suspension is generally higher and where the flow regime is turbulent. Also, in this dependence, we can notice the change in flow regime at ε ≈0.85.

Analogy between momentum and heat transfer in vertical liquid-solids flow

In the 1930s, based on the Nernst Film Theory, two duPont researchers, Chilton-Colburn, proposed an analogy between heat transfer and momentum transfer (equation 1). They defined a dimensionless number termed a j-factor, j_H:

$$j_H = \frac{Nu}{\mathrm{Re}\cdot \mathrm{Pr}^{1/3}} = \frac{f_f}{2} \qquad (23)$$

where Re number for the flowing mixture is modified as:

$$\mathrm{Re}_m = \frac{D_t\, \rho_m\, U_m}{\mu_m} \qquad (24)$$

Treating a flowing mixture as a pseudofluid, the effective flowing mixture viscosity is [15]:

$$\mu_m = \mu \cdot \exp\left(\frac{5(1-\varepsilon)}{3\varepsilon}\right) \qquad (25)$$

The heat transfer factor and mixture-wall friction coefficient as a function of Reynolds number for the flowing mixture for hydraulic transport is shown in Figure 6.

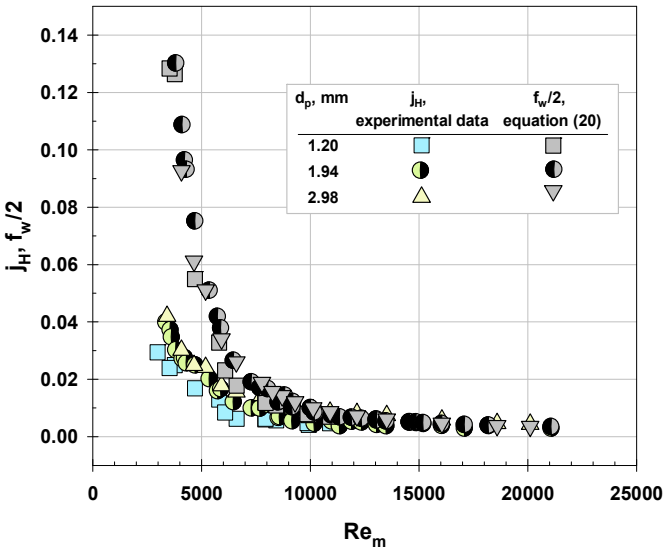

Figure 6. j_H and $f_w/2$ as a function of flowing mixture Re_m number in a vertical liquid-solids flow.

In this figure could be noticed that momentum and heat transfer, analogy, exists only for parallel flow regime of fluid-particles mixture (Re_m>15000). Temperature influence on heat transfer factor, mixture-wall friction coefficient (from this and our previous work [11]), and modified Re_m number, was shown in Figure 7. It is obvious that temperature influence is more significant for turbulent vertical flow (Re_m<15000), while is negligible for parallel flow regime. At low velocities i.e. low Re_m mean fluid temperature is high and because of that influence of density and viscosity on flow parameters of mixture fluid-particles is more considerable.

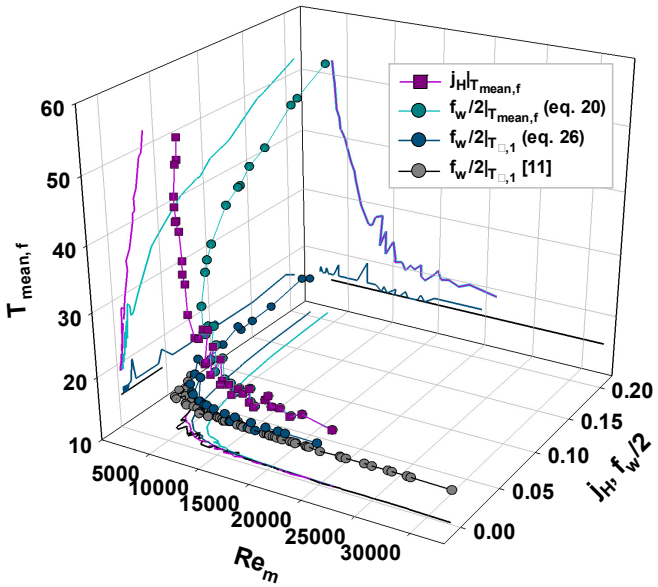

Figure 7. Interdependence j_H, $f_w/2$, $T_{mean,f}$ and Re_m in a vertical liquid-solids flow.

To avoid temperature influence on momentum transfer obtained experimental results are processed the same way as it done in our previous investigations [6, 9, 11], which means that values of $f_w/2$ are calculated for the fluid inlet temperature $T_{\infty,1}$, cold water (Figure 7, Figure 8), using correlation (26):

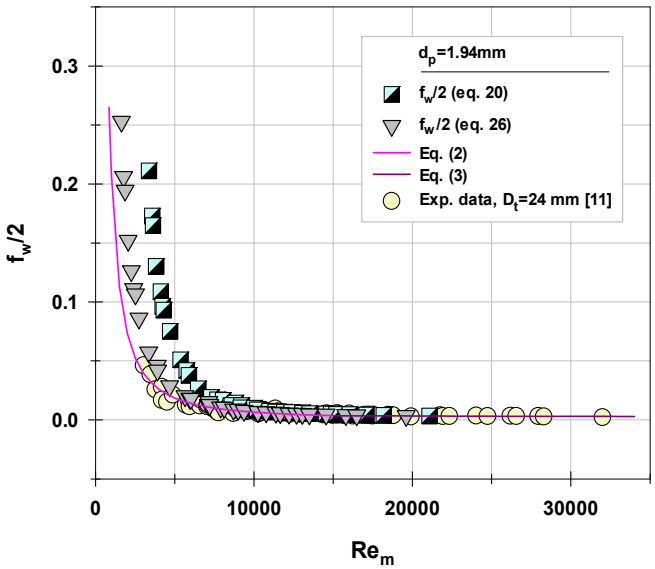

Figure 8. Correction $f_w/2$ and flowing mixture Re_m number on the inlet fluid temperature (cold water).

$$(f_w/2)_{T_{\infty,1}} = (f_w/2)_{T_{sr,f}} \frac{(\mathrm{Re}_m^{0.25})_{T_{sr,f}}}{(\mathrm{Re}_m^{0.25})_{T_{\infty,1}}} \qquad (26)$$

Figure 8 presents obtained data for friction coefficient $f_w/2$, at $T_{mean,f}$ (equation 20), but also friction coefficients $f_w/2$ calculated for the inlet fluid temperature $T_{\infty,1}$ (equation 26). On the same Figure previous experimental data [11] as well as obtained analogies, equations (2) and (3), are also shown.

All of the experimental data for the j_H factor in our hydraulic transport runs are plotted against the modified mixture Reynolds number together with the data for the mixture-wall friction coefficient corrected on the inlet fluid temperature (cold water) are shown in Figure 9.

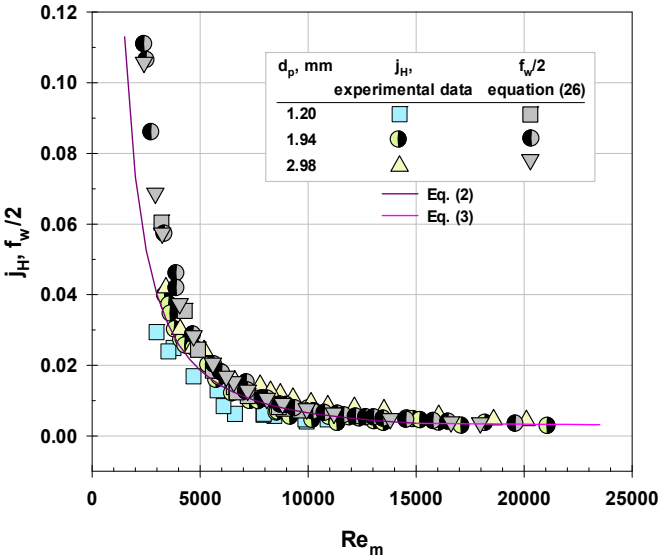

Figure 9. j_H and $f_w/2$ as a function of flowing mixture Re_m number in a vertical liquid-solids flow.

On the Figure 9 could be seen good agreement between corrected values of $f_w/2$ with equations (2) and (3). These values are practically the same in the range of investigated conditions, clearly indicating an analogy between the two phenomena. Medium relative deviations δ between corrected values of $f_w/2$ for the inlet fluid temperature (equation 26) and equations (2) and (3) are respectively 20.7% and 10.4%.

CONCLUSION

Simultaneous momentum and heat transfer in hydraulic transport of coarse spherical glass particles was studied.

In hydraulic transport of coarse spherical glass particles two characteristic flow regimes were observed: "parallel" flow and "turbulent" flow regime. A parameter γ^* appears as criterion for the regime distinction.

The data were correlated treating the flowing fluid-particle mixture as a pseudofluid, by introducing mixture-wall friction coefficient (f_w) and modified mixture Reynolds number (Re_m).

The data for wall-to-bed heat transfer in hydraulic transport of coarse spherical glass particles shows that an analogy between momentum and heat transfer exist since there is clear realationship between experimental values for j_H and values for mixture-wall friction coefficient at inlet temperature of the fluid.

Acknowledgement

Financial support of the Serbian Ministry of Education and Science (Project ON172022) is gratefully acknowledged.

REFERENCES

[1] T.H. Chilton, A.P. Colburn, Mass transfer (absorption) coefficients prediction from data on heat transfer and fluid friction, *Ind. Engng. Chem*., 26, 1934, pp. 1183-1187

[2] Z. Astolfi-Filho, E. Basílio de Oliveirac, J. Sélia dos Reis Coimbrac, J. Telis-Romeroa, Friction factors, convective heat transfer coefficients and the Colburn analogy for industrial sugarcane juices, *Biochemical Engineering Journal*, 60, 2012, pp. 111-118.

[3] N.J. Heppel, Measurement of the liquid-solid heat transfer coefficient during continuous sterilization of liquids containing particles, Presented at the 4th Intl. Cong. on engineering and food, Edmonton, Alberta, Canada, 1985.

[4] M. Barigou, S. Mankad, P.J. Fryer, Heat transfer in twophase solid-liquid food flows: a review, Food and Bioproducts Processing vol. 76 issue 1 (1998), pp. 3-29.

[5] R.V. Garić-Grulović, Ž.B. Grbavčić, Z. Lj. Arsenijević, Heat Transfer and Flow Pattern in Vertical Liquid-Solids Flow, Powder Technol., 145 (3), (2004), pp. 163-171.

[6] D.R. Jaćimovski, R.V. Garić-Grulović, Ž.B. Grbavčić, M.M. Đuriš and N.M. Bošković-Vragolović, Momentum, heat, and mass transfer analogy for vertical hydraulic transport of inert particles, Chem. Ind., 68 (1), 2014, pp. 15–25.

[7] R.B. Bird, W.E. Stewart and E.N. Lightfoot, Transport Phenomena, Wiley, New York, 1960.

[8] J. Welty, C.E. Wicks, G.L. Rorrer and R.E. Wilson, Fundamentals of Momentum, Heat and Mass transfer, 5th ed., John Wiley and Sons, New York, 2008.

[9] H.J. Perry, Chemical Engineer's Handbook, 6th ed., McGraw-Hill, New York, 1987.

[10] C. E. Capes and K. Nakamura, Vertical pneumatic conveying: An experimental study with particles in the intermediate and turbulent flow regimes, *Can. J. Chem. Eng*., 51, 1973, pp. 31-38.

[11] Ž.B. Grbavčić, R.V. Garić, D.V. Vuković´, Dž. E. Hadžisma-jlović, H. Littman, M.H. Morgan III and S.Dj. Jovanović, Hydro-dynamic modelling of vertical liquid-solids flow, *Powder Technol.*, 72, 1992, pp. 183– 191.

[12] Y. Day, H. Littman and M.H. Morgan III, A New Choking Velocity Correlation for Vertical Pneumatic Conveying, *Chem. Eng. Sci*., 45, pp. 1990,355.

[13] L.S. Leung, in: J.R. Grace, J.M. Matsen (Eds.), Fluidization, Plenum Press, New York, 1980, pp. 25– 68.

[14] R.V. Garić-Grulović, Ž.B. Grbavčić and Z. Lj. Arsenijević, A pseudo-fluid representation of vertical liquid–coarse solids flow**,** *J. Serb. Chem. Soc. 70* (5), 2005, pp. 775–784.

[15] E. Barnea and J. Mizrahi, A generalized approach to the fluid dynamics of particulate systems: Part 1. General correlation for fluidization and sedimentation in solid multiparticle systems, *Chem. Engng. J*., 5 (2), 1973, pp. 171-189.

ENHANCEMENT OF FORCED-CONVECTION SUBCOOL BOILING HEAT TRANSFER BY ELECTRIC FIELD

Mitsuhiro UEMURA
Institute of Industrial Science,
The University of Tokyo,
4-6-1 Komaba, Meguro-ku, Tokyo,
Japan
E-mail: uemura@iis.u-tokyo.ac.jp

ABSTRACT

Enhancement of forced-convection boiling heat transfer by electric field is investigated experimentally. In an early stage of the immersion process of a high temperature horizontal filament into water, a gas sheet is formed around and after the filament and it markedly decreases the boiling cooling rate of the filament. In this study, in order to enhance the boiling cooling rate, forced collapse of the gas sheet by imposing electric field was attempted. The experimental conditions is boiling of a pure water occurs on horizontal platinum wire 0.5mm in diameter under the atomospheric pressure, and a D.C. voltage up to 600V is applied between the heat transfer surface and an electrode made of electrical conductivity glass of 1mm thick apart. The whole boiling curve is mesured under different applied voltages and different the falling velocity of wire of 0.5 to 2.2 m/s, and subcool temperature 40K, 60K, 80K. The experimental results are effective for the electric field to promote disintegration of the gas sheet when the dipping speed(0.5 ~ 2.2m/s), subcooling degree(40K, 60K, 80K) boiling cooling rate applied electric field of 600V/cm are shown to be increased twice.

INTRODUCTION

In rapid solidification processes that aim at micro-structuring, formation of amorphous phases, and solute capture, a rapid cooling rate is generally required. The rotating-water spinning method is typical of the rapid solidification systems that produce fine-wire materials by rapid cooling, using liquid boiling. In this method, a molten liquid is ejected into rotating water as a jet, and downstream of this jet, a gas-sheet is formed. This gas sheet is at the initial states of film-boiling, which causes the cooling rate to decrease [1, 2]. Several methods are known to have effects of varying degrees on promoting heat transfer under film boiling. For example, application of an electric field (including its ability to forcefully break up the film-boiling state) and ultra-sonic wave each have an effect to some degree [3, 4]. Further, it is also know that application of an electric field on the gas-liquid interface formed in film boiling leads to instability in the interface [5]. Therefore, there is a possibility that the above-mentioned gas-sheet can be made to collapse by destabilizing the interface with the application of an electric field on the interface. In order to investigate the possibility of forceful collapsing of the gas-sheet, an electric field is applied in this work, on the gas-sheet that is formed during the fall of a heated horizontal wire through water at a sub-cooled temperature.

NOMENCLATURE

C_p	[J/kgK]	Specific heat at constant pressure
g	[m/s^2]	Gravitational acceleration
k	[W/mK]	Thermal conductivity
L	[J/kg]	Latent heat of vaporization
U	[m/s]	Velocity

Special characters

α	[m^2/s]	Thermal diffusivity
δ	[m]	Vapor thickness
ε	[-]	Relative permittivity
η	[-]	Interface disturbance
λ	[m]	Wavelength of vapor
ν	[m^2/s]	Kinematic viscosity
ρ	[kg/m^3]	Density
σ	[N/m]	Surface tension
ω	[1/s]	Disturbance angular frequency

Subscripts

l	Liquid
v	Vapor
W	Wall surface
sat	Saturation
sub	Subcool

EXTERNAL APPARATUS

Figure 1 shows a schematic diagram of the experimental apparatus used in this work. The heat transfer surface is a fine platinum wire of 0.5mm dia., which models the Rotation underwater spinning process. In order to prevent the end-point collapse of the vapor film from the point where the electrode is connected to the fine platinum wire, this platinum wire is bent in a 'U' shape. The wire is kept horizontally and is 80 mm long. In this horizontal section, ultra-fine platinum wires of 0.03mm dia. are spot-welded at 30 mm intervals in order to measure voltage. To conduct the experiments, the fine platinum wire is first heated in the atmosphere to 1300°C by direct flow of current through the wire, using a DC stabilized power supply. Next, the wire is dipped at a constant speed U in a pool of water

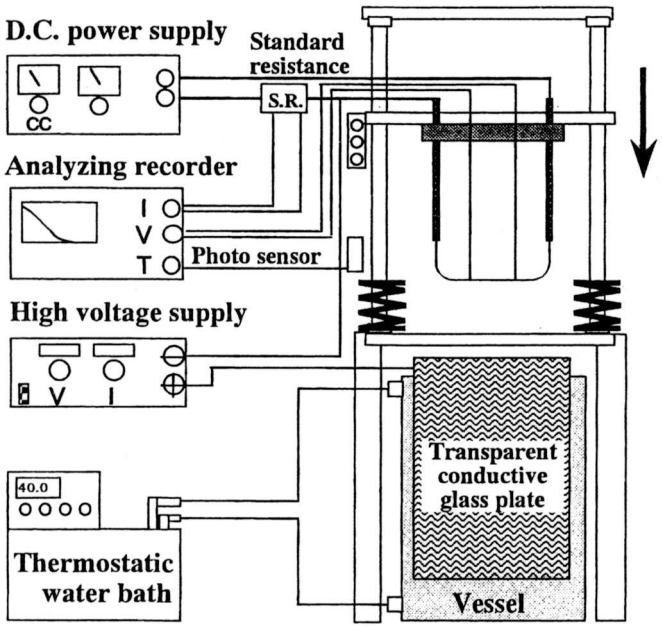

Figure 1 Experimental apparatus

maintained at a fixed sub-cooling ΔT_{sub} and atmospheric pressure. An experiment run is continued until the wire comes to a stop after falling a distance H=150mm through the pool of water. In the experiments, ΔT_{sub} is varied as 40, 60 and 80 K. The falling speed U is varied between 0.5 and 2.2 m/s by changing the falling height of the wire above the bath.

Inside the water bath, electrically-conducting flat glass strips (used as positive electrodes) have been placed vertically at intervals of 10 mm, centred about the falling path of the horizontal wire. In the experiments where an electric field is applied, a DC voltage E is applied between the conducting glass strips and the horizontal wire; note that the horizontal wire is used as the earth connection. The state of the falling wire is recorded in the back-lit method in which lighting is made through the conducting the glasses and a high-speed video camera of 500 frames/sec used.

The experiments carried out are of the following two types. The first type is the experiments in which fundamental data on the cooling rates of the falling horizontal wire are obtained. To do this experiment, first the horizontal wire is heated in the air, and dropped through the water bath after reducing the wire current to a very small value and with the applied voltage E=0V. The voltage variation of this fine wire during the cooling process is measured, and the cooling curve of the fine wire is obtained from a relationship between the resistance of the platinum wire and temperature. The second type is the experiment in which the effect of applied voltage is investigated. In this experiment, obtaining the cooling curve from the changes in the wire resistance is rather difficult because of the applied voltage. Therefore, only the high-speed video observations are recorded.

PRELIMINARY CONSIDERATIONS

Figure 2 shows the cooling curve of the fine wire when it falls through the water bath. The figure shows that the film boiling condition prevails on the platinum wire for up to about the wire temperature of 500°C. This film boiling condition is such that it consists of two conditions: the first is the one in which the cooling rate is drastically low due to the existence of a gas-sheet and the second is the condition that the cooling rate increases due to the detachment of the gas-sheet from the wire [1, 2].

It should be noted that the gas-sheet formed in the system shown in Fig. 1 (or described by Fig. 2) can be destabilized by the application of an electric field if the characteristic length of the gas-sheet exceeds the instability critical wavelength. Further, for the generated disturbances to cause the instability

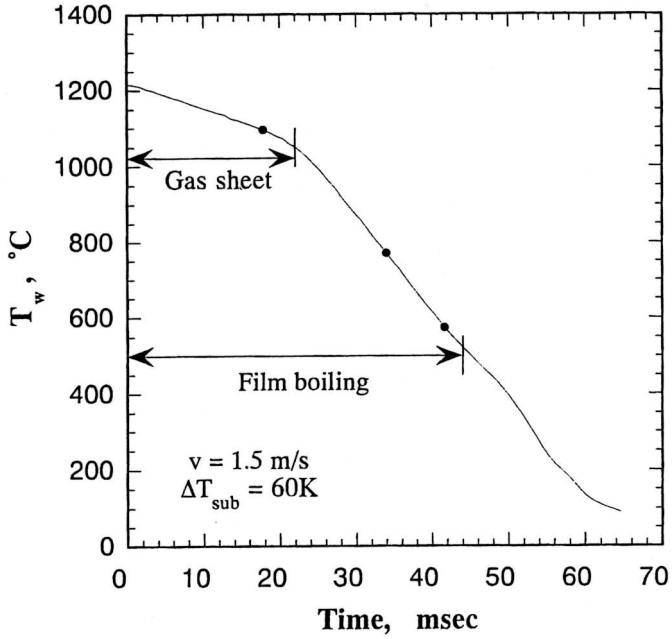

Figure 2 Cooling curve of horizontal platinum thin line

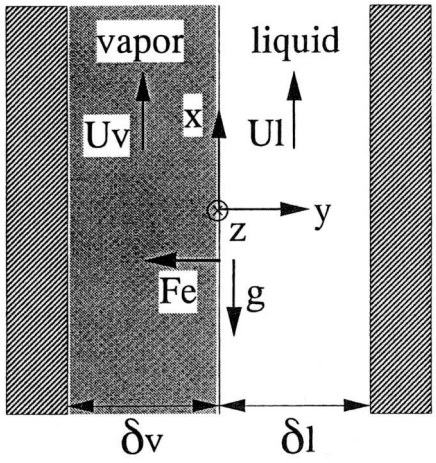

Figure 3 Model for instabillity analysis

in the interface in a short time as in the present experiment of the falling horizontal wire, the growth rate of the disturbances should be high enough. Therefore, preliminary considerations are made here regarding the effect of electric field on the critical wavelength and growth rate of disturbances. To do so, it is necessary to destabilize the liquid-vapor inter-surface soon after the fine wire plunges into the liquid. Thus, a disturbance is introduced to the vapor film formed around the fine wire as soon as the wire enters the liquid, and its destabilizing effect on the gas-sheet is examined. To simplify this problem and examine the effect of the applied electric field, the state of film boiling on the wire at a position 90° from the lowest point on the wire is approximated by the system of film boiling on a vertical surface as shown in Figure 3, under a uniform electric field. The test liquid considered is water, which has a charge saturation time of [μsec] order. Therefore, by considering water as a fully-conducting fluid, the following equation for the disturbance is obtained.

$$\begin{aligned}&[\rho_v \coth(M\delta_v)+\rho_l \coth(M\delta_l)]\omega^2\\&+2m[\rho_v U_v \coth(M\delta v)+\rho_l U_l \coth(M\delta_l)]\omega\\&+m^2[\rho_v U_v^2 \coth(M\delta v)+\rho_l U_l^2 \coth(M\delta_l)]\\&=\sigma M^3-8.85\times10^{-12}\varepsilon_v\left(\frac{E}{\delta_v}\right)^2\coth(M\delta_v)M^2\end{aligned} \quad (1)$$

Here, liquid phase velocity U_l is the velocity of the falling wire; ω is the angular velocity of the disturbance; σ is surface tension; ε_v is the dielectric constant of vapor; m and n are the wave numbers in x and y directions, respectively, and $M^2=m^2+n^2$;

Note that the vapor film thickness is small in the circumferential direction of the fine wire (i.e. x direction in Fig. 3), and therefore, the disturbances in the axial direction of the wire has a strong effect on the vapor-liquid interface formed by film boiling. Hence, if m=0 in Eq.(1), then the minimum or the critical voltage E_{cr} that generates a disturbance on the gas-liquid interface of Fig. 3 due to the electric field can be obtained from the following equation

$$E_{cr}=\sqrt{\frac{n\delta_v^2\sigma}{8.85\times10^{-12}\varepsilon_v\coth(n\delta_v)}} \quad (2)$$

Using this equation, it is possible to obtain the critical wavelength at a given applied voltage *E*, and also the rate of growth of a disturbance and the most dangerous wavelength (or the wavelength of the most rapidly growing wave) at a given *E* can be obtained in the same manner. Figure 4 shows the critical wavelengths (by curves) and the most dangerous wavelengths (by symbols) as a function of the applied voltage *E*. However, the vapor film thickness cannot be evaluated accurately from the experiments because of the entrapment of air in vapor, and is thus treated as a parameter in the calculations. The straight line in the figure is drawn at a coordinate equal to the length of the horizontal fine wire used in the experiments. The figure shows that if E<100V, the critical wavelength is less than the wire length even at a larger vapor film thickness. Thus, it is possible to obtain disturbances along the wire.

Figure 5 shows an example of how the applied electric field affects the growth rate of disturbances. It can be seen that the growth rate increases sharply with the applied electric field. The above preliminary considerations show that the gas-sheet can be destabilized by the application of an electric field *E* of the order of 100V

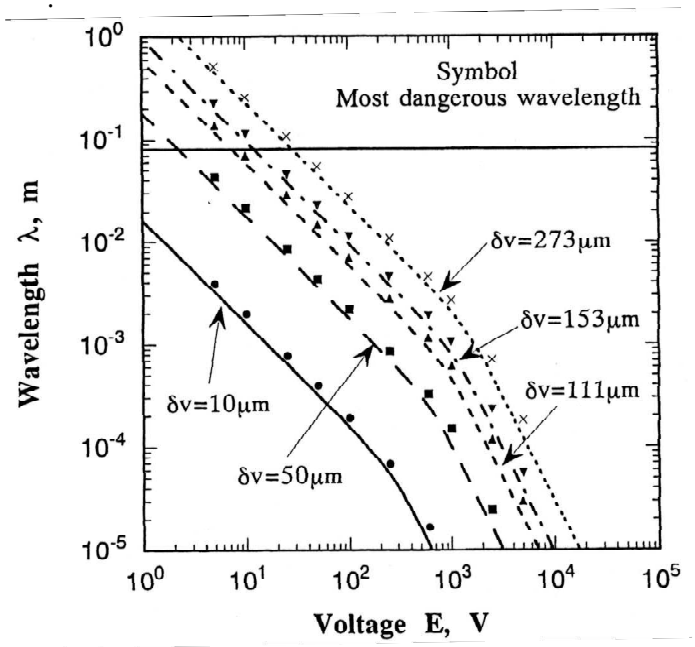

Figure 4 Effect of imposed voltage on unstable wavelength

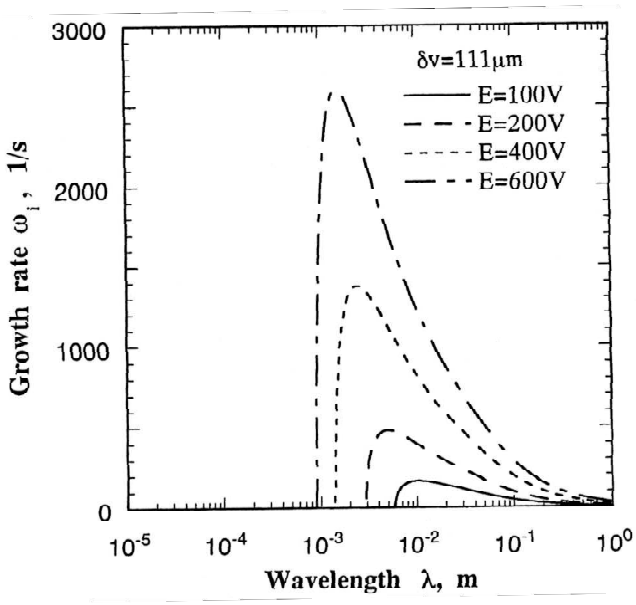

Figure 5 Effect of imposed voltage on growth rate

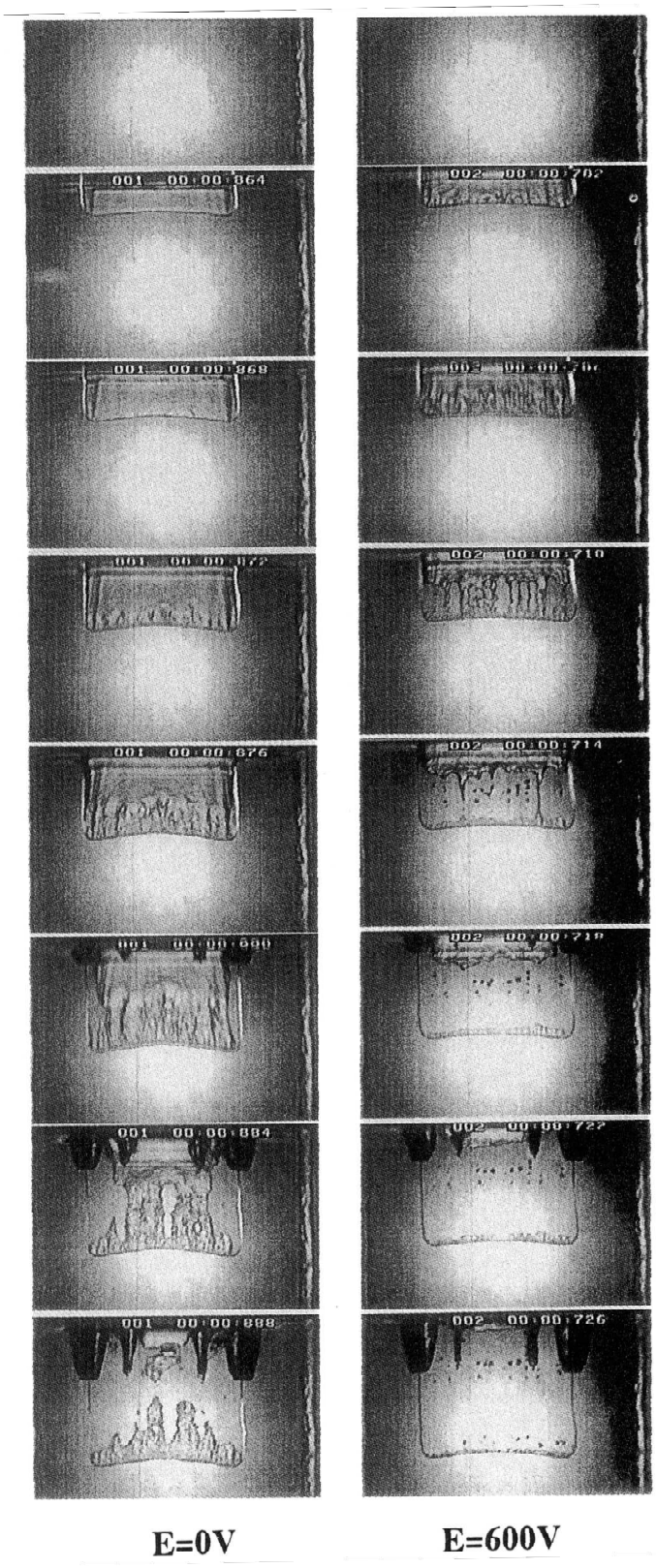

Figure 6 Visual observation of efcts of imposed voltage

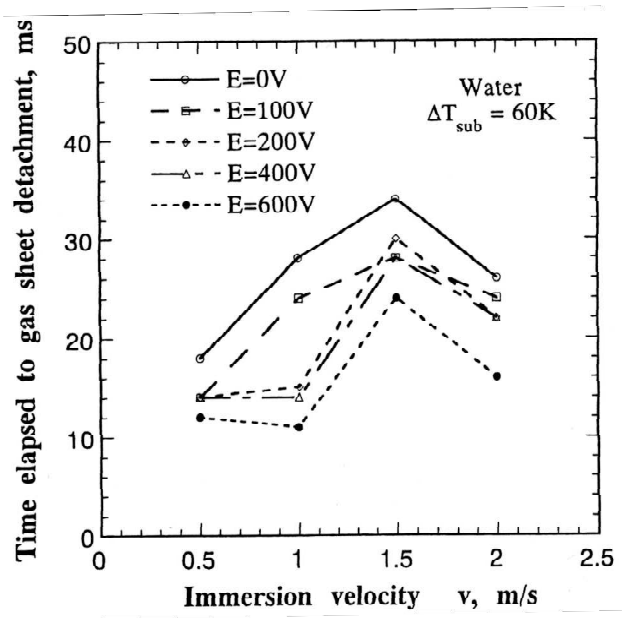

Figure 7 Effects of imposed voltage on time elaped to gas sheet detachment

EXPERIMENTAL RESULTS: APPLICATION OF ELECTRIC FIELD

Figure 6 shows a comparison of the states of the fine wire for E=0 and 600 V when the wire is being immersed in a liquid bath where ΔT_{sub}=60 K at a rate v=2.2 m/s. The figure shows that E=600 V results in more disturbances in the gas sheet soon after the immersion in comparison to the case of E=0 V. In addition, it shows that both the time taken for the gas-sheet to detach itself from the wire, and the time taken for the bubbling to stop have reduced on the application of the electric field. As stated in the preliminary considerations section, the turbulences that occur on the gas-liquid interface of the gas sheet form waves in the horizontal direction, causing the gas-sheet to break up into several vertical gas cylinders with the passing of time from the starting point of immersion.

As a measure of the effect of the forced gas-sheet collapse by the applied electric field, the time taken for the gas-sheet to collapse is shown in Figure 7 as a function of the immersion velocity, at different applied voltages E for ΔT_{sub}=60 K. The figure shows that the application of the electric field has made it possible to obtain about a two-fold cooling improvement in the time taken for the gas-sheet collapse.

CONCLUSIONS

The aim of this work was to promote the rate of rapid cooling in the rotating-water spinning method, which is a typical example of a rapid solidification system that uses liquid boiling for rapid cooling. To promote the cooling rate, the possibility of breaking the gas-sheet forcefully by application of an electric field was investigated. It was found that the application of an electric field is effective in breaking up the gas-sheet forcefully. Also, it was shown that forceful breakage of the gas-sheet promotes the rapid cooling rate.

REFERENCES

[1] Ohnaka, Itsuo; Shimaoka, Mitsuyoshi., Heat transfer in in-rotating-liquid-spinning process, *Heat and mass transfer in materials processing*, (A93-10826 01-31), p. 315-329.

[2] Cho, K.-S., and Takamatsu, H., and Honda, H., Effect of Spinning conditions on the shape of metallic wires produced by the In-Rotating-Water Spinning Method, *Nippon Kinzoku Gakkaishi*, Vol. 62, No.2, 1998, pp. 189-196

[3] Uemura, M., Nishi, S., and Tanasawa, I., Enhancement of pool boiling heat transfer by static electric field, *International Heat Transfer Conference*, Vol. 9, 1990, pp. 75-80

[4] Serizawa, S., Aoki, N., Mukai, M.,and Takahashi, O., Effect of ultrasonic waves on boiling heat transfer, *National Heat Transfer Symposium*, Vol. 29,, 1992 pp. 295-297

[5] Tanasawa, I., Nishio, S., Takano, K., and Uemura, M., Enhancement of boiling heat transfer by electric field, *Ienergy conversion and utilization with high efficiency*, 1990, pp. 58-58